Biosensor activatable in both fluorescence and 129Xe NMR for detection of recombinant proteins

Emilie Mari

To cite this version:

Emilie Mari. Biosensor activatable in both fluorescence and 129Xe NMR for detection of recombinant proteins. Analytical chemistry. Université Paris Saclay (COmUE), 2017. English. NNT : 2017SACLV067 . tel-01733118

HAL Id: tel-01733118
https://theses.hal.science/tel-01733118

Submitted on 14 Mar 2018

HAL is a multi-disciplinary open access archive for the deposit and dissemination of scientific research documents, whether they are published or not. The documents may come from teaching and research institutions in France or abroad, or from public or private research centers.

L'archive ouverte pluridisciplinaire **HAL**, est destinée au dépôt et à la diffusion de documents scientifiques de niveau recherche, publiés ou non, émanant des établissements d'enseignement et de recherche français ou étrangers, des laboratoires publics ou privés.

université
PARIS-SACLAY

NNT : 2017SACLV067

Thèse de doctorat

Biosensor activatable in both fluorescence and ^{129}Xe NMR for detection of recombinant proteins

Thèse de doctorat de l'Université Paris-Saclay
préparée à L'Université Versailles-Saint-Quentin

École doctorale n°573 Interfaces
Approches interdisciplinaires : Fondements, applications et innovations
Spécialité de doctorat: Les sciences du Vivant

Thèse présentée et soutenue à Gif-sur-Yvette, le 06 Novembre 2017, par

Emilie Mari

Composition du Jury :

Bruno Kieffer Professeur, Université de Strasbourg (IGBMC/CNRS)	Président
Céline Landon Chargée de recherche, CNRS Orléans (CBM)	Rapporteur
Guy Lippens Professeur, INSA Toulouse (LISBP)	Rapporteur
Marie Erard Professeure, Université Paris Saclay (LCP/CNRS)	Co-Directrice de thèse
Bernard Rousseau Directeur de recherches CEA, Université Paris Saclay (DRF/SCBM)	Co-Directeur de thèse
Patrick Berthault Directeur de recherches CEA, Université Paris Saclay (DRF/NIMBE)	Directeur de thèse
Ewen Lescop Chargé de recherche, Université Paris Saclay (ICSN/CNRS)	Invité

THÈSE DE DOCTORAT DE L'UNIVERSITÉ PARIS SACLAY PRÉPARÉE À L'UNIVERSITÉ VERSAILLES-SAINT-QUENTIN

ECOLE DOCTORALE 573
INTERFACES : APPROCHES INTERDISCIPLINAIRES: FONDEMENTS, APPLICATIONS ET INNOVATIONS
SPÉCIALITÉ : LES SCIENCES DU VIVANT

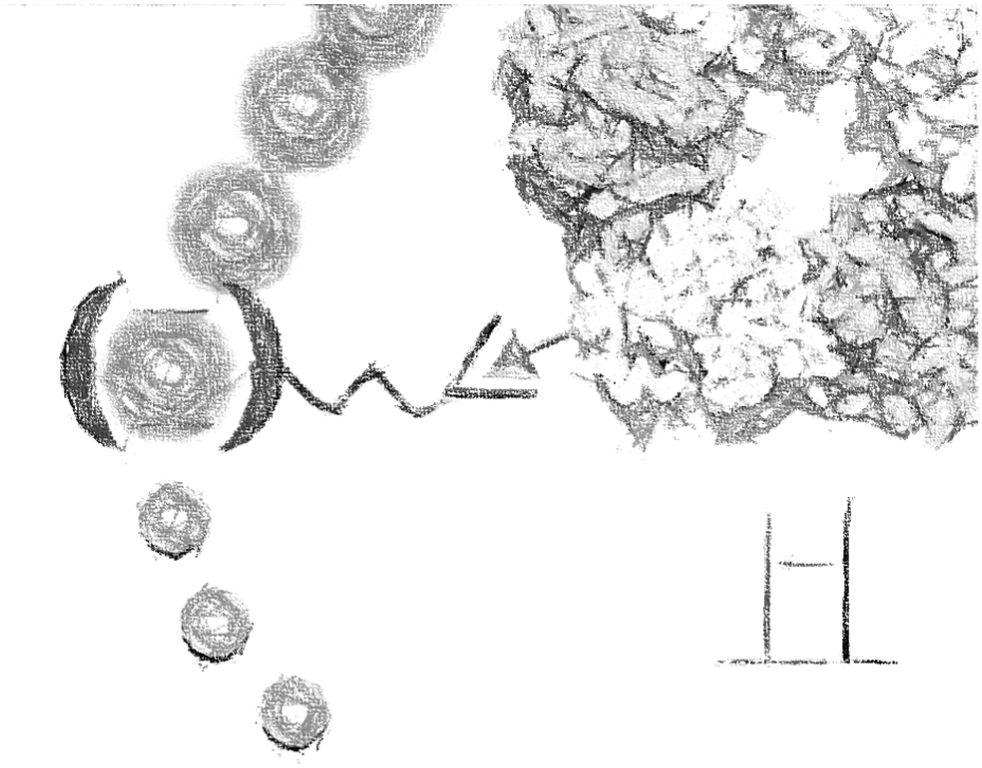

Par Emilie Mari

Biosensor activatable in both fluorescence and ^{129}Xe NMR for detection of recombinant proteins

[November 06, 2017– `PhD thesis` by Emilie Mari]

A Nam.

PUBLICATIONS

Scientific papers

1. **^{129}Xe NMR-based sensors: biological applications and recent methods**
   E. Mari and P. Berthault
   Analyst, ***142****, 3298 - 3308 (2017) DOI: 10.1039/C7AN01088E*

2. **Note: Spin-Exchange Optical Pumping in a Van**
   C. Chauvin, L. Liagre, C. Boutin, E. Mari, E. Léonce, G. Carret, B. Coltrinari, and P. Berthault
   Rev. Sci. Instrum. ***87****, 1, 016105 (2016) DOI: 10.1063/1.4940928*

3. **A doubly-responsive probe for the detection of Cys4-tagged proteins**
   N. Kotera, E. Dubost, G. Milanole, E. Doris, E. Gravel, N. Arhel, T. Brotin, J.-P. Dutasta, J. Cochrane, E. Mari, C. Boutin, E. Léonce, P. Berthault and B. Rousseau
   Chem. Commun. ***51****, 11482-11484 (2015) DOI: 10.1039/C5CC04721H*

4. **Synthesis of Cryptophanes with Two Different Reaction Sites**
   L-L. Chapellet, J. Cochrane, E. Mari, C. Boutin, P. Berthault, and Thierry Brotin
   J. Org. Chem. ***80****, 12, 6143–6151(2015) DOI: 10.1021/acs.joc.5b00653*

Submitted papers

1. **A Fluorescence-^{129}Xe NMR Probe Enabling Detection and Biological Inhibition of EGFR in Non-Small Cell Lung Cancer**
   G. Milanole, B. Gao, A. Paoletti, G. Pieters , C. Dugave, E. Deutsch, S. Rivera, F. Law, J-L. Perfettini, E. Mari, E. Léonce, C. Boutin, P. Berthault, H. Volland, F. Fenaille, T. Brotin and B. Rousseau
   Bioorg. Med. Chem. (2017)

2. **A Straightforward Access to Cyclotriveratrylene Analogues with C1-Symmetry: Toward the Synthesis of Water-Soluble Monofunctionalizable Cryptophanes**
   G. Milanole, B. Gao, E. Mari, P. Berthault, G. Pieters, B. Rousseau
   J. Org. Chem. (2017)

Oral communications

1. **^{129}Xe sensing tagged proteins**
   CEA, France (December 2016)

2. **Intracellular probe for fluorescence-NMR detection**
   European Molecular Imaging Meeting, Utrecht, Holland (March 2016)
3. **^{129}Xe biosensors and biological applications**
   CEA, France (December 2015)
4. **A smart probe for intracellular detection**
   Grand Bassin Parisien, France (May 2015)

Poster communications

1. **Bimodal ^{129}Xe NMR and fluorescence biosensor for tagged proteins**
   Ecole Paris Saclay, France (April 2016)
2. **Detection of tagged peptides by a doubly smart sensor**
   Interfaces, Ecole Polytechnique, France (November 2015)
3. **Design and synthesis of a doubly responsive biosensor**
   XeMat congress, Dresden, Germany (September 2015)

ACKNOWLEDGEMENTS

D'abord un grand merci à Céline Landon et Guy Lippens d'avoir accepté d'étudier et de juger ce travail. Plus que 238 pages, courage ! Merci à Bruno Kieffer d'avoir accepté de faire partie de mon jury de thèse et Ewen Lescop de m'avoir si gentiment conseillée et encouragée à mi-parcours.

Je remercie tout particulièrement mes trois directeurs de thèse qui ont chacun su se rendre indispensable et présent pendant ces trois années. Merci Bernard d'avoir cru en mes capacités de synthèse organique alors que c'était loin d'être gagné, merci pour tes blagues et tes pertes de mémoire intempestives - loin de moi l'idée d'attaquer les personnes âgées. Merci Marie d'avoir su gérer mes allées et venues à l'improviste, d'avoir pris le relais quand il a fallu, d'avoir été là en journée en soirée et même le week-end. J'avais peut être un bureau, un ordinateur et une chaise mobiles et pas toujours disponibles, mais toi en revanche tu as toujours été un point fixe pour moi. Enfin, merci Patrick de m'avoir accueillie en stage de fin d'études, de m'avoir donné le goût de la recherche, de m'avoir donné l'opportunité de faire une thèse, de m'avoir formée et permis de participer à tant de projets variés et plus passionnants les uns que les autres. Merci de m'avoir laissé tant d'autonomie et d'avoir placé les filets au cas où. Sincèrement, merci à vous trois.

Mes chers collègues de synthèse ! Je ne vous citerai pas vous êtes bien trop nombreux à avoir rythmé le SCBM, à m'avoir appris tous les rudiments et avoir répondu à mes innombrables questions. Mention spéciale à la CryptoTeam: Gaëlle merci d'avoir pris sous ton aile la néophyte que j'étais, Bo merci d'avoir été mon second mentor. A celui qui a partagé ma paillasse, Alaric, merci pour tes invasions barbares. Céline, merci pour les purifs à gogo et tes petits passe-droits.

Mes chers collègues du LCP ! Merci Yasmina de ton aide, de ta présence et de ton sourire, utiles à de maintes reprises pendant ces manips difficiles ! Cornélia merci pour ta bienveillance, tes cellules en extra et tes conseils. Je te souhaite bonne chance pour la suite ! Aïcha, Xavier et Yasmine, merci d'avoir embelli mes allées et venues. A Jérémy, merci d'être une épaule attentive et toujours présente. Discuter de la morale, de la vie et des rapports humains tout en préparant des expériences cellulaires très délicates, ce n'est pas donné à tout le monde. Enfin merci à Fabienne Merola et Philippe Maitre d'avoir rendu mon séjour au LCP possible.

Mes très chers collègues du LSDRM ! Céline, tant de partage dans ce bureau. Merci pour tout. Estelle, toujours présente que ce soit pour le boulot ou les bobos de la vie, je regretterai nos discussions ! Gaspard, merci pour ta bienveillance à mon égard et ton optimisme de tous les jours ! Mélanie, rayon de soleil du labo, continue d'égayer ceux qui t'entourent ! A Jean-Pierre, Rodolphe, Alan, Thibault, Erwann, Thierry et Rodolphe, nos pauses déjeuner, café me manqueront. A Guillaume, merci pour tes bons "camarade de pause", tes bières, ta bonne bouffe et tes soirées jeux. Merci d'avoir été un soutien et un ami pendant 4 ans.

Aux collaborateurs qui m'ont permis de découvrir d'autres horizons ! Sandra, William et Fred merci pour votre accueil, votre confiance et vos explications pour ces denses sessions in vivo. Thierry, merci pour ta disponibilité, tes idées permanentes et d'avoir permis la synthèse de la biosonde grâce à tes cryptophanes. Merci d'avoir été un parrain de thèse, toujours concerné.

A une rencontre professionnelle mais surtout amicale, Samy. Ta vision sur la recherche, le monde dans son ensemble, ta culture et ta gentillesse font de toi un chercheur hors pair et une superbe rencontre.

Un grand merci à Lilou pour ses parenthèses parisiennes, et à Caro et Thibault pour leurs parenthèses à 4 lettres en verlan. Caro, Pierrick et Louise, merci pour vos soirées crêpes et de mettre mon verre toujours trop près de la crêpière. Merci pour ce texte de Saint-Exupéry qui résonne depuis chaque jour.

A la Kip'4, merci pour votre bonne humeur et votre soutien. Ces pauses sportives étaient du pur régal: " Force et honneur !".

Aux Nadine, merci. Que ce soit pour leurs compétences informatiques, leur soutien, leur chats fluorescents imaginaires, leurs capacités de plomberie, de démolisseur ou pour leur amitié. Merci d'être là.

A ma famille et belle-famille bien aimées, merci d'avoir été d'un soutien sans faille et d'avoir si bien prétendu comprendre ce que je faisais dans la vie. Un soutien aveugle, la plus belle preuve d'amour !

Au zoo ! Nala, Wasabi, Sushi et Maki, merci d'avoir envahi mon bureau pendant mes longues heures de rédaction. Miette, merci pour la couverture chauffante, un délice ! Alpha, doggo des enfers, merci de t'être occupé de ma santé en débranchant mon ordinateur. Deux fois.

Aux conditions extérieures d’être intervenues dans le dernier mois de rédaction ! Merci la foudre d’avoir brulé notre box et de m’avoir privée d’internet. Merci à nos eaux usées d’avoir insisté pour rencontrer notre sous-sol. Puis notre jardin.

Enfin merci à toi, d’être toi et de me faire moi.

CONTENTS

I CONCEPTS, STATE OF THE ART AND RELATED WORK 1
1 AN INTERDISCIPLINARY PROJECT 3
2 STATE OF THE ART 7
  2.1 Molecular Imaging 7
  2.2 MRI probes 9
    2.2.1 Relaxation contrast agents 10
      2.2.1.1 Transverse relaxation time agents 10
      2.2.1.2 Longitudinal relaxation time agents 11
    2.2.2 Chemical Exchange Saturation Transfer agents 12
    2.2.3 Heteronuclear tracers 14
      2.2.3.1 ^{19}F agents 14
      2.2.3.2 Hyperpolarized probes 15
  2.3 Optical probes 17
    2.3.1 Endogenous contrast of tissues 17
    2.3.2 Fluorochromes 18
    2.3.3 Fluorescent proteins 18
    2.3.4 Fluorescent quantum dots 20
    2.3.5 Bioluminescence 20
  2.4 Toward multimodal molecular imaging 21
3 SPIN-HYPERPOLARIZATION 29
  3.1 NMR Sensitivity 29
  3.2 Main xenon hyperpolarization methods 31
    3.2.1 Dissolution Dynamic Nuclear Polarization 31
    3.2.2 Spin-Exchange Optical Pumping 33
    3.2.3 Our recent contribution: optical pumping in a van 37
  3.3 Details of the xenon SEOP experiment 40
4 XENON BIOSENSORS 47
  4.1 Xenon : a spy with multiple facets 47
  4.2 Xenon carriers 50
    4.2.1 Vectorized biosensors 52
    4.2.2 Smart sensors 56
    4.2.3 Strategies for water-soluble xenon carriers 59
  4.3 A Fluorescence-^{129}Xe NMR probe for biological inhibition of EGFR in Non-Small Cell Lung Cancer 61
    4.3.1 Structure of the biosensor 61
    4.3.2 ^{129}Xe NMR characterization 62
    4.3.3 Biological activity asssays 64
    4.3.4 ^{129}Xe NMR-based detection of the biosensor in cell samples 64
  4.4 Future directions 67

5 NMR SEQUENCES OPTIMIZED FOR ^{129}XE NMR-BASED SENSORS 75
  5.1 Direct detection methods 75
    5.1.1 1D Frequency-Selective excitation sequence 75
    5.1.2 2D Frequency-selective excitation sequence 79
  5.2 Indirect detection methods 80
    5.2.1 Depolarization sequence 80
    5.2.2 Ultrafast Z spectroscopy 83
  5.3 Conclusions about direct and indirect - UFZ and depolarization - methods 86
    5.3.1 Discussion of the methods 86
    5.3.2 Chemical Shift Imaging 89

II DETECTION OF RECOMBINANT PROTEINS 93
6 BIMODAL SENSOR 95
  6.1 Objectives 96
  6.2 NMR detection part 96
  6.3 Fluorescence detection part 96
    6.3.1 Small ligand : biarsenical dye 98
      6.3.1.1 Bis-arsenical ligand variant 100
      6.3.1.2 Carboxy-FlAsH : CrAsH 102
    6.3.2 Peptidic target: tetracysteine tag sequences 104
      6.3.2.1 Binding process 104
      6.3.2.2 Optimized tetracysteine peptides 106
        6.3.2.2.1 WEAAAREA**CC**RE**CC**ARA . 106
        6.3.2.2.2 FLN**CC**PG**CC**MEP 107
        6.3.2.2.3 AREA**CC**PG**CC**K 107
        6.3.2.2.4 G**CC**GGSGNDAGG**CC**GG . . 107
  6.4 Biosensor synthesis 108
7 *in vitro* DUAL DETECTION OF TETRACYSTEINE PEPTIDES 117
  7.1 Experimental conditions 117
  7.2 Study of various detection partners 118
    7.2.1 Influence of the environment on the NMR response 118
    7.2.2 "RE" tetracysteine-tag 121
      7.2.2.1 Fluorescence experiments 121
      7.2.2.2 Hyperpolarized ^{129}Xe NMR experiments 122
  7.3 FLN-PG- and SlyD- tetracysteine tags 127
    7.3.1 "PG" tetracysteine-tag 128
      7.3.1.1 Hyperpolarized ^{129}Xe NMR experiments 128
      7.3.1.2 Fluorescence experiments 130
  7.4 Conclusion 131
8 *in vitro* DUAL DETECTION OF TETRACYSTEINE-TAGGED PROTEINS 135
  8.1 Conception of a tagged-protein 135
    8.1.1 Förster resonance energy transfer: Conditions 135

8.1.2 Two strategies for the tagged-protein construction 137
8.1.2.1 Fluorescent protein (D) - Biosensor (A) 138
8.1.2.2 Biosensor (D) - Fluorescent protein (A) 139
8.1.3 Direct consequences on the ^{129}Xe NMR and fluorescence signals 140
8.2 Plasmid construction and purification 143
8.3 Proof of concept of the detection of recombinant proteins 146
8.3.1 Construction I 146
8.3.1.1 Fluorescence signal 146
8.3.1.2 ^{129}Xe NMR signal 150
8.3.2 Constructions II and III 150
8.3.2.1 Fluorescence signal 150
8.3.2.2 Hyperpolarized ^{129}Xe NMR signal 150
8.3.3 Constructions IV and V 151
8.3.3.1 Fluorescence signal 151
8.3.4 Hyperpolarized ^{129}Xe NMR experiments 154
8.4 Conclusion 155
9 IN-CELL DETECTION OF TETRACYSTEIN-TAGGED PROTEINS 159
9.1 Internalization in bacteria 159
9.2 Protocol for eukaryotic cell uptake 161
9.2.1 Surface coating method 161
9.2.2 Optimization of conditions for cell uptake 163
9.2.3 Proof of cell uptake and quantification 165
9.3 ^{129}Xe NMR detection of the sensor inside the cells 170
9.4 Detection of the sensor inside cells expressing tetracysteine tagged proteins 171
9.5 Conclusion 173
10 OUTLOOK AND CONCLUSION 177
III APPENDIX 185
A APPENDIX 187
A.1 Materials and Methods 187
A.1.1 Solvents and reagents 187
A.1.2 Organic synthesis 187
A.1.2.1 Compounds **11** and **12** 187
A.1.2.2 Compounds **13** and **14** 188
A.1.2.3 Compounds **15** and **16** 188
A.1.2.4 Compounds **17** and **18** 189
A.1.2.5 Compounds **MM-1** and **MM-2** 190
A.1.2.6 Compound **PP-1** 192
A.1.3 DNA Sequencing 193
A.1.4 Buffers 195
A.1.5 Methods 196
A.1.5.1 Bacterial cell culture 196

- A.1.5.2 Plasmid preparation 196
  - A.1.5.2.1 Standard protocol (mini-preparation) 196
  - A.1.5.2.2 Endotoxin-free protocol (maxi-preparation) 196
- A.1.5.3 Plasmid cloning 197
- A.1.5.4 Protein production and purification 198
- A.1.5.5 Eukaryotic cell culture 199
- A.1.5.6 Transient transfection of COS cells 199
- A.1.5.7 Electrophoresis 200
- A.1.5.8 Flow cytometry 200
- A.1.5.9 Fluorescence microscopy 201
- A.1.5.10 Fluorescence lifetime imaging 201
- A.1.5.11 Evaluation of the biosensor quantity internalized in the cells 202

LIST OF FIGURES

Figure 1 Most popular medical imaging modalities and their main applications. 8

Figure 2 *In vivo* systemic persistent luminescent imaging of a mouse before (Bkg) and after intravenous injection of nanoparticles which had been excited prior to injection and imaged at 2, 12, 20 and 60 minutes to excitation light. 8

Figure 3 Main classes of MRI constrast agents (in purple and dark blue) and MRI tracers (in light blue). 10

Figure 4 Magnetic Resonance images of a rat head 6 days following transplantation of magnetically labeled rat fetal striatal tissue (one of the nuclei in the subcortical basal ganglia of the forebrain). The transplanted tissue was prior incubated with super-paramagnetic ferrite particles coupled to wheat germ agglutinin. Labeled tissue was injected unilaterally into the striatum. The images represent adjacent coronal 2.5 mm thick sections through a rat head (from A to D). The brain appears as an area of relative high signal intensity in the dorsomedial aspect of the images indicated by the open arrows in panels A and B. The transplanted tissue appears as an area of very low signal intensity indicated by an arrow in panel C. Adapted from [17]. 11

Figure 5 Illustration of the CEST mechanism showing the Boltzmann distribution of proton spins and the simulated NMR spectra for two chemically distinct pools of protons. Application of a frequency selective RF pulse causes saturation of the NMR signal, which is then transferred to the bulk water proton pool by chemical exchange. 13

Figure 6 Temperature maps of a phantom containing a solution of paraCEST agent $Eu(L)^-$. T_{air} on images indicates the temperatures of the air flowing over the sample, while those reported by imaging are shown by the color bar in units of °C. Adapted from [27]. 14

Figure 7 ^{1}H, ^{19}F merged MR images of human neural stem cells labeled with ^{19}F (C) 2 days and (E) 6 days after implantation in the mouse striatum. The animal received two deposits of ^{19}F-labeled cells in the left striatum and one deposit in the right striatum. Reproduced from [30]. 15
Figure 9 Two hyperpolarized ^{3}He MR images of a healthy volunteer during inhalation (left) and breath hold (right). Adapted from [35]. 16
Figure 10 Main classes of optical imaging agents. 17
Figure 11 Fluorescence microscopy images of cells incubated with the macromolecular structure bearing multiple cyanine dyes. **A** A phase contract image. **B** immediately after injection of the activatable fluorochrome, no fluorescence signal is observed. **C** After 15 min of incubation, the probe is internalized and degraded resulting in a fluorescent signal. **D** Light (left) and near infrared range fluorescence (right) images these same tumor cells implanted into mammary fat pad of a mouse. Adapted from [39]. 19
Figure 12 Lateral whole-body image of metastatic liver lesions of a GFP-expressing human colon cancer in the left (thick arrow) and right lobes (fine arrow) of a live nude mouse at day 21 after surgical orthotopic transplantation. Adapted from [41]. 20
Figure 13 . Dependence on magnetic field strength B_0 of the separation of nuclear energy levels (Δ E) for spin I= 1/2 and the relative populations of the energy levels assuming one has approximately ten million protons in the sample. 30
Figure 14 . Zeeman energy levels of an electron-nucleus system presenting the Electron Spin Resonance (ESR) transitions, Nuclear Magnetic Resonance (NMR) transitions and flip-flop transitions. 31
Figure 15 . In a dynamic nuclear polarization experiment, MR-active nuclei (here ^{13}C) are mixed with a low concentration of unpaired electrons in a glass matrix. The sample is then irradiated with high-power microwaves at the electron resonance frequency in a high magnetic field ($\approx$ 3 T) and at low temperatures ($\approx$ 1 K). This enables ^{13}C hyperpolarization via polarization transfer from free electrons. Adapted from [3]. 32

Figure 16 Scheme of orbital and spin angular momenta and the spin-orbit coupling J. 34
Figure 17 Spin-Exchange Optical Pumping setup requires an optical cell containing a noble gas - xenon -, buffer gases (N_2 and He), and a small quantity of vaporized alkali metal (typically Rb). Nuclei are irradiated by a laser light (795 nm for Rb D_1 transition). Photons fully circularly polarized (Δm_j = +1) are absorbed. Since angular momentum is conserved, this leads to an absorption from one of two Rb ground electronic (m_j = -1/2) states. After collisions with gas atoms, the ground states are repopulated at effectively equal rates. However, since only one ground state is depleted by the laser, ground-state population accumulates on the other m_J = 1/2 state, leaving the Rb electronically spin-polarized. A weak magnetic field along the direction of laser propagation (drawn in green) enables the degeneracy of the spin levels. Gas-phase collisions then allow spin exchange between the polarized Rb electron spins and the noble gas nuclear spins. 35
Figure 18 ^{129}Xe NMR spectrum (in blue) obtained after 15 hours of acquisition and exhibiting a polarization of 10^{-5}. Hyperpolarized ^{129}Xe NMR spectrum (in red) obtained after only 1 s of acquisition. Polarization has been enhanced by more than 5 orders of magnitude. 36
Figure 19 Production of laser-polarized xenon. Top: Photograph of our SEOP setup; bottom: schematic drawing. BE: beam expander; BS: beam splitter; $\lambda/4$: quarterwave plates; PW: powermeter. B: magnetic field (100 G) colinear to the light beam. 37
Figure 20 Drawing of the SEOP setup, side and front views. For explanation of the indicated numbers, see the main text. 38
Figure 21 Photograph of the chariot that enables us to transport the hyperpolarized xenon toward the magnet. 42
Figure 22 Photograph of the glass bridge permitting the hyperpolarized xenon transfer from the glass coil to the NMR tube. 42

Figure 23 **A.**^{129}Xe (upper and lower row) and ^{3}He (middle row) imaging of healthy human lungs, hyperpolarized gas distributed uniformly throughout the ventilated airspaces of the lung. **B.** ^{129}Xe imaging of diseased human lung with asthma (upper row), Chronic Obstructive Pulmonary Disease (middle row) and cystic fibrosis (lower row). **C.** ^{129}Xe exchange between lung airspaces and tissue. Reproduced from [2]. 48
Figure 24 Principle of the ^{129}Xe NMR-based biosensing approach. 50
Figure 25 Carriers encapsulating hyperpolarized xenon and targeting analytes of interest leading to density-based and smart sensors. 51
Figure 26 Generic structure of the cryptophane cores. 52
Figure 27 Structure of the first biosensor molecule designed to bind xenon to a protein with high affinity and specificity. Below, the ^{129}Xe NMR spectrum shows the binding of the biosensor to avidin, thanks to the biotin moiety attached on the host molecule. Adapted from [24]. 53
Figure 28 Structure of the molecular relay consisting in a two-faced guest that is a xenon binding competitor. Reproduced from [28]. 54
Figure 29 Modular construction of a sensor based on avidin-conjugated antibody and a set of biotin-conjugated read-out moieties for dual - NMR and fluorescence - functionality. CrA: Cryptophane-A. Adapted from [32]. 55
Figure 30 Time evolution of the ^{129}Xe NMR spectrum (high-field region) of xenon caged in a biosensor let in the presence of oxygenated water. Each arylboronate group transformed into phenol group by action of H_2O_2 leads to a high field shift variation of the Xe@cage signal by ca. 10 ppm. Such an effect has been understood thanks to DFT calculation including relativistic terms for the interaction. Adapted from [41]. 57
Figure 31 Approach combining the use of hyperpolarized ^{129}Xe NMR of a cage-molecule functionalized by a ligand able to chelate different cations, showing simultaneous detection of lead, zinc, and cadmium ions at nanomolar concentration. Reproduced from [38]. 58

Figure 32 Molecular relay produces an ^{129}Xe NMR signal upon analyte detection. Reproduced from [48]. 59
Figure 33 Structure of the permetalated water-soluble crytophane-111 and its peculiar ^{129}Xe NMR chemical shift. Reproduced from [10]. 60
Figure 34 Generic structure of the new molecular platform : a cryptophane with two different reaction sites. Reproduced from [49]. 60
Figure 35 Synthesis and generic structure of the bimodal fluorescence-^{129}Xe NMR biosensor. 62
Figure 36 Direct (**A.**) and indirect (**B.**) ^{129}Xe NMR detection of biosensor before multigrafting (intermediate I) in PBS at 11.7 T. **A.** spectrum recorded in 1 scan for a 46 μM solution. **B.** ultra-fast Z spectroscopy on the same sample. In this last experiment, for one scan (in red) CW saturation is applied at an offset $\Delta\nu$ of -18 kHz from the main xenon signal with a rf strength B_1 of 20 μT for 4 s. For the second scan (in blue), no rf saturation is applied. 63
Figure 37 Hyperpolarized ^{129}Xe NMR spectrum of II at 3 μM in PBS obtained in one scan. Insert: subspectrum obtained by 64 fast repetitions of the sequence soft 90deg - Gaussian pulse centered at 60 ppm - acquisition (inter-scan delay: 93 ms). 63
Figure 38 **A.** Flow cytometry experiments on HCC827 cells and **B.** A549 cells incubated with bimodal biosensor, and **C.** immunofluorescence experiments on HCC827 cells incubated with the same probe. 65

Figure 39 ^{129}Xe NMR spectra obtained with selective excitation at the expected Xe@biosensor frequency (at ca. 70 ppm, i. e. 130 ppm upfield from the dissolved xenon signal), at 308 K. For these experiments the same experimental conditions were used both for HCC827 cells (green) and A549 cells (red): 80 million cells were incubated at 310 K during 2 hours with II at 25 μg/mL. After centrifugation the supernatant was separated from the cell clot (bottom spectra). The cells were washed two times in phosphate buffer saline (PBS, pH 7.4) and re-suspended in 600 μL of PBS and 50 μL of D_2O (top spectra). The NMR subspectra shown were obtained with a succession of sequences (frequency-selective Gaussian 90deg pulse - acquisition) with an inter-scan delay of 93 ms. 66
Figure 40 HyperCEST depolarization curves for (A) biosensor in HCC827 cells, (B) biosensor in A549 cells. Filled symbols: on-resonance saturation, empty symbols: off-resonance saturation. In (C), Z-spectrum obtained for the sample ofb biosensor in HCC827 cells (the abscissa indicates the frequency offset from the free xenon signal). 66
Figure 41 Frequency-selective rf pulse sequence used for the direct detection of encapsulated xenon in its cage (with n the number of times the sequence is repeated). 76
Figure 42 Comparison between ^{129}Xe NMR spectra obtained with a fast succession of soft pulses (in red) and a simulation of the exchange effect (in blue) of a sample containing a mixture of four different cryptophanes, differing by the length of their linkers: Cr-AM, Cr-223M, Cr-233M, Cr-EM. 77
Figure 43 Comparison between ^{129}Xe NMR spectra obtained with a fast succession of soft pulses (in red) and a simulation in the absence of xenon exchange (in green) of the same mixture of 4 cryptophanes. 78
Figure 44 Comparison between two simulations of the exchange effect without (in red) and with higher weighting coefficient for the FIDs arriving last (in blue) of the same mixture of 4 cryptophanes. 78

Figure 45 2D ^{129}Xe NMR spectrum obtained with selective excitation at the expected Xe@biosensor frequency of a solution of 1.1 μM of Cr-AM at 293 K. 1D spectra correspond to the sum of the first 51 or 128 scans of the 2D experiments. Signal to noise ratios of each condition are indicated. 79

Figure 46 **A.** The ^{129}Xe NMR spectrum of a 50 μM solution of cryptophane displays a weak resonance from encapsulated xenon at δ_3 corresponding to Xe@biosensor. Chemical exchange with free Xe outside the cage (resonance δ_1) enables sensitivity enhancement by depolarizing the δ_3 nuclei and detecting at δ_1 **B.** Selective saturation of Xe@biosensor (green) and chemical exchange with the free xenon (blue) allows accumulation of depolarized nuclei (red). This corresponds to the continuous depolarization of caged-related magnetization that can be measured indirectly after several cycles by the difference between initial and final bulk magnetization. Adapted from [4]. 81

Figure 47 ^{129}Xe HyperCEST depolarization sequence: pulse sequence providing a 2D matrix with each row corresponding to a saturation time t_{sat}. 81

Figure 48 ^{129}Xe HyperCEST depolarization curves: Example of pulse sequence (providing a 2D matrix with each row corresponding to a saturation time tsat) and plots of the xenon magnetization as a function of t_{sat} off-resonance (pale blue) and on-resonance (dark blue). Consecutive data points are separated by 0.5 s; saturation: repetition of 100 D-SNOB pulses, max. saturation field strength of 12 μT. The sample was a xenon biosensor at 478 μM in PBS. 82

Figure 49 ^{129}Xe Ultra-Fast Z-spectroscopy used pulse sequence. Both arrows indicate offset changes, from the Xe@biosesnsor region (O1) to the free xenon signal (O1$'$). A field gradient is applied during saturation (enabling saturation of a slice in the sample) and, after the rf read pulse, another field gradient is applied during detection (giving the profile of the sample). The dashed part is optional, but enables the recording of several successive FIDs with only one excitation thanks to a multiple spin echo. Reproduced from [9]. 83

Figure 50 Z-spectrum revealing the presence of cryptophane Cr-A (200 µM) into pulmonary A549 cells (green) is extracted in only two scans : a reference with no saturation S_{off} (blue) and an on-resonance saturation S_{on} (red). 84

Figure 51 UFZ-spectrum of a mixture of four cryptophanes (745 nM) in PBS obtained with B_{sat} = 12 µT during t_{sat} = 6 s. 85

Figure 52 **A** ^{129}Xe direct detection spectrum showing two Xe@biosensors signals separated by $\Delta\nu$ = 1.3 ppm. **B** Ultra-Fast Z-spectra of the same mixture acquired with an acquisition gradient of 16 G.cm^{-1} and a saturation gradient varying from 0.6 to 6 G.cm^{-1}. The apparent frequency separation between both Xe@biosensors dips is $\Delta\nu G_{acq}/G_{sat}$. These spectra were obtained using B_{sat} = 12 µT and t_{sat} = 6 s. 85

Figure 53 Comparison between principles, spectra and saturated region of the NMR tube with direct and indirect - UFZ or depolarization - detection methods. 86

Figure 54 Kickout mechanism for the in-out xenon exchange. 89

Figure 55 Hyperpolarized ^{129}Xe CSI experiment. The sample was an aqueous mixture of two cryptophanes at 100 µM in an 8 mm-o.d. NMR tube. The axial imaging is divided in 32x32 points in the spatial dimensions (experiment time 1 min 40 s). 90

Figure 56 Structure of the bimodal biosensor. 95

Figure 57 Doubly responsive probe for recombinant protein detection. 97

Figure 58 Synthesis of water-soluble cryptophane-AM (Cr-AM). 98

Figure 59 Three constitutional isomers of cryptophane. 98
Figure 60 Comparison between GFP and FlAsH sizes. On this scheme, the fluorescent protein features the protein of interest. 99
Figure 61 **A.** Schematic representation of cell surface receptor constructions, modified as indicated either at the C-terminus, or at the third intracellular loop. **B.** Confocal microscopy images of the three receptor constructions transiently expressed in Hela cells and labeled with FlAsH. Top row shows CFP fluorescence whereas bottom row shows FlAsH fluorescence. Cells expressing constructs containing the FlAsH binding motif (center and right) show a strong yellow fluorescence at the cell surface. **C.** FRET between CFP and FlAsH in cell constructions. Adapted from [12]. 101
Figure 62 Biarsenical dyes and their fluorescence emission wavelength. 102
Figure 63 4-steps synthesis of 5- and 6-carboxyFlAsH or CrAsH, the small ligand. 103
Figure 64 Interaction between a trivalent arsenic atom and a dithiol leading to a 5-bond ring. Reproduced from [22]. 104
Figure 65 Reversible complexation of biarsenical dye on a tetracysteine motif in the presence of an excess of EDT. 105
Figure 66 Two complexing pathways of biarsenical probe towards tetracysteine motif. 106
Figure 67 Structure calculation of the peptide bound to ReAsH, based on NOESY-derived distance constraints. Reproduced from [25]. 107
Figure 68 Synthesis of CrAsH linked to etylene diamine : compounds **17** and **18**. 109
Figure 69 Coupling reaction between Cr-AM and compounds **17** and **18**: synthesis of the bimodal biosensors **21** and **22**. 109
Figure 70 Structure of four different bimodal sensors 110
Figure 71 Comparison of the fluorescence spectra (excitation wavelength at 480 nm) of the CrAsH moiety (green) and **MM-1** (blue). 111
Figure 72 **A** Photograph of the "NMR-tuve". **B** Fluorescence spectra of **MM-1** (2.5 µM) with (red) and without (blue) xenon. 111
Figure 73 Triscarboxyethylphosphine (TCEP) structure. 117
Figure 74 β-mercaptoethanol structure. 117

Figure 75 1,2-Ethanedithiol structure. 118
Figure 76 One-scan ^{129}Xe NMR spectra of **A. MM-1** in blue at 25 µM, **B. MM-2** in red at 15 µM, **C. PP-1** at 8 µM in the absence of peptide and **D.** Hexacarboxylate Cryptophane-A : Cr-AM at 30 µM). 119
Figure 77 ^{129}Xe NMR spectra of xenon in **A. MM-1** bound to different target peptides : flexible strand (AREACCPGCCK), β-hairpin (GCCGGSGNDAGGCCGG) and α-helix peptide (WEAAAREACCRECCARA). Yellow balls represent cystein residues. **B. MM-1** and **MM-2** bound to the same target peptide. The only difference between these two structures is that cryptophane is grafted to the $\mathcal{C}_5$ or $\mathcal{C}_6$ of the CrAsH moiety. **C. MM-1** and **PP-1** bound to the same target peptide. These two biosensors have been synthesized from the two enantiomeric forms of the cryptophane. 120
Figure 78 **A.** 0.1 to 10 equivalents of WEAAAREACCRECCARA peptide (from the brightest to the darkest blue color) were added to 10 µM **MM-1** and illuminated at 480 nm in biotek SynergyH1 Multi-Mode Plate Reader. Maxima of fluorescence intensity between λ_{em} = 505 nm and λ_{em} = 650 nm were monitored at 37°C for 90 minutes after 30 seconds of mechanical shaking in a 96-well plate. **B.** Saturation binding curve : Fluorescence intensity maxima at the end of the experiment (90 minutes) plotted against concentration of peptide. A non linear fit of specific binding was applied following the equation $Y = \frac{B_{max}X}{(K_{d\ app}+X)}$ with B_{max} the maximum specific binding, $K_{d\ app}$ the equilibrium binding constant. This fit was obtained with a correlation coefficient of 0.9945. 122
Figure 79 One-scan ^{129}Xe NMR spectrum of a racemic mixture of **MM-1** and **PP-1** (25 µM) in phosphate buffer, after a 90°impulsion sequence. Insert: sub-spectra obtained by 64 fast repetitions of the sequence soft 90°Gaussian pulse centered at 67 ppm and acquisition (inter-scan delay: 47 ms) without (blue) and with 10 equivalents of "RE" tetracysteine-tag (red). 123

Figure 80 One-scan ^{129}Xe NMR spectrum of **MM-1** (25 µM) in phosphate buffer, after a 90°readout pulse sequence. Blue box: sub-spectra obtained by 64 fast repetitions of the sequence soft 90°Gaussian pulse centered at 67 ppm and acquisition (inter-scan delay: 47 ms) of **MM-1** without (black) and with 10 equivalents of "RE" tetracysteine-tag (green). 124

Figure 81 Sub-spectra obtained by 64 fast repetitions of the sequence soft 90°Gaussian pulse centered at 67 ppm and acquisition (inter-scan delay: 47 ms) of **MM-1** without (black) and with 0.5 (orange), 1 (blue) and 10 (green) equivalents of "RE" tetracysteine-tag. 125

Figure 82 One-scan ^{129}Xe NMR spectrum of **MM-2** 15 µM) in phosphate buffer, after a 90°impulsion sequence. Blue box exhibits selective spectra of **MM-2** without (black) and with 10 equivalents of "RE" tetracysteine-tag (green). 126

Figure 83 ^{129}Xe NMR spectra of a racemic mixture of **MM-1** and **PP-1** (25 µM) with 10 equivalents of SlyD peptide (upper spectrum) and 10 equivalents of an other FLN-PG peptide (lower spectrum). 127

Figure 84 One-scan ^{129}Xe NMR spectrum of **MM-1** (8 µM) in phosphate buffer, after a 90°impulsion sequence. Blue box: sub-spectra obtained by 64 fast repetitions of the sequence soft 90°Gaussian pulse centered at 67 ppm and acquisition (inter-scan delay: 93 ms) of **MM-1** without (black) and with 10 equivalents of "PG" tetracysteine-tag (green) 128

Figure 85 One-scan ^{129}Xe NMR spectrum of **PP-1** (8 µM) in phosphate buffer, after a 90°impulsion sequence. Blue box: sub-spectra obtained by 32 fast repetitions of the sequence soft 90°Gaussian pulse centered at 67 ppm and acquisition (inter-scan delay: 93 ms) of **PP-1** without (black) and with 10 equivalents of "PG" tetracysteine-tag (green). 129

Figure 86 **A.** 0.1 to 10 equivalents of AREACCPGCCK peptide (from the brightest to the darkest blue color) were added to 10 µM **PP-1** and illuminated at 480 nm. The fluorescence intensity maxima were monitored and reported at 37°C for 90 minutes after 30 seconds of mechanical shaking in a 96-well plate between λ_{em} = 510 nm and λ_{em} = 650 nm. **B.** Saturation binding spectrum : Fluorescence intensity maxima at the end of the experiment (90 minutes) plotted against concentration of peptide. The same non linear specific binding fit was employed here with a correlation coefficient of 0.9989. **C.** Evolution of the emission wavelength of normalized fluorescence spectra under addition of equivalents of peptide. **D.** Relation between the wavelength of the maximum fluorescence emission the and proportion of bound biosensors. 130

Figure 87 **A.** Construction I with the tetracysteine tag at the C-term of Aquamarine. **B.** Construction II with the tetracysteine tag at the N- term of Aquamarine. **C.** Construction III with the tetracysteine tag at the N-term of the Aquamarine separated by a 17-aminoacid spacer. 137

Figure 88 Normalized absorption (dotted lines) and emission spectra (solid lines) of Histag-Aquamarine-tetracysteine tag (in cyan) and **PP1** (in green). This system is excited at λ = 405 nm, which corresponds to the half-maximum of fluorescent protein absorption. Overlap between donor emission and acceptor absorption is drawn in pale red. 138

Figure 89 **A.** Construction IV with the tetracysteine tag at the NH_2 terminal part of mCherry. **B.** Construction V with the tetracysteine tag at the NH_2 terminal part of mCherry separated by 17 aminoacids. 139

Figure 90 Normalized absorption (dotted lines) and emission spectra (solid lines) of Histag-Tetracysteine tag-mCherry (in red) and **PP1** (in green). This system is excited at λ = 480 nm, which corresponds to the half-maximum of fluorescent protein absorption. Overlap between donor emission and acceptor absorption is drawn in pale red. 140

Figure 91 Principle of the functioning of the biosensor with construction I (Histag-Aquamarine-TC). **A.** Free **PP-1** gives rise to the original encapsulated xenon chemical shift and a very low fluorescence. **B. PP-1** bound to TC-tag of construction I gives rise to a chemical shift variaton for encapsulated xenon and a fluorescence increase. **B′.** The same molecular construct gives rise to Förster Resonance Energy Transfer from the fluorescent protein to **PP-1**, diminishing the fluorescence signal and lifetime of the protein and increasing the fluorescence of **PP-1**. 141

Figure 92 UV-Vis absorption spectrum of **A.** Histag-Aquamarine-tetracysteine tag (in black) with a maximum absorbance at 430 nm. **C.** Histag-tetracysteine tag-Aquamarine (in purple) and Histag-tetracysteine tag-Linker-Aquamarine (in black). The orange dotted line represents the shape of the UV-Vis absorption spectrum of the native Aquamarine, serving as a reference for the double band. **D.** Histag-tetracysteine tag-mCherry (in yellow) and Histag-tetracysteine tag-Linker-mCherry (in black). The maximum absorbance is at 560 nm. The green dotted line represents the UV-Vis absorption spectrum of the native mCherry. **B.** Polyacrilamide gel electrophoresis of both TC-tagged Aquamarine and Aquamarine, the first column being the molecular weight marker. 144

Figure 93 $\frac{A_{280}}{A_{430}}$ or $\frac{A_{280}}{A_{560}}$ ratios and structure modification of the five constructions compared to the two references Histag-Aqua and Histag-mCherry. 146

Figure 94 **A.** Fluorescence emission spectra of 0 to 5 equivalents of **PP-1** (from the darkest to the brightest green color) added to a 2µM Aquamarine-tetracysteine tag solution after illumination at 405 nm. The orange curve corresponds to the fluorescence emission of **PP-1** bound to 5 equivalents of model "PG" peptide illuminated by a 405 nm light. The red box focuses on the decrease of fluorescence intensity of the donor. **B.** Normalized fluorescence emission spectra at 405 nm, showing two modified regions. The blue box focuses on the increase of fluorescence intensity of the acceptor. The yellow box highlights the modification of the fluorescence spectrum of the donor. **C.** Normalized fluorescence emission spectra of samples containing 0.5 to 5 equivalents of **PP-1** illuminated with a 480 nm source. The orange and purple curves are used as a reference of free **PP-1** and **PP-1** bound to 5 equivalents of model "PG" peptide. 147

Figure 95 **A.** Mean fluorescence lifetimes of 0 to 5 equivalents of **PP-1** added to a 2µM Aquamarine-tetracysteine tag solution after illumination at 450 nm. **B.** Proportion of bound fluorescent proteins (α_{short}), after analysis of the biexponential decay functions. 149

Figure 96 ^{129}Xe NMR selective spectra of free **PP-1** (2µM) and bound to 10 equivalents of Aquamarine-tetracysteine tag. 150

Figure 97 ^{129}Xe NMR sub-spectra of free xenon in **PP-1** (2µM) and bound to 2 equivalents of tetracysteine tag-Aquamarine and tetracysteine tag-linker-Aquamarine. Sub-spectra obtained by 2D Frequency-selective excitation sequence, when adding the 30 first scans. 151

Figure 98 **A.** Fluorescence emission spectra of 0 to 5 equivalents of Histag-Tetracysteine tag-mCherry (from the darkest to the brightest green color) added to a 2µM **PP-1** solution after illumination at 480 nm. Spectra have been corrected by the fluorescence emission of construction IV directly illuminated by the 480 nm light and displayed in red dotted line (contribution of 1%). **B.** Normalized fluorescence emission spectra at 480 nm demonstrating a FRET transfer from the biosensor to the tagged-protein. **C.** Normalized fluorescence emission spectra of samples containing 0 to 5 equivalents of Histag-Tetracysteine tag-mCherry illuminated with a 480 nm source, showing the spectral shift of the emission spectrum upon binding. 152

Figure 99 ^{129}Xe NMR spectra of free **PP-1** (2µM) and bound to 4 equivalents of Histag-Tetracysteine tag-mCherry. Spectra were obtained with a frequency-selective excitation sequence (2D) with an half-gaussian pulse. 154

Figure 100 Reduction of a -SS- bond by DTT. 159

Figure 101 Fluorescence microscopy of DH5α cells incubated with 26 µM of racemic biosensor for 2 hours, **A.** rinsed in PBS, **B.** treated with DTT reagent, **C.** electroporated and then treated with DTT. **D.** Fluorescence spectra of the biosensor in the three conditions, illuminated at λ_{ex} = 470 nm and observed between λ_{em} = 490 nm and λ_{em} = 570 nm. The spectrum of electroporated bacteria is used as a blank. The red and blue areas enlighten maximum of fluorescence emission: 518 nm for incubated biosensor, 534 nm for incubated biosensor in electroporated bacteria. 160

Figure 102 **A.** Fluorescence emission spectra of 30.000 COS7-cells incubated 1 hour with 10 µM of racemic biosensor with or without protein corona (via FBS). Spectra were recorded after an excitation at λ_{exc} = 480 nm using a plate reader. **B.** Fluorescence microscopy images of COS7-cells incubated with 10 µM of biosensor and 30% FBS and illuminated via the biosensor filter cube during t_{exp} = 2 s. 162

Figure 103 Influence of the incubation time and biosensor concentration on incubated quantities. The cells were incubated for 15, 45, 75 and 115 minutes with 0.47, 2.8, 24 and 55µM of racemic biosensor. After being rinsed 3 times with PBS, fluorescence microscopy images of the cells in PBS were recorded with the biosensor filter cube. A region of interest (ROI) of the size of a cell was chosen and mean fluorescence intensities of 10 cells in 10 different fields of view were measured using a routine in ImageJ software. The mean values for each sample are reported here, as well as the standard deviation. 163

Figure 104 **A. and B.** Influence of EDT and β-mercaptoethanol concentration and cell condition -adhered or suspended - on the cell uptake of the racemic biosensor at 1 mM of TCEP. Cells in sample E,F and G were prior detached from the surface with 200µL of trypsin, a protease that hydrolyses proteins. They are centrifuged, resuspended into DMEM (30% FBS) and incubated with biosensor for 1 hour at 37°C. After being rinsed 3 times with PBS, fluorescence microscopy images of the cells in PBS with different concentration of β-mercaptoethanol and EDT were recorded. A region of interest (ROI) of the size of a cell was chosen and mean fluorescence intensity of 10 cells in 10 fields of view was measured using a routine in ImageJ software. The mean value for each sample is reported here, as well as the standard deviation. **C.** Transmission microscopy image of cells in U conditions. **D.** Fluorescence microscopy images of the same cells. 164

Figure 105 Confocal images of COS7-cells incubated for 1 hour at 37°C with 140 µM of biosensor, reducing mixture and DMEM (30% FBS). After after being rinsed 2 times with PBS, cells were illuminated with a laser at 488 nm and detected between 500 and 550 nm and imaged in PBS. 36 slices corresponding to 36 different depths (z = 130 nm) of the cells are displayed as well as the projection of the fluorescence and the mean fluorescence of each depth. 166

Figure 106 Flow cytometry experiments (Gain = 280) of suspended COS7-cells incubated for 1 hour at 37°C with 100 μM of β-mercaptoethanol, 1 mM of TCEP, 500 μM of EDT, DMEM (30% FBS) and **A.** 70 μM of racemic biosensor, **B.** without biosensor. Fluorescence microscopy images using an YFP filter cube of **C.** suspended cells incubated with racemic biosensor and **D.** suspended cells as a reference. The yellow lane corresponds to the intensity profile of a cell incubated **E.** with biosensor and **F.** without biosensor. 168

Figure 107 **A.** The fluorescence emission spectrum of cells incubated with 70 μM of the racemic biosensor. **B.** The maximum fluorescence intensities (gain = 90) of four dilutions - 0.06, 0.18, 0.36 and 0.72 μM - of racemic biosensor. The linear regression fit indicates a slope α = 7972 μM^{-1}. 169

Figure 108 Z-spectra of **A.** the supernatant containing 140 μM of **PP-1** and **B.** cells incubated with 140 μM of **PP-1**. Data were fitted with a Lorentzian curve using OriginPro software. Both experiments were performed with these parameters: Consecutive data points are separated by 0.5 s; saturation: repetition of 100 D-SNOB pulses, max. saturation field strength of 12 μT. 170

Figure 109 Fluorescence microscopy images of **PP-1** incubated on cells expressing **A.** TC-tagged Aquamarine (Aquamarine excitation), **B.** TC-tagged Aquamarine (biosensor excitation), **C.** Aquamarine and **D.** TC-tagged Aquamarine with an excess of EDT. The chart displays mean fluorescence intensities measured in a ROI in 40 cells. 172

Figure 110 Photographs of: **A.** the van transporting the hyperpolarization setup. **B.** Hyperpolarization setup in the van. 179

Figure 111 **A.** TRUE-FISP Coronal encoding images of hyperpolarized ^{129}Xe in the lungs of a mouse. FOV 5 x 3 cm; Slice 3 cm; 64 x 64, only 2D-FFT, TE = 1.3 ms, TR = 2.6 ms and 0.5 s per image. **B.** 0.15 mmol of Cr-AM were instilled into the lungs and 90° Gaussian pulses of 800 μs centered at 60ppm were implemented with TR = 73.5 ms, NS = 2 and TD1 = 512. 180

Figure 112 HPLC purification and MS analysis of compounds **11** and **12**. 188
Figure 113 HPLC purification and MS analysis of compounds **15** and **16**. 189
Figure 114 HPLC purification and MS analysis of compounds **17**, **18**, **19** and **20**. 190
Figure 115 Purity check of **MM-1** on Luna PFP. Gradient H_2O/AcCN 95:5 to 30:70. 191
Figure 116 Purity check of **MM-2** on Luna PFP. Gradient H_2O/AcCN 95:5 to 30:70. 192
Figure 117 Purity check of **PP-1** on Luna PFP. Gradient H_2O/AcCN 95:5 to 30:70. 192
Figure 118 DNA sequencing of construction I. 193
Figure 119 DNA sequencing of construction II. 193
Figure 120 DNA sequencing of construction III. 194
Figure 121 DNA sequencing of construction IV. 194
Figure 122 DNA sequencing of construction V. 195
Figure 123 **A** Designed sequence of the insert coding for tetracystein core, fused at the end of the Aquamarine sequence with NdeI restriction site. **B** Map of the designed vector coding for Aquamarine fused to Histag in NH_2-terminal part and tetraCysteine tag in COOH-terminus 198

LIST OF TABLES

Table 1 Performance of different imaging techniques for *in vivo* detection. 7
Table 2 Tetracysteine tags for Biarsenical Probes 105

ACRONYMS

BE	Beam Expander
BS	Beam Splitter
CB	Cucurbituril
CEST	Chemical Exchange Saturation Transfer
CFP	Cyan Fluorescent Protein
COS	CV-1 in Origin with SV40 genes
Cr-A	Cryptophane-222
Cr-AM	Hexacarboxylate Cryptophane-222
Cr-EM	Hexacarboxylate Cryptophane-333
CSI	Chemical Shift Imaging
CT	Computed Tomography
CTV	Cyclotriveratrylene
CW	Continuous wave
DFT	Density Functional Theory
DIEA	N, N-diisopropylethylamine
DMEM	Dulbecco's Modified Eagle Medium
DMSO	Dimethyl sulfoxide
DNA	Deoxyribonucleic Acid
DNP	Dynamic Nuclear Polarization
DTT	Dithiothreitol
ECFP	Enhanced Cyan Fluorescent Protein
EDCI	1-ethyl-3-[3-(dimethylamino)propyl]carbodiimide
EDT	Ethane Dithiol
EDTA	Ethylenediaminetetraacetic Acid
EGF	Epidermal Growth Factor
EGFR	Epidermal Growth Factor Receptor

ESR	Electron Spin Resonance
FACS	Fluorescence-Activated Cell Sorting
FBS	Fetal Bovine Serum
FDA	Food and Drug Administration
FID	Free Induction Decay
FLIM	Fluorescence-Lifetime Imaging Microscopy
FP	Fluorescent Protein
FRET	Förster Resonance Energy Transfer
FWHM	Full Width at Half Maximum
GFP	Green Fluorescent Protein
HPLC	High-performance Liquid Chromatography
HyperCEST	Hyperpolarized ^{129}Xe Chemical Exchange Saturation Transfer
IPTG	Isopropyl β-D-1-thiogalactopyranoside
LCMS	Liquid Chromatography–Mass Spectrometry
nsLTP	Nonspecific Lipid Transfer Protein
MHC	Major Histocompatibility Complex
MRI	Magnetic Resonance Imaging
NHS	N-Hydroxysuccinimide
NMDA	N-methyl-D-aspartate
NMR	Nuclear Magnetic Resonance
NOESY	Nuclear Overhauser Effect Spectroscopyy
NSCLC	Non-Small Cell Lung Cancer
NTA	Nitrilotriacetic Acid
OP	Optical Pumping
ParaCEST	Paramagnetic Chemical Exchange Saturation Transfer
PBS	Phosphate buffered saline
PET	Positron Emission Tomography
PFCs	Perfluorocarbons

PRESS	Point-RESolved Spectroscopy
PW	Powermeter
QY	Quantum Yield
RF	Radio Frequency
ROI	Region Of Interest
SAR	Specific Absorption Rate
SDS	Sodium Dodecyl Sulfate
SEOP	Spin-Exchange Optical Pumping
SPECT	Single-photon emission computed tomography
SPINOE	Spin Polarization-Induced Nuclear Overhauser Effect
SPIO	Superparamagnetic Iron Oxide
STEAM	STimulated Echo Acquisition Mode
TC	Tetra Cysteine
TCEP	Tris(2-carboxyethyl)phosphine
TE	Echo Time
TR	Repetition Time
tf-MION	Transferrin and Monocrystalline Iron Oxide
UFZ	UltraFast Z-Spectroscopy
UV	UltraViolet
YFP	Yellow Fluorescent Protein

Part I

CONCEPTS, STATE OF THE ART AND RELATED WORK

This first part introduces all the basic knowledges required to appreciate the work gathered in this thesis. The first chapter serves as an introduction to the whole manuscript. Chapter 2 is a brief introduction to the general framework of molecular imaging techniques. Chapter 3 describes the NMR imaging technique and one of its improvement: the NMR of hyperpolarized gases. Chapter 4 focuses on the process required to conduct molecular imaging studies with hyperpolarized gases. Finally chapter 5 presents NMR sequences adapted to hyperpolarized gases in exchange.

1

AN INTERDISCIPLINARY PROJECT

This project is an interdisciplinary work that unites three recognized teams for research and innovation. Bringing physicists, chemists and biologists together leads to a thoughtful and comprehensive project. The latter comes within medical approach, well upstream of diagnosis and therapy. Long before curing a pathology, we need to fully understand molecular processes that occur. In most cases, these intracellular mechanisms are monitored by fluorescence labels such as fluorescent proteins[1]. Unfortunately, such an heavy construct does not allow molecular level information and might induce biased measurements.

Collaboration between Laboratoire Structure et Dynamique par Résonance Magnétique at CEA Saclay, Service de Chimie Bioorganique et de Marquage at CEA Saclay and Laboratoire Chimie Physique at Orsay. These laboratories now belong to University Paris-Saclay.

The very ambitious goal of this project is to enable the tracking of *in cellulo* mechanisms by combination of the properties of fluorescence imaging with those of another advanced imaging technique, nuclear magnetic resonance (NMR). This approach will not only *highly precisely locate protein of interest* but also bring a *structural resolution* for comprehension of unknown biological processes *at the molecular level*.

Its uniqueness is its combination between the latest technical advances in NMR and fluorescent labeling. NMR suffers from a very low intrinsic detection sensitivity due to the low energies involved. The use of xenon is of increasing interest for sensitive MRI, owing to its large nuclear spin hyperpolarization afforded by optical pumping[2] that enhances the NMR signal by several orders of magnitude. The biosensor that is conceived in this project consists in two moieties:

- a cage-molecule that reversibly encapsulates xenon
- a small fluorogenic ligand that is activated after complexation with its target[3]

This target is a 6-amino-acid motif easily incorporated into the sequence of the protein of interest.

This molecular association enables simultaneous acquisition of very specific NMR and fluorescence signals upon detection of the targeted protein. Thus, the doubly responsive probe combines all characteristics of the two imaging techniques, allowing *sensitive detection and longitudinal follow-up* of the intracellular mechanism of interest.

BIBLIOGRAPHY

[1] Osamu Shimomura, Frank H. Johnson, and Yo Saiga. Extraction, purification and properties of aequorin, a bioluminescent protein from the luminous hydromedusan,aequorea. *Journal of Cellular and Comparative Physiology*, 59(3):223–239, jun 1962.

[2] Alfred Kastler. Quelques suggestions concernant la production optique et la détection optique d'une inégalité de population des niveaux de quantifigation spatiale des atomes. Application à l'expérience de Stern et Gerlach et à la résonance magnétique. *J. Phys. Radium*, 11(6):255–265, 1950.

[3] B. A. Griffin. Specific covalent labeling of recombinant protein molecules inside live cells. *Science*, 281(5374):269–272, jul 1998.

2

STATE OF THE ART

2.1 MOLECULAR IMAGING

Modern molecular imaging techniques supposedly lead to revolutionary paradigm shift in health care and clinical practice. As it renders information that cannot be provided by conventional radiological imaging, it desperately needs integration of anatomy and function to be fully understood. From simple photograph of the inside of the human body, providing information on bone structure or form and abnormalities of various organs, imaging now offers a dynamic view of those organs and allows visualizing up to cellular metabolism. The development of these imaging techniques is the key to earlier diagnosis of disease, best follow-up treatments and also biomedical research tools. Thus the physician can not only locate the pathology (anatomical imaging), but also assess the activity of processes within it and provide information to improve the suitable treatment. These techniques developed particularly in the 21th century form part of the molecular imaging concept. This concept requires two elements:

1. molecular probes whose physical properties are altered by the studied biological process

2. a sensitive technique to detect these molecular probes

Within the spectrum of macroscopic medical imaging, sensitivity ranges from the detection of millimolar to micromolar concentrations with computed tomography (CT) and magnetic resonance imaging (MRI) respectively, to picomolar concentrations in single-photon emission computed tomography (SPECT) and positon emission tomogrraphy (PET). All the techniques presented in Table 1 and Figure 1 have different characteristics and purposes that may be complementary according to the nature and symptoms of the disease.

	PET/SPECT	X-ray	Optical	MRI	Ultrasound
Spatial resolution	1-10mm	100µm	1-5mm	10-100 µm	30µm
Temporal resolution	60-1000s	10-100ms	1-200ms	10-100ms	1-100ms
Penetration	+++	+++	+	+++	++
Radiation	++	++	-	-	-
Sensitivity	pM	µM	fM-nM	µM-mM	µM-mM
Cost	+++	++	+	+++	+

Table 1: Performance of different imaging techniques for *in vivo* detection.[1]

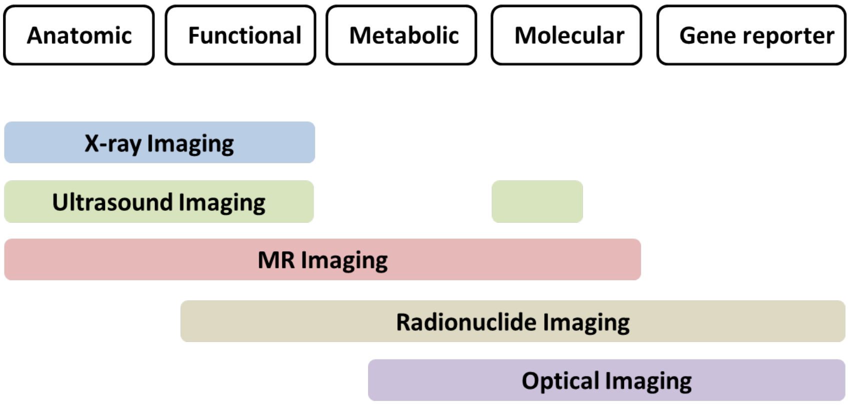
Anatomic
Functional
Metabolic
Molecular
Gene reporter
X-ray Imaging
Ultrasound Imaging
MR Imaging
Radionuclide Imaging
Optical Imaging

Figure 1: Most popular medical imaging modalities and their main applications.

Optical imaging has unparalleled sensitivity but the strong light scattering by heavy tissues limits their observation to thicknesses of less than 1-2 mm, which is not suitable for *in vivo* experiments. This penetration depth may be increased up to 10 cm using fluorescent semiconductor nanocrystals (quantum dots)[2], photon migration measurements in the frequency domain[3] or semiconducting polymer nanoparticles[4] (Figure 2).

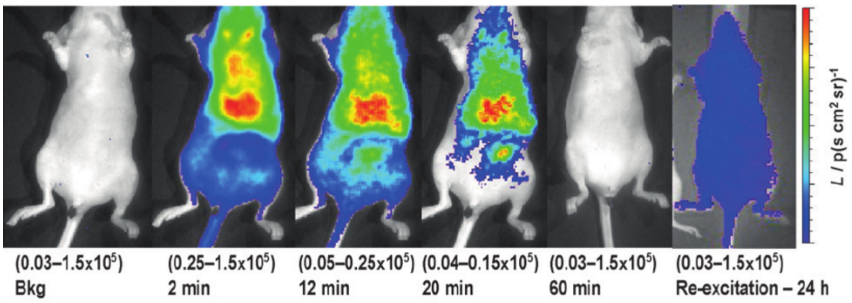
L / p(s cm² sr)⁻¹
(0.03–1.5x10⁵) Bkg
(0.25–1.5x10⁵) 2 min
(0.05–0.25x10⁵) 12 min
(0.04–0.15x10⁵) 20 min
(0.03–1.5x10⁵) 60 min
(0.03–1.5x10⁵) Re-excitation – 24 h

Figure 2: *In vivo* systemic persistent luminescent imaging of a mouse before (Bkg) and after intravenous injection of nanoparticles which had been excited prior to injection and imaged at 2, 12, 20 and 60 minutes to excitation light.

Ultrasound imaging is relatively inexpensive, widely available, portable and has a higher penetration depth than optical techniques. It is the most physiological modality, able to image structure and function with less sedation than other modalities. This means that function is minimally disturbed, and multiple repeat studies can easily be assessed. However ultrasound has received less attention than other imaging modalities because it has a very low sensitivity. More recently, the development of microbubble contrast agents has opened many new opportunities, including new functional imaging methods, the ability to image capillary flow and the possibility of molecular targeting using labelled microbubbles.[5]

Positron emission tomography and single photon emission computed tomography (PET and SPECT) have the advantage of being functional imaging techniques (probing the function and metabolism of the entire human body), but are limited by their spatial and temporal resolutions (1-2 mm in clinical scanners). Furthermore, the short life of the required radioligands, such as 2-[^{18}F]fluoro-2-deoxy-D-glucose, does not allow the long-term monitoring of the biological process of interest. The X-ray modality is, for its part, heavily limited to bone and solid tumors. The latter three techniques are also subjected to the use of ionizing radiation which also implies the management of radioactive wastes.

Finally, magnetic resonance imaging is a good compromise to achieve functional imaging *in vivo* in real time and without any radiation. It is notable that the major advantage of MRI is its high spatial resolution (25-100 µm level) and the excellent tissue contrast. In this context, MRI overruns other molecular imaging approaches up to date and is available for both morphological and functional assessments. However, this technique suffers from very low sensitivity due to the very low population differences between energy levels at Boltzmann equilibrium. We will focus specifically on this method thereafter.

2.2 MRI PROBES

When placed in a magnetic field, nuclear magnetic moments precess at a given frequency and are able to accept energy from a radiofrequency wave applied at this resonance frequency. The behavior of the energy inserted into the system is described by two relaxation constants: the T2 or transverse relaxation time and the T1 or longitudinal relaxation time.

The interest of MRI for molecular imaging has experienced a renewed enthusiasm 20 years ago with the development of the first activatable contrast agents that act as biosensors in response to a specific biological activity. There are different types of biosensors (contrast agents, hyperpolarized endogenous and exogenous substances. . .) which may reflect a physiological alteration due to a pathology : extracellular pH,[6] partial pressure of O_2 in tumor cells,[7] lactate,[8] Ca^{2+} ions,[9] Zn^{2+} ions,[10] temperature etc.

Most of the agents fall into four classes, based on the MRI contrast mechanisms they engage: (1) longitudinal relaxation time (T1) agents, detected by T1 relaxation-weighted MRI [11]; (2) transverse relaxation time (T2) agents, usually based on superparamagnetic iron oxide (SPIO), and detected by T2 relaxation-weighted MRI;[12](3) chemical exchange saturation transfer (CEST) agents, monitored by a variant of magnetization transfer imaging;[13] and (4) heteronuclear agents, detected by nuclear magnetic resonance (NMR) signals from nuclei other than protons, most prominently ^{19}F[14] or hyperpolarized ^{31}P[15] and ^{129}Xe.

The main classes (Figure 3) of these sensors and the major applications highlighted will be presented in this chapter.

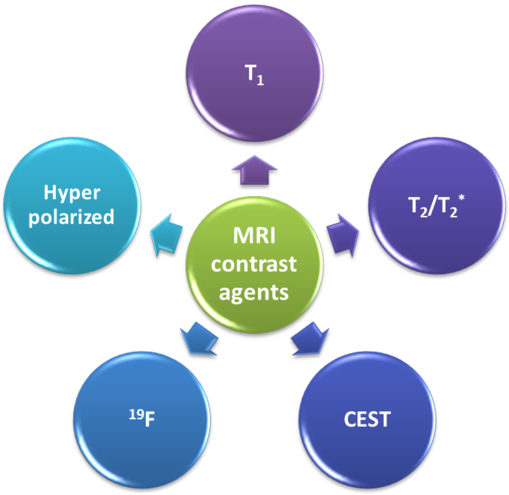

Figure 3: Main classes of MRI constrast agents (in purple and dark blue) and MRI tracers (in light blue).

2.2.1 *Relaxation contrast agents*

Contrast agents are designed to accelerate the magnetic relaxation rates $1/T_1$ and $1/T_2$ of protons of water molecules, that is, to shorten the time during which the populations of protons return to their initial state after excitation by radio frequency wave. The ability of these contrast agents to accelerate those speeds and therefore increase the contrast is measured by their relaxivity (expressed in $mM^{-1}s^{-1}$). Ideally, a biosensor has a great relaxivity when it reaches its target ("on" state) and a relaxivity near zero the rest of the time ("off" state).

2.2.1.1 *Transverse relaxation time agents*

T_2 agents are capable of shortening the T_2/T_2^* of water protons in their vicinity through a local magnetic field effect. Thus, their presence in the MRI image is witnessed by a signal loss (darkening). Nanoparticles are often used to modify the local magnetic susceptibility. Iron oxide nanoparticles are the best known agents of this class. SPIOs (Superparamagnetic iron oxides) were first utilized to label and track transplanted cells in the rat brain (see Figure 4).[16, 17]

Their relaxivity can be modified by playing with the strength of the induced magnetic field. It can be achieved by changing the size of the agent, for example by controlled agglomeration. This gives rise to higher relaxivities and enables more efficient intracellular labeling.[18, 19]

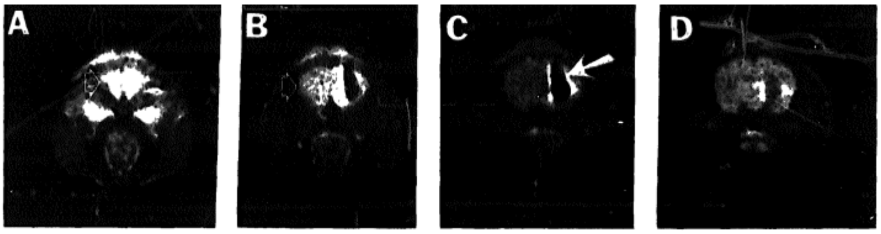

Figure 4: Magnetic Resonance images of a rat head 6 days following transplantation of magnetically labeled rat fetal striatal tissue (one of the nuclei in the subcortical basal ganglia of the forebrain). The transplanted tissue was prior incubated with super-paramagnetic ferrite particles coupled to wheat germ agglutinin. Labeled tissue was injected unilaterally into the striatum. The images represent adjacent coronal 2.5 mm thick sections through a rat head (from A to D). The brain appears as an area of relative high signal intensity in the dorsomedial aspect of the images indicated by the open arrows in panels A and B. The transplanted tissue appears as an area of very low signal intensity indicated by an arrow in panel C. Adapted from [17].

A limitation to the use of these SPIO nanoparticles is their occasional extracellular deposition in tissues, either by active exocytosis or passive release through the death of transplanted cells. Furthermore these agents are often considered not to be the candidates of choice for designing smart agents, due to the difficulty to modulate the T_2/T_2^* contrast as a function of the microenvironment characteristics. Also, the signal loss is not desirable when the target has an intrinsically low signal, which is the case for lungs for example.

2.2.1.2 *Longitudinal relaxation time agents*

T1 agents, however, require direct interaction with the water protons. For modulating the relaxivity of these agents, the three main parameters are :

1. hydration (q) : number of water molecules bound to the agent
2. exchange kinetics of water ($1/\tau_m$) : rate at which the water molecules bind to and detach from the agent
3. rotational correlation time of the agent (τ_R).

Gadolinium complexes are the most common agents of this class. This metal ion has a symmetric electron distribution (Gd(III) f^7). This means Gd(III) has a long electron relaxation time and operate on the relaxation of close nuclei.
Their relaxivity may be modified by specifically modulating the number of available sites.
Achieving responsive biosensors based on gadolinium combines this concept to the use of a ligand or a conformational change to target a specific receptor or a physiological parameter. This permits for example, pH detection[6]. In this example, 7 of the 9 coordination sites of gadolinium are held by a chelator, 1 site is held by a nitrophenol group and the last one by a water molecule. Once nitrophenol group is protonated, it dissociates from gadolinium and leaves free access to a water molecule. The hydration number goes from q=1 to q=2 that increases the relaxivity of the agent. The biosensor therefore has an "off" state with low relaxivity and an "on" state with a high relaxivity corresponding to the protonation or low pHs.

As a research tool, Gd^{3+} has been used to label and track different types of stem cells, such as hematopoietic progenitor cells, monocytic cells, endothelial progenitor cells and mesenchymal stem cells in cell transplantation studies in small animals.[20, 21] This strategy can be extended to the study of many physiological parameters, but the toxicity of free gadolinium strongly limits the contrast agent doses. This has been reported for patients with impaired kidney function, causing severe fibrosis and even death.

In addition to Gd^{3+}, manganese (Mn II) is another potentially useful positive contrast agent for T1-weighted MRI. As the kinetics and behavior of Mn^{2+} ions inside the cell mimic those of calcium ions, Mn^{2+}-enhanced MRI has been used to study neuronal activity.[22]

2.2.2 *Chemical Exchange Saturation Transfer agents*

A new class of magnetic resonance contrast agents called chemical exchange saturation transfer (CEST) agents, introduces image contrast in a fundamentally different way. Their action is not based on proton relaxation; instead, CEST contrast relies on the existence of at least two pools of protons with different NMR chemical shifts. One pool is made up of the exchangeable protons of the contrast agent (pool A). The second pool is bulk water (pool B). If proton spins in pool A are saturated by a continuous frequency-selective RF saturation pulse, exchange of protons from pool A to pool B during this saturation period decreases the intensity of pool B spins (see Figure 5).

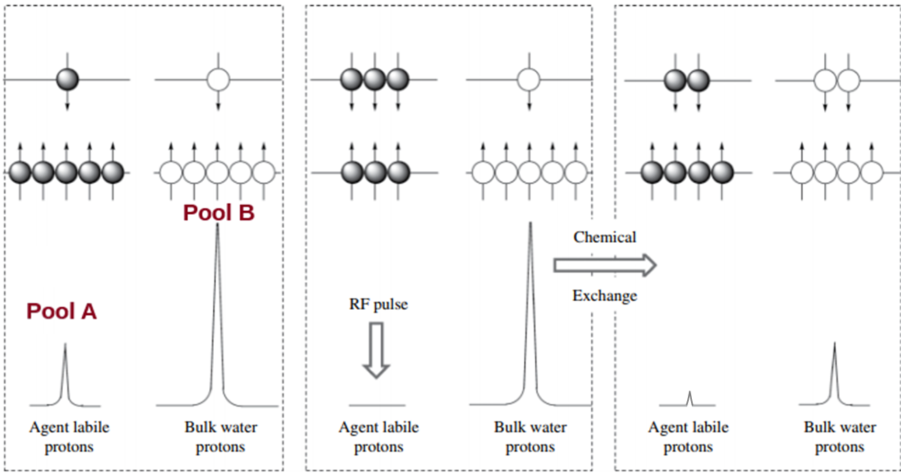

Figure 5: Illustration of the CEST mechanism showing the Boltzmann distribution of proton spins and the simulated NMR spectra for two chemically distinct pools of protons. Application of a frequency selective RF pulse causes saturation of the NMR signal, which is then transferred to the bulk water proton pool by chemical exchange.

There are two main classes of CEST agents: diamagnetic and paramagnetic agents. Diamagnetic agents are based on amino acids, proteins and sugars. They rely on exchanging protons belonging to –NH and –OH groups whose signals are usually separated by 2-5 ppm from the water signal. They are referred to as DIACEST agents. They can be used to image their own presence, or environmental factors such as pH, temperature and transplanted cells.[23, 24, 25]
PARACEST agents, however, contain paramagnetic metals with a high magnetic moment that do not affect T_1 but instead induce large frequency difference ($\Delta\omega$) between the exchanging proton (or water molecule) with respect to the bulk water frequency. Unlike Gd((III), PARACEST agents has unpaired f electrons. The electron relaxation time is then shorter and therefore does not induce a nuclear relaxation but a dipolar shift. The most common of these agents are derived from paramagnetic lanthanide ion complexes with either exchangeable –NH protons or lanthanide ion-bound water molecules. The large frequency difference allows much easier RF saturation of the paramagnetically shifted proton without indirect partial saturation of bulk water protons. Similar to diaCEST agents, these paraCEST agents exhibit characteristics strongly dependent on physicochemical parameters such as temperature or pH. They can therefore be used to map these parameters.[26, 27]
Figure 6 shows the thermometry images obtained by locating the ^{1}H chemical shift of a Eu^{3+}-based paraCEST agent.

Although the amplification factor reached is promising (FA $\approx 10^5$ to 10^6), the recorded detection threshold is 60 μM *in vitro*. In order

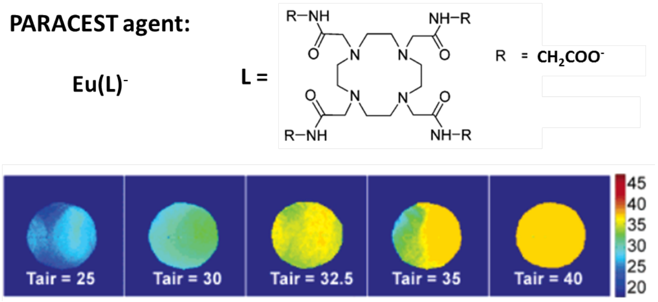

Figure 6: Temperature maps of a phantom containing a solution of paraCEST agent Eu(L)$^-$. T_{air} on images indicates the temperatures of the air flowing over the sample, while those reported by imaging are shown by the color bar in units of °C. Adapted from [27].

to counter this lack of sensitivity, Silvio Aime's group worked on the concentration of paraCEST agents into liposomes. These new contrast agents are called lipoCEST.[28] However, at such concentrations, these paramagnetic metal agents might become toxic when present in the body for prolonged periods, as in the case for Gd^{3+} described above.

2.2.3 *Heteronuclear tracers*

Heteronuclear agents are technically not "contrast" agents (because there is no water signal to contrast with) and can be referred to as MRI "tracers". Among them, two classes have shown promising results for humans: ^{19}F agents and hyperpolarized probes.

2.2.3.1 ^{19}F *agents*

^{19}F nuclei are the most sensitive spins after protons. They can therefore be detected by MRI without any enrichment. Also, ^{19}F is an exogenous nucleus which avoids background noise. The detection sensitivity is similar to CEST agents (mM range of fluorine atoms) and the advantage is the proportionality between the concentration of the ^{19}F and the signal intensity. The signal can thus be quantified directly from the acquired images. Perfluorocarbons (PFCs), which contain many fluorine atoms with identical chemical shifts, are most commonly used for ^{19}F MRI *in vivo* cell tracking applications and neural stem cells labeling.[29, 30]

Figure 7 shows a transplanted tissue experiment as in Figure 4, using PFCs labeling.[30]

The high spatial resolution of ^{19}F MRI allows the two cell clusters in the left hemisphere to be clearly distinguished, demonstrating the

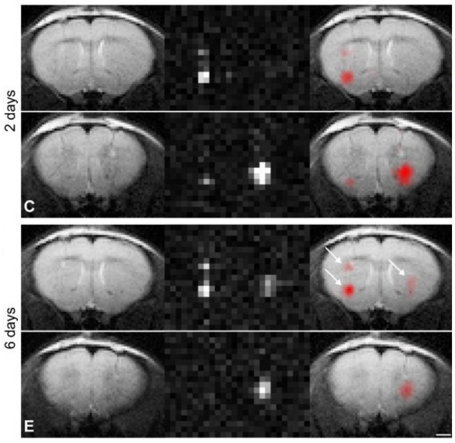

Figure 7: ^{1}H, ^{19}F merged MR images of human neural stem cells labeled with ^{19}F (C) 2 days and (E) 6 days after implantation in the mouse striatum. The animal received two deposits of ^{19}F-labeled cells in the left striatum and one deposit in the right striatum. Reproduced from [30].

potential of this technique for the detection of small numbers of cells in vivo within a restricted area.

2.2.3.2 *Hyperpolarized probes*

A newer class of biosensors that can help to achieve molecular imaging is MRI using hyperpolarized endogenous substances.[31] Despite the relatively long time of preparation of hyperpolarized species with DNP (30-90 minutes), DNP substrates have shown the greatest promise for oncological applications in vivo and summarize the bio-chemical mechanisms responsible for label transfer from pyruvate to other metabolites in tumors (see Figure 8).[32]

To date, [1-^{13}C]pyruvate has been the most commonly used metabolite for DNP. Intravenous injection of[1-^{13}C]pyruvate can result in the appearance of [1-^{13}C]lactate, [1-^{13}C]alanine, and $^{13}CO_2$ resonances. In tumors, lactate labeling is increased and this can be used to help distinguish tumor from normal tissue[33]. Pyruvate-lactate exchange can be also used to identify tumor grade.[32] We can now produce more easily the same metabolites (pyruvate, succinate, etc.) by using parahydrogen-induced polarization.[34]

At the atomic scale, hyperpolarized gases (e.g., ^{3}He and ^{129}Xe) are clinically used for imaging the respiratory apparatus as shown in Figure 9.[35]

But for molecular imaging, a very promising combination between hyperpolarized and CEST agents has been proposed using ^{129}Xe NMR-based sensors. The contrast arising from these agents called HyperCEST agents relies on the reversible binding of hyperpolarized

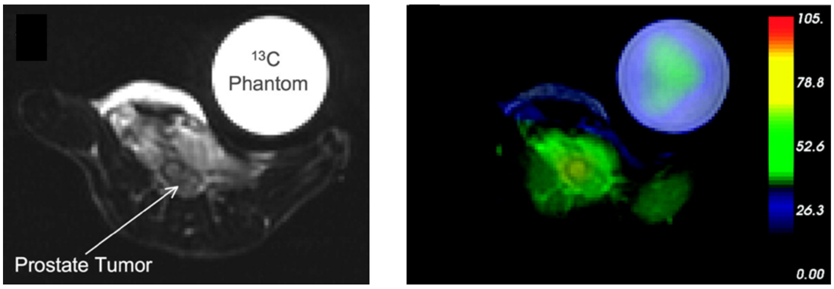

(a) Overlay of ^{1}H and interpolated hyperpolarized ^{13}C lactate image.

(b) Visualization of the hyperpolarized lactate levels in the prostate.

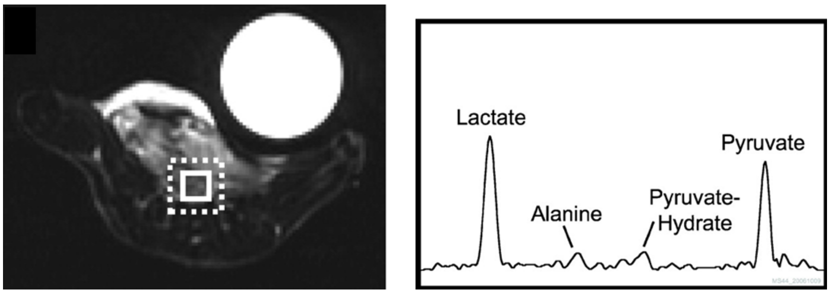

(c) Selection of one voxel from the primary tumor.

(d) Spectrum of the voxel shows prominent signals from lactate and pyruvate and smaller signals from alanine and pyruvate hydrate.

Figure 8: Axial T_2-weighted ^{1}H image depicting the primary tumor from a mouse with a low-grade primary tumor following the injection of 350 µL of hyperpolarized [1-^{13}C] pyruvate. Adapted from [32].

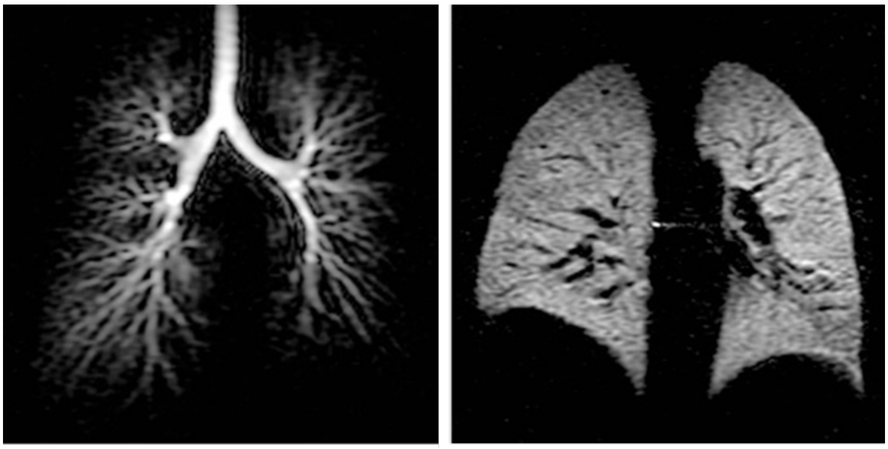

Figure 9: Two hyperpolarized ^{3}He MR images of a healthy volunteer during inhalation (left) and breath hold (right). Adapted from [35].

xenon with a molecular host, as described in Chapter 4. The large chemical shift difference between the exchanging free and encapsulated species allows the generation of a CEST contrast where the presence of very small amounts of host molecules can be detected through saturation of their resonance frequency and detection of the free xenon.

The enhanced sensitivity of these MRI probes allows to take advantage of the good spatial and temporal resolution of the magnetic resonance imaging modality, increasing its competitiveness in the molecular imaging field.

2.3 OPTICAL PROBES

Optical imaging is a molecular imaging modality available in a variety of techniques that take advantage of absorption, reflection, fluorescence or bioluminescence of a tissue or an imaging agent such as fluorochromes, fluorescent proteins or fluorescent quantum dots. (Figure 10).

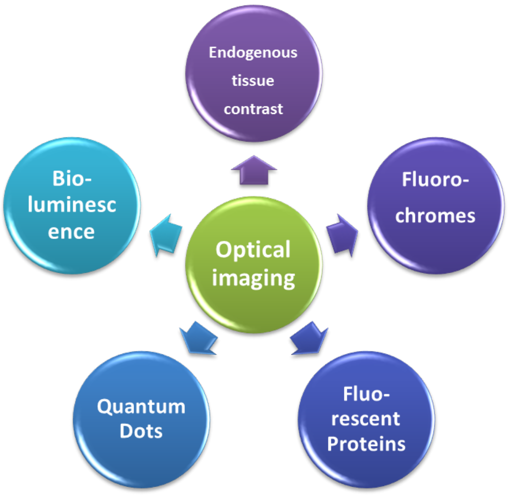

Figure 10: Main classes of optical imaging agents.

2.3.1 *Endogenous contrast of tissues*

Absorption of light in the near infrared range is mainly due to te hemo- and myo-globin content, which is dependent on the vascularization in the tissue. Scattering, however, is dependent on intracelullar composition. Spectral dependence measurement of tissue absorption and scattering provides additional information concerning tissue contents - water, lipids, deoxyhemoglobin - which is useful in breast disease imaging.[36]

In addition, tissues inherently exhibit autofluorescence since all tissues contain low amounts of fluorophores which absorb light and subsequently emit light. Nicotinamide (NAD[H]), flavins, collagen, and elastin are commonly known tissue fluorophores. An abnormal tissue therefore presents a change in the spectroscopic properties based likely on changes in the concentration of these components.[37] For instance, protoporphyrins IX are fluorescent molecules that have been shown to accumulate in pre-malignant tissue and may be used for early cancer detection.

2.3.2 *Fluorochromes*

most of fluorochromes have non specific localization in live cell - such as cyanine dyes. Depending on their structure, they can stain the cell membrane, the cytosol or organelles. For a more specific targeting, it is required to conjugate them with specific ligands. Since many cancers overexpress various receptors, conjugating fluorochromes to specific ligands leads to selective tumor visualization. For example, functionalized by a somatostatin analog, cyanine dye revealed promising results for optical tumor imaging.[38]

Nevertheless, this approach operates with a relatively low signal-to-noise ratio, since non-bound probes are fully fluorescent and thus contribute to background noise. In order to counter this background noise, activatable fluorochromes were developed. The first generation of activatable fluorochromes consisted in a poly-lysine backbone shielded by multiple methoxy-polythylene-glycol sidechains. Several cyanine dyes were loaded onto this macromolecule, resulting in an absence of fluorescence signal due to quenching among the fluorochromes. Non-fluorescent in its native state, fluorochromes were released after enzymatic cleavage. This led to a strong fluorescence signal enabling detection of a protease, as shown in Figure 11.[39]

Another generation of fluorogenic probes consisting in fluorescein derivative bearing trivalent arsenic atoms has been developed by Tsien's group in 1998 and will be discussed in Chapter 6.

2.3.3 *Fluorescent proteins*

Fluorescent proteins (FPs) of the Green Fluorescent Protein (GFP) family consist of 220–240 amino acid residues (25 kDa), which fold into a barrel formed by 11 β-sheets that accommodates an internal distorted helix. The chromophore is formed by a posttranslational modification of the three amino acid residues of the helix at positions 65–66-67. The resulting chromophore is located in the very center of the β-barrel and therefore is well protected from contact with the solvent by the surrounding protein shell. In addition, the barrel of FPs is stabilized by multiple noncovalent interactions that ensure its extremely high stability to thermal or chemical denaturation as well as

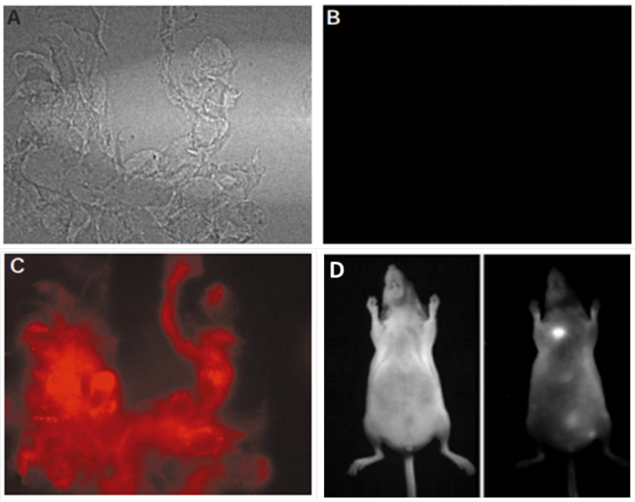

Figure 11: Fluorescence microscopy images of cells incubated with the macromolecular structure bearing multiple cyanine dyes. **A** A phase contract image. **B** immediately after injection of the activatable fluorochrome, no fluorescence signal is observed. **C** After 15 min of incubation, the probe is internalized and degraded resulting in a fluorescent signal. **D** Light (left) and near infrared range fluorescence (right) images these same tumor cells implanted into mammary fat pad of a mouse. Adapted from [39].

resistance to proteolysis.

The gene coding for the FP can be fused to the gene of a protein of interest or a targetting sequence. The resulting fusion can then be transfected in isolated live cell, tissues or animals. This makes it possible to study *in situ* the expression and the distribution of this protein by fluorescence. This discovery was rewarded by the Nobel Chemistry Prize in 2008 attributed to Chalfie, O. Shimomura and R.Tsien.

GFP and its variants and homologs of different colors are used in a variety of applications to study the organization and function of living systems. FPs encoded in frame with proteins of interest make it possible to observe their localization, movement, turnover, and even "aging" (i.e., time passed from protein synthesis).[40] Nucleic acids also can be labeled via RNA- or DNA-binding protein domains. FPs targeted to cell organelles by specific protein localization signals enable visualization of their morphology, fusion and fission, segregation during cell division, etc. FPs are essential tools for individual cell and tissue labeling to visualize morphology, location, and movement. For instance Figure 12 shows the *in vivo* visualization of a colon cancer cells inside a living mouse.[41]

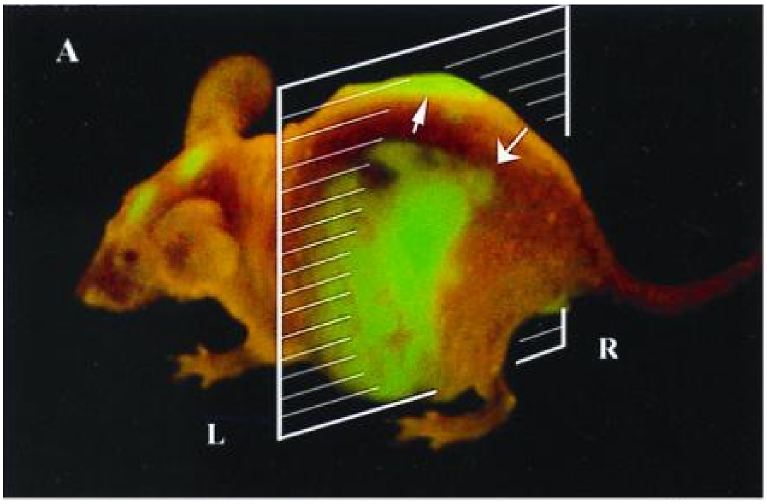

Figure 12: Lateral whole-body image of metastatic liver lesions of a GFP-expressing human colon cancer in the left (thick arrow) and right lobes (fine arrow) of a live nude mouse at day 21 after surgical orthotopic transplantation. Adapted from [41].

2.3.4 *Fluorescent quantum dots*

In the past 15 years a whole range of functionalizable fluorescent nanoparticles were developped. Among them the quantum dots familly already proved its suitability of fluorescence imaging. They are nanocrystals of semiconductor material whose dimensions are less than 10 nm.These nanoparticles posses an excellent stability, a high molar extinction coefficient and quantum yield. Their size controls their emission wavelength. This fine tuning make it possible to follow several molecular targets simultaneously.

Their main advantage resides in their resistance to bleaching over long periods of time (minutes to hours). This increased photostability is especially useful for three-dimensional optical sectioning, where a major issue is bleaching of fluorophores during acquisition. Since their excitation wavelength is localized in the near infrared range, it also allows greater penetration into the tissue. Quantum dots can be utilized as contrast agents for optical imaging, particularly for deep tissue imaging. Deep tissue imaging provides more information about the pathological status of the disease, which makes the treatment more effective and efficient.

2.3.5 *Bioluminescence*

Luciferases are enzymes that emit light in the presence of oxygen and a substrate (luciferin). They have been used for real-time, low-light imaging of gene expression in cell cultures, individual cells, whole organisms, and transgenic organisms. Oxidation of luciferin by luciferase leads to a photon emission: this process is called bioluminescence. Luciferase can act like an internal sensor that emits light wherever luciferase is expressed.

2.4 TOWARD MULTIMODAL MOLECULAR IMAGING

The main challenge in molecular imaging is that modalities with the highest sensitivity have relatively poor spatial resolution, while those with high resolution have relatively poor sensitivity. The idea of combining multiple modalities has grown in the past few years and researchers have come to realize that complementary abilities of different imaging techniques could be exploited by using them in tandem.

In late 80's and early 90's, researchers from the University of California San Francisco, pioneered the development of hybrid SPECT/CT devices which could record both SPECT and x-ray CT data for correlated functional/structural imaging. Since, this new technology has been exploited leading to various multimodal systems which combine two or even three of the molecular imaging techniques. In this work, we present the combination of optical and MR imaging techniques for a bimodal fluorescence-^{129}Xe NMR probe.

BIBLIOGRAPHY

[1] Juhana M. Hakumäki and Timo Liimatainen. Molecular imaging of apoptosis in cancer. *European Journal of Radiology*, 56(2):143 – 153, 2005.

[2] Maria E. Åkerman, Warren C. W. Chan, Pirjo Laakkonen, Sangeeta N. Bhatia, and Erkki Ruoslahti. Nanocrystal targeting in vivo. *Proceedings of the National Academy of Sciences*, 99(20):12617–12621, 2002.

[3] Eva M Sevick-Muraca, Jessica P Houston, and Michael Gurfinkel. Fluorescence-enhanced, near infrared diagnostic imaging with contrast agents. *Current Opinion in Chemical Biology*, 6(5):642 – 650, 2002.

[4] V. Kesava Rao and T. P. Radhakrishnan. Tuning the SERS response with Ag-Au nanoparticle-embedded polymer thin film substrates. *ACS Applied Materials & Interfaces*, 7(23):12767–12773, 2015.

[5] Fabian Kiessling, Stanley Fokong, Patrick Koczera, Wiltrud Lederle, and Twan Lammers. Ultrasound microbubbles for molecular diagnosis, therapy, and theranostics. *Journal of Nuclear Medicine*, 53(3):345–348, 2012.

[6] Woods, Mark, Kiefer, Garry E., Bott, Simon, Castillo-Muzquiz, Aminta, Eshelbrenner, Carrie, Michaudet, Lydie, McMillan, Kenneth, Mudigunda, Siva D. K., Ogrin, Doug, Tircso, Gyula, Zhang, Shanrong, Zhao, Piyu, Sherry, and A. Dean. Synthesis, relaxometric and photophysical properties of a new pH-responsive MRI contrast agent: the effect of other ligating groups on dissociation of a p-nitrophenolic pendant arm. *Journal of the American Chemical Society*, 126(30):9248–9256, 2004.

[7] Christine Baudelet and Bernard Gallez. How does blood oxygen level-dependent (BOLD) contrast correlate with oxygen partial pressure (pO2) inside tumors? *Magnetic Resonance in Medicine*, 48(6):980–986, 2002.

[8] Matthew E. Merritt, Crystal Harrison, Charles Storey, F. Mark Jeffrey, A. Dean Sherry, and Craig R. Malloy. Hyperpolarized 13C allows a direct measure of flux through a single enzyme-catalyzed step by NMR. *Proceedings of the National Academy of Sciences*, 104(50):19773–19777, 2007.

[9] Ilgar Mamedov, Santiago Canals, Jörg Henig, Michael Beyerlein, Yusuke Murayama, Hermann A. Mayer, Nikos K. Logothetis, and Goran Angelovski. In vivo characterization of a smart MRI agent that displays an inverse response to calcium concentration. *ACS Chemical Neuroscience*, 1(12):819–828, 2010.

[10] Jody L. Major, Rene M. Boiteau, and Thomas J. Meade. Mechanisms of znii-activated magnetic resonance imaging agents. *Inorganic Chemistry*, 47(22):10788–10795, 2008.

[11] Randall B. Lauffer. Paramagnetic metal complexes as water proton relaxation agents for NMR imaging: theory and design. *Chemical Reviews*, 87(5):901–927, 1987.

[12] Randall B. Lauffer. Paramagnetic metal complexes as water proton relaxation agents for NMR imaging: theory and design. *Chemical Reviews*, 87(5):901–927, 1987.

[13] A. Dean Sherry and Mark Woods. Chemical exchange saturation transfer contrast agents for magnetic resonance imaging. *Annual Review of Biomedical Engineering*, 10:1–411, aug 2008.

[14] Jian xin Yu. 19F: A versatile reporter for non-invasive physiology and pharmacology using magnetic resonance. *Current Medicinal Chemistry*, 12(7):819–848, 2005.

[15] Michael J. Burns, Peter J. Rayner, Gary G. R. Green, Louise A. R. Highton, Ryan E. Mewis, and Simon B. Duckett. Improving the hyperpolarization of 31P nuclei by synthetic design. *The Journal of Physical Chemistry B*, 119(15):5020–5027, 2015.

[16] Nicholas Hawrylak, Pratik Ghosh, Julie Broadus, Carol Schlueter, William T. Greenough, and Paul C. Lauterbur. Nuclear magnetic resonance (NMR) imaging of iron oxide-labeled neural transplants. *Experimental Neurology*, 121(2):181 – 192, 1993.

[17] Andrew B. Norman, Stephen R. Thomas, Ronald G. Pratt, Sunny Y. Lu, and Robert B. Norgren. Magnetic resonance imaging of neural transplants in rat brain using a superparamagnetic contrast agent. *Brain Research*, 594(2):279 – 283, 1992.

[18] Michael K. Nkansah, Durga Thakral, and Erik M. Shapiro. Magnetic poly(lactide-co-glycolide) and cellulose particles for MRI-based cell tracking. *Magnetic Resonance in Medicine*, 65(6):1776–1785, 2011.

[19] Kevin S. Tang and Erik M. Shapiro. Enhanced magnetic cell labeling efficiency using –NH2 coated MPIOs. *Magnetic Resonance in Medicine*, 65(6):1564–1569, 2011.

[20] Carlos A. Agudelo, Yoichi Tachibana, Andres F. Hurtado, Takayuki Ose, Hidehiro Iida, and Tetsuji Yamaoka. The use of magnetic resonance cell tracking to monitor endothelial progenitor cells in a rat hindlimb ischemic model. *Biomaterials*, 33(8):2439 – 2448, 2012.

[21] Jamal Guenoun, Gerben A. Koning, Gabriela Doeswijk, Lizanne Bosman, Piotr A. Wielopolski, Gabriel P. Krestin, and Monique R. Bernsen. Cationic Gd-DTPA liposomes for highly efficient labeling of mesenchymal stem cells and cell tracking with MRI. *Cell Transplantation*, 21(1):191–205, 2012.

[22] Afonso C. Silva and Nicholas A. Bock. Manganese-enhanced MRI: An exceptional tool in translational neuroimaging. *Schizophrenia Bulletin*, 34(4):595–604, 2008.

[23] Guanshu Liu, Matthew Moake, Yah-el Har-el, Chris M. Long, Kannie W.Y. Chan, Amanda Cardona, Muksit Jamil, Piotr Walczak, Assaf A. Gilad, George Sgouros, Peter C.M. van Zijl, Jeff W.M. Bulte, and Michael T. McMahon. In vivo multicolor molecular MR imaging using diamagnetic chemical exchange saturation transfer liposomes. *Magnetic Resonance in Medicine*, 67(4):1106–1113, 2012.

[24] Phillip Zhe Sun, Thomas Benner, Ashok Kumar, and A. Gregory Sorensen. Investigation of optimizing and translating pH-sensitive pulsed-chemical exchange saturation transfer (CEST) imaging to a 3T clinical scanner. *Magnetic Resonance in Medicine*, 60(4):834–841, 2008.

[25] Jinyuan Zhou, Jean Francois Payen, David A. Wilson, Richard J. Traystman, and Peter C M Van Zijl. Using the amide proton signals of intracellular proteins and peptides to detect pH effects in MRI. *Nature Medicine*, 9(8):1085–1090, 8 2003.

[26] Alex X. Li, Filip Wojciechowski, Mojmir Suchy, Craig K. Jones, Robert H.E. Hudson, Ravi S. Menon, and Robert Bartha. A sensitive PARACEST contrast agent for temperature MRI: Eu3+-DOTAM-glycine (Gly)-phenylalanine (Phe). *Magnetic Resonance in Medicine*, 59(2):374–381, 2008.

[27] Shanrong Zhang, Craig R. Malloy, and A. Dean Sherry. MRI Thermometry based on PARACEST agents. *Journal of the American Chemical Society*, 127(50):17572–17573, 2005.

[28] Silvio Aime, Daniela Delli Castelli, and Enzo Terreno. Highly sensitive MRI chemical exchange saturation transfer agents using liposomes. *Angewandte Chemie International Edition*, 44(34):5513–5515, 2005.

[29] Kathryn C. Partlow, Junjie Chen, Jason A. Brant, Anne M. Neubauer, Todd E. Meyerrose, Michael H. Creer, Jan A. Nolta, Shelton D. Caruthers, Gregory M. Lanza, and Samuel A. Wickline. 19F magnetic resonance imaging for stem/progenitor cell tracking with multiple unique perfluorocarbon nanobeacons. *The FASEB Journal*, 21(8):1647–1654, 2007.

[30] Philipp Boehm-Sturm, Luam Mengler, Stefan Wecker, Mathias Hoehn, and Therése Kallur. In vivo tracking of human neural stem cells with 19F magnetic resonance imaging. *PLOS ONE*, 6(12):1–9, 12 2011.

[31] Klaes Golman, Jan H. Ardenkjær-Larsen, J. Stefan Petersson, Sven Månsson, , and Ib Leunbach. Molecular imaging with endogenous substances. *Proc. Natl. Acad. Sci.*, 100(18):10435–10439, 2003.

[32] Mark J. Albers, Robert Bok, Albert P. Chen, Charles H. Cunningham, Matt L. Zierhut, Vickie Yi Zhang, Susan J. Kohler, James Tropp, Ralph E. Hurd, Yi-Fen Yen, Sarah J. Nelson, Daniel B. Vigneron, and John Kurhanewicz. Hyperpolarized 13C lactate, pyruvate, and alanine: Noninvasive biomarkers for prostate cancer detection and grading. *Cancer Research*, 68(20):8607–8615, 2008.

[33] Klaes Golman, René in't Zandt, Mathilde Lerche, Rikard Pehrson, and Jan Henrik Ardenkjaer-Larsen. Metabolic imaging by hyperpolarized 13C magnetic resonance imaging for in vivo tumor diagnosis. *Cancer Research*, 66(22):10855–10860, 2006.

[34] K. Golman, O. Axelsson, H. Jóhannesson, S. Månsson, C. Olofsson, and J.S. Petersson. Parahydrogen-induced polarization in imaging: Subsecond 13C angiography. *Magnetic Resonance in Medicine*, 46(1):1–5, 2001.

[35] Angela C. Tooker, Kwan Soo Hong, Erin L. McKinstry, Philip Costello, Ferenc A. Jolesz, and Mitchell S. Albert. Distal airways in humans: Dynamic hyperpolarized 3He MR imaging—feasibility. *Radiology*, 227(2):575–579, 2003.

[36] Vasilis Ntziachristos and Britton Chance. Breast imaging technology: Probing physiology and molecular function using optical imaging - applications to breast cancer. *Breast Cancer Research*, 3(1):41, Dec 2000.

[37] Georges A. Wagnieres, Willem M. Star, and Brian C. Wilson. In vivo fluorescence spectroscopy and imaging for oncological applications. *Photochemistry and Photobiology*, 68(5):603–632, 1998.

[38] Kai Licha, Carsten Hessenius, Andreas Becker, Peter Henklein, Michael Bauer, Stefan Wisniewski, Bertram Wiedenmann, and Wolfhard Semmler. Synthesis, characterization, and biological properties of cyanine-labeled somatostatin analogues as receptor-targeted fluorescent probes. *Bioconjugate Chemistry*, 12(1):44–50, 2001.

[39] Umar Mahmood Ralph Weissleder, Ching-Hsuan Tung and Jr Alexei Bogdanov. In vivo imaging of tumors with protease-activated near-infrared fluorescent probes. *Nature Biotechnology*, 17:375–378, 1999.

[40] Richard N. Day, Ammasi Periasamy, and Fred Schaufele. Fluorescence resonance energy transfer microscopy of localized protein interactions in the living cell nucleus. *Methods*, 25(1):4 – 18, 2001.

[41] Meng Yang, Eugene Baranov, Ping Jiang, Fang-Xian Sun, Xiao-Ming Li, Lingna Li, Satoshi Hasegawa, Michael Bouvet, Maraya Al-Tuwaijri, Takashi Chishima, Hiroshi Shimada, A. R. Moossa, Sheldon Penman, and Robert M. Hoffman. Whole-body optical imaging of green fluorescent protein-expressing tumors and metastases. *Proceedings of the National Academy of Sciences*, 97(3):1206–1211, 2000.

3

SPIN-HYPERPOLARIZATION

3.1 NMR SENSITIVITY

Any charged particle in motion has a magnetic moment and produces a magnetic field. Nuclear magnetic moments in a magnetic field take different orientations that corresponds to distinct energy levels. The initial populations of the energy levels are determined by thermodynamics, as described by the Boltzmann distribution (1):

$$\frac{N_{upper}}{N_{lower}} = e^{-\Delta E/kT} = e^{-h\nu/kT} = e^{-\gamma\bar{h}B_0/kT} \tag{1}$$

where N_{upper} and N_{lower} represent the population of nuclei in upper and lower energy states, respectively, k is the Boltzmann constant, T is the absolute temperature (K), $\bar{h}$ is the Planck's constant divided by 2π, γ the gyromagnetic ratio and B_0 the magnetic field. ΔE represents the required energy to induce flipping and to obtain an NMR signal (see Figure 13).

Figure 13 represents the distribution of a small number (ten millions) of hydrogen nuclei, calculated from (1) for protons in a 11.4 T magnetic field (ν = 500 MHz). At thermal equilibrium at room temperature, the population ratio will be 0,999921713. That means for every 5,000,000 nuclei in the upper energy state, there are 5,000,391 nuclei in the lower energy state.

Such a small population difference leads to a significant sensitivity problem for NMR because only the difference in populations - 805 of 2,000,805 nuclei) is detected. The magnetization, defined in (2), emanating from a real sample is simply the sum of all the individual nuclear magnetic moments (spins). It will be the total magnetization that determines an NMR signal – not the magnetic moment of an individual nucleus.

$$M = \frac{\gamma\bar{h}N}{2}P \tag{2}$$

where γ denotes the nuclear gyromagnetic ratio, $\bar{h}$ is the Planck's constant divided by 2π, N is the total number of spins, and P is the nuclear polarization, defined in (3).

$$P = \frac{N_{lower} - N_{upper}}{N_{lower} + N_{upper}} = \frac{N_{lower} - N_{upper}}{N} \tag{3}$$

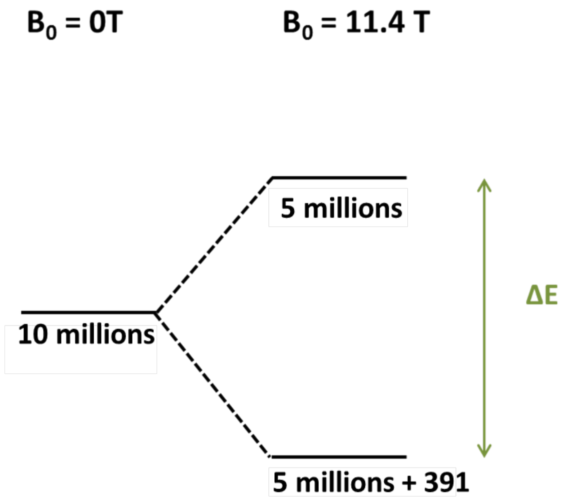

Figure 13: . Dependence on magnetic field strength B_0 of the separation of nuclear energy levels (Δ E) for spin I= 1/2 and the relative populations of the energy levels assuming one has approximately ten million protons in the sample.

where N_{lower} and N_{upper} are the number of spins in low and high energy states, respectively.

It is then possible to determine the polarization P at thermal equilibrium ((4)):

$$P = \frac{N_{lower} - N_{upper}}{N_{lower} + N_{upper}} = \frac{exp(\frac{\gamma\bar{h}B_0}{2kT}) - exp(\frac{-\gamma\bar{h}B_0}{2kT})}{exp(\frac{\gamma\bar{h}B_0}{2kT}) + exp(\frac{-\gamma\bar{h}B_0}{2kT})} = tanh(\frac{\gamma\bar{h}B_0}{2kT}) \tag{4}$$

At physiologically relevant temperatures, P is extremely small even at very high applied fields, therefore $P \approx \frac{\gamma\bar{h}B_0}{2kT}$ (high temperature approximation). For instance, the ^1H percent polarization in a 1,000 MHz NMR spectrometer is only 0.008% and for other relevant biomedically relevant nuclei such as ^{13}C, ^{15}N or ^{129}Xe, polarization P remains relatively low (10^{-6} - 10^{-4}). The low sensitivity of NMR is probably its greatest limitation for applications to biological systems.

However, in some cases P can be artificially increased well above its low thermal equilibrium level. This can be performed by polarization transfer from a more ordered state: it can be photons,[1] or electrons.[2] This significant (usually orders-of-magnitude) increase in nuclear spin polarization above the thermal-equilibrium level was later called *hyperpolarization*.

3.2 MAIN XENON HYPERPOLARIZATION METHODS

Hyperpolarization consists in transiently imbalancing the nuclear spin repartition of the energy level populations initially at the Boltzmann distribution, by polarization transfer from a more ordered system. In the case of xenon, it can be done via Optical Pumping (OP) or Dynamic Nuclear Polarization (DNP).

3.2.1 *Dissolution Dynamic Nuclear Polarization*

The d-DNP technique relies on unpaired electrons as the source of large spin polarization, by transferring their polarization to the nuclear spins. Indeed, when electrons are subjected to sufficiently low temperatures in a static magnetic field of several Tesla, their polarization at Boltzmann equilibrium is 660 times higher than the one of protons.

In liquid state, the predominant transfer phenomenon is the *Overhauser Effect*. During this process, the huge Boltzmann polarization of unpaired electrons is transfered to vicinal nuclear spins by saturation of the corresponding electron spin resonance (ESR) transitions.This is possible via the spontaneous electron-nucleus cross relaxation (flip-flop mechanism in Figure 14) .

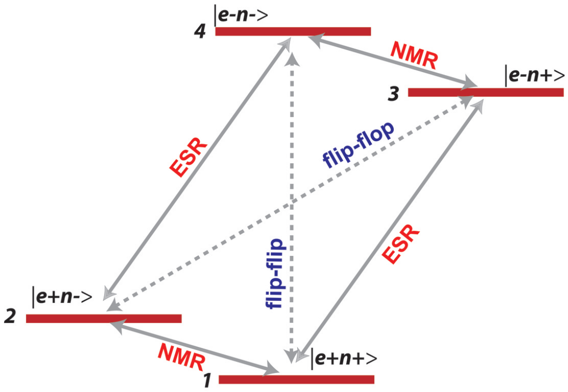

Figure 14: . Zeeman energy levels of an electron-nucleus system presenting the Electron Spin Resonance (ESR) transitions, Nuclear Magnetic Resonance (NMR) transitions and flip-flop transitions.

As a result, the main parts of a DNP polarizer are its cryostat, where the sample doped with radicals is usually immersed in a superfluid helium bath, a superconducting magnet that provides a sufficient field to achieve optimal electron spin polarization P(e), and a microwave irradiation device (typically power about 100 mW) operating at a frequency suitable for the saturation of electron spin resonance (ESR) transitions (see Figure 15). After this first step, the sample is warmed and quickly (some seconds) transported in the NMR magnet for detection.

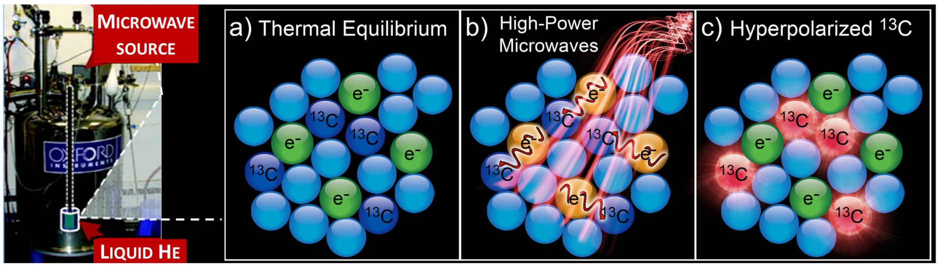

Figure 15: . In a dynamic nuclear polarization experiment, MR-active nuclei (here ^{13}C) are mixed with a low concentration of unpaired electrons in a glass matrix. The sample is then irradiated with high-power microwaves at the electron resonance frequency in a high magnetic field (≈ 3 T) and at low temperatures (≈ 1 K). This enables ^{13}C hyperpolarization via polarization transfer from free electrons. Adapted from [3].

In the liquid state DNP experiment, three steps can be distinguished:

1. Polarization of the sample by microwave irradiation at low temperature (of the order of 1K)
2. Dissolution of the sample in a hot solvent and transport to the spectrometer or imager.
3. Transferring the solution into an NMR tube or injecting it into an animal.

The method can be applied to a wide variety of molecules, including xenon.[4] The procedure for hyperpolarizing xenon via DNP includes a first production of an amorphous solid pellet containing xenon in an adequate frozen solvent doped with free radicals. In this solid state, the high electron spin polarization due to the combined use of low temperature and high static magnetic field is transferred in part to the nuclear spins by microwave irradiation in some tens of minutes. Then a fast sublimation step ensures separation of the noble gas from the radicals.

The polarization of xenon is about 100 times higher than its polarization in Boltzmann equilibrium.[4] The characteristic time for producing hyperpolarized xenon via DNP, according to Capozzi et al. is about 1 hour and half for a 80-mL batch.[5]

The polarization produced then decays back to thermal equilibrium through relaxation at a rate dependent on the inherent properties of the molecule under study (typically 1-2 minutes). Thus, a current limitation of the method is that the enhanced signal is only available for a short period of time.

Another hyperpolarization technique that generates hyperpolarized noble gases (^{3}He, ^{129}Xe, ^{83}Kr, etc.) with high nuclear spin polarization has been implemented: Spin-Exchange Optical Pumping (SEOP).

3.2.2 *Spin-Exchange Optical Pumping*

This technique requires the intervention of photons and an alkali metal. Indeed, a photon beam can be fully circularly polarized (spin +1 or -1), and therefore can be the ideal polarization source. However, as optical transitions do not influence the nuclear spins directly (only the rearrangement of the orbital motion of an electron can be responsible for photon absorption), the experiment is a two-step process. The Spin-Exchange Optical Pumping (SEOP) experiment involves an alkali metal that is heated so that the gas phase absorbs circularly polarized photons at the wavelength corresponding to the transition between its ground state and its first excited state (795 nm for rubidium). The principle is based on the use of selection rules governing the light-atom interaction and on the conservation of the angular momentum of the photons. The selection rules for an electronic transition are $\Delta S = 0$, $\Delta L = 0, \pm 1$ and $\Delta J = 0, \pm 1$. Let us remind that atomic states are described by term symbols of the form:

$$^{2S+1}L_J$$

where

- L is the orbital angular momentum of the electron (in spectroscopic notation)
- S its spin angular momentum. 2S+1 represents the spin multiplicity or the number of possible states of J for a given L and S
- J the total electron angular momentum as described in Figure 16.

Rubidium, as an alkali metal has only one electron on its 5s layer. But it has also a nuclear spin that is neglected here. Rubidium has a ground state $^{2}S_{1/2}$ - [...]$4p^{6}$ $5s^{1}$ - described by $s = 1/2$ $l = 0$ and $j = 1/2$. It also has two excited states $^{2}P_{1/2}$ and $^{2}P_{3/2}$ - [...]$4p^{5}$ $5s^{2}$ leads to $s = 1/2$ $l = 1$ and $j = 1/2, 3/2$. In the presence of a static magnetic field, degeneracy of the spin levels occurs: each of the energy levels is subdivided into Zeeman sub-levels. $^{2}S_{1/2}$ and $^{2}P_{1/2}$ levels split into two states each ($m_j = 1/2, -1/2$) and $^{2}P_{3/2}$ level into four states ($m_j = 3/2, 1/2, -1/2, -3/2$). At thermal equilibrium, the two sub-levels of the ground state are populated (with the Boltzmann distribution for electrons).

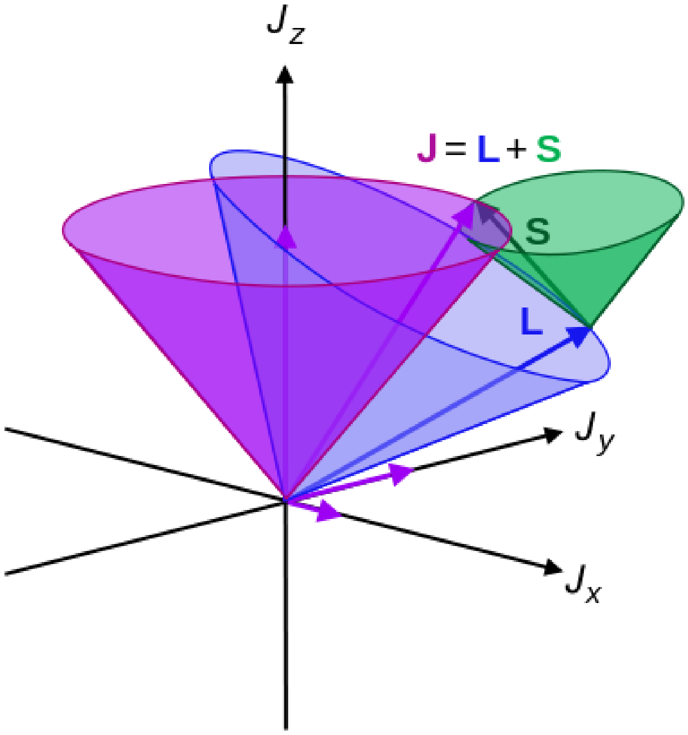

Figure 16: Scheme of orbital and spin angular momenta and the spin-orbit coupling J.

When irradiating with a left polarized light - photons have an angular momentum of Δm_j = +1 - only the transitions which retain the angular momentum are possible. This means that photons can only be absorbed by atoms in the $^2S_{1/2}$ state with m_j = -1/2. The state $^2P_{1/2}$ with m_j = + 1/2 is then populated as seen in Figure 17.

Consequently to collisions with gas atoms in the cell, the excited level m_j = + 1/2 of $^2P_{1/2}$ is depopulated and populates each of the sub-levels m_j = ± 1/2 of the ground state with equiprobable de-excitation rates between the levels m_j = - 1/2 and m_j = + 1/2 of the $^2S_{1/2}$ state.

Thus the level m_j = +1/2 of the ground state is not excited due to the constraints imposed by the selection rules and it is populated as the upper state is depopulated. This results in a hyperpolarization of the ground state of the spins of the valence electrons of the rubidium as seen in Figure 17.

This first step is extremely fast and complete hyperpolarization of the electron spins occurs in microsecond to millisecond time scale depending on the experimental conditions. As the cell also contains the noble gas, a second step occurs, consisting in polarization transfer from the electron spins of the alkali metal to the xenon nuclear spins. This second step, based on cross-relaxation phenomenon during the transient formation of van der Waals Rb-Xe pairs or during xenon-alkali metal collisions, is obviously less efficient and slower than the

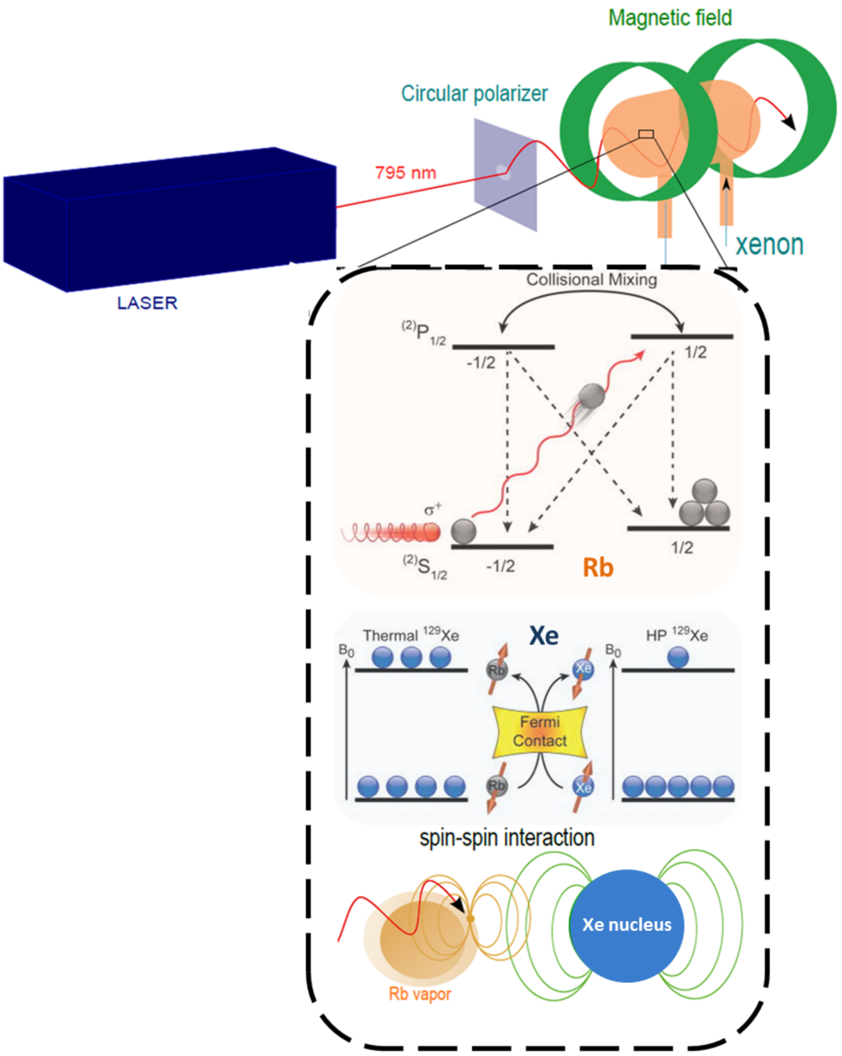
Magnetic field
Circular polarizer
795 nm
LASER
xenon
Collisional Mixing
$^{(2)}P_{1/2}$
-1/2
1/2
σ^+
$^{(2)}S_{1/2}$
-1/2
1/2
Rb
Thermal ^{129}Xe
Xe
HP ^{129}Xe
B_0
B_0
Rb
Xe
Fermi Contact
Rb
Xe
spin-spin interaction
Xe nucleus
Rb vapor

Figure 17: Spin-Exchange Optical Pumping setup requires an optical cell containing a noble gas - xenon -, buffer gases (N_2 and He), and a small quantity of vaporized alkali metal (typically Rb). Nuclei are irradiated by a laser light (795 nm for Rb D_1 transition). Photons fully circularly polarized (Δm_j = +1) are absorbed. Since angular momentum is conserved, this leads to an absorption from one of two Rb ground electronic (m_j = -1/2) states. After collisions with gas atoms, the ground states are repopulated at effectively equal rates. However, since only one ground state is depleted by the laser, ground-state population accumulates on the other m_J = 1/2 state, leaving the Rb electronically spin-polarized. A weak magnetic field along the direction of laser propagation (drawn in green) enables the degeneracy of the spin levels. Gas-phase collisions then allow spin exchange between the polarized Rb electron spins and the noble gas nuclear spins.

first one (see Figure 17).
In our experimental conditions (non-narrowed laser diodes, pressure

inside the pumping cell beyond 1 bar) the typical time scale for obtaining a fully hyperpolarized nuclear spin system is on the order of one to five minutes for a 12-mL batch.

Thus, time to produce hyperpolarized xenon via SEOP advantageously compares with the characteristic time scale of DNP. While for DNP it is easier to increase the hyperpolarized xenon quantities by increasing the solid-state sample volume, the SEOP experiment is cheaper and prone to provide in a short time xenon with a polarization exceeding 0.2, in quantities enabling *in vitro* and *in vivo* (mainly for small animals) NMR/MRI studies.
As an example, Figure 18 shows the difference between between thermic and hyperpolarized ^{129}Xe NMR spectra on a 11.4 T magnet.

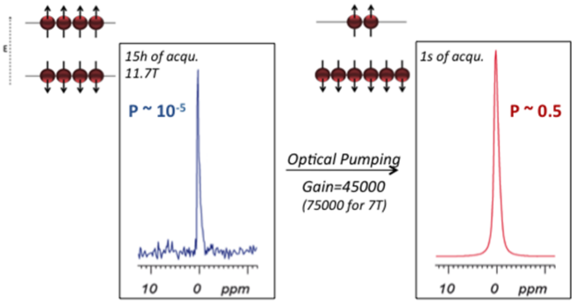

Figure 18: ^{129}Xe NMR spectrum (in blue) obtained after 15 hours of acquisition and exhibiting a polarization of 10^{-5}. Hyperpolarized ^{129}Xe NMR spectrum (in red) obtained after only 1 s of acquisition. Polarization has been enhanced by more than 5 orders of magnitude.

For biomedical applications using laser-polarized xenon, a concern has to be addressed dealing with the chemical species other than xenon inside the optical pumping cell. In addition to the noble gas, the cell contains some droplets of the alkali metal, a few hundred torrs of nitrogen (a quenching gas designed to avoid radiative deexcitation susceptible to give rise to photons with opposite polarization) and some bars of helium (the pressure broadening enables a better matching between the emission and absorption bandwidths). Xenon can easily be separated from nitrogen and helium via condensation in liquid nitrogen in the presence of a strong static magnetic field for avoiding fast nuclear relaxation. This step enables hyperpolarized xenon accumulation through multiple optical pumping batches or in flow mode. A concern could appear for the presence of the alkali metal with xenon. At this step, let us mention that inside the cell, at the temperature used during OP (usually < 100°C), the pressure vapor of, for instance, rubidium, is only 0.2 mTorr. The residual traces of rubidium can thus easily be trapped by passing the mixture through a getter cooled at -98°C by a methanol/liquid nitrogen mixture placed between the OP cell outlet and the storage reservoir.

The advantage of DNP technique compared to optical pumping is that the required instruments can be found near imagers. With this in mind, we designed a mobile spin-exchange optical pumping setup that enables production of laser-polarized noble gases in a standalone mode, in close proximity to hospitals or research laboratories.

3.2.3 *Our recent contribution: optical pumping in a van*

Figure 19 displays the schematic drawing of the experimental setups. Its additional particularity lies in the removable wheels that enable us to move it easily and place it inside a dedicated van, equipped with a double wall and anoxia detectors. With this setup, xenon optical pumping can be performed in the near vicinity of the imagers or spectrometers, which reduces the handling risks.

This work was published in [6]

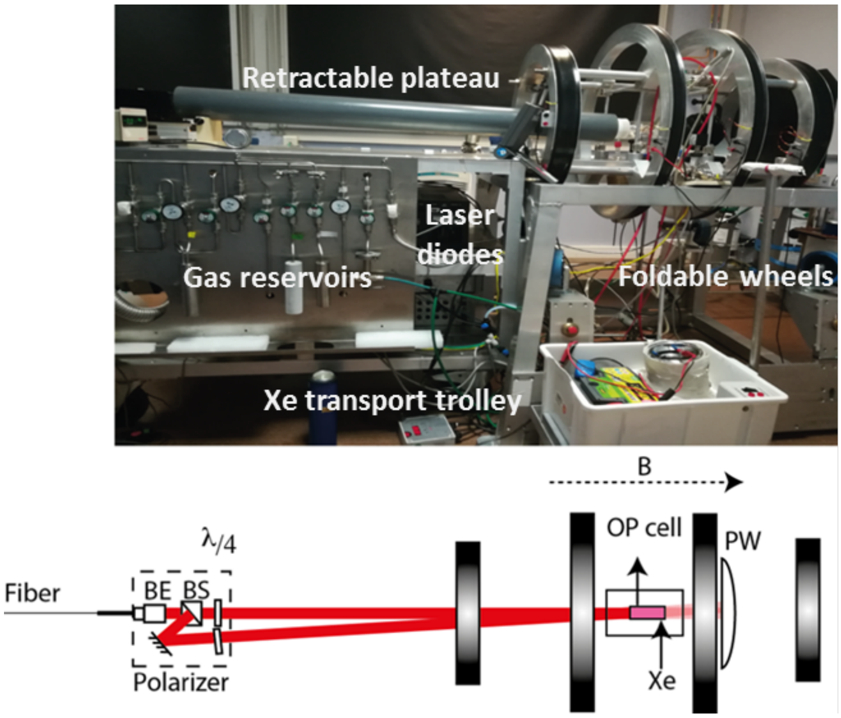

Figure 19: Production of laser-polarized xenon. Top: Photograph of our SEOP setup; bottom: schematic drawing. BE: beam expander; BS: beam splitter; λ/4: quarterwave plates; PW: powermeter. B: magnetic field (100 G) colinear to the light beam.

The device has been conceived in two parts, the coils being separated from the rest of the setup (pumping cell, optics, gas distribution system, pump, power supply, etc.). With this principle, at the difference of the other transportable polarizers proposed in the literature,[7, 8, 9] it becomes possible by keeping only the latter part to use the fringe field of a horizontal MRI magnet to perform in the same place SEOP and imaging.

An ensemble of four coils with diameter of 620 mm for the two central ones and of 440 mm for the two outer ones creates a unidirectional magnetic field of 100 G when supplied with a DC current of 8 A (Electric supply, Delta Electronika), with a field homogeneity better than 10^{-4} in a volume of 120 cm^3. An aluminum frame supports these coils. Four foldaway wheels have been added in order to easily move it. At the rear extremity of the frame, a large plastic beaker that slides along a vertical rod enables collection of hyperpolarized noble gas in a removable receptacle. The second part (in blue in Figure 20 of the device is contained on a chariot. It contains the laser diodes (1), the electric supply for the coils (2), the heating system (3), the pumping group (4), the plate containing the gas reservoirs and the tubing (5), the polarizer (6), and the SEOP cell (7).

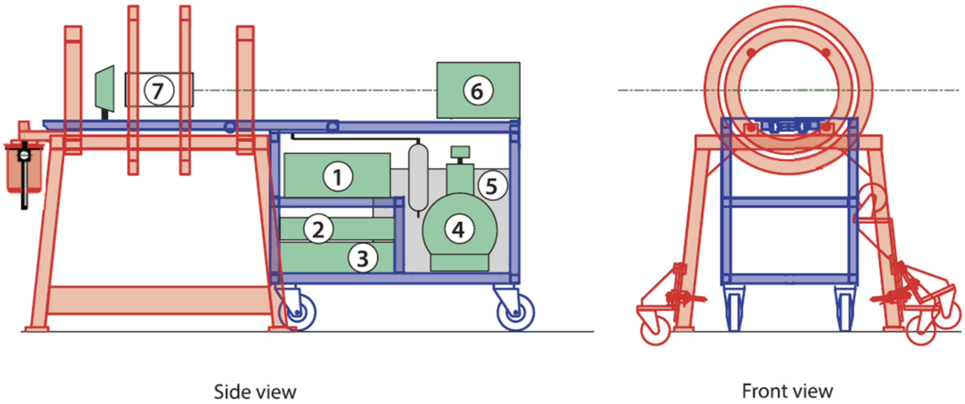

Figure 20: Drawing of the SEOP setup, side and front views. For explanation of the indicated numbers, see the main text.

The latter is placed on a plateau, which is retractable, thanks to a system of rails and wheels placed under it. While in the transport mode it is in retracted position, it is extended to reach the center of the coils during operation. When the wheels of the device containing the coils are folded away, vertically the two parts fit perfectly together through the sliding plateau and the SEOP cell comes at the exact center of the coils.

The light source consists in a fibered laser diode (Coherent Duo FAP, 2 x 30 W maximal power (1)) entering in a circular polarizing unit (Coherent) (6) after having crossed a homogenizer in which the bundle consisting of two 800 µm diameter solid-core fibers is transformed into a unique randomly polarized beam with Gaussian shape. The circular polarizing unit essentially consists in a polarization beamsplitter cube, a mirror, and two adjustable quarterwave plates. Photons with one polarization cross the cube and then a quarterwave plate, while photons with the other polarization are reflected by the face of the cube, then by a mirror and cross the other quarterwave plate.

The large uniform collimated beams converge at the SEOP cell front face situated 130 cm away from the polarizer. Behind the cell, a LM- 100-HTD powermeter connected to a FieldMaster-GS display unit (Coherent) measures the light intensity that has not been absorbed by the alkali vapors. Heating is performed by a flow of hot air in a double envelope. The temperature of the air is regulated via a Eurotherm B-VT 2000 unit. In the cell however the input of the gases is different from the exit not only for the heating gas (outer compartment) but also for the inner compartment. The front face of the SEOP cell is a borosilicate glass disk treated to be transparent at 795 nm (Fichou), corresponding to the D1 line of rubidium. This disk is fixed onto the rest of the cell, thanks to Teflon rings.
Grains of metallic rubidium are introduced into it in a glove box under argon. Then, it is connected to the tubing: upstream to Swagelok plastic tubes, downstream to a glass coil placed just at its output. This glass coil is intended to be thermalized at -98°C by a methanol-nitrogen cooling bath in order to trap potential rubidium traces during the transfer of the gas mixture to the storage reservoir. Afterwards, the SEOP cell is filled with xenon, nitrogen, and helium, sequentially, or from a 1.8 L bottle containing the mixture already prepared (opposite face of the plate). Typical values for the pressures inside the SEOP cell are 0.1 bars xenon, completed with nitrogen to reach 0.4 bars and then with helium to reach 3.5 bars at room temperature. An aluminum plate contains several valves and reservoirs. For the arrival of helium from the bottle, a quarter-turn ball valve is sufficient (this gas is used at a super-atmospheric pressure), while for nitrogen and for xenon, quarter-turn ball valves are completed by precision valves. Between the quarter-turn valves and the precision valves, the gases cross Sertronics filters (Air Liquide) in order to be purified from O2 or H2O traces (opposite side of the plate). Two reservoirs contain natural abundance and 83% ^{129}Xe-enriched xenon, while a third one having an output pipe different from the inlet pipe serves to separate xenon from other gases by condensation.

A dry scroll vacuum pump (model SH110 from Agilent) enables to reach a primary vacuum in all the gas tubes and serves to separate xenon from helium and nitrogen after optical pumping. When necessary, it can be completed by a turbo-pumping group (model VLP70 fromVarian). Pressure is measured in different points of the device through diaphragm gauges (Varian CDG-500) and vacuum gauge controllers (Varian AGC100-DV100). In such a SEOP setup, the limiting factor for producing quickly hyperpolarized xenon is the time required to heat the cell. In order to save time, a derivation system using a hose continuously heated at 70°C (Kenovel) has been installed on the heating circuit. It is connected each time a new SEOP experiment starts and disconnected before polarized xenon is collected. The complete SEOP experiment can then be achieved in less than 5 min. Thanks to the wheels both parts of the device can be easily transported to the interior of a van equipped with a power liftgate.

In addition to the SEOP setup, during operation, the van compartment contains two chariots. One of these chariots supports the nitrogen and helium gas bottles (20 l-bottles of N_2 quality BIP and helium quality Premier XSS, from Air Products, both equipped with manometer and pressure reducer), and the second one is a home-built chariot for the transport of polarized xenon. In this chariot, xenon is stored frozen in a glass coil inside a solenoid immersed in liquid nitrogen. The cold solenoid, driven by a car battery, delivers a magnetic field of 5 kG. Although no precise measurement was done, the xenon relaxation in these conditions is on the order of hours.

The simplicity of use and the robustness of our mobile SEOP setup providing milliliters of xenon per minute with high useful polarization - xenon production rates of 5 ml/min with polarization of 0.15 were obtained for instance. pave the way to numerous experiments and collaborations. The lightweight of the device (that could be further miniaturized), the operating flexibility, and the production rate of the hyperpolarized species contrast with other techniques such as dynamic nuclear polarization and give versatility to the approach.

3.3 DETAILS OF THE XENON SEOP EXPERIMENT

For each optical pumping and NMR experiment on a sample of hyperpolarized ^{129}Xe, the protocol is carried out in the following way:

- First, paramagnetic species (especially O_2) are removed from the solution in the NMR tube thanks to a helium flow. This step is crucial for xenon experiments, paramagnetic species being the most important cause of xenon relaxation. Vacuum is then made into the tube using a static pump.
- Establishment of the vacuum in the circuit. Indeed, like all alkaline, rubidium reacts very violently in the presence of oxygen, it is therefore essential to guarantee a good vacuum in the whole circuit arriving and leaving the optical cell. For this purpose, a primary pump provides a vacuum the order of 10^{-5} bar inside the optical cell and throughout the assembly circuit.
- Filling of the optical cell with the gas mixture (xenon, then nitrogen to prevent from radiative de-excitations, then helium 4

providing the pressure necessary to widen the absorption line of rubidium).

- Heating of the optical cell at the chosen temperature.
- Once the temperature is reached, switching on the magnetic field surrounding the optical cell.
- Optical pumping time (around 5 minutes).
- During pumping, insert the Dewar containing the solenoid and liquid nitrogen bath around the coil. Establishment of a pressure greater than 1 bar of nitrogen (of the order of 1.5 bar on average) in the circuit between the outlet of the cell and the vacuum pump. This is for avoiding a too sudden expansion between the high pressure cell and the rest of the circuit, which could cause a fast xenon relaxation by a fast diffusion in too efficient field gradients. This is also to prevent leakage and, therefore, oxygen in the assembly.
- Once pumping is complete, the optical cell is cooled by turning off the heating resistor and the heating ribbon so that the rubidium returns to the solid state and remains inside the optical cell. At the output of the optical cell is a first tank cooled by a 175K "liquid nitrogen-methanol" mixture whose function is to trap the possible rubidium vapors that would have escaped from the optical cell.
- Then the first transfer is made: the cell is opened and the vacuum pump is switched on: the xenon is stored in solid form in a glass coil. To trap xenon, the glass coil that serves as storage tank is immersed in a 77K liquid nitrogen bath in a Dewar. At this temperature, xenon is condensed (condensation from 163K) and nitrogen and helium remaining in the gaseous state are evacuated by the vacuum pump. The cold storage tank of hyperpolarized xenon was designed as a glass coil to maximize the contact surface with liquid nitrogen and thus trap more xenon (see Figure 21).
- When xenon is stored in the glass coil, the valves allowing the gas inlet inlets are closed and the plugs making the connection with the rest of the assembly are unscrewed while the assembly is insulated from the air of the room by means of Swagelok valves before the assembly coil is disconnected.
- The Dewar is then disconnected from its support and the chariot containing the glass coil, the solenoid delivering a field of 300 mT immersed in the liquid nitrogen and the battery, is brought to the spectrometer. Once the rare gas is condensed in the glass

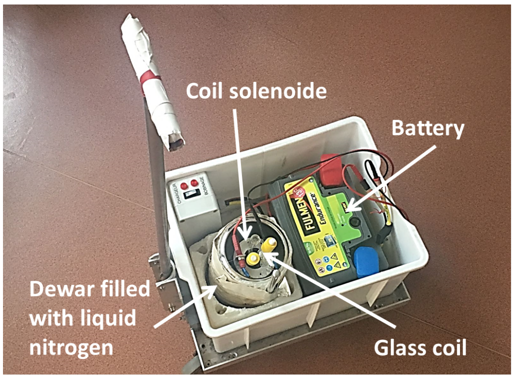

Figure 21: Photograph of the chariot that enables us to transport the hyperpolarized xenon toward the magnet.

coil, the xenon T_1 in the solid phase is several hours thanks to the field supplied by the solenoid.

- The xenon transfer between the glass coil and a vacuumed NMR tube is carried out some centimeter from the magnet of the spectrometer in a leakage field of about one hundred gauss. The transfer of xenon in gas phase is permitted by a glass bridge which is connected to a pump which establishes the vacuum between the NMR tube and the glass coil, as displayed in Figure 22.

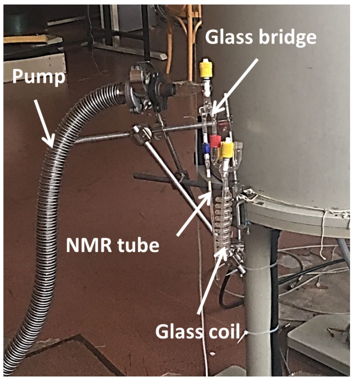

Figure 22: Photograph of the glass bridge permitting the hyperpolarized xenon transfer from the glass coil to the NMR tube.

Thus, xenon condensates from the glass coil (which is heated with hot water) to the NMR tube by a cold point with liquid nitrogen. According to Henry's law, at constant temperature and equilibrium, the quantity of gas dissolved in a liquid is proportional to the partial pressure exerted by this gas on the liquid. This leads to this equation (5):

$$c_i^L = p_i k_i^H \tag{5}$$

Where p_i is the partial pressure of a pure gaseous body i in bar, c_i^L its gas concentration (mol/L) in a solvent L and k_i^H the Henry's constant of the given gas i in mol.$L^{-1}bar^{-1}$ at 298.15 K.

As an example, Henry's constant for xenon at 298.15 K in water solution is 0.0043 mol.$L^{-1}bar^{-1}$. This means that 1 bar of gaseous xenon inside the NMR tube corresponds to 4.3 mM of dissolved xenon in water solution.

In order to increase the molar fraction of xenon inside the aqueous solution, the NMR tube is shaken and then introduced into the spectrometer and the NMR experiment can begin.

BIBLIOGRAPHY

[1] M. A. Bouchiat, T. R. Carver, and C. M. Varnum. Nuclear polarization in he^3 gas induced by optical pumping and dipolar exchange. *Phys. Rev. Lett.*, 5:373–375, Oct 1960.

[2] T. R. Carver and C. P. Slichter. Polarization of nuclear spins in metals. *Phys. Rev.*, 92:212–213, Oct 1953.

[3] Panayiotis Nikolaou, Boyd M. Goodson, and Eduard Y. Chekmenev. NMR Hyperpolarization techniques for biomedicine. *Chemistry – A European Journal*, 21(8):3156–3166, 2015.

[4] E. L. Hahn. Spin echoes. *Phys. Rev.*, 80:580–594, Nov 1950.

[5] Andrea Capozzi, Jean-Noël Hyacinthe, Tian Cheng, Tim R. Eichhorn, Giovanni Boero, Christophe Roussel, Jacques J. van der Klink, and Arnaud Comment. Photoinduced nonpersistent radicals as polarizing agents for X-nuclei dissolution Dynamic Nuclear Polarization. *The Journal of Physical Chemistry C*, 119(39):22632–22639, 2015.

[6] C. Chauvin, L. Liagre, C. Boutin, E. Mari, E. Léonce, G. Carret, B. Coltrinari, and P. Berthault. Note: Spin-exchange optical pumping in a van. *Review of Scientific Instruments*, 87(1):016105, 2016.

[7] Panayiotis Nikolaou, Aaron M. Coffey, Laura L. Walkup, Brogan M. Gust, Nicholas Whiting, Hayley Newton, Iga Muradyan, Mikayel Dabaghyan, Kaili Ranta, Gregory D. Moroz, Matthew S. Rosen, Samuel Patz, Michael J. Barlow, Eduard Y. Chekmenev, and Boyd M. Goodson. XeNA: An automated 'open-source' 129Xe hyperpolarizer for clinical use. *Magnetic Resonance Imaging*, 32(5):541 – 550, 2014.

[8] Samuel Patz, F. William Hersman, Iga Muradian, Mirko I. Hrovat, Iulian C. Ruset, Stephen Ketel, Francine Jacobson, George P. Topulos, Hiroto Hatabu, and James P. Butler. Hyperpolarized 129Xe MRI: A viable functional lung imaging modality? *European Journal of Radiology*, 64(3):335 – 344, 2007.

[9] Sergey E. Korchak, Wolfgang Kilian, and Lorenz Mitschang. Configuration and performance of a mobile 129Xe polarizer. *Applied Magnetic Resonance*, 44(1):65–80, Feb 2013.

4

XENON BIOSENSORS

4.1 XENON : A SPY WITH MULTIPLE FACETS

Among the species that can be spin-hyperpolarized, xenon is of high interest, due to its exogenous nature (leading to the absence of background noise) and the fact that it can act as a spy of biological events without interfering on them. Moreover, it can be endlessly reloaded and simply removed from the sample exposing no ionizing radiation for the patient - for ^{129}Xe isotope. Finally, owing to the high deformability of its large electron cloud xenon is deeply sensitive to its local environment and constitutes a perfect probe for various biological interactions. Soluble in most biological fluids, xenon can cross the plasma membrane in a few tens of milliseconds without losing its hyperpolarization.[1]

The first initial applications of hyperpolarized ^{129}Xe NMR in biology were the anatomical imaging of the lung whereas the vast majority of work in human images has been performed using hyperpolarized ^{3}He instead. Unfortunately, the price of helium skyrocketed due to the emergence of neutron detectors after the 9/11 terrorist attacks. This demand far exceeded the replenishment rate from the primary source, leading to a strict regulation of the supply of ^{3}He. Even if it has a lower gyromagnetic ratio, xenon was a perfect candidate since it is naturally abundant on Earth and its cost is relatively low. As a matter of fact, there are more than 29 isotopes of xenon of which 9 are stable and 2 have non-zero spins that are therefore detectable in NMR. Those two candidates are isotope ^{129}Xe with spin 1/2 and natural abundance 26.44% and isotope ^{131}Xe with spin 3/2 and natural abundance 21.24%. Xenon 129 is the isotope with the highest gyromagnetic ratio ($\frac{\gamma_{^{129}Xe}}{\gamma_{^{1}H}} = 0.278$) and the longest relaxation time, it is a gas of choice for NMR. More than being an alternative to ^{3}He, ^{129}Xe permits exploration of lung function, such as gas exchange and uptake which can not be accessed using hyperpolarized ^{3}He due to its lack of chemical shift variability. Actually, following inhalation, a dynamic equilibrium is quickly established between xenon in the airspaces and xenon dissolved in the parenchyma and blood, resulting in diffusion-driven exchange of xenon between the airspaces (blue Xe atoms in Figure 23C) and dissolved-phase compartments (red and gold Xe atoms Figure 23C). A fraction of dissolved xenon is transported to other organs by the bloodstream. Figure 23A shows the tremendous improvement of the quality of ^{129}Xe images and comparison to ^{3}He images, as well as anatomical ^{129}Xe images of lung diseases. Figure 23B focuses on the different hyperpolarized xenon distribution profiles associated with different pathologies. Ventilation defects associated with functional abnormalities from pulmonary disease are therefore clearly depicted with ^{129}Xe.[2]

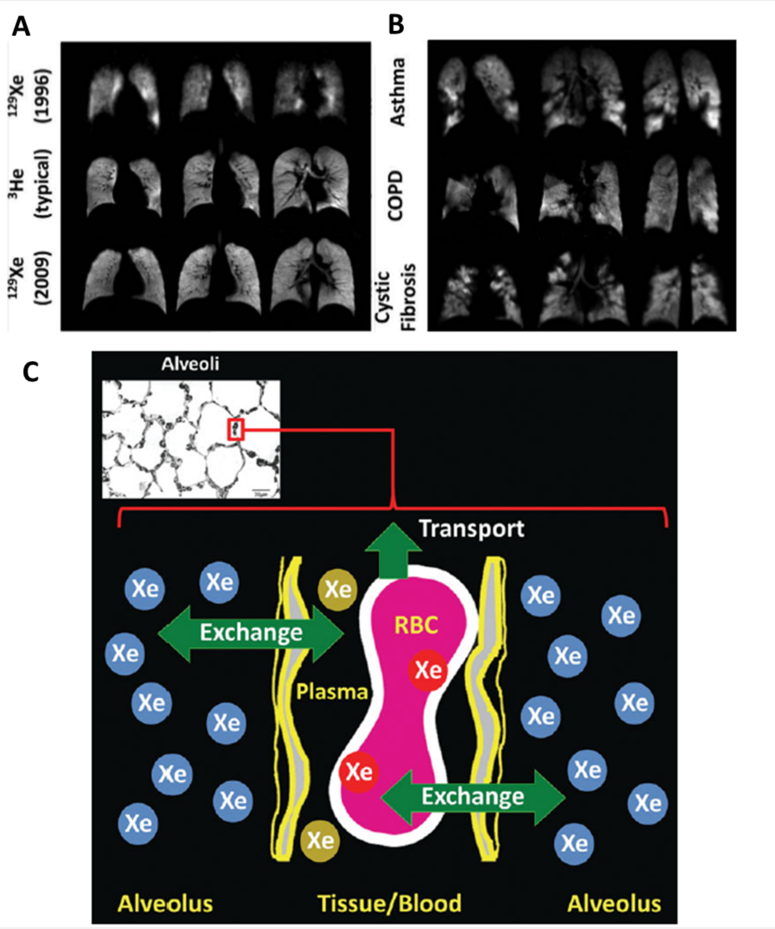
A
B
129Xe (1996)
3He (typical)
129Xe (2009)
Asthma
COPD
Cystic Fibrosis
C
Alveoli
Transport
Exchange
RBC
Plasma
Xe
Exchange
Alveolus
Tissue/Blood
Alveolus

Figure 23: **A.**^{129}Xe (upper and lower row) and ^{3}He (middle row) imaging of healthy human lungs, hyperpolarized gas distributed uniformly throughout the ventilated airspaces of the lung. **B.** ^{129}Xe imaging of diseased human lung with asthma (upper row), Chronic Obstructive Pulmonary Disease (middle row) and cystic fibrosis (lower row). **C.** ^{129}Xe exchange between lung airspaces and tissue. Reproduced from [2].

Since the probe is quite lipophilic, the investigation of hydrophobic binding pockets in proteins is also one of the applications of ^{129}Xe NMR. In this last domain, xenon provides information both through direct observation of its NMR spectrum and via transfer of its enhanced polarization to surrounding spins. In the original experiment, Navon *et al.* observed a transient enhancement of the proton signal by dissolving hyperpolarized xenon in benzene, without the need of radio-frequency irradiation of the ^{129}Xe spins.[3] This spontaneous enhancement was interpreted as a consequence of cross-relaxation and polarization transfer between the dissolved hyperpolarized gas and the surrounding spins in solution. The idea was then to use this effect, so called SPINOE, to 'light-up' the NMR spectra of the protein sites visited by xenon and provide a powerful tool to study hydrophobic cavities of proteins. Since the solubility of xenon in water is a factor of 30 smaller than in organic solvents like benzene or chloroform, the observation of SPINOE enhancements for molecules dissolved in water is particularly challenging. The first proton-enhanced spectrum of a protein was observed by Landon *et al.* in 2001 and revealed that ns-LTP from wheat presents a large hydrophobic cavity with a volume of 400Å^3.[4] A third tool for determination of the structure of a protein hydrophobic cavity is the observation of chemical shift changes of the protein nuclei (^{1}H, ^{15}N, or ^{13}C) induced by xenon atoms in the hydrophobic cavity, leading to chemical shift mapping useful to extract the thermodynamics parameters of the interaction.[5]

In medical applications xenon is, at this stage, employed as tracer in ventilation scintigraphy (with the radioactive isotope ^{133}Xe)[6] and as anaesthetic for high-risk patients since 2007 in Europe and perceived as "the anaesthetic gas of the future".[7] Even though the mechanism is unclear, the inhibition of N-methyl-D-aspartate (NMDA) receptors by xenon has been viewed as a primary cause of xenon anaesthesia. Except this, xenon has no affinity for any given receptor which means that it will disperse over the entire body, which is far from ideal for obtaining a contrast and studying a particular pathology or biological event of interest. To avoid this, hyperpolarized xenon can be targeted toward specific biological receptors or analytes through the design of functionalized molecular systems whose the principle is shown in Figure 24.

These systems are composed of two parts: a molecular system or assembly reversibly trapping the noble gas and a tethered ligand designed to recognize a given biological function or chemical group. This chapter presents the recent applications of these ^{129}Xe NMR-based sensors and the prerequisites of vectorization systems.

Figure 24 presents the common ^{129}Xe NMR spectrum where free dissolved hyperpolarized xenon has a specific resonance frequency depending and xenon bound to a host molecule has another. Values of the resonance frequency of free xenon in different media are listed in tables and can be calibrated on this spectrum. All experiments in this work were performed in water at room temperature so the resonance frequency of free dissolved xenon was calibrated at 196 ppm.

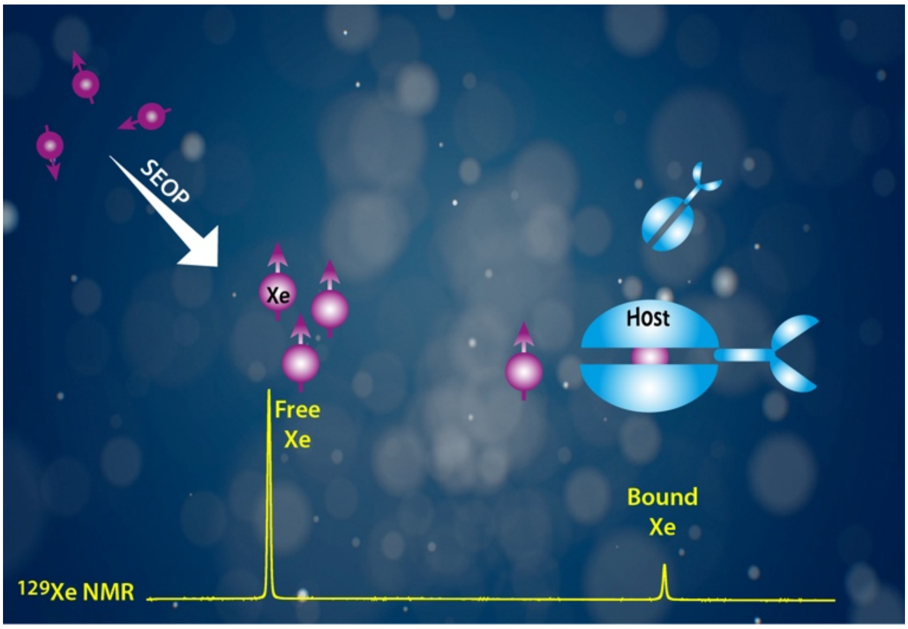

Figure 24: Principle of the ^{129}Xe NMR-based biosensing approach.

4.2 XENON CARRIERS

Recent biomolecular magnetic resonance imaging biosensors such as superparamagnetic iron oxide nanoparticles (SPIO) require sufficient quantity - i.e. for contrast signal - for efficient diagnosis and treatment and therefore deal with biocompatibility and cytotoxicity exposure.[8] Comparatively, this new concept of xenon carriers provides numerous benefits for in vitro and in vivo applications since only a small quantity of host molecule is required in the sample or tissues, which may drastically decrease the toxicity of the method. Only a small quantity of host molecule is required in the sample or tissues, which may drastically decrease the toxicity of the method compared to traditional imaging techniques using magnetic resonance contrast agents.[9]

Furthermore, xenon is a noble gas that is de facto inert to most common chemical reactions. As a result, quantities of xenon can be introduced and may lead to repetitive measures, enabling a longitudinal follow-up of biological events, provided that the interaction with the carrier is reversible. Moreover, the powerful benefit of this concept is that a dedicated molecular host specifically alters the resonance frequency of the encapsulated xenon nuclei. For instance, for cryptophanes, due to the large shielding created by the aromatic rings, the ^{129}Xe NMR signal corresponding to the caged xenon is shifted from the dissolved xenon signal by more than 18 kHz, giving it a unique spectral signature even at moderate magnetic field.

For ^{129}Xe NMR-based biosensing applications, the main challenge is to design xenon carriers with suitable properties toward the hyperpolarized gas. Their first role is to slow down the exchange between two states (free and bound xenon) at the NMR timescale, helped in that by the frequency separation between their signals. The crucial parameter for these host molecules is the in-out xenon exchange rate that must be lower than this frequency separation, but fast enough to enable constant replenishment of the cage in hyperpolarized xenon. Also, the large non-equilibrium spin polarization of xenon has to be maintained by using host systems in which the relaxation time is not too fast.

For the design of ^{129}Xe NMR-based biosensors, the host systems need to be easily functionalized so that xenon can be addressed to a specific biological target. An important concern can also be the ability of the biosensor to cross the cell membrane. Considering all these requirements, various host structures have been synthesized through the recent years: cryptophanes,[10] cucurbiturils,[11] cucurbituril-based rotaxanes,[12] pillararenes,[13] Fe4L6 cages[14] (respectively 1 to 5 in Figure 25), cyclodextrines,[15] calixarenes.[16]

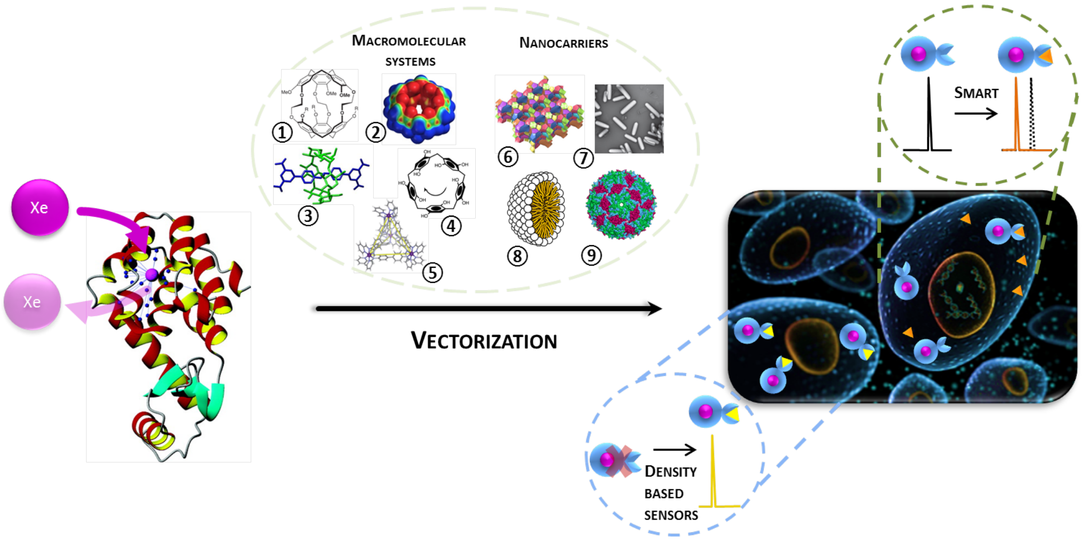

Figure 25: Carriers encapsulating hyperpolarized xenon and targeting analytes of interest leading to density-based and smart sensors.

For trapping multiple xenon atoms, zeolites,[17] gas vesicles,[18] nano emulsions,[19] bacteriophages[20] (respectively 6 to 9 in Figure 25), nanodroplets[21] or genetically-encoded proteins[22] have been proposed. These xenon nanocarriers have the particular feature of encapsulating a high number of hyperpolarized xenon atoms, thereby condensing the NMR signal. These different structures are the elementary bricks of this powerful generation of ^{129}Xe NMR-based biosensors. In our works, we have use cryptophanes as xenon host systems, since these cage-molecules are the specialty of our collaborators and have many properties for the ^{129}Xe NMR-based biosensing approach. Cryptophanes consist of an assembly of two cup-shaped CTV (cyclotriveratrylene) units linked by three O-$(CH_2)_n$-O chains and having various substituents on the aromatic rings of the two CTV units (Figure 26).

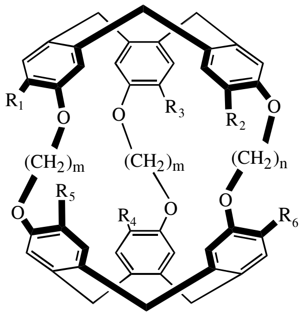

Figure 26: Generic structure of the cryptophane cores.

When referring to a cryptophane, we usually precise the n and m numbers and the groups carried by the aromatic rings. Considering this notation, cryptophane-222 corresponds to cryptophane-A (with $n = m = 2$ and bearing six methoxy groups on the aromatic rings) and abbreviated Cr-A. Water-soluble cryptophane-AM (Cr-AM) is Cr-A bearing six carboxylate groups on the aromatic rings.[23]

From these xenon carriers, ^{129}Xe NMR-based sensors have been conceived following two strategies. Either they will give rise to a signal intensity corresponding to their local density or interaction with their target will lead to a new signal, distinct from the initial one. The concept of vectorized and smart biosensors will now be described.

4.2.1 *Vectorized biosensors*

To reach biological receptors, the xenon carriers have to be chemically or biologically functionalized with antennas that are able to recognize a specific target.

A first proof-of-principle has been achieved in vitro by the group of Alexander Pines in 2001, detecting avidin using xenon functionalized by a biotinylated supramolecular cage.[24]

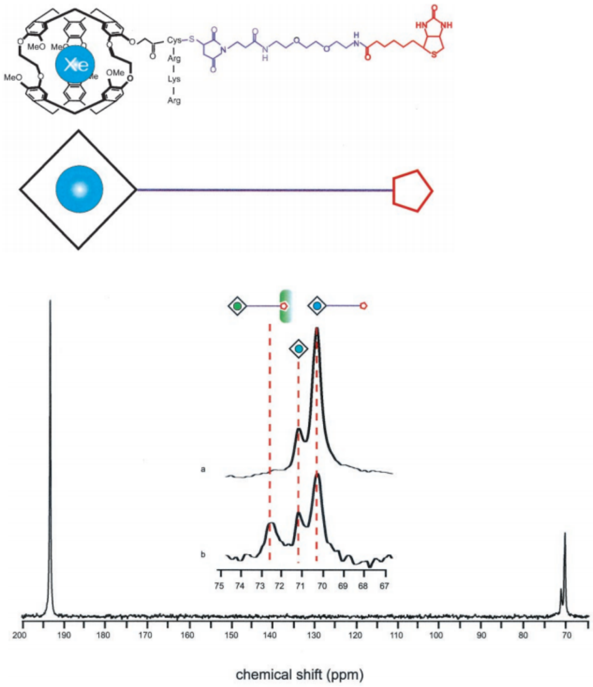

Figure 27: Structure of the first biosensor molecule designed to bind xenon to a protein with high affinity and specificity. Below, the ^{129}Xe NMR spectrum shows the binding of the biosensor to avidin, thanks to the biotin moiety attached on the host molecule. Adapted from [24].

Figure 27 shows the full ^{129}Xe NMR spectrum of the hyperpolarized xenon in the absence (*a*) or in the presence (*b*) of the protein of interest, avidin. If different chemical shifts are observed in the absence of avidin, corresponding to xenon caged in cryptophane-A and functionalized xenon, an additional signal arose when adding small quantities of avidin. This 2.3 ppm downfield peak corresponds to functionalized xenon bound to the protein and represents the first demonstration of this technique, paving the way to sensors that exploits the chemical shift of functionalized xenon on binding to an analyte.

At that time, the investigation about the mechanism of the chemical shift change on binding was babbling and hypotheses were implicating a contact between the cryptophane cage and the protein leading to cage deformation and distortion of the xenon electron cloud as well as changes in the rotational and vibrational motions of the cryptophane affecting the xenon chemical shift. It is specifically for that reason that it is surprising to observe only one signal corresponding to Xe@biosensor bound to an enantiopur chiral protein (avidin) while using a racemic mixture of two cryptophanes. In this configuration, the two created diastereomers should exhibit two different resonance frequencies. In any event, it is what we will observe in the present research.

Typically, cryptophane-A has been the xenon host of choice and has been subsequently functionalized with peptides for detection of human carbonic anhydrase,[25] $\alpha 2b\beta 3$ integrins,[26] and major histocompatibility complex (MHC) class II protein.[27]
Due to the difficult synthesis of cryptophanes, the low synthetic yields and most of the time the unavoidable presence of diastereomers, recent studies have turned to cucurbiturils (mainly cucurbit[6]uril = CB6). They present a xenon in-out exchange rate faster than cryptophanes, but they are however difficult to chemically substitute and to date no cucurbituril decorated with a ligand has been synthesized. An approach where cucurbituril is used as a molecular relay is rather proposed in Figure 28, where compertition between xenon complexation and that of a two-faced guest is used to detect interaction of this guest with the target protein.[28, 29] Such an original strategy unfortunately has an uncertain future for *in vivo* development, due to the extreme quantity of competitors that can interfere. Furthermore, this structure is only water-soluble in low pH.

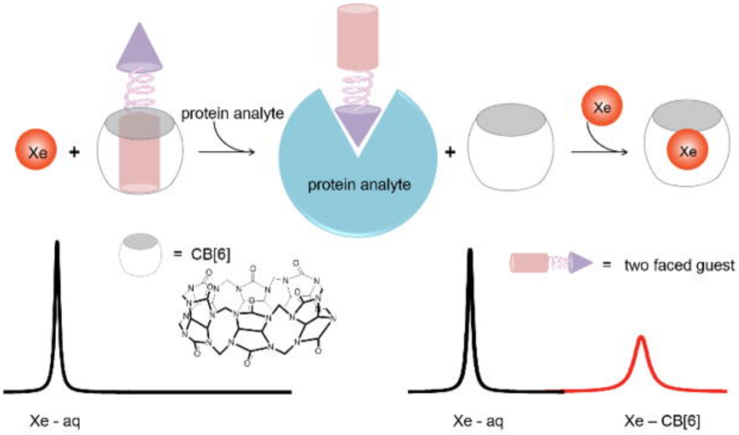

Figure 28: Structure of the molecular relay consisting in a two-faced guest that is a xenon binding competitor. Reproduced from [28].

Since xenon can cross the plasma membrane without any significant polarization loss, the targeted receptors can be situated either on the cell surface or inside the cell. Proving that xenon biosensors can be addressed to intracellular markers is a real challenge for *in cellulo* molecular imaging and can promote the development of intracellular sensors. The first detection via hyperpolarized ^{129}Xe NMR of the cell uptake of a biosensor was made with the transferrin system.[30] This construction is based on the non specific grafting of cryptophane precursors on the primary amines of a protein interacting with a specific receptor. This new strategy gives versatility to the approach and enables further gain in sensitivity by the multiplicity of xenon hosts on the protein. Distinct xenon NMR signals corresponding to the biosensor in the lipidic part and the aqueous compartment could be evidenced. Other biosensors were also designed to distinguish between different cell types based on their surface markers, such as specific binding and detection of lymphoma[20] and cancer cells.[31]

Because *in vivo* molecular imaging application is the Holy grail, this new ^{129}Xe NMR technology requires a versatile biosensor. Schröder et al. developed a modular construction (see Figure 29) that allows for quick and easy adaptation of the biosensor to any cell surface target for which there is a specific antibody.[32] A commercially available avidin conjugation kit is used in addition to cryptophane-A monoacid, fluorescein and the antibody corresponding to the chosen receptor. It is possible to adapt this system to a variety of biological targets and to detect concentrations of cryptophane-based biosensors as low as 20 nM, paving the way to innovative xenon MRI applications.

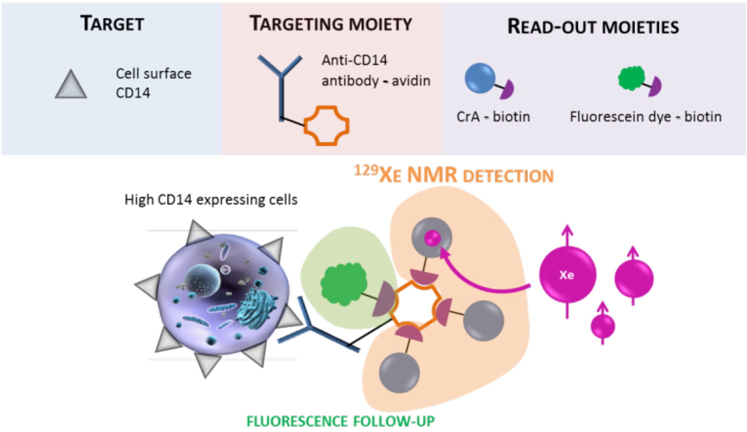
TARGET
Cell surface CD14
TARGETING MOIETY
Anti-CD14 antibody - avidin
READ-OUT MOIETIES
CrA - biotin
Fluorescein dye - biotin
^{129}Xe NMR DETECTION
High CD14 expressing cells
Xe
FLUORESCENCE FOLLOW-UP

Figure 29: Modular construction of a sensor based on avidin-conjugated antibody and a set of biotin-conjugated read-out moieties for dual - NMR and fluorescence - functionality. CrA: Cryptophane-A. Adapted from [32].

The spatial resolution of magnetic resonance imaging in its current implementation is limited by the pulsed gradient strength and by xenon transverse relaxation. For a ^{129}Xe gyromagnetic ratio ca. 4 times lower than this of proton, reaching a sub-cellular resolution is illusory. Therefore, in order to be able to localize a biosensor inside the cell, bimodal fluorescence - ^{129}Xe NMR biosensors have been conceived.[30, 32, 33]

4.2.2 *Smart sensors*

One of the most impressive properties of xenon is its extreme sensitivity towards tiny disruption of its local environment. This sensitivity translates into a very large range of NMR parameter values. In particular the chemical shift of the monoatomic species can span values ranging from 0 ppm (gas phase) to more than 310 ppm (xenon in metalated cryptophanes).
This property can be used to detect small analytes or variation of the physiological environment (pH, temperature), which are markers of major interest for various applications: studying the role of proteins, understanding biological processes, detecting cancer cells, diseases, etc. Today there is a strong demand for highly sensitive analytical methods aiming at the selective and ratiometric detection of these markers.

In analogy to what was developed for MRI contrast agents,[34] the concept of smart or responsive sensor consists in net modification of the ^{129}Xe NMR spectrum when the sensor and its target are in contact, behaving in that as an actuator facilitating detection: instead of (or in addition to) a density-based signal, now the signals of the ’free’ sensor and of the sensor in interaction with its target are distinct. Conception of various responsive sensors have allowed specific detection of physical parameter changes (pH,[35, 36] temperature[37]), of cations,[38, 39, 40] or of chemical species (H2O2,[41] rhodamine 6G,[42] dithiols[43]). The design of molecular systems that enable variation of the bound xenon chemical shift upon complexation of the analyte or variation of the external medium can be achieved by different ways. The use of ionisable groups close to the cavity of cryptophanes leads to pH-sensitive sensors, the caged xenon chemical shift experiencing a large variation in the region of the pKa of these groups.[35] Also, the grafting of chemical functions that will react with the targeted analyte may lead to significant chemical shift variations for caged xenon (Figure 30).[41]

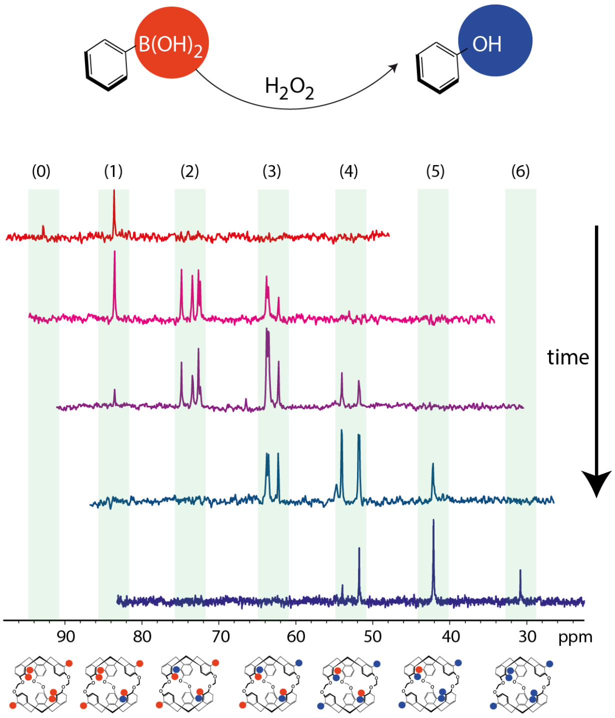

Figure 30: Time evolution of the ^{129}Xe NMR spectrum (high-field region) of xenon caged in a biosensor let in the presence of oxygenated water. Each arylboronate group transformed into phenol group by action of H_2O_2 leads to a high field shift variation of the Xe@cage signal by ca. 10 ppm. Such an effect has been understood thanks to DFT calculation including relativistic terms for the interaction. Adapted from [41].

A third category consists in cage-molecules bearing a generic functional group, such as ethylenediaminetetraacetic acid (EDTA), nitrilotriacetic acid (NTA),... designed to non-specifically chelate metal cations. An hydrophilic cryptophane core bearing a NTA group was shown in Figure 31 to be able to chelate Pb^{2+}, Zn^{2+} and Cd^{2+} ions, giving rise to a unique ^{129}Xe spectral signature for each of these ions.[38] Detection of Pb^{2+} ions at a concentration of 10 nM was shown possible with a single hyperpolarized xenon batch.

Another design based on cage molecules bearing a nucleotide strand enables detection of the complementary DNA sequence, extending the sensor concept to complex systems, such as DNA hybridization which deals with much weaker associations ($K \approx 10^6$ M^{-1}) than the previously studied systems.[44]

A detailed understanding and a reliable modeling of the interactions responsible for such effects on the resonance frequency of caged xenon are therefore of high value. Being able to precisely predict the chemical shift variation of xenon caged in a ^{129}Xe NMR-based sensor in response to a specific analyte is a powerful tool for this field. By taking into account the relativistic effects of the interaction with xenon

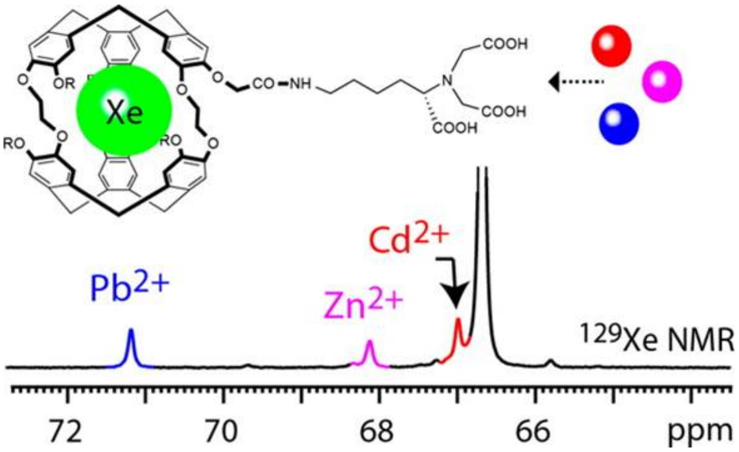

Figure 31: Approach combining the use of hyperpolarized ^{129}Xe NMR of a cage-molecule functionalized by a ligand able to chelate different cations, showing simultaneous detection of lead, zinc, and cadmium ions at nanomolar concentration. Reproduced from [38].

in DFT calculation, a high precision can be achieved in the prediction or simulation of caged xenon chemical shift. In particular, it has been possible to understand the chemical shift evolution of xenon encaged in a cryptophane bearing groups reacting with H_2O_2, in clusters separated by 10 ppm according to the progression of the chemical reaction (Figure 30).[41]
The variations of the caged xenon chemical shift upon activation of the sensor can however be poor, and in case of sample heterogeneity or of broad ^{129}Xe signals, be difficult to detect. Therefore the quest for new molecular constructions with which there is modification of another NMR parameter upon target binding is of importance. Some recent works have proposed sensors in which the xenon transverse[45] or longitudinal[46] relaxation rates are modified when the biosensor encounters the target. However, as they give rise to a negative contrast (the signal disappears faster when the target is reached) their applicability for inhomogeneous samples such as cell suspensions or in vivo is not yet demonstrated.

Another modular platform, based on cucurbituril rotaxanes,[47] has been developed by Pines et al.[12, 48] For detection of a given enzyme, the terminal part of a peptidic motif known to be cleaved by the enzyme is grafted to a triazole diammonium moiety and a bulky group R1. When left in the presence of cucurbit[6]uril (CB6), it constitutes a rotaxane, which can then be sealed by another bulky group R2 (see Figure 32). At this stage, as xenon cannot enter the cavity of CB6, there is no Xe@CB6 signal. This one appears only when CB6 is released by action of the protease on the peptidic motif, which constitutes a selective activation. This platform can be diversified and developed towards in situ detection of biological events of interest.

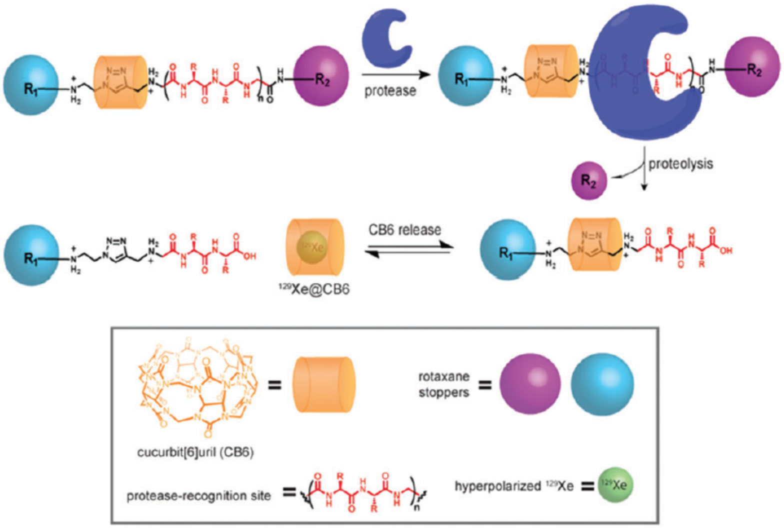

Figure 32: Molecular relay produces an ^{129}Xe NMR signal upon analyte detection. Reproduced from [48].

4.2.3 *Strategies for water-soluble xenon carriers*

For *in vitro* and *in vivo* applications, xenon carriers must be water-soluble to avoid the formation of self-assemblies such as micelles or vesicles.[44] Quite a few strategies are usually employed: either changing the xenon carrier surface interaction or suitably choosing the recognition antenna. In this domain, a first strategy was to replace the methyl groups of cryptophane-A by suitable hydrophilic groups such as carboxylate groups.[23] This strategy will be extensively discussed in Figure 6.1. Another strategy was the metalation of the six arene rings of cryptophane-111 by [Cp*Ru]+ moieties leading to cryptophane salts which exhibit a very high water solubility at physiological pH and the highest xenon affinity ever reported.[10] The resonance frequency of xenon encapsulated into this new cryptophane, as seen in Figure 33 proves the extreme sensitivity of xenon toward its environment and the extensive range of chemical shifts that arises therefrom. Study of further functionalization of Cp* moieties for multiplexed sensing applications are underway.

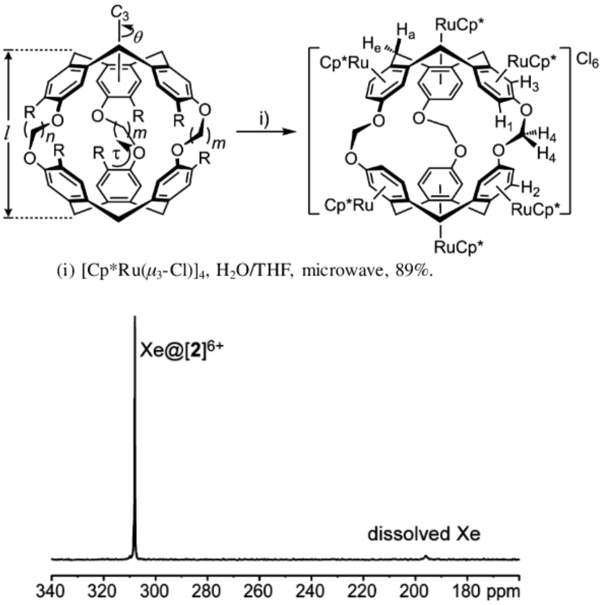
C3
θ
l
R
O
n
m
τ
i)
Cp*Ru
RuCp*
Ha
He
H1
H2
H3
H4
Cl6
Xe@[2]6+
dissolved Xe
340
320
300
280
260
240
220
200
180 ppm

(i) [Cp*Ru(μ_3-Cl)]$_4$, H_2O/THF, microwave, 89%.

Figure 33: Structure of the permetalated water-soluble crytophane-111 and its peculiar ^{129}Xe NMR chemical shift. Reproduced from [10].

More recently, a new cryptophane skeleton has been developed : cryptophane with two ethylenedioxy linkers and the third linker of the propylenedioxy type bearing a unique secondary alcohol (Figure 34).[49] A second solubilizing or functional group can therefore be selectively introduced, facilitating the synthesis of new molecular platforms.

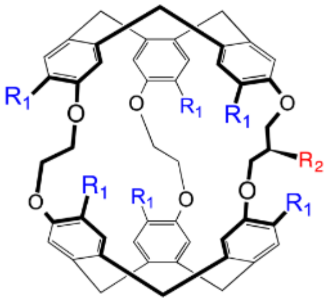

Figure 34: Generic structure of the new molecular platform : a cryptophane with two different reaction sites. Reproduced from [49].

4.3 A FLUORESCENCE-^{129}XE NMR PROBE FOR BIOLOGICAL INHIBITION OF EGFR IN NON-SMALL CELL LUNG CANCER

The construction of this bimodal fluorescence-^{129}Xe NMR biosensor is a collaborative effort of three groups : Bernard Rousseau's group who synthesized the probe, Eric Deutsch's group who analyzed the fluorescence properties *in cellulo* and finally our group for the ^{129}Xe NMR detection of the biosensor.

This work led to a paper which is currently under submission.

The approach, that can be applied to any other antibody-receptor couple, is here engineered for detection of Non-Small Cell Lung Cancer (NSCLC). Although other constructions for antibody-based xenon biosensors have been proposed in the literature,[32, 31] the driving force of our work was to use an antibody daily used for patient treatment in order to build a theranostic tool.
To date, the high mortality rate of NSCLC is mainly owed to its detection at late stages of development. Hence, the limited knowledge and improvement in characterization of NSCLC predictive biomarkers highlights the unmet medical need for a more efficient and a highly sensitive non-invasive imaging technique. We therefore worked on the development of a biosensor based on a therapeutic antibody that constitutes a powerful theranostic tool and molecular imaging agent. It enables highly sensitive detection and follow-up of NSCLC by ^{129}Xe NMR and fluorescence.

4.3.1 *Structure of the biosensor*

It should be noted that I was not involved in the synthesis of the biosensor, only in the^{129}Xe NMR experiments and characterization discussed in Section 4.3.4. The biosensor is constructed by bioconjugation of a cryptophane-fluorescein adduct to the therapeutic anti-EGFR monoclonal antibody called cetuximab, as depicted in Figure 35.

The ^{129}Xe NMR-based biosensor has been designed with three functional components. The first one is cetuximab, a FDA approved chimeric mouse-human IgG1 monoclonal antibody for cancer treatment. Indeed, the antibody is directed toward the EGFR overexpressed in many cancer cells with a high affinity and specificity. The second one is the water-soluble hexacarboxylic acid cryptophane-222 (Cr-AM) in order to prevent anchoring of the biosensor into cell membra nes[30] and formation of self-organized systems in biological media.[44] The third part is a fluorescein moiety, essential to confirm interaction of the biosensor with cells overexpressing EGFR and to quantify the biosensor uptake by fluorescence spectroscopy or microscopy.

A ratio of 4 cryptophane moieties per antibody has been measured using mass spectrometry.

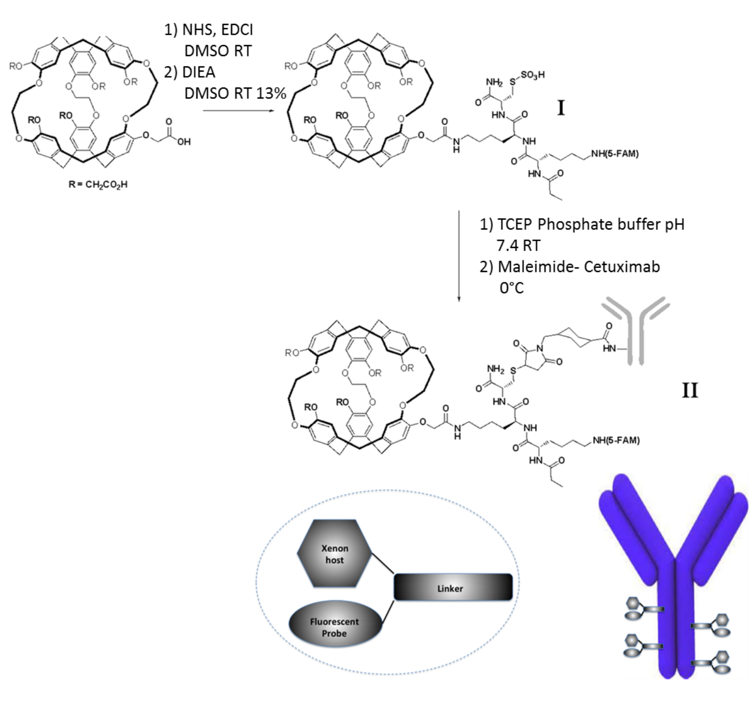
1) NHS, EDCI
DMSO RT
2) DIEA
DMSO RT 13%
R = CH₂CO₂H
I
NH(5-FAM)
1) TCEP Phosphate buffer pH 7.4 RT
2) Maleimide- Cetuximab 0°C
II
NH(5-FAM)
Xenon host
Linker
Fluorescent Probe

Figure 35: Synthesis and generic structure of the bimodal fluorescence-^{129}Xe NMR biosensor.

4.3.2 ^{129}*Xe NMR characterization*

Before the multi-grafting on the antibody (intermediate I), we have checked through hyperpolarized ^{129}Xe NMR experiments that the xenon exchange in and out of the cryptophane cavity is preserved. Precisely, direct detection methods[50] and indirect detection methods of the HyperCEST type[51] have been successfully employed and will be discussed in Chapter 5. As expected - and discussed in Section 4.2.1, the presence of a racemic cryptophane moiety and asymmetrical sites on the peptidic linker gives rise to two major signals in the Xe@cryptophane spectral region at 65.3 ppm and 65.7 ppm, as displayed in Figure 36.

Experiment on Figure 36B proves that there exists a continuous in-out xenon exchange that can be used to enhance the NMR sensitivity in HyperCEST-type sequences, but contrarily to direct detection, in the current experimental conditions, does not reveal two signals for encapsulated xenon corresponding to the presence of two diastereomers.

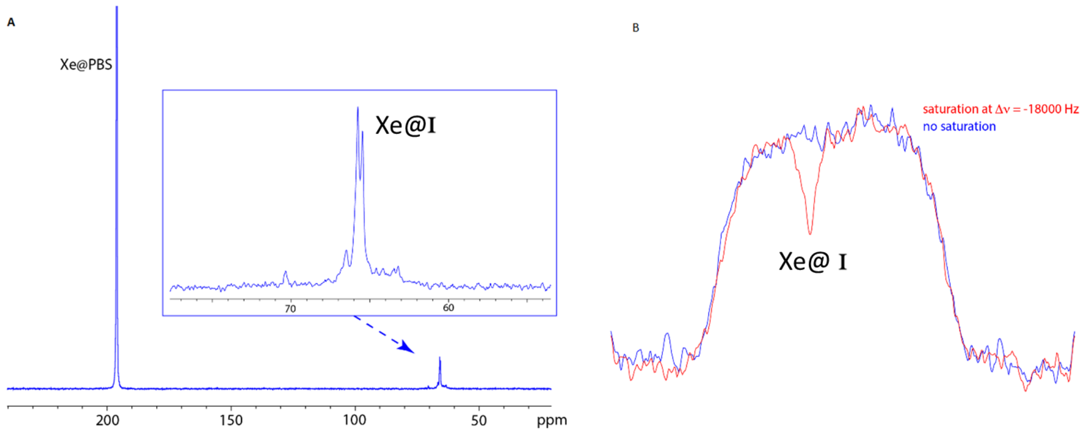

Figure 36: Direct (**A.**) and indirect (**B.**) ^{129}Xe NMR detection of biosensor before multigrafting (intermediate I) in PBS at 11.7 T. **A.** spectrum recorded in 1 scan for a 46 µM solution. **B.** ultra-fast Z spectroscopy on the same sample. In this last experiment, for one scan (in red) CW saturation is applied at an offset Δν of -18 kHz from the main xenon signal with a rf strength B_1 of 20 µT for 4 s. For the second scan (in blue), no rf saturation is applied.

Other hyperpolarized ^{129}Xe NMR experiments have then been performed to ensure that the grafting of the cryptophane scaffold on the antibody did not affect the xenon encapsulation properties. Figure 37 displays the hyperpolarized ^{129}Xe NMR spectrum of the biosensor II in PBS.

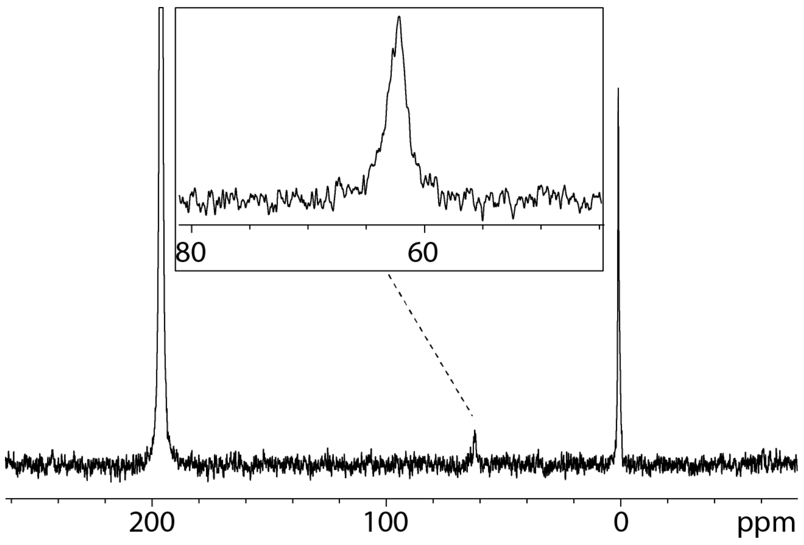

Figure 37: Hyperpolarized ^{129}Xe NMR spectrum of II at 3 µM in PBS obtained in one scan. Insert: sub-spectrum obtained by 64 fast repetitions of the sequence soft 90deg - Gaussian pulse centered at 60 ppm - acquisition (inter-scan delay: 93 ms).

While the signals of the gas and of dissolved xenon appear at 0 ppm and 196 ppm, respectively, the signal of Xe caged in II resonates at 63 ppm. Although the racemic cryptophane moiety has been used, it is not possible to observe two distinct peaks because of the broadness of the signal (FWMH ca. 200 Hz). This is due to the presence of the antibody that decreases the xenon T_2 relaxation time and therefore broadens the signal. Also, the non specificity of the grafting leads to several signals.

4.3.3 *Biological activity asssays*

For *in cellulo* fluorescence and ^{129}Xe NMR detection, we have chosen two cell lines that express low level (A549 pulmonary cells) and high level of EGFR (HCC827) and they display inhibited proliferation in response to the cetuximab treatment. It should be noted that these fluorescence experiments have been performed by Eric Deutsch's group at Institut Gustave Roussy.
Both types of cells have been treated with II at various serial dilutions: 1/100th, 1/1000th and 1/10000th of 0.29 mg/mL (Figure 38). Significant fluorescence intensity arising from the fluorescein moiety have been found for the HCC827 (Figure 38A) and A549 (Figure 38B) cells upon treatment with the biosensor in dose-related manner. These data confirm that the fixation of the bimodal sensor is correlated with EGFR expression into cells. Moreover, immunofluorescence has revealed its fixation on the HCC827 cell membrane (Figure 38C).

4.3.4 *^{129}Xe NMR-based detection of the biosensor in cell samples*

The biosensor has been incubated in parallel with HCC827 cells and A549 cells according to the protocol developed for a precedent transferrin ^{129}Xe NMR-based biosensor enabling separation of the cell clot and the supernatant. 80 million HCC827 cells and 80 million A549 cells were detached by incubating cells with Accutase during 5 minutes at 37degC in order to preserve EGF receptors. Cells were washed with complete medium and incubated with 25 µg/mL of biosensor in complete medium during 2h at 37°C. After centrifugation, the supernatant was separated from the cell pallet. Cells were washed twice in phosphate buffer saline (PBS, pH 7.4) and finally re-suspended in 600 µL of PBS and 50 µL of D_2O. Viability of the cells was controlled by trypan blue exclusion. Prior to the NMR experiments, the cell suspensions were introduced into NMR tubes equipped with J. Young valves. The quantity of biosensor internalized in each cell line was evaluated to 2 ng/mL in HCC827 cells and to 0.45 ng/mL in A549 cells by measuring the fluorescence emission at 496 nm on a plate reader.

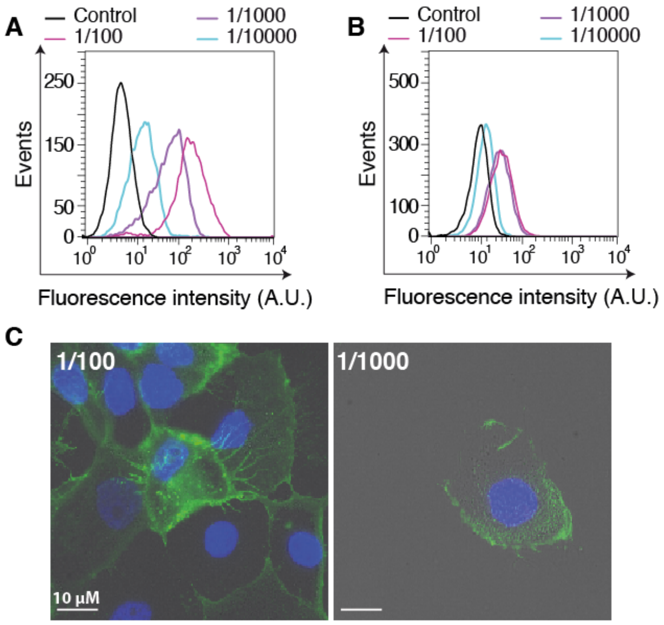

Figure 38: **A.** Flow cytometry experiments on HCC827 cells and **B.** A549 cells incubated with bimodal biosensor, and **C.** immunofluorescence experiments on HCC827 cells incubated with the same probe.

Immediately after introduction of laser-polarized xenon into the NMR tubes, several experiments taking benefit of the fast in-out xenon exchange have been performed. Thoses sequences will be discussed in Chapter 5. As displayed in Figure 39 , for the two cell lines we have been able to detect the biosensor in the supernatants, but not in the cell suspensions.

Finally, we have used HyperCEST depolarization monitoring. This was employed principally by the Dmochowski's group to identify xenon biosensor at low concentration.[36, 52] This detection method will be discussed in Chapter 5.

Figure 40 compares for each cell line (A: HCC827 cells; B: A549 cells) the loss of polarization of the main ^{129}Xe signal as a function of the saturation time when saturation is applied on-resonance (at 67 ppm, i. e. 18 kHz upfield to this signal) or off-resonance (at 327 ppm, i. e. 18 kHz downfield to this signal). Clearly, in contrast to the A549 cells, a significant difference in the depolarization curves appears for the HCC827 cells. In order to comfort this result, the sequence was applied at different frequencies around 67 ppm, giving rise to the Z-subspectrum displayed in Figure 40C. Note that a 4 ppm downfield chemical shift with respect to the signal of Xe@biosensor in PBS (Figure 36) is observed, likely due to a different local environment.

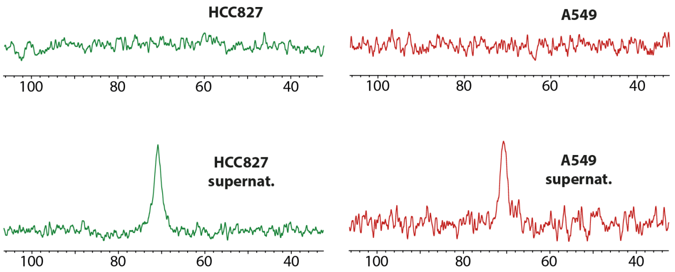

Figure 39: ^{129}Xe NMR spectra obtained with selective excitation at the expected Xe@biosensor frequency (at ca. 70 ppm, i. e. 130 ppm upfield from the dissolved xenon signal), at 308 K. For these experiments the same experimental conditions were used both for HCC827 cells (green) and A549 cells (red): 80 million cells were incubated at 310 K during 2 hours with II at 25 μg/mL. After centrifugation the supernatant was separated from the cell clot (bottom spectra). The cells were washed two times in phosphate buffer saline (PBS, pH 7.4) and re-suspended in 600 μL of PBS and 50 μL of D_2O (top spectra). The NMR subspectra shown were obtained with a succession of sequences (frequency-selective Gaussian 90deg pulse - acquisition) with an inter-scan delay of 93 ms.

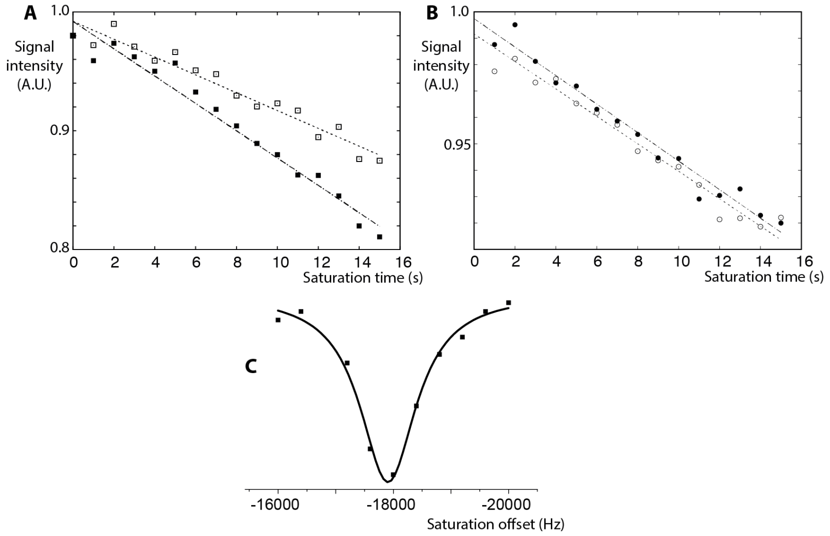

Figure 40: HyperCEST depolarization curves for (A) biosensor in HCC827 cells, (B) biosensor in A549 cells. Filled symbols: on-resonance saturation, empty symbols: off-resonance saturation. In (C), Z-spectrum obtained for the sample ofb biosensor in HCC827 cells (the abscissa indicates the frequency offset from the free xenon signal).

Detection of the biosensor in cells over-expressing EGFR through ^{129}Xe NMR is thus successful. This study aimed at evaluating the use of hyperpolarized ^{129}Xe NMR to detect non-small cell lung cancer. In this purpose, a biosensor made by the grafting of xenon hosts onto an antibody targeting the EGFR present on NSCLC cells has been conceived. Flow cytometry and immunofluorescence experiments with cells overexpressing or not the EGFR have shown that the biosensor reaches the receptors, and that the biological and therapeutic activities are maintained. *In cellulo* ^{129}Xe NMR detection of the biosensor has been successfully performed. The xenon in-out exchange properties are maintained upon binding of the biosensor to the EGFR, enabling sensitive NMR detection at realistic concentration, and using a moderate rf power used during saturation.

This biosensor belongs to the latest generation of bimodal probes conceived in order to be localized inside the cell. However, many avenues have to be pursued to improve the detection capability of such a biosensor in order to envision in vivo applications: grafting of more xenon hosts per antibody, use of a more flexible linker between the xenon host and the antibody, etc.

4.4 FUTURE DIRECTIONS

The new generation of sensors trends towards host systems, combining complementary molecular imaging techniques, able to target a specific receptor and furthermore to be activated by its presence. That is my overall job, designing, synthesizing and characterizing a doubly responsive biosensor and detecting proteins. Another doubly smart construction based on the same principle has been developed by Zhou and co-workers for biothiols in-cell detection.[53]

Finally, biosensors leading to multiplexed detection should be investigated in the future in order to simultaneously visualize multiple markers and therefore be a powerful tool for disease diagnosis.

Xenon has amazing properties and its combination with host molecules makes it the unique system allowing longitudinal follow-up of the sample, by simply adding hyperpolarized xenon over time. As for the final objective which is to follow pathology in vivo through this approach, ^{129}Xe NMR-based sensors offer a huge potential and applications are finally at hand.

BIBLIOGRAPHY

[1] Céline Boutin, Hervé Desvaux, Marie Carrière, François Leteurtre, Nadège Jamin, Yves Boulard, and Patrick Berthault. Hyperpolarized 129Xe NMR signature of living biological cells. *NMR in Biomedicine*, 24(10):1264–1269, 2011.

[2] John P. Mugler and Talissa A. Altes. Hyperpolarized 129Xe MRI of the human lung. *Journal of Magnetic Resonance Imaging*, 37(2):313–331, 2013.

[3] G. Navon, Y. Q. Song, T. Room, S. Appelt, R. E. Taylor, and A. Pines. Enhancement of solution NMR and MRI with laser-polarized xenon. *Science*, 271:1848–1851, Mar 29 1996.

[4] Céline Landon, Patrick Berthault, Françoise Vovelle, and Hervé. Desvaux. Magnetization transfer from laser-polarized xenon to protons located in the hydrophobic cavity of the wheat nonspecific lipid transfer protein. *Protein Sci.*, 2001.

[5] Lionel Dubois, Pedro Da Silva, Céline Landon, J. Gaspard Huber, Michel Ponchet, Françoise Vovelle, Patrick Berthault, and Hervé Desvaux. Probing the hydrophobic cavity of lipid transfer protein from nicotiana tabacum through Xenon-based NMR spectroscopy. *Journal of the American Chemical Society*, 126(48):15738–15746, 2004.

[6] Toyoharu Isawa, Karlman Wasserman, and George V. Taplin. Lung scintigraphy and pulmonary function studies in obstructive airway disease. *American Review of Respiratory Disease*, 102(2):161–172, 1970.

[7] O. Delhaye, E. Robin, J.-E. Bazin, J. Ripart, G. Lebuffe, and B. Vallet. Avantages décisifs, indications et limites de l'anesthésie au xénon. *Annales Françaises d'Anesthésie et de Réanimation*, 29(9):635 – 641, 2010.

[8] Greta Jarockyte, Egle Daugelaite, Marius Stasys, Urte Statkute, Vilius Poderys, Ting-Chen Tseng, Shan-Hui Hsu, Vitalijus Karabanovas, and Ricardas Rotomskis. Accumulation and toxicity of superparamagnetic iron oxide nanoparticles in cells and experimental animals. *International Journal of Molecular Sciences*, 17(8), 2016.

[9] Moshe Rogosnitzky and Stacy Branch. Gadolinium-based contrast agent toxicity: a review of known and proposed mechanisms. *BioMetals*, 29(3):365–376, 2016.

[10] Robert M. Fairchild, Akil I. Joseph, K. Travis Holman, Heather A. Fogarty, Thierry Brotin, Jean-Pierre Dutasta, Céline Boutin, Gaspard Huber, and Patrick Berthault. A water-soluble Xe@cryptophane-111 complex exhibits very high thermodynamic stability and a peculiar 129Xe NMR chemical shift. *Journal of the American Chemical Society*, 132(44):15505–15507, 2010.

[11] Francis Hane, Tao Li, Peter Smylie, Raiili Pellizzari, Jennifer Plata, Brenton DeBoef, and Mitchell Albert. In vivo detection of cucurbit[6]uril, a hyperpolarized xenon contrast agent for a xenon magnetic resonance imaging biosensor. *Scientific Reports*, (7), 2017.

[12] Joel A. Finbloom, Clancy C. Slack, Carson J. Bruns, Keunhong Jeong, David E. Wemmer, Alexander Pines, and Matthew B. Francis. Rotaxane-mediated suppression and activation of cucurbit[6]uril for molecular detection by 129Xe hyperCEST NMR. *Chem. Commun.*, 52:3119–3122, 2016.

[13] Tal Adiri, Daniele Marciano, and Yoram Cohen. Potential 129Xe-NMR biosensors based on secondary and tertiary complexes of a water-soluble pillar[5]arene derivative. *Chem. Commun.*, 49:7082–7084, 2013.

[14] Juho Roukala, Jianfeng Zhu, Chandan Giri, Kari Rissanen, Perttu Lantto, and Ville-Veikko Telkki. Encapsulation of xenon by a self-assembled Fe4L6 metallosupramolecular cage. *Journal of the American Chemical Society*, 137(7):2464–2467, 2015.

[15] Yi-Qiao Song, Boyd M. Goodson, Rebecca E. Taylor, David D. Laws, Gil Navon, and Alexander Pines. Selective enhancement of NMR signals for α-cyclodextrin with laser-polarized xenon. *Angewandte Chemie International Edition in English*, 36(21):2368–2370, 1997.

[16] Junko Fukutomi, Yuko Adachi, Akari Kaneko, Atsuomi Kimura, and Hideaki Fujiwara. Inclusion complex formation of thiacalix[4]arene and Xe in aqueous solution studied by hyperpolarized 129Xe NMR. *Journal of Inclusion Phenomena and Macrocyclic Chemistry*, 58(1):115–122, 2007.

[17] Frederic Lerouge, Oleg Melnyk, Jean-Olivier Durand, Laurence Raehm, Patrick Berthault, Gaspard Huber, Herve Desvaux, Andre Constantinesco, Philippe Choquet, Julien Detour, and Monique Smaihi. Towards thrombosis-targeted zeolite nanoparticles for laser-polarized 129Xe MRI. *J. Mater. Chem.*, 19:379–386, 2009.

[18] Mikhail Shapiro, Matthew Ramirez, Lindsay Sperling, George Sun, Alexander Pines, David Schaffer, and Vikram. Baja. Ge-

netically encoded reporters for hyperpolarized xenon magnetic resonance imaging. *Nature CHemistry*, 6:629–634, 2014.

[19] Todd K. Stevens, R. Matthew Ramirez, and Alexander Pines. Nanoemulsion contrast agents with sub-picomolar sensitivity for xenon NMR. *Journal of the American Chemical Society*, 135(26):9576–9579, 2013.

[20] Keunhong Jeong, Chawita Netirojjanakul, Henrik K. Munch, Jinny Sun, Joel A. Finbloom, David E. Wemmer, Alexander Pines, and Matthew B. Francis. Targeted molecular imaging of cancer cells using MS2-based 129Xe NMR. *Bioconjugate Chemistry*, 27(8):1796–1801, 2016.

[21] Stefan Klippel, Christian Freund, and Leif Schröder. Multichannel MRI labeling of mammalian cells by switchable nanocarriers for hyperpolarized xenon. *Nano Letters*, 14(10):5721–5726, 2014.

[22] Yanfei Wang, Benjamin W. Roose, Eugene J. Palovcak, Vincenzo Carnevale, and Ivan J. Dmochowski. A genetically encoded β-lactamase reporter for ultrasensitive 129Xe NMR in mammalian cells. *Angewandte Chemie*, 128(31):9130–9133, 2016.

[23] Gaspard Huber, Thierry Brotin, Lionel Dubois, Hervé Desvaux, Jean-Pierre Dutasta, and Patrick Berthault. Water soluble cryptophanes showing unprecedented affinity for xenon: Candidates as NMR-based biosensors. *J. Am. Chem. Soc.*, 128(18):6239–6246, may 2006.

[24] Megan M. Spence, Seth M. Rubin, Ivan E. Dimitrov, E. Janette Ruiz, David E. Wemmer, Alexander Pines, Shao Qin Yao, Feng Tian, and Peter G. Schultz. Functionalized xenon as a biosensor. 98(19):10654–10657, 2001.

[25] Jennifer M. Chambers, P. Aru Hill, Julie A. Aaron, Zhaohui Han, David W. Christianson, Nicholas N. Kuzma, and Ivan J. Dmochowski. Cryptophane xenon-129 nuclear magnetic resonance biosensors targeting human carbonic anhydrase. *Journal of the American Chemical Society*, 131(2):563–569, 2009.

[26] Garry K. Seward, Yubin Bai, Najat S. Khan, and Ivan J. Dmochowski. Cell-compatible, integrin-targeted cryptophane-129XeNMR biosensors. *Chem. Sci.*, 2:1103–1110, 2011.

[27] Andreas Schlundt, Wolfgang Kilian, Michael Beyermann, Jana Sticht, Sebastian Günther, Sabine Höpner, Kirsten Falk, Olaf Roetzschke, Lorenz Mitschang, and Christian Freund. A xenon-129 biosensor for monitoring MHC–peptide interactions. *Angewandte Chemie International Edition*, 48(23):4142–4145, 2009.

[28] Yanfei Wang, Benjamin W. Roose, John P. Philbin, Jordan L. Doman, and Ivan J. Dmochowski. Programming a molecular relay for ultrasensitive biodetection through 129Xe NMR. *Angewandte Chemie International Edition*, 55(5):1733–1736, 2016.

[29] Tal Adiri, Daniele Marciano, and Yoram Cohen. Potential 129Xe-NMR biosensors based on secondary and tertiary complexes of a water-soluble pillar[5]arene derivative. *Chem. Commun.*, 49:7082–7084, 2013.

[30] Céline Boutin, Antoine Stopin, Fatimazohra Lenda, Thierry Brotin, Jean-Pierre Dutasta, Nadège Jamin, Alain Sanson, Yves Boulard, François Leteurtre, Gaspard Huber, Aurore Bogaert-Buchmann, Nawal Tassali, Hervé Desvaux, Marie Carrière, and Patrick Berthault. Cell uptake of a biosensor detected by hyperpolarized 129Xe NMR: The transferrin case. *Bioorganic & Medicinal Chemistry*, 19(13):4135 – 4143, 2011.

[31] Krishnan K. Palaniappan, R. Matthew Ramirez, Vikram S. Bajaj, David E. Wemmer, Alexander Pines, and Matthew B. Francis. Molecular imaging of cancer cells using a bacteriophage-based 129Xe NMR biosensor. *Angewandte Chemie International Edition*, 52(18):4849–4853, 2013.

[32] Honor M. Rose, Christopher Witte, Federica Rossella, Stefan Klippel, Christian Freund, and Leif Schröder. Development of an antibody-based, modular biosensor for 129Xe NMR molecular imaging of cells at nanomolar concentrations. *Proceedings of the National Academy of Sciences*, 111(32):11697–11702, 2014.

[33] Garry K. Seward, Qian Wei, and Ivan J. Dmochowski. Peptide-mediated cellular uptake of cryptophane. *Bioconjugate Chemistry*, 19(11):2129–2135, 2008.

[34] Célia S. Bonnet and Eva Tóth. Smart contrast agents for magnetic resonance imaging. *CHIMIA International Journal for Chemistry*, 70(1), 2016.

[35] Patrick Berthault, Hervé Desvaux, Thierry Wendlinger, Marina Gyejacquot, Antoine Stopin, Thierry Brotin, Jean-Pierre Dutasta, and Yves Boulard. Effect of pH and counterions on the encapsulation properties of xenon in water-soluble cryptophanes. *Chemistry – A European Journal*, 16(43):12941–12946, 2010.

[36] Brittany A. Riggle, Yanfei Wang, and Ivan J. Dmochowski. A “smart” 129Xe NMR biosensor for pH-dependent cell labeling. *Journal of the American Chemical Society*, 137(16):5542–5548, 2015.

[37] Franz Schilling, Leif Schröder, Krishnan K. Palaniappan, Sina Zapf, David E. Wemmer, and Alexander Pines. MRI

thermometry based on encapsulated hyperpolarized xenon. *ChemPhysChem*, 11(16):3529–3533, 2010.

[38] Nawal Tassali, Naoko Kotera, Céline Boutin, Estelle Léonce, Yves Boulard, Bernard Rousseau, Emmanuelle Dubost, Frédéric Taran, Thierry Brotin, Jean-Pierre Dutasta, and Patrick Berthault. Smart detection of toxic metal ions, Pb 2+ and Cd 2+ , using a 129 Xe NMR-based sensor. *Anal. Chem.*, 86(3):1783–1788, feb 2014.

[39] Qianni Guo, Qingbin Zeng, Weiping Jiang, Xiaoxiao Zhang, Qing Luo, Xu Zhang, Louis-S. Bouchard, Maili Liu, and Xin Zhou. A molecular imaging approach to mercury sensing based on hyperpolarized 129Xe molecular clamp probe. *Chemistry – A European Journal*, 22(12):3967–3970, 2016.

[40] Keunhong Jeong, Clancy C. Slack, Christophoros C. Vassiliou, Phuong Dao, Muller D. Gomes, Daniel J. Kennedy, Ashley E. Truxal, Lindsay J. Sperling, Matthew B. Francis, David E. Wemmer, and Alexander Pines. Investigation of DOTA–metal chelation effects on the chemical shift of 129Xe. *ChemPhysChem*, 16(17):3573–3577, 2015.

[41] Emmanuelle Dubost, Jean-Pierre Dognon, Bernard Rousseau, Gaëlle Milanole, Christophe Dugave, Yves Boulard, Estelle Léonce, Céline Boutin, and Patrick Berthault. Understanding a host-guest model system through 129Xe NMR spectroscopic experiments and theoretical studies. *Angewandte Chemie International Edition*, 53(37):9837–9840, 2014.

[42] Praveena D. Garimella, Tyler Meldrum, Leah S. Witus, Monica Smith, Vikram S. Bajaj, David E. Wemmer, Matthew B. Francis, and Alexander Pines. Hyperpolarized xenon-based molecular sensors for label-free detection of analytes. *Journal of the American Chemical Society*, 136(1):164–168, 2014.

[43] Shengjun Yang, Yaping Yuan, Weiping Jiang, Lili Ren, He Deng, Louis S. Bouchard, Xin Zhou, and Maili Liu. Hyperpolarized 129Xe magnetic resonance imaging sensor for H2S. *Chemistry – A European Journal*, 23(32):7648–7652, 2017.

[44] Roy. Vincent, Brotin. Thierry, Dutasta. Jean-Pierre, Charles. Marie-Hélène, Delari. Thierry, Mallet. François, Huber. Gaspard, Desvaux. Hervé, Boulard. Yves, and Berthault. Patrick. A cryptophane biosensor for the detection of specific nucleotide targets through Xenon NMR spectroscopy. *ChemPhysChem*, 8(14):2082 – 2085, 2007.

[45] Muller D. Gomes, Phuong Dao, Keunhong Jeong, Clancy C. Slack, Christophoros C. Vassiliou, Joel A. Finbloom, Matthew B.

Francis, David E. Wemmer, and Alexander Pines. 129Xe NMR relaxation-based macromolecular sensing. *Journal of the American Chemical Society*, 138(31):9747–9750, 2016.

[46] Francesco Zamberlan, Clémentine Lesbats, Nicola J. Rogers, James L. Krupa, Galina E. Pavlovskaya, Neil R. Thomas, Henryk M. Faas, and Thomas Meersmann. Molecular sensing with hyperpolarized 129Xe using switchable chemical exchange relaxation transfer. *ChemPhysChem*, 16(11):2294–2298, 2015.

[47] Chenfeng Ke, Ronald A. Smaldone, Takashi Kikuchi, Hao Li, Anthony P. Davis, and J. Fraser Stoddart. Quantitative emergence of hetero[4]rotaxanes by template-directed click chemistry. *Angewandte Chemie International Edition*, 52(1):381–387, 2013.

[48] Clancy C. Slack, Joel A. Finbloom, Keunhong Jeong, Carson J. Bruns, David E. Wemmer, Alexander Pines, and Matthew B. Francis. Rotaxane probes for protease detection by 129Xe hyperCEST NMR. *Chem. Commun.*, 53:1076–1079, 2017.

[49] Laure-Lise Chapellet, James R. Cochrane, Emilie Mari, Céline Boutin, Patrick Berthault, and Thierry Brotin. Synthesis of cryptophanes with two different reaction sites: Chemical platforms for xenon biosensing. *The Journal of Organic Chemistry*, 80(12):6143–6151, 2015.

[50] Patrick Berthault, Aurore Bogaert-Buchmann, Hervé Desvaux, Gaspard Huber, and Yves Boulard. Sensitivity and multiplexing capabilities of MRI based on polarized 129Xe biosensors. *Journal of the American Chemical Society*, 130(49):16456–16457, 2008.

[51] Leif Schröder, Thomas J. Lowery, Christian Hilty, David E. Wemmer, and Alexander Pines. Molecular imaging using a targeted magnetic resonance hyperpolarized biosensor. *Science*, 314(5798):446–449, 2006.

[52] Yanfei Wang and Ivan J. Dmochowski. Cucurbit[6]uril is an ultrasensitive 129Xe NMR contrast agent. *Chem. Commun.*, 51:8982–8985, 2015.

[53] Jian Zhang, Xiaolong Bao, Junliang Zhou, Fangfang Peng, Hang Ren, Xiaochun Dong, and Weili Zhao. A mitochondria-targeted turn-on fluorescent probe for the detection of glutathione in living cells. *Biosensors and Bioelectronics*, 85:164 – 170, 2016.

5

NMR SEQUENCES OPTIMIZED FOR ^{129}XE NMR-BASED SENSORS

This chapter aims at demonstrating how tough it is to work with hyperpolarized species and to what extent it is necessary to reinvent adequate NMR sequences. Xenon loses its hyperpolarization either progressively via longitudinal relaxation (^{129}Xe relaxation times from 5 s to 700 s have been reported when the noble gas is dissolved in the blood and in deuterated water, respectively) or more suddenly when a coherent rf pulse is applied. In a closed system where only a bolus of xenon is considered, the polarization returns totally to the equilibrium defined by the Boltzmann distribution after a single 90° pulse : hyperpolarization is lost all at once.
A powerful property of xenon is its high diffusivity combined to its propensity to take a specific chemical shift for every local environment, which makes that xenon is constantly in exchange on the NMR frequency time scale. For cryptophanes, the xenon in-out exchange, on the order of a few tens of milliseconds, induces a strong constraint on sequence parameters such as pulse length or shape. Optimized sequences for encapsulated hyperpolarized xenon have been implemented in order to take advantage of this exchange and further increase the detection sensitivity. The methods used to detect a small reservoir of hyperpolarized xenon in exchange with a large reservoir can be sorted in two classes: direct and indirect detection. These terms refer to the fact that either the small reservoir signal or variations on the large signal are observed. Without this exchange, none of these sequences would be usable. The goal of this chapter is to define these two classes, present the different detection sequences and their specificity toward hyperpolarized gas in exchange and discuss their applications.

5.1 DIRECT DETECTION METHODS

5.1.1 *1D Frequency-Selective excitation sequence*

In the direct detection methods, fast repetition of spectrally-selective pulses around the small reservoir resonance frequency (and detection after each pulse) uses the chemical exchange between the two environments to gradually increase the signal-to-noise ratio. The repetition rhythm is chosen according to the exchange rate of xenon between the two environments.

Figure 41 shows the direct method where a series of rf pulses is selectively applied at the frequency of encapsulated xenon.

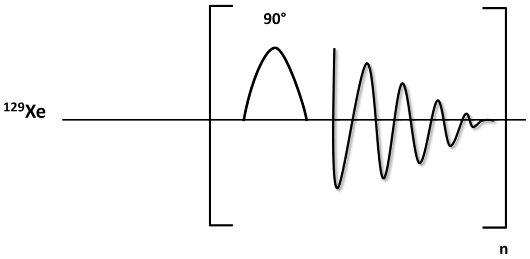

Figure 41: Frequency-selective rf pulse sequence used for the direct detection of encapsulated xenon in its cage (with n the number of times the sequence is repeated).

The main limitation of this technique remains in the low spectral resolution due to the kinetics of the system. As a matter of fact, the typical xenon in-out exchange rate considering a cryptophane-222 is about 30 ms at room temperature, which suits perfectly the acquisition time in MRI but induces strong limitations in spectroscopy: very low number of points for the FID which can pose problem for the signal oversampling and the spectral resolution, constraints on the pulse length which induces a lack of spectral selectivity of the rf pulse. For this sequence, we chose a pulse length of 500 µs, which is not very selective and which is no longer negligible before the exchange rate of xenon. With such a delay between excitation pulses, many acquisitions can be done before the pool of hyperpolarized xenon is depleted and must be refreshed.

In the sequence using fast repetitions of soft pulses centered on the encaged xenon resonance frequency region, in some cases the signals can be distorted and their shapes no longer appear as Lorenzian. Zeroth-order (not dependent on frequency) and first-order (linearly dependent on frequency) phase corrections are sometimes not sufficient, and a non-flat baseline can also appear. As far as I know, the NMR literature has already treated the case of semi-selective (*i.e.* covering a large frequency bandwidth) excitation. Based on magnetization trajectory computations, several pulse shapes have been proposed, to provide a nearly uniform excitation in amplitude and phase for all the signals. In particular, the goal here was to minimize the phase difference between peaks due to evolution of the magnetization during the pulse under chemical shift and scalar coupling effects.[1, 2]

Here the situation is different: due to the in-out xenon exchange which characteristic timescale is not drastically longer than the pulse length, during the soft pulse in a incoherent processus some freshly hyperpolarized xenon atoms take the place of other xenon atoms in the cages. Thus for all these xenon spins having experienced different flip angle pulses at different moments, the delay separating their flipping in the transverse plane and the start of the acquisition is not constant. At first glance, we can simulate this effect by considering that the FID is the sum of several time-shifted FIDs. It is thus obvious that this will lead to i) superposition of signals with different phases, ii) some truncature effect due to the fact that for one xenon spin the FID can be suddenly interrupted.

A Bruker automation program has been written to simulate - at least qualitatively - this effect. Figure 42 shows in red the Xe NMR spectrum obtained with a fast succession of soft pulse - acquisition sequences on a mixture of four water-soluble cryptophanes differing by the length of their linkers.

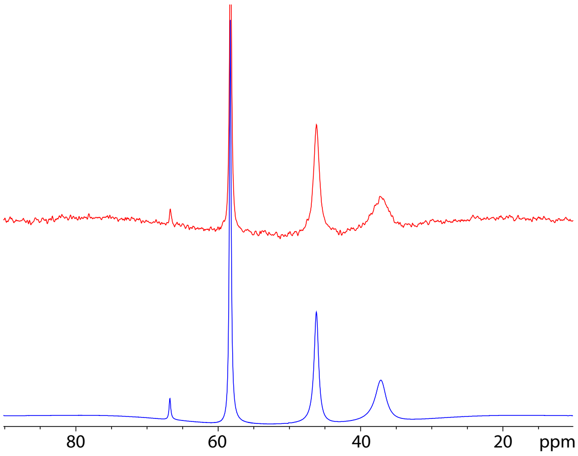

Figure 42: Comparison between ^{129}Xe NMR spectra obtained with a fast succession of soft pulses (in red) and a simulation of the exchange effect (in blue) of a sample containing a mixture of four different cryptophanes, differing by the length of their linkers: Cr-AM, Cr-223M, Cr-233M, Cr-EM.

Parameters for the simulation:

Cage	Intensity (A.U.)	Freq (Hz)	$1/T_2$ (Hz)	k_{ex} (Hz)
Cr-AM	300	2300	20	7
Cr-223M	6000	1127	20	10
Cr-233M	4280	-548	20	110
Cr-EM	4000	-1806	20	350

Comparatively, Figure 43 displays the same simulation in the absence of xenon exchange.

Following this line of reasoning, it can easily be remarked that a pulse which has maximal action close to the acquisition, (*i.e.* maxi-

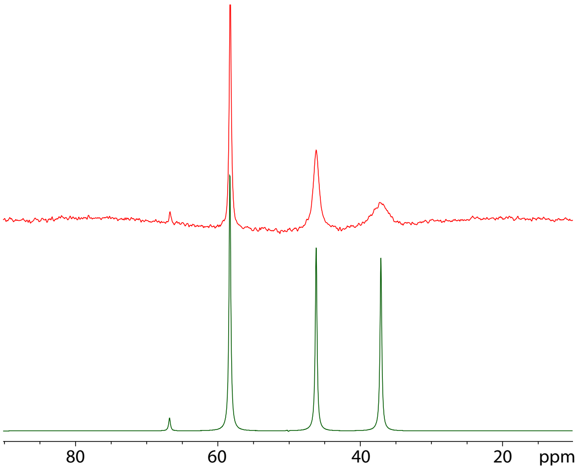

Figure 43: Comparison between ^{129}Xe NMR spectra obtained with a fast succession of soft pulses (in red) and a simulation in the absence of xenon exchange (in green) of the same mixture of 4 cryptophanes.

mal intensity in the time domain close to its end) would induce less spectral distortions. This is simulated in Figure 44, where comparison between the previous spectrum (in red) and a spectrum obtained by higher weighting coefficient for the FIDs arriving last (in blue) is displayed.

This is also observed experimentally when comparing the results obtained with a Gaussian excitation and a Half-Gaussian excitation of the same duration.

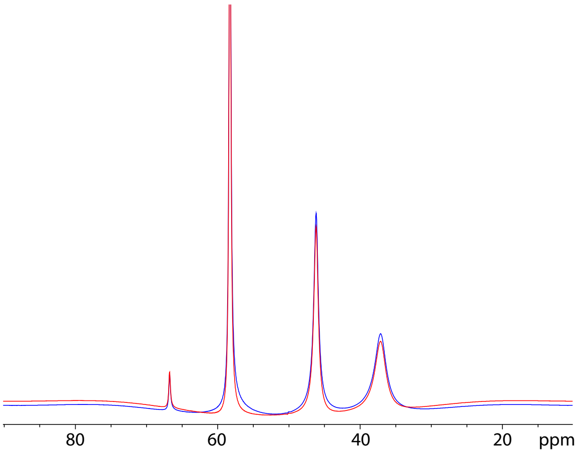

Figure 44: Comparison between two simulations of the exchange effect without (in red) and with higher weighting coefficient for the FIDs arriving last (in blue) of the same mixture of 4 cryptophanes.

Finally, the last drawback of this method is to add noise at each scan which is an obstacle to reach detection thresholds even lower.

In contrast, advantages of this method lie in the simplicity of the sequence, the good selectivity in frequency, the ease of implementation and adaptation in imaging. It also offers the possibility of multiplexing *i.e.* simultaneous detection of several biosensors, as displayed in Figure 42.

This method allowed our group to reach a detection threshold of 2.10^{12} spins (4pm), representing a concentration of 12.8 nM of cryptophane at 11.7 T and 310 K with n = 3600 scans and a sequence duration of 154 s.[3]

5.1.2 *2D Frequency-selective excitation sequence*

The pulse sequence can be written so as to provide a 2D data matrix, enabling measurement of the apparent relaxation rate in the second dimension and thereby adapting the number of experiments to be summed for obtaining a spectrum with optimized signal-to-noise ratio.

In Figure 45 the 2D spectrum of xenon encapsulated in a Cr-AM at 1.1 µM obtained with selective excitation at the Xe@Cr-AM frequency is reported as well as the 1D spectra corresponding to the sum of the first 128 and 51 rows. When adding only scans with signal, the signal to noise ratio of the obtained spectrum is 14.26 whereas when adding the 128 scans - *i.e* 77 scans of noise - the signal to noise ratio drops to 10.30. It is then possible to circumvent the problem of noise accumulation and to reach lower detection thresholds.

Also, this 2D sequence allows us to access parameters such as xenon in-out exchange rate and its relaxation time T_1.

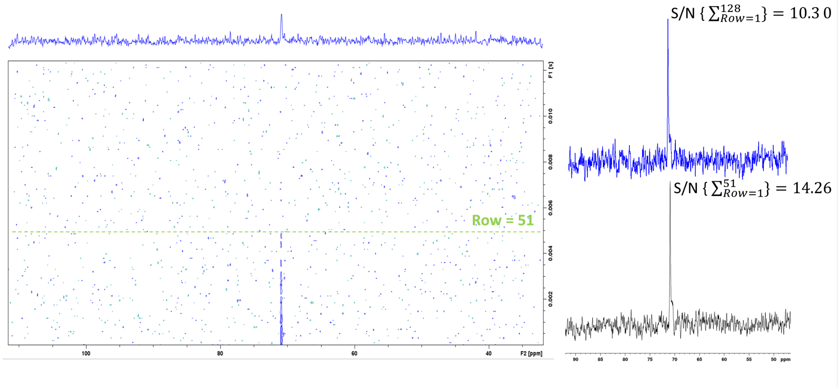

Figure 45: 2D ^{129}Xe NMR spectrum obtained with selective excitation at the expected Xe@biosensor frequency of a solution of 1.1 µM of Cr-AM at 293 K. 1D spectra correspond to the sum of the first 51 or 128 scans of the 2D experiments. Signal to noise ratios of each condition are indicated.

.

5.2 INDIRECT DETECTION METHODS

The indirect detection methods - originally proposed by the Pines' group under the acronym HyperCEST - consist in saturation at the small reservoir frequency and detection of the reduction of the large reservoir signal intensity induced by the chemical exchange.[4] It belongs to the CEST (Chemical Exchange Saturation Transfer) techniques[5], represented for instance by PARACEST in ^{1}H MRI using paramagnetic species.[6]

In order to perform this experiment, two approaches are possible :

- Alternating a saturation sequence at the Xe@Biosensor frequency and off-resonance (ideally symmetrically with respect to the frequency of the free xenon signal). The residual signal obtained after subtraction of the two spectra is the witness of the exchange between the dissolved xenon reservoir (or the gas phase reservoir) and the reservoir of xenon in the cryptophane cavity.
- Using a saturation pulse at different frequencies resulting in variation of the free xenon signal intensity as a function of the frequency. The series of peaks is thus obtained and draws an envelope testifying the presence of the biosensor and revealing its resonance frequency. This spectrum is called a z-spectrum.

Even if the first approach is sufficient to detect the presence of the small reservoir, it can also be interesting to recover the whole spectrum through varying the saturation frequency and acquiring data points over a large spectral range (Figure 46).

The HyperCEST scheme, available in several sequences (*vide infra*), has been used by several authors to detect trace amounts of xenon hosts. Two sequences have recently been implemented and will be discussed in the following paragraph.

5.2.1 *Depolarization sequence*

When sensitivity is a concern, the most straightforward sequence is to record depolarization curves - i.e. acquiring spectra for different saturation times - with saturation applied at a frequency close to the bound xenon resonance frequency (on resonance) and far from the free- and bound xenon resonance frequencies (off-resonance). Because of xenon exchange, the selective depolarization results in a concomitant loss from the free dissolved xenon peak, which is readily monitored. This signal is compared with a reference measurement in which an "off-resonance" saturation is applied to account for the natural self-relaxation of free dissolved xenon over time.

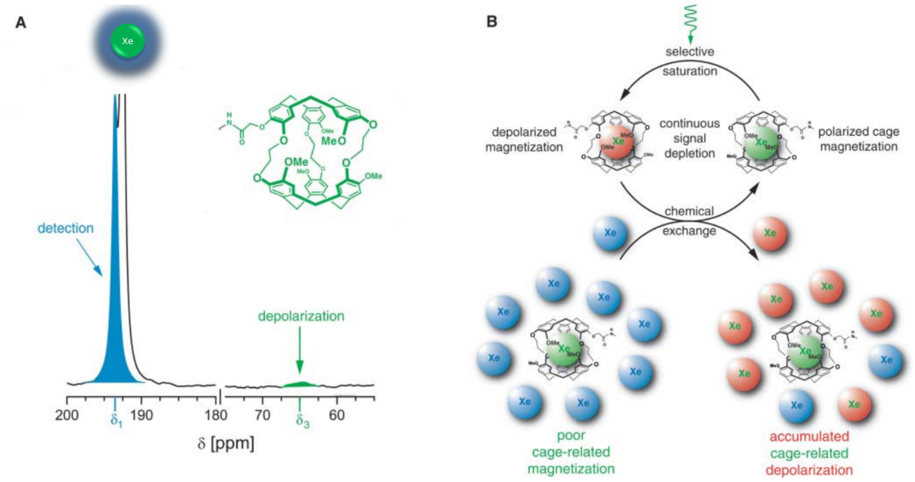
A
Xe
detection
depolarization
OMe
MeO
200
δ1
190
180
70
δ3
60
δ [ppm]
B
selective
saturation
depolarized
magnetization
continuous
signal
depletion
polarized cage
magnetization
chemical
exchange
Xe
poor
cage-related
magnetization
accumulated
cage-related
depolarization

Figure 46: **A.** The ^{129}Xe NMR spectrum of a 50 μM solution of cryptophane displays a weak resonance from encapsulated xenon at δ_3 corresponding to Xe@biosensor. Chemical exchange with free Xe outside the cage (resonance δ_1) enables sensitivity enhancement by depolarizing the δ_3 nuclei and detecting at δ_1 **B.** Selective saturation of Xe@biosensor (green) and chemical exchange with the free xenon (blue) allows accumulation of depolarized nuclei (red). This corresponds to the continuous depolarization of caged-related magnetization that can be measured indirectly after several cycles by the difference between initial and final bulk magnetization. Adapted from [4].

Indirect detection via Hyper-CEST is performed by applying a loop of 100 DSnob-shaped radiofrequency saturation pulses as displayed in Figure 47. This pulse sequence provides a 2D matrix with each row corresponding to a saturation time t_{sat}.

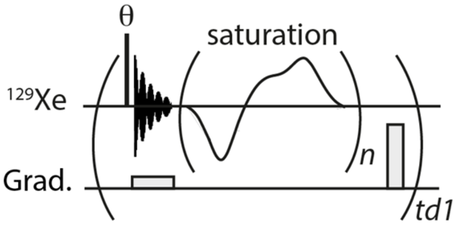
θ
saturation
129Xe
Grad.
n
td1

Figure 47: ^{129}Xe HyperCEST depolarization sequence: pulse sequence providing a 2D matrix with each row corresponding to a saturation time t_{sat}.

As an example, a solution of 478 μM of xenon biosensor was prepared and the depolarization sequence was performed in PBS with a maximum field strength of 12 μT in Figure 48. For each saturation offset, the sample has to be removed from the magnet, shaken in order to dissolved hyperpolarized xenon into the solvent and placed again inside the magnet for the pulse sequence to run. Each curve consists in consecutive data points that are separated by 0.5 s of t_{sat}. When the saturation offset corresponds to Xe@biosensor (dark blue), signal intensity of free dissolved xenon consequently decreases. After being transformed, phased in and normalized by off-resonance saturation (pale blue), those curves can be fitted by monoexponential functions and depolarization rates can be extracted. When plotting the depolarization rate against the saturation offset, a dip corresponding to the Xe@biosensor signal is obtained.

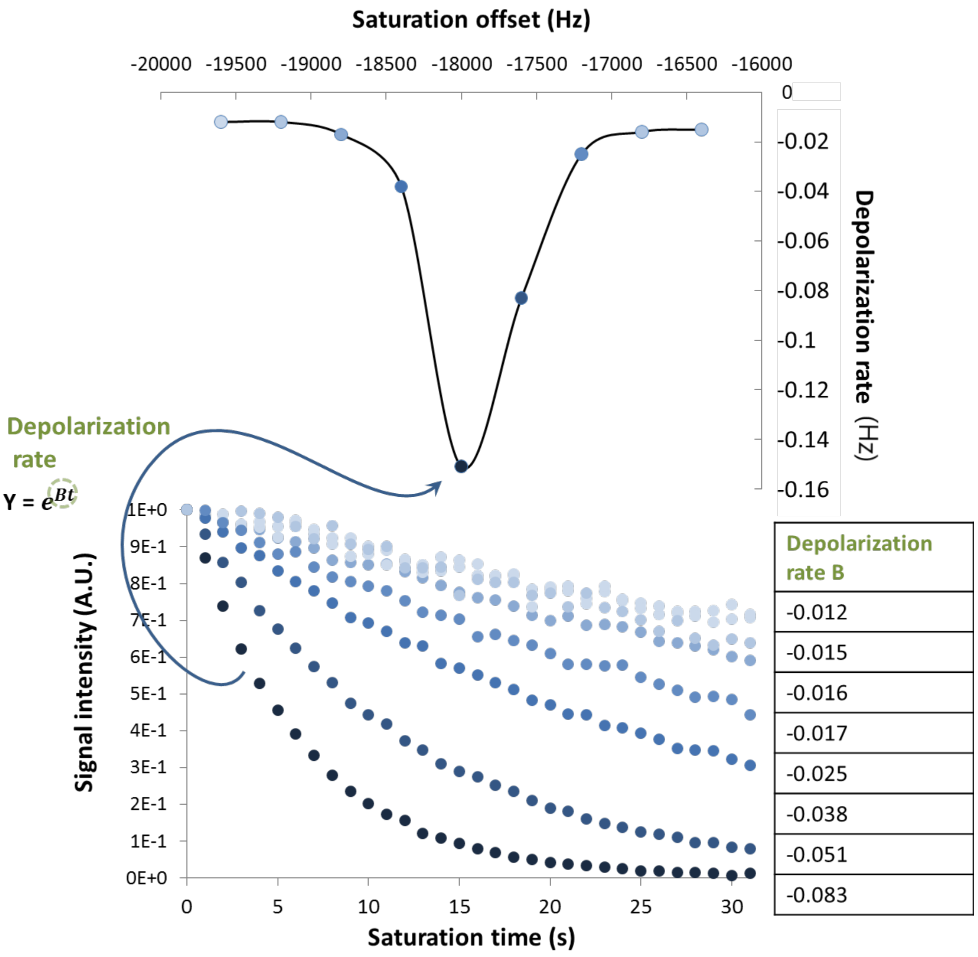

Depolarization rate B
-0.012
-0.015
-0.016
-0.017
-0.025
-0.038
-0.051
-0.083

Figure 48: ^{129}Xe HyperCEST depolarization curves: Example of pulse sequence (providing a 2D matrix with each row corresponding to a saturation time tsat) and plots of the xenon magnetization as a function of t_{sat} off-resonance (pale blue) and on-resonance (dark blue). Consecutive data points are separated by 0.5 s; saturation: repetition of 100 D-SNOB pulses, max. saturation field strength of 12 μT. The sample was a xenon biosensor at 478 μM in PBS.

The only drawback of this approach is that each saturation frequency requires an experiment.

5.2.2 *Ultrafast Z spectroscopy*

A single-shot acquisition method would be preferred to achieve reproducible and mutually compatible results. Ultrafast Z-spectroscopy (UFZ) sequence was implemented by Xu and his group in ^{1}H.[7] The UFZ method uses spatial encoding of the Z-spectrum as other ultrafast NMR spectroscopic approaches.[8] A pulsed field gradient G_{sat} operating during the continuous wave irradiation enables a saturation of the small reservoir signal in a given region of the NMR tube (slice in the sample). The profile of the sample subsequently obtained via another gradient during the acquisition, called G_{acq} enables the recording of the Z-polarization of the large reservoir signal.

This technique enables recording of the Z-spectrum in only two scans: comparison of the profiles obtained without saturation (as a reference) and on-resonance saturation directly leads to the Z-spectrum. It then has been adapted for hyperpolarized ^{129}Xe NMR spectroscopy by our group (Figure 49).[9] Due to the large resonance frequency difference between the signals of free xenon and encapsulated xenon, the sequence had to be improved by applying the saturation in the middle of the high field region corresponding to caged xenon, while for detection the offset is placed at the resonance frequency of free xenon. This new version enables the use of much lower gradient values covering only a spectral window of 30 ppm instead of 200 ppm.

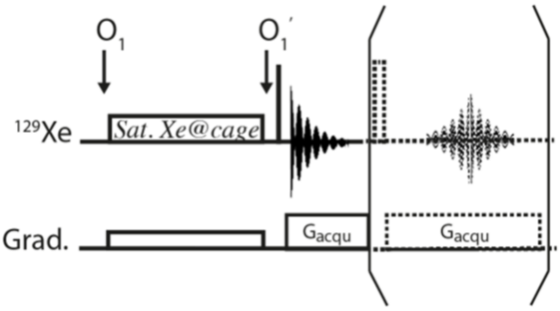

Figure 49: ^{129}Xe Ultra-Fast Z-spectroscopy used pulse sequence. Both arrows indicate offset changes, from the Xe@biosesnsor region (O1) to the free xenon signal (O1$'$). A field gradient is applied during saturation (enabling saturation of a slice in the sample) and, after the rf read pulse, another field gradient is applied during detection (giving the profile of the sample). The dashed part is optional, but enables the recording of several successive FIDs with only one excitation thanks to a multiple spin echo. Reproduced from [9].

This is illustrated in Figure 50 on a cryptophane internalized in biological cells. A solution of 200 µM of Cr-AM was incubated 2 hours in 80 millions of eucaryotic cells A549 at 37°C in DMEM medium containing 30% of Fetal bovine serum (FBS). This technique highly helps the cellular uptake of the biosensor and will be discussed in Chapter 9. Cells were then rinsed 3 times in PBS and put in NMR tube for ^{129}Xe UltraFast Z-spectroscopy. The presence of the cryptophane into pulmonary A549 cells (green) is revealed in only two scans, by comparison of the profiles obtained without saturation S_{off} (blue) and with on-resonance saturation (red). The on-resonance spectrum (S_{on}) was recorded with a saturation field of 2.4 µT and a saturation time of 1 s, in the presence of a 4 G.cm^{-1} gradient (G_{sat}) along Z axe. For both spectra, the acquisition gradient G_{acq} was 4 G.cm^{1}. The green spectrum in Figure 50 is the normalized ^{129}Xe UFZ spectrum obtained by computing (S_{off} - S_{on})/S_{off}.

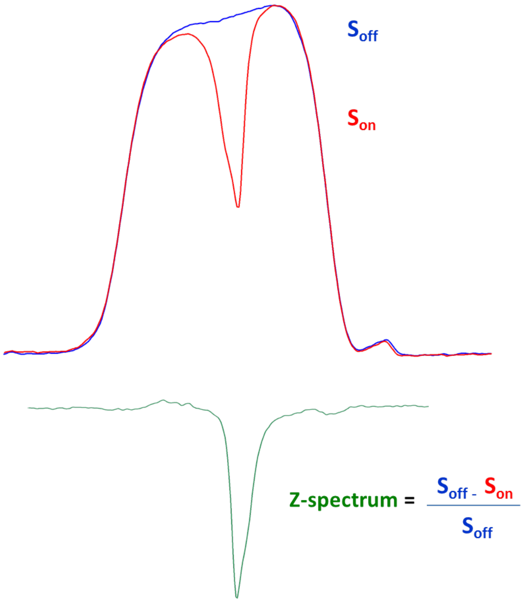

Figure 50: Z-spectrum revealing the presence of cryptophane Cr-A (200 µM) into pulmonary A549 cells (green) is extracted in only two scans : a reference with no saturation S_{off} (blue) and an on-resonance saturation S_{on} (red).

We applied ^{129}Xe Ultra-Fast Z-spectroscopy on a 23 times diluted version of the mixture of four different cryptophanes prepared in Section 5.1.1, so that cryptophanes are now at a concentration of 745 nM (see Figure 51). We can easily detect at sub-micromolar concentration as well as distinguish each one of the four Xe@cryptophanes signals. Moreover, the apparent separation of multiple xenon signals can be modified through the ratio between the two gradients G_{sat} and G_{acq}. With $\Delta\nu$ the frequency separation between two signals, the gap displayed in the Z-spectrum will be $\Delta\nu G_{acq}/G_{sat}$. Figure 52A displays the direct detection spectrum of a system of two biosensors separated by 1.3 ppm. Optimization of G_{acq}/G_{sat} ratio - we kept G_{acq} = - 8%

that is to say 16 G.cm^{-1} and applied different values of G_{sat} from 0.6 to 6 G.cm^{-1} - on Ultra-Fast Z-spectra Figure 52B allows us to obtain an apparent frequency separation up to 35.7 ppm between both dips.

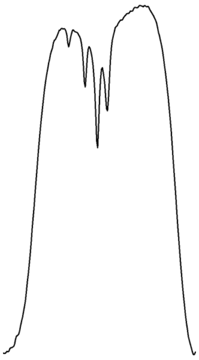

Figure 51: UFZ-spectrum of a mixture of four cryptophanes (745 nM) in PBS obtained with B_{sat} = 12 μT during t_{sat} = 6 s.

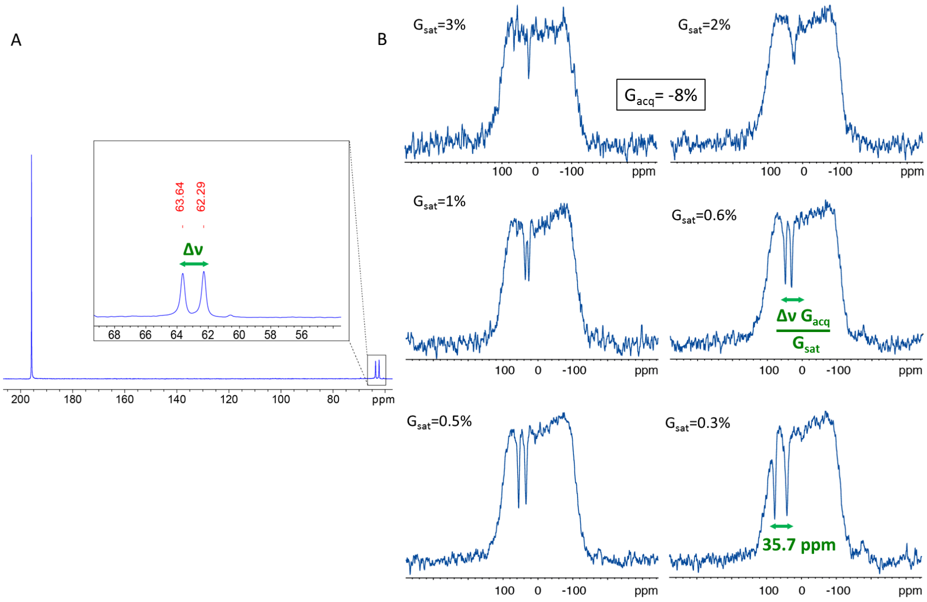

Figure 52: **A** ^{129}Xe direct detection spectrum showing two Xe@biosensors signals separated by $\Delta\nu$ = 1.3 ppm. **B** Ultra-Fast Z-spectra of the same mixture acquired with an acquisition gradient of 16 G.cm^{-1} and a saturation gradient varying from 0.6 to 6 G.cm^{-1}. The apparent frequency separation between both Xe@biosensors dips is $\Delta\nu G_{acq}/G_{sat}$. These spectra were obtained using B_{sat} = 12 μT and t_{sat} = 6 s.

This Ultra-Fast Z-spectrum sequence is a powerful method that enables extremely low detection threshold and enhanced separation of multiple signals in complex systems.

The fact that saturation at the Xe@biosensor frequency occurs only in a minor part of the NMR tube means that only a small part of the biosensor present in the tube can be detected. That is the main defect of this approach.

5.3 CONCLUSIONS ABOUT DIRECT AND INDIRECT - UFZ AND DEPOLARIZATION - METHODS

5.3.1 *Discussion of the methods*

These three detection methods, displayed in Figure 53 are based on different principles.

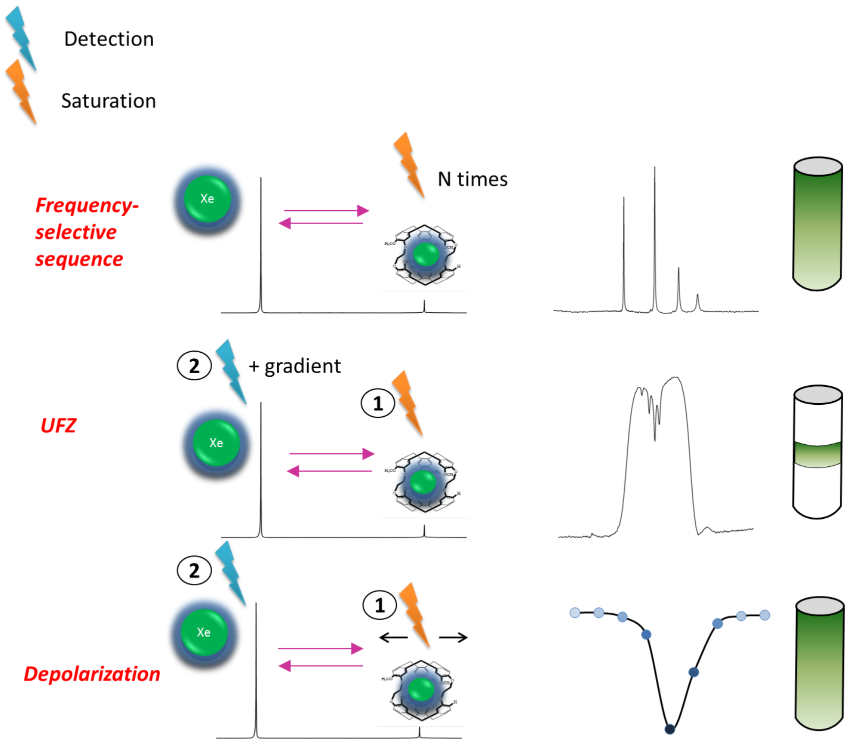

Figure 53: Comparison between principles, spectra and saturated region of the NMR tube with direct and indirect - UFZ or depolarization - detection methods.

The frequency-selective and depolarization sequences both have the whole tube as detection region whereas UFZ approach only targets a slice of the tube. The direct detection method is based on saturations (N times) immediately followed by detection around the resonance frequency of the Xe@biosensor while indirect methods rely upon saturation around the Xe@biosensor and afterwards detection on the reservoir of free dissolved xenon. In UFZ case, two saturations are needed : on-resonance (on Xe@biosensor frequency) and off-resonance, usually applied at an offset symmetrical with respect to the signal of free xenon. The depolarization method needs as much saturations as desired number of data points on the Z-spectrum, applied at different offsets in the vicinity of the Xe@biosensor frequency.

For the HyperCEST-type methods, a simplistic view would consider that the faster the xenon in-out exchange and the stronger the saturation the more sensitive the detection. However several other parameters must be taken into account. Denoting I the spin of free xenon and S the spin of encapsulated xenon, of relative proportions $\mathcal{F}_I$ and $\mathcal{F}_S$ = 1- $\mathcal{F}_I$, respectively, and the exchange rates k_{in} and k_{out}, one has: $k_{in}\ \mathcal{F}_I = k_{out}\ \mathcal{F}_S$. An rf irradiation of amplitude ω_1 applied at a frequency ω_0 tilts the magnetization of the two species by an angle $\theta_{I,S}$ from the static field axis in the rotating frame:

$$\theta_{I,S} = \arctan(\frac{\omega_1}{\omega_{I,S}-\omega_0}).$$

The effective longitudinal relaxation rates along this axis are: $\rho_I = \cos^2\theta_I\ R_{1I} + \sin^2\theta_I\ R_{2I}$

$$\rho_S = \cos^2\theta_S\ R_{1S} + \sin^2\theta_S\ R_{2S}$$

where $R_{1I,S}$ and $R_{2I,S}$ are the pure longitudinal and transverse relaxation rates of spins I or S.[10] Studying the dynamics of the magnetization can be simplified by considering the secular approximation. The six magnetization components (I_X, I_Y, I_Z, S_X, S_Y, S_Z) can be reduced to the two aligned with the effective field axes. They are coupled by the exchange rates k_{in} and k_{out}:

$$\frac{dI_Z}{dt} = -(\rho_I + k_{in})I_Z + k_{out}\ S_Z$$

$$\frac{dS_Z}{dt} = -(\rho_S + k_{out})S_Z + k_{in}\ I_Z$$

Here we have considered that the thermal equilibrium magnetization values are negligible with respect to hyperpolarized magnetization.

For an rf saturation applied exactly at the resonance of the small reservoir signal ($\omega_0 = \omega_S$) and assuming no spillover effects on the large xenon pool, they simplify to:

$$\frac{dI_Z}{dt} = -(R_{1I} + k_{in})I_Z + k_{out}\ S_Z$$

$$\frac{dS_Z}{dt} = -(R_{2S} + k_{out})S_Z + k_{in}\ I_Z$$

Considering the evolution of the global xenon magnetization $\frac{d(I_Z+S_Z)}{dt} = -R_{1I}I_Z - R_{2S}S_Z$ it is notable that important parameters are the longitudinal relaxation rate of free xenon and the transverse relaxation rate of bound xenon. The HyperCEST experiments work in transient mode and take benefit of the exchange for observing differential decay rates of the I spins according to the on- and off-resonance saturation of the S magnetization. Considering that k_{out} » R_{2S} » R_{1I} so that we can neglect the relaxation terms, then the Hyper-CEST efficiency is expressed as:[11, 12]

$$\mathrm{HYPERCEST}(\omega_1,\omega_0,t_{sat}) = 1 - e^{-k_{out}\frac{\mathcal{F}_S}{\mathcal{F}_I}\alpha(\omega_1,\omega_0)t_{sat}}$$

where $\alpha(\omega_1,\omega_0) = \frac{\omega_1^2}{(\omega_1^2+k_{out}^2+(\omega_S-\omega_0)^2)}$ is the saturation efficiency.

Logically, the faster the xenon exchange - the lower the residence time of xenon in its host -, the less efficient the saturation for a given rf strength. From this Lorentzian shape with a full width at half maximum equal to $(2(\omega_1^2 + k_{out}^2))^{1/2}$, it follows that using an intense B_1 field has the advantage of maximizing the saturation efficiency, but enlarges the spectral dip which is detected.[13] In relation with this potential issue, let us mention an experimental problem that can easily occurs with high saturation strength with the most rudimentary version of HyperCEST consisting in simply comparing the depolarization response as a function of saturation duration applied on-resonance and off-resonance (at a frequency offset symmetrical with respect to the free xenon signal). Considering the expression of ρ_I as a function of ω_1, the large difference between longitudinal and transverse xenon relaxation and the fact that temperature increase and Bloch-Siegert effects can slightly shift the free xenon signal, this can easily induce a difference between the on- and off-resonance cases even in the absence of xenon host. This is for this particular reason that we do not exceed 15-20 µT of saturation strength in our experiments.

Actually for most of the xenon hosts and particularly cryptophanes, it has been observed that the line width of the caged xenon signal is influenced by the xenon concentration,[14, 15] which is the signature of a degenerate exchange[16] (or kick-out) mechanism, where a caged xenon atom is expelled by another xenon atom (see Figure 54). The shortening of the caged xenon lifetime depends on the ratio of the noble gas concentration over the concentration of the host. Therefore, the Hyper-CEST efficiency will strongly depend on this ratio, and the saturation strength and duration will need to be adjusted according to the previous expressions.[14]

Finally, while for the same experiment time and for a large range of exchange rates the HyperCEST-type methods are more sensitive than the direct detection methods (due to the fact that noise is acquired only once), they only provide a dip in the large reservoir signal dependent on the amount of small reservoir but also on the duration of

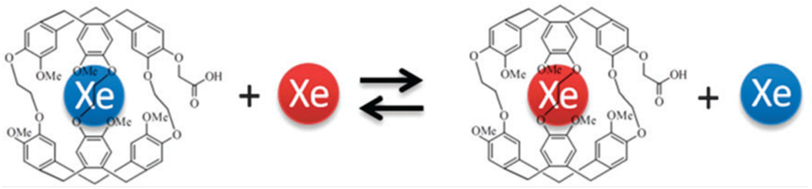

$$CXe + Xe^* \longrightarrow CXe^* + Xe$$

Figure 54: Kickout mechanism for the in-out xenon exchange.

saturation, the relaxation and chemical exchange rates. HyperCEST sequence directly alters the magnetization amplitude and is consequently not a phase encoding sequence: the notion of phase is lost. It means that the generation of pulse sequences beyond simple signal observation is less straightforward. For instance, this prevents localized spectroscopy or spectroscopic imaging which are wished to observe the space distribution in the case of several ^{129}Xe NMR-based sensors or a smart biosensor delivered *in vivo*.

5.3.2 *Chemical Shift Imaging*

^{1}H spectroscopic imaging (or Chemical Shift Imaging CSI) consists in recording the spectroscopic data for a group of slices (1D), pixels (2D), or voxels (3D). The common sequences are of the STEAM and PRESS types.[17] The number and direction of phase encoding gradients depend on the number of dimensions selected (1D, 2D or 3D). For a hyperpolarized ^{129}Xe CSI experiment, these two sequences are not adapted. Actually handling hyperpolarized xenon in exchange hinders the use of several pulses for volume selection. Not only magnetization trajectories after succession of 90° and/or 180° pulses are difficult to predict (inversion of a polarized system can lead to radiation damping and mixture of positively and negatively polarized region in the tube),[18] but also rapid xenon exchange during this volume selection comes to complicate the situation. We therefore developed a simple method using the xenon in-out exchange in the direct detection scheme: addition of two phase gradients after the initial excitation pulse provides a 3D experiment with two spatial dimensions and one spectral dimension, in which it is possible to observe the ^{129}Xe NMR (sub)spectrum on Figure 55. The excitation pulse can be applied simultaneously with a gradient to obtain a slice selection. However there is a limitation for the slice gradient strength, arising from the fact that the large reservoir signal should not be excited. But it is not stringent in most of the cases, given the large spectral separation between the free and caged xenon signals.

Figure 55 displays such an experiment, performed with a single bolus of hyperpolarized xenon before the NMR experiment, where it is possible to localize pixels containing different distributions of water-soluble cryptophanes, at micromolar concentration. Performing such an experiment in the indirect mode would have been much more cumbersome.

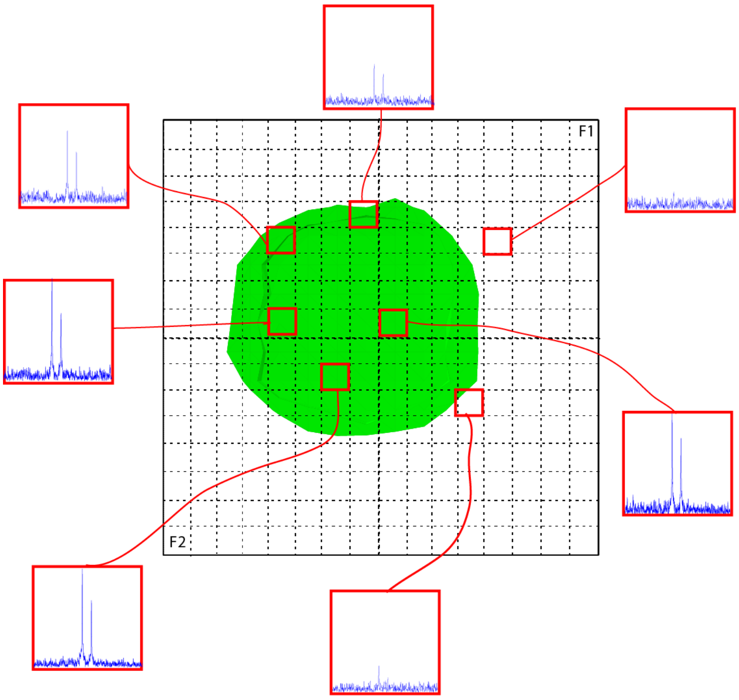

Figure 55: Hyperpolarized ^{129}Xe CSI experiment. The sample was an aqueous mixture of two cryptophanes at 100 µM in an 8 mm-o.d. NMR tube. The axial imaging is divided in 32x32 points in the spatial dimensions (experiment time 1 min 40 s).

This work is currently under submission

We then extended this approach to a more complicate system that are under development in the lab : an ^{129}Xe-NMR based pH sensor .

BIBLIOGRAPHY

[1] H Kessler, U Anders, G Gemmecker, and S Steuernagel. Improvement of NMR experiments by employing semiselective half-gaussian-shaped pulses. *Journal of Magnetic Resonance (1969)*, 85(1):1 – 14, 1989.

[2] Lyndon Emsley and Geoffrey Bodenhausen. Gaussian pulse cascades: New analytical functions for rectangular selective inversion and in-phase excitation in NMR. *Chemical Physics Letters*, 165(6):469 – 476, 1990.

[3] Patrick Berthault, Gaspard Huber, and Hervé Desvaux. Biosensing using laser-polarized xenon NMR/MRI. *Progress in Nuclear Magnetic Resonance Spectroscopy*, 55(1):35 – 60, 2009.

[4] Leif Schröder, Thomas J. Lowery, Christian Hilty, David E. Wemmer, and Alexander Pines. Molecular imaging using a targeted magnetic resonance hyperpolarized biosensor. *Science*, 314(5798):446–449, 2006.

[5] Dan Zhou, Jun Xu, Jihong Yu, Lei Chen, Feng Deng, and Ruren Xu. Solid-state NMR spectroscopy of anionic framework aluminophosphates: A new method to determine the Al/P ratio. *The Journal of Physical Chemistry B*, 110(5):2131–2137, 2006.

[6] Silvio Aime, Daniela Delli Castelli, and Enzo Terreno. Highly sensitive MRI chemical exchange saturation transfer agents using liposomes. *Angewandte Chemie International Edition*, 44(34):5513–5515, 2005.

[7] Xiang Xu, Jae-Seung Lee, and Alexej Jerschow. Ultrafast scanning of exchangeable sites by NMR spectroscopy. *Angewandte Chemie International Edition*, 52(32):8281–8284, 2013.

[8] Assaf Tal and Lucio Frydman. Single-scan multidimensional magnetic resonance. *Progress in Nuclear Magnetic Resonance Spectroscopy*, 57(3):241 – 292, 2010.

[9] Céline Boutin, Estelle Léonce, Thierry Brotin, Alexej Jerschow, and Patrick Berthault. Ultrafast Z-spectroscopy for 129Xe NMR-based sensors. *J. Phys. Chem. Lett.*, 4(23):4172–4176, dec 2013.

[10] H. Desvaux and P. Berthault. Study of dynamic processes in liquids using off-resonance rf irradiation. *Progress in Nuclear Magnetic Resonance Spectroscopy*, 35(4):295 – 340, 1999.

[11] Elena Vinogradov, A. Dean Sherry, and Robert E. Lenkinski. CEST: From basic principles to applications, challenges and opportunities. *Journal of Magnetic Resonance*, 229:155–172, apr 2013.

[12] M. Kunth, C. Witte, and L. Schröder. Quantitative chemical exchange saturation transfer with hyperpolarized nuclei (qHyper-CEST): Sensing xenon-host exchange dynamics and binding affinities by NMR. *The Journal of Chemical Physics*, 141(19):194202, 2014.

[13] Martin Kunth, Christopher Witte, Andreas Hennig, and Leif Schroder. Identification, classification, and signal amplification capabilities of high-turnover gas binding hosts in ultra-sensitive NMR. *Chem. Sci.*, 6:6069–6075, 2015.

[14] Kristin Bartik, Michel Luhmer, Jean-Pierre Dutasta, André Collet, and Jacques Reisse. 129Xe and 1H NMR study of the reversible trapping of xenon by cryptophane-A in organic solution. *Journal of the American Chemical Society*, 120(4):784–791, 1998.

[15] Gaspard Huber, Laetitia Beguin, Herve Desvaux, Thierry Brotin, Heather A. Fogarty, Jean-Pierre Dutasta, and Patrick Berthault. Cryptophane-xenon complexes in organic solvents observed through NMR spectroscopy. *J. Phys. Chem. A*, 112(45):11363–11372, nov 2008.

[16] Sergey Korchak, Wolfgang Kilian, and Lorenz Mitschang. Degeneracy in cryptophane-xenon complex formation in aqueous solution. *Chem. Commun.*, 51:1721–1724, 2015.

[17] Chrit T. W. Moonen, Markus Von Kienlin, Peter C. M. Van Zijl, Jack Cohen, Joe Gillen, Peter Daly, and Gerald Wolf. Comparison of single-shot localization methods (steam and press) for in vivo proton NMR spectroscopy. *NMR in Biomedicine*, 2(5-6):201–208, 1989.

[18] Patrick Berthault, Hervé Desvaux, Gérald Le Goff, and Michel Pétro. A simple way to properly invert intense nuclear magnetization: application to laser-polarized xenon. *Chemical Physics Letters*, 314(1):52 – 56, 1999.

Part II

DETECTION OF RECOMBINANT PROTEINS

This second part presents the bimodal biosensor from its conception, its synthesis, its optical and ^{129}Xe NMR properties to its biological applications. Chapter 6 describes the function and the synthesis of each unit of the biosensor. Chapter 7 focuses on the first *in vitro* results, being the dual detection of tagged peptides. Chapter 8 is a proof of concept of *in vitro* dual-detection of tagged-proteins. It also describes the five molecular constructions based on fluorescent proteins that we have developed. Preliminary results presented in chapter 9 proves that the bimodal responsive biosensor is suitable for *in cellulo* detection of tagged-proteins. Finally, chapter 10 serves as a brief conclusion to ^{129}Xe NMR-based biosensors and their future *in vivo* directions.

6

BIMODAL SENSOR

The study of intracellular biological mechanisms requires sensitive and non-invasive techniques. The combined use of several methods of analysis makes it possible to overcome the disadvantages of each of them and combine their respective advantages. This is the viewpoint of multimodal approaches, highly developed in recent years. Within this frame, our project aims at the conception of a bimodal fluorescence and NMR sensor. Fluorescence has a high sensitivity and a good spatial resolution, but does not allow the study of deep tissues. NMR, which has this property, suffer from low sensitivity. The strategy is to combine the recent developments in both fluorescence and NMR techniques in order to obtain a doubly responsive sensor. This biosensor consists in 2 moieties, an NMR and a fluorescence detection parts linked by an organic spacer. The fluorescence detection part consists itself in two partners: an organic ligand fused to the cage and a peptide being the target that can be fused to the protein of interest (Figure 56).

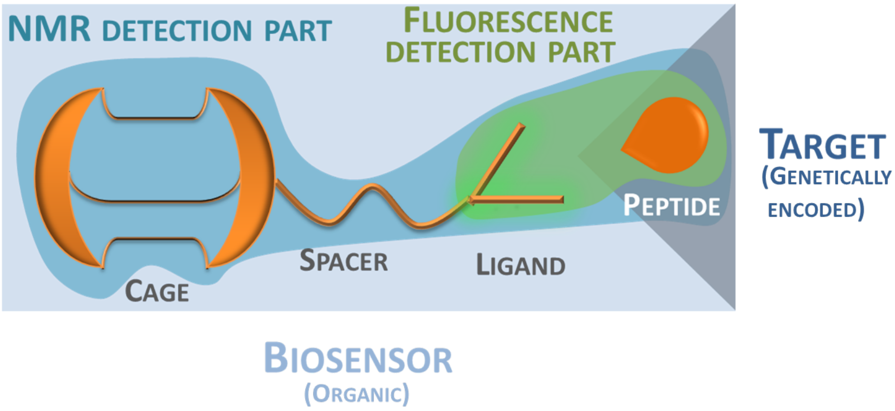

Figure 56: Structure of the bimodal biosensor.

In order to facilitate the understanding of the bimodal construction, each moiety - NMR detection part, spacer and both partners of the fluorescence detection part - will be schematized in the margins of this chapter and then drawn in synthesis diagrams.

This chapter aims to define possible candidates known in the literature for each part and to explain, considering the requirements specification implied by the combination of all these entities, which ones were of best interest.

6.1 OBJECTIVES

The objectives of the sensor is to detect a recombinant protein which is tagged. In this purpose, two different modalities will be used to witness the binding:

- A strong fluorescence has to appear upon binding.
- A specific ^{129}Xe signal should appear.

  Figure 57 shows the principle of the bimodal detection of the first doubly smart biosensor in ^{129}Xe NMR and fluorescence.

6.2 NMR DETECTION PART

As described in Chapter 4, ^{129}Xe NMR-based sensors belong to a new generation of tracers. For this approach, let us recall that the chosen host molecule has to be water-soluble.

Cr-AM is obtained by the use of a lithium base (PPh2Li) on Cr-A (Figure 58). It leads to a cryptophane having six phenol functions, cryptophanol-A. Nucleophilic substitution reactions with methyl bromoacetate at each of these phenols subsequently leads to a cryptophane carrying six ester functions, whose hydrolysis produces the six carboxylic acid functions. Synthesis of this water-soluble cryptophane was performed by Thierry Brotin and his group and is described in Figure 58.

As CTV moieties are chiral, two configurations are possible for cryptophanes. If the two attached CTV units are identical, the configuration anti will be obtained. On the contrary, if the two CTV units are enantiomers, the cryptophane will be syn (Figure 59).[1]

Cr-AM was synthesized from two identical CTV, leading to the anti racemic mixture. Since previous investigations have demonstrated that two enantiomers related to the helicity of the linkers (see (M,M) and (P,P) in Figure 59 can produce different ^{129}Xe NMR signals upon binding to structures bearing stereogenic centers,[2] the two enantiomers (M,M) and (P,P) have been synthesized separately by a multistep procedure from enantiopure cryptophanol-A in Thierry Brotin's laboratory.[3]

6.3 FLUORESCENCE DETECTION PART

Fluorescence techniques are the most commonly used in the field of cellular and molecular imaging as they have a high sensitivity and

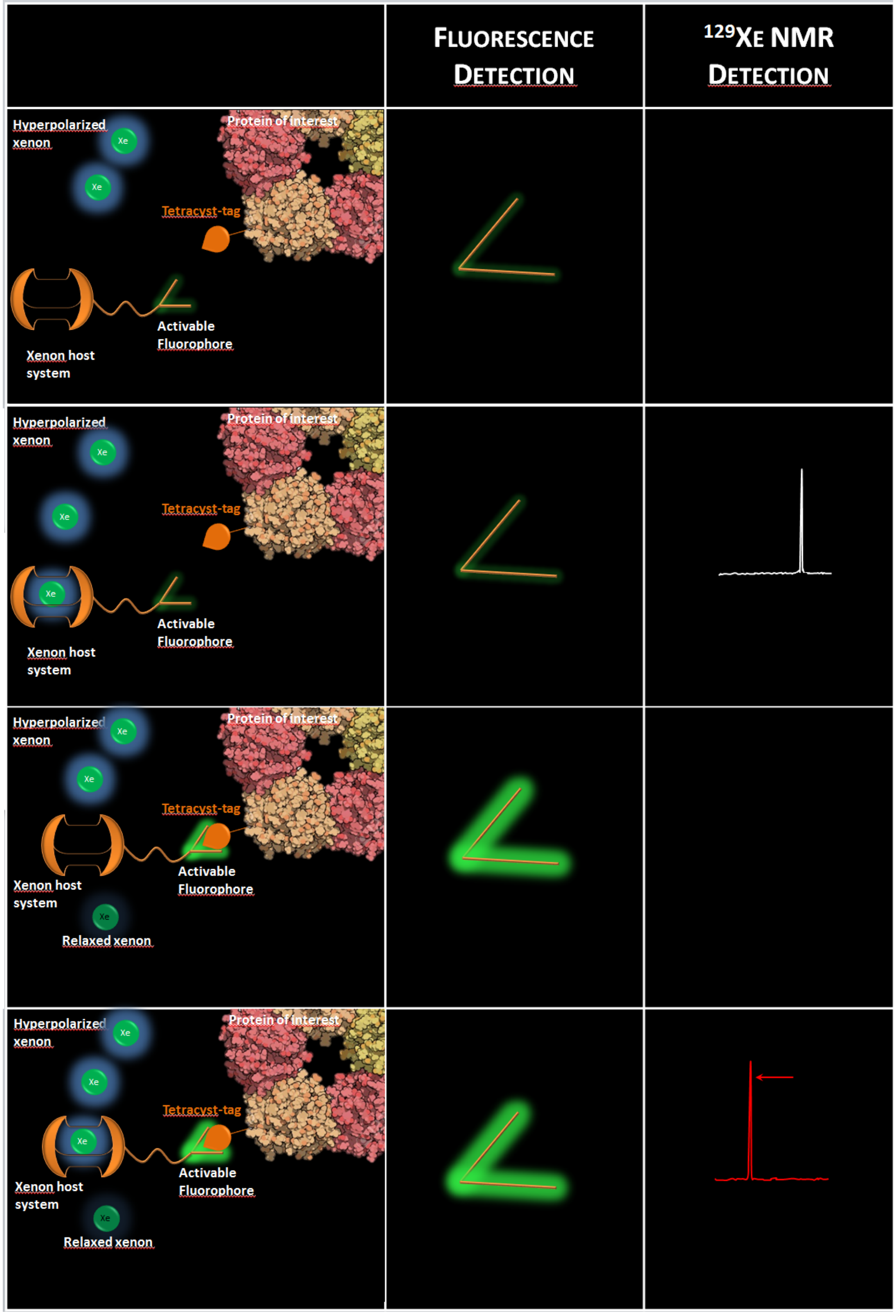
FLUORESCENCE DETECTION
^{129}XE NMR DETECTION
Hyperpolarized xenon
Xe
Protein of interest
Tetracyst-tag
Activable Fluorophore
Xenon host system
Hyperpolarized xenon
Xe
Protein of interest
Tetracyst-tag
Activable Fluorophore
Xenon host system
Hyperpolarized xenon
Xe
Protein of interest
Tetracyst-tag
Activable Fluorophore
Xenon host system
Relaxed xenon
Hyperpolarized xenon
Xe
Protein of interest
Tetracyst-tag
Activable Fluorophore
Xenon host system
Relaxed xenon

Figure 57: Doubly responsive probe for recombinant protein detection.

spatio-temporal resolution. A fluorophore commonly used in the last twenty years for the study and *in cellulo* monitoring of proteins of interest is the Green Fluorescent Protein (GFP). This genetically encoded probe was isolated from the jellyfish *Aequorea victoria*.[4, 5] The gene of this fluorescent protein can be fused to the gene of the pro-

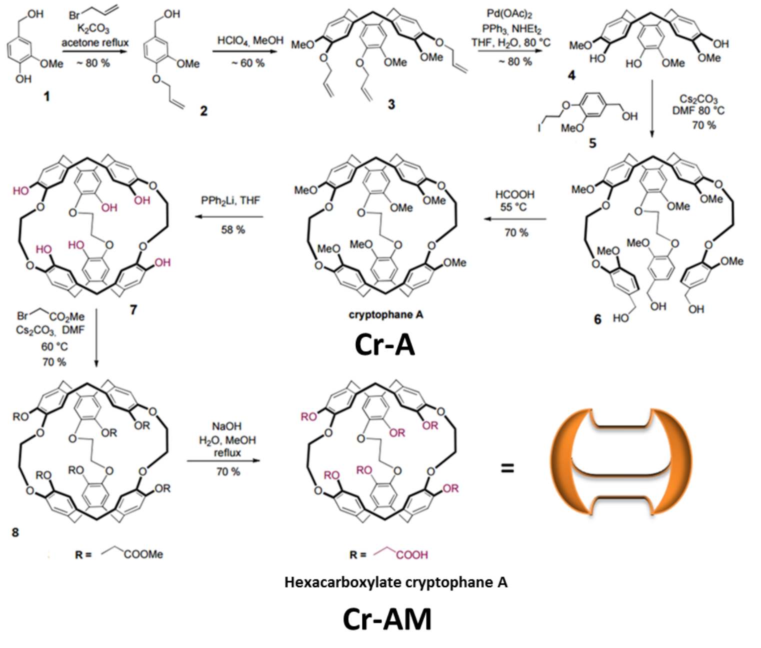
Br
K$_2$CO$_3$
acetone reflux
~ 80 %
HClO$_4$, MeOH
~ 60 %
Pd(OAc)$_2$
PPh$_3$, NHEt$_2$
THF, H$_2$O, 80 °C
~ 80 %
Cs$_2$CO$_3$
DMF 80 °C
70 %
HCOOH
55 °C
70 %
PPh$_2$Li, THF
58 %
Br CO$_2$Me
Cs$_2$CO$_3$, DMF
60 °C
70 %
NaOH
H$_2$O, MeOH
reflux
70 %
1
2
3
4
5
6
7
8
cryptophane A
Cr-A
R = COOMe
R = COOH
Hexacarboxylate cryptophane A
Cr-AM

Figure 58: Synthesis of water-soluble cryptophane-AM (Cr-AM).

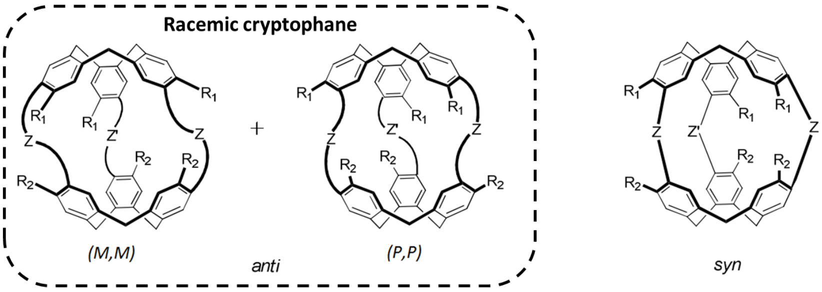
Racemic cryptophane
(M,M)
anti
(P,P)
syn
R$_1$
R$_2$
Z
Z'

Figure 59: Three constitutional isomers of cryptophane.

tein of interest to produce a fluorescent probe *in situ*.[6] However, the non-negligible size of this fluorescent protein (238 amino acids) can disrupt or constrain the studied protein behavior. Efforts have been made with the conception of small fluorophores. One strategy is discussed in the following paragraph.

6.3.1 *Small ligand : biarsenical dye*

Griffin *et al.* worked in 1998 on the development of two partners: a peptidic target consisting of only 6 amino acids that can be genetically incorporated into the sequence of the studied protein, and a small synthetic fluorogenic ligand (<700 Dalton).[7] This partnership is based on the reversible formation of covalent bonds between the two pairs of thiol groups present in the peptide target, called the tetracysteine motif **CC**XX**CC** (TC) and two atoms of arsenic of the ligand as displayed in Figure 60.[8, 9]. The main advantage of this system is that the ligand has very low fluorescence until it binds its target. Upon binding, it becomes strongly fluorescent, leading to a ligand that is not only a fluorophore but a fluorogenic probe (or a responsive probe). This has a particular advantage concerning the signal to noise ratio as the system switches between dark and fluorescent. Another advantage of this system is that the ligand has relatively few binding sites in mammalian cells. It binds to the peptide target with a nanomolar or even lower dissociation constant.

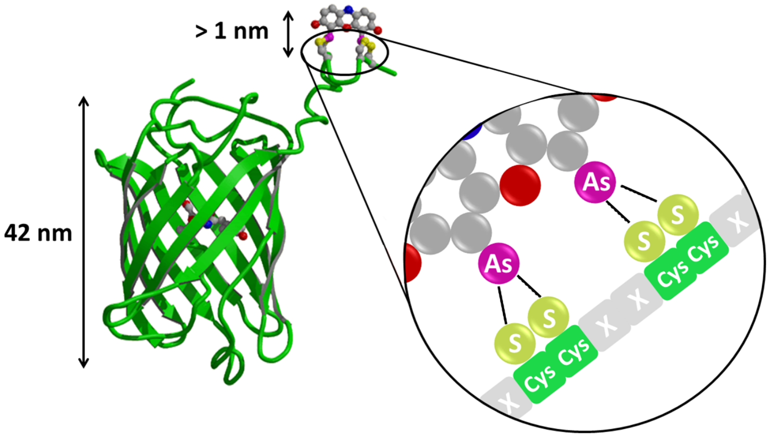

Figure 60: Comparison between GFP and FlAsH sizes. On this scheme, the fluorescent protein features the protein of interest.

Its small size, displayed in Figure 60, also minimizes the perturbation of activity of the tagged protein. Notably, the biarsenical ligand is membrane-permeable and does not require complicated procedures such as microinjection. The small size increases the versatility, in particular it is easily grafted on different positions on the protein of interest. The peptide target can, depending on its three-dimensional structure, be genetically incorporated on the N-terminal part, C-terminal part, inside an α helix or a β strand of the protein, demonstrating its numerous possibilities.[7]

In the past, this method has been widely used to study a number of *in vivo* cellular events and subcellular structures in animal cells such as β-tubulin dynamics,[10] Ebola virus matrix protein,[11] conformational changes in a G protein-coupled receptor[12] and protein misfolding *in vivo*.[13]

Figure 61 presents an example of an experiment with cells expressing different surface receptor constructions and labeled with the first version of this ligand: a fluorescein derivative called FlAsH (Fluorescein ArSenical Hairpin binder).[12] Let us mention that these receptors have been fused with Cyan Fluorescent Protein (CFP) in C-terminus and with FlAsH binding motif (peptidic sequence) either at the C-terminus, at the third intracellular loop (Figure 61A). The experiment in Figure 61B shows that cells expressing the FlAsH binding motif exhibits a strong FlAsH fluorescence at the cell membrane (intracell). Indeed, this ligand is known to exhibit a fluorescence multiplied by more than 100 when it binds the 6 amino acids sequence. The FlAsH-peptide target complex has demonstrated Förster resonance energy transfer (FRET) from fluorescent proteins such as CFP (Figure 61C) or GFP (a phenomenon that will be explained in Chapter 8.[14] We can also note a background fluorescence inside the cells owing to non-specifically bound FlAsH to thiol-rich endogenous proteins but this remains very low. Several versions of this ligand were synthesized in order to optimize such parameters.
This demonstrates the high versatility of this method.

6.3.1.1 *Bis-arsenical ligand variant*

The modification of the fluorescein moiety (see Figure 62) allows multicolor analysis in the same way as the large panel of fluorescent proteins that are available to date. After the development of green-fluorescent FlAsH (λ_{ex} = 508 nm, λ_{em} = 528 nm), several derivatives including red-fluorescent ReAsH (λ_{ex} = 593 nm, λ_{em} = 608 nm) and blue-fluorescent CHoXAsH (λ_{ex} = 380 nm, λ_{em} = 430 nm) were also reported.[14] An environment-sensitive nile red-based biarsenical dye, BArNile, was synthesized and successfully imaged the conformational changes of tetracysteine-fused calmodulin upon Ca^{2+} increase in living cells.[15]

In order to improve the fluorescent character of FlAsH, two derivatives, difluorinated F2FlAsH and tetrafluorinated F4FlAsH were developed by Jares-Erijman *et al.* (Figure 62). F2FlAsH exhibits a higher absorbance, quantum yield, photostability, a larger Stokes shift and a reduced pH dependence compared to FlAsH. F4FlAsH exhibits a fluorescence emission in a region intermediate to that of FlAsH and ReAsH, allowing a new color and an excellent brightness.[16]

In all the FlAsH derivatives a 6Å interatomic distance is conserved between the two arsenic moieties. This constrains the nature of the fluorophore and the structure of the peptide. This therefore complicates the selective labeling of multiple proteins with different reporters. To

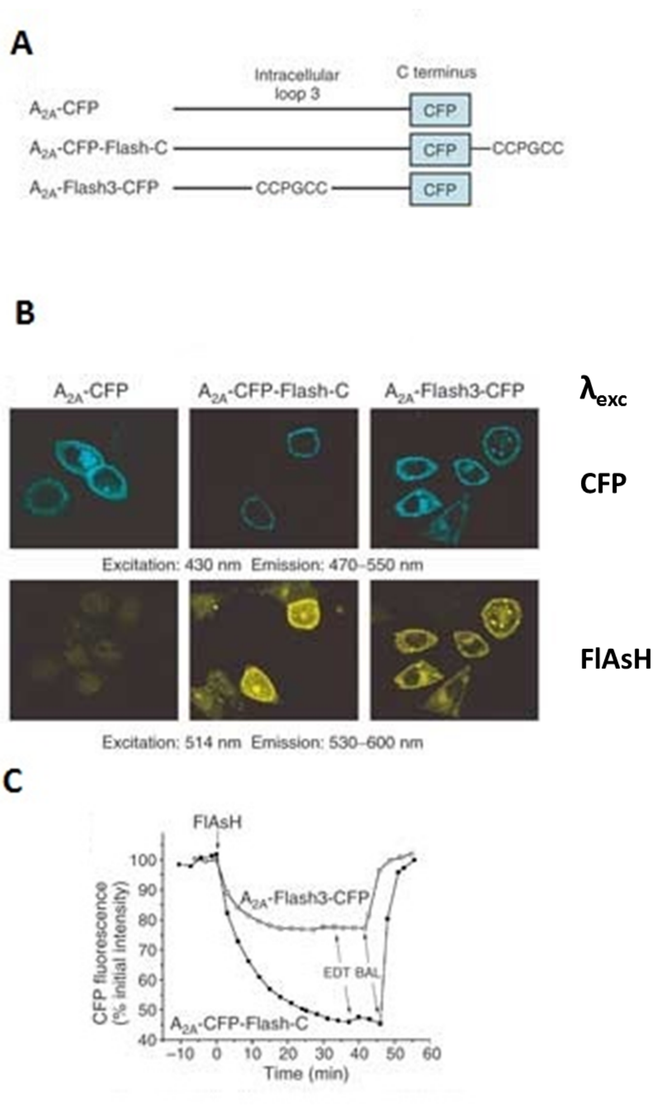

Figure 61: **A.** Schematic representation of cell surface receptor constructions, modified as indicated either at the C-terminus, or at the third intracellular loop. **B.** Confocal microscopy images of the three receptor constructions transiently expressed in Hela cells and labeled with FlAsH. Top row shows CFP fluorescence whereas bottom row shows FlAsH fluorescence. Cells expressing constructs containing the FlAsH binding motif (center and right) show a strong yellow fluorescence at the cell surface. **C.** FRET between CFP and FlAsH in cell constructions. Adapted from [12].

achieve that, Mayer *et al.* designed a new Cy3-based biarsenical probe, AsCy3, with a large 14.5Å interatomic distance between the two arsenics enabling a high-affinity binding with other type of motif with 5 amino acids between the double pair of cyteines such as Cy3Tag

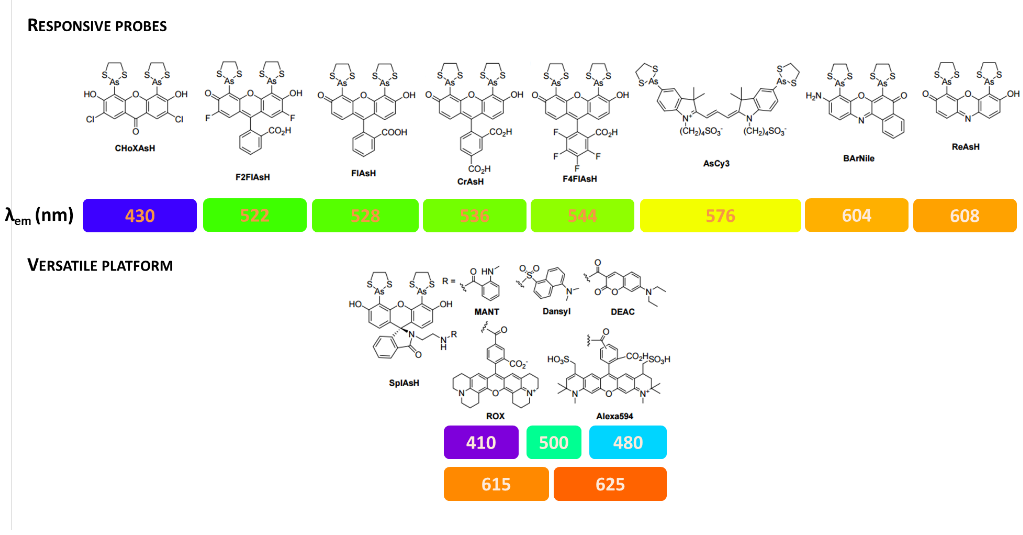
RESPONSIVE PROBES
CHoXAsH
F2FlAsH
FlAsH
CrAsH
F4FlAsH
AsCy3
BArNile
ReAsH
λ_{em} (nm)
430
522
528
536
544
576
604
608
VERSATILE PLATFORM
SplAsH
MANT
Dansyl
DEAC
ROX
Alexa594
410
500
480
615
625

Figure 62: Biarsenical dyes and their fluorescence emission wavelength.

(**CC**KAEAA**CC**).[17]

To limit the undesirable binding observed in Figure 61B, a carboxy-FlAsH (CrAsH) that is less hydrophobic had been synthesized by Tsien's group.[14] CrAsH exhibits indeed a lower non-specific binding to hydrophobic proteins than FlAsH although the affinity of CrAsH with tetracysteine sequence is one order of magnitude weaker than FlAsH.

Finally, although various biarsenical probes were reported, structural requirements for both fluorescence and the rigid display of arsenic atoms strictly limit the range of possible fluorophores. Moreover, since the scope of compatible dyes is both narrow and difficult to predict, a modular approach wherein the biarsenical targeting moiety is separated from the fluorophore in order to remove any restriction on its structure has been developed by Miller *et al.*[18] In the latter case, the biarsenical targeting moiety is the non fluorescent SplAsH (Spirolactam Arsenical Hairpin binder). It can be conveniently attached with a variety of fluorophores for various applications. Despite the advantage of being a versatile technique, this platform is no longer a responsive dye, as it is always fluorescent.

6.3.1.2 *Carboxy-FlAsH : CrAsH*

For the bimodal ^{129}Xe NMR-fluorescence probe, some features were required for the choice of the fluorescent ligand. Since the long-term goal is to detect protein of interest *in cellulo*, we needed a dye that is optimized for biological conditions. Then, the fluorogenic ligand should be easily attached to Cr-AM by for instance a non-hindered

carboxyl group. The CrAsH moiety qualifies for all these requirements and its synthesis is well described in the literature.[19, 20]
I conducted this four-step synthesis (see Figure 63).

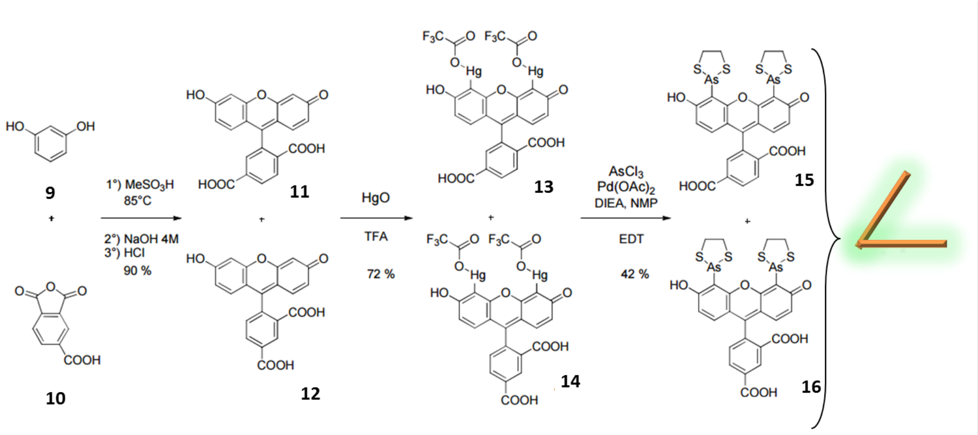

Figure 63: 4-steps synthesis of 5- and 6-carboxyFlAsH or CrAsH, the small ligand.

The mixture of anhydride **9** and 2 equivalents of resorcinol **10** leads to an equimolar mixture of 5 and 6-carboxyfluorescein **11** and **12**. At this step, it is possible to isolate those two structural isomers through consecutive crystallizations but since the yields of this additional step are very low, we decided to pursue the reaction on the mixture. In the presence of mercury oxide in trifluoroacetic acid, these compounds give derivatives **13** and **14** with 72% yield. Then they undergo a transmetallation which makes it possible to introduce the two arsenic which are complexed with ethanedithiol to give the two isomers of the dye CrAsH **15** and **16** with 42% yield after a column chromatography. Detailed protocol and characterization are given in Appendix A. These two separated isomers will allow us to develop different sensors that may have different properties.

Purified CrAsH dye, which is an orange powder, is water-soluble at any pH. It has an unique pK$_a$ calculated to be 5.8. This means a fluorescence stability of CrAsH above pH≈6.8, which is in the physiological range. Compared to FlAsH that has two distinct pKas, CrAsH is then the preferred probe for quantitative fluorescence measurements, especially for labeled proteins which move between different cellular environments.[21]

When excited at 480 nm, CrAsH-peptide exhibits a fluorescence emission spectrum centered at 536 nm. Parameters such as fluorescence increasing or binding constant are strictly peptide-dependent and will be discussed in this chapter for the most common tetracysteine sequences.

6.3.2 *Peptidic target: tetracysteine tag sequences*

6.3.2.1 *Binding process*

The trivalent arsenic atoms form particularly stable compounds with dithiols whose S-H bonds are arranged to form a ring, the most stable ring consisting in 5 bonds (see Figure 64).

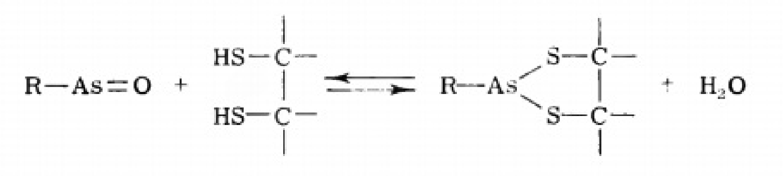

Figure 64: Interaction between a trivalent arsenic atom and a dithiol leading to a 5-bond ring. Reproduced from [22].

Thus, they can complex and reduce the adjacent cysteine pairs of proteins.[22] This affinity explains in particular the high retention of the organoarsenical compounds in the rat blood, complexed with Cys13α of the hemoglobin.[23] In fact, the absence of this amino acid in the human sequence of hemoglobin allows a faster blood removal of arsenic. Such binding, which is responsible for much of the toxicity of arsenic compounds is completely reversed by small vicinal dithiols such as 1,2-ethanedithiol (EDT), which form tighter complexes with the organoarsenical than do cellular dithiols : they act like antidote.[24] For the bimodal project, the peptidic target needs to have an affinity higher than the antidotes for the organoarsenical ligand in order to bind the ligand in the presence of an excess of antidote and to specifically bind the desired peptide target without poisoning other proteins.

Figure 65 describes the reversible complexation of the biarsenical probe on the tetracysteine motif leading to either a great enhancement of the fluorescence -*i.e.* when bound to the tetracysteine motif and called FlAsH-peptide- or a very low fluorescent compound -*i.e.* when bound to two molecules of antidote EDT and called FlAsH-EDT$_2$.

The small size of EDT probably permits rotation of the aryl-arsenic bond and excited state quenching by vibrational deactivation or photoinduced electron transfer, whereas the peptide complex may evade such quenching because its more rigid conformation should hinder conjugation of the arsenic lone pair electrons with the fluorescein orbitals.[22]

The equilibrium reaction FlAsH-EDT$_2$ + peptide = FlAsH-peptide + 2 EDT favored FlAsH-peptide at $\leqslant 10\ \mu$M EDT and FlAsH-EDT$_2$ at $\geqslant$ 1 mM EDT, so that labeling is reversed by millimolar concentrations of EDT. Griffin and his group also proved that monothiols such as β-

mercaptoethanol or glutathione are helpful to catalyze equilibration but do not compete themselves.[7]

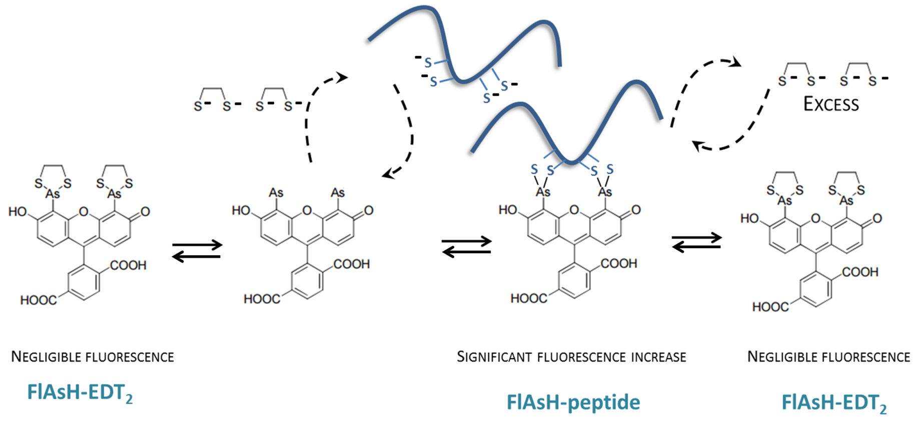

Figure 65: Reversible complexation of biarsenical dye on a tetracysteine motif in the presence of an excess of EDT.

Several peptides have been chosen in such a way that the distance between the two pairs of cysteines matches the spacing between the two arscenics so that the two dithiol-arsenic interactions are highly cooperative and entropically favorable. Let us present now peptide targets designed for FlAsH dye that may be extended for CrAsH ligand.

Table 2: Tetracysteine tags for Biarsenical Probes

Tag	Sequence	$K_{d\ app}$	$\Delta\Phi$	Ref
RE-tag	WEAAAREA**CC**RE**CC**ARA	4.0	120	[7]
PG-tag	AREA**CC**PG**CC**K	0.25	170	[14]
HRW-PG-tag	HRW**CC**PG**CC**KTF	0.10	140	[25]
FLN-PG-tag	FLN**CC**PG**CC**MEP	0.15	100	[25]
YRE-PG-tag	YRE**CC**PG**CC**MWR	0.25	*n/a*	[25]
KA-tag	**CC**KA**CC**	0.85	150	[26]
SlyD	G**CC**GGSGNDAGG**CC**GG	0.25	280	[27]

The apparent dissociation constant ($K_{d\ app}$ in µM) and increase in fluorescent quantum yield ($\Delta\Phi$) of the FlAsH-tetracysteine tags are in the presence of 200 µM EDT. To calculate the real K_d, one has to take into account the other species present into the sample. The four peptide target highlighted in yellow in Table 2, will be discussed in this work. They have been synthesized by Biomatik.

6.3.2.2 *Optimized tetracysteine peptides*

6.3.2.2.1 WEAAAREA**CC**RE**CC**ARA This peptide, studied by Roger Tsien and his group in 1998, has two pairs of cysteines spaced by an arginine and a glutamic acid.[7] This peptide was selected for its ability to promote the formation of an α helix - due to the the EAAAR sequence -, the four thiols then forming a parallelogram on one of its faces: positions i, i+1, i+4 and i+5. It is then possible to envisage two complexing pathways: either an arsenic attaches to two adjacent thiol groups or it binds to two thiols groups separated by one turn of an helix of the peptide (see Figure 66).

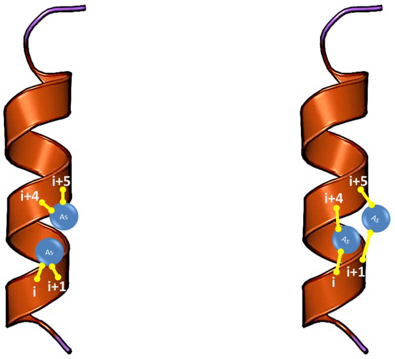

Figure 66: Two complexing pathways of biarsenical probe towards tetracysteine motif.

FlAsH dye is capable of complexing this tetracysteine sequence with dissociation constants a the picomolar range (without EDT) and the fluorescence of the complex is 120 times brighter than that of the free molecule.[7]

6.3.2.2.2 FLNCCPGCCMEP This second peptide, studied seven years later by the same group, was chosen for its three-dimensional hairpin structure, brought by the presence of a proline and a glycine between the two pairs of cysteines.[25] The complex thus formed between this peptide and the biarsenical molecule has a fluorescence 20 times greater than that generated by the α helical peptide. Recent NMR studies have shown the non-traditional β-hairpin structure of the ligand-peptide complex.[28] On Figure 67, arsenic atoms are fixed to the cysteines (colored in red) at a distance of 2.25 Å. The three amino acids before and after the two pairs of cysteines have shown their influence on the complexation properties. This optimal sequence leads to a lower dissociation constant than the previous RE-tag by more than an order of magnitude. It may form a β-turn as Pro-Gly is a known type-I and type-II β-turn sequence.

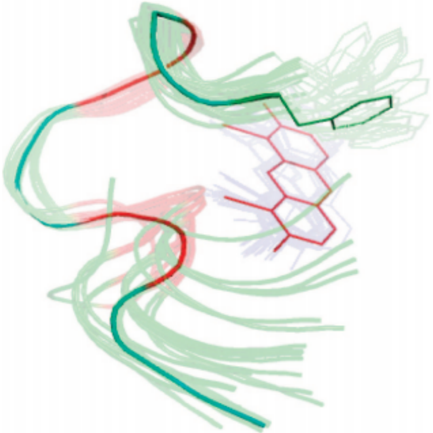

Figure 67: Structure calculation of the peptide bound to ReAsH, based on NOESY-derived distance constraints. Reproduced from [25].

6.3.2.2.3 AREACCPGCCK This is the PG-tag version optimized for CrAsH dye which is well known for having lower affinities for tetracysteine motifs than other variants. Bound to this flexible strand, CrAsH-peptide complex has an apparent dissociation constant of 407 nM compared to 250 nM for FlAsH, which is the same order of magnitude. Its small size (only 11 amino acids) is an advantage for protein labeling.

6.3.2.2.4 GCCGGSGNDAGGCCGG The last peptide, studied by Uljana Mayer and her group, has vicinal pairs of cysteines separated by 9 residues and an approximately twofold increase in fluorescence with FlAsH over the FLN**CC**PG**CC**MEP TAG. The sequence exists in the C-terminal domain of the SlyD protein, a peptidylpropyl isomerase playing a primordial role in protein folding. This chain of amino acids creates a flexible loop promoting the formation of intramolecular disulfide bridges within the uncomplexed peptide. After reduction, these sites are available for complexation with the biarsenical molecule with dissociation constants in the picomolar range. This structure thus provides more stable complexations and a fluorescence gain due to the flexibility of the loop which protects the fluorophores from the deactivation of the solvent. Despite its great spectral properties, to date their characteristics have not been demonstrated *in vivo*.

6.4 BIOSENSOR SYNTHESIS

Once we determined the NMR and fluorescence detection parts, the next step is to find a strategy to combine those two moieties. Cr-AM and CrAsH bearing respectively six and two carboxy groups, can be linked by a diamine spacer through a peptide bond. Some studies have shown that the linker between the host molecule and the ligand has a crucial importance.[29] If the ligand and/or the biological receptor have high molecular weights, too short or too rigid linkers have strong consequence on the NMR signal. Indeed, the moiety hosting xenon can take the same correlation time as the macromolecule. This leads to accelerated xenon transverse relaxation, which has the main consequence of broadening the signal of bound xenon. To achieve this, we chose ethylene diamine as the spacer between the cage and the ligand.

For the synthesis, both carboxylic acid groups of compounds **15** and **16** are activated to form hydroxysuccinimide esters, which in the presence of an excess of ethylene diamine lead to compounds **17**, **18**, **19** and **20** in Figure 68. Compounds **17** and **18** are separated from **19** and **20** by HPLC and both mixtures are coupled to Cr-AM through the same strategy than the previous step.

Cr-AM is activated by 1.0 equivalent of N-hydroxysuccinimide (NHS) and 1.1 equivalents of EDCI (1-Ethyl-3-(3-dimethylamino propyl) carbodiimide). EDCI is a carboxyl activating agent commonly used for the coupling of primary amines. It is combined with NHS for the immobilisation of large molecules. After 5 hours of activation, a follow-up by LC/MS reveals that the mixture consists in mono-activated Cr-AM (predominant product), di and tri-activated Cr-AM. Compounds **17** and **18** are solubilized in DMSO and in the N,N-Diisopropylethyl amine (DIEA) base and then introduced in the reaction mixture. In parallel, we do the same with compounds **19** and **20**. Reactions are left under stirring at room temperature for 12 hours. Biosensors **21** and **22** are obtained, as well as residual Cr-AM, **17** and **18**.

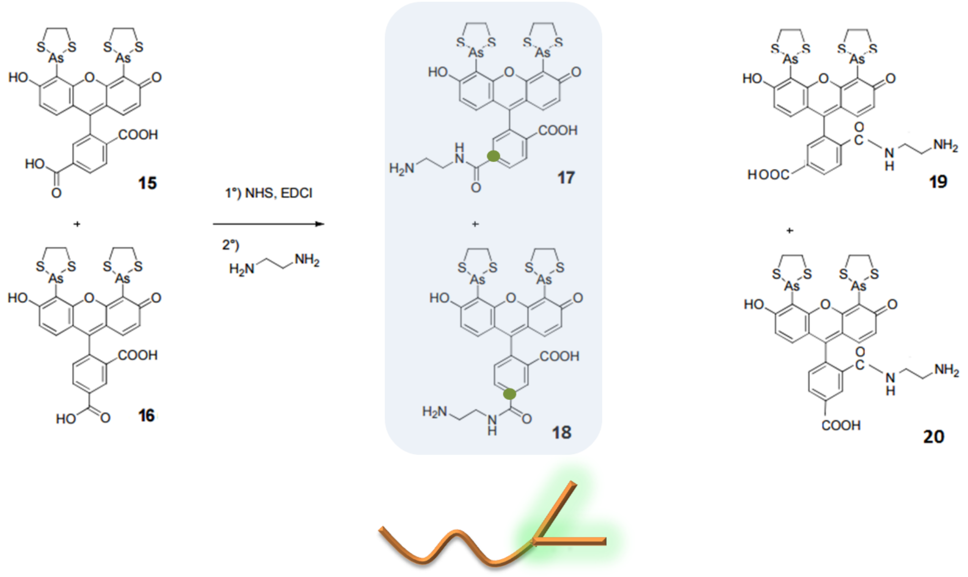
15
16
1°) NHS, EDCI
2°)
17
18
19
20

Figure 68: Synthesis of CrAsH linked to etylene diamine : compounds **17** and **18**.

Isomers **21** and **22** are separated by HPLC and isolated with respectively 15 and 9 % of yield (see Figure 69). For the second reaction mixture, only Cr-AM and compounds **19** and **20** were found, confirming the hypothesis that this carboxy group is too hindered for the addition of a macromolecular structure such as a cryptophane.

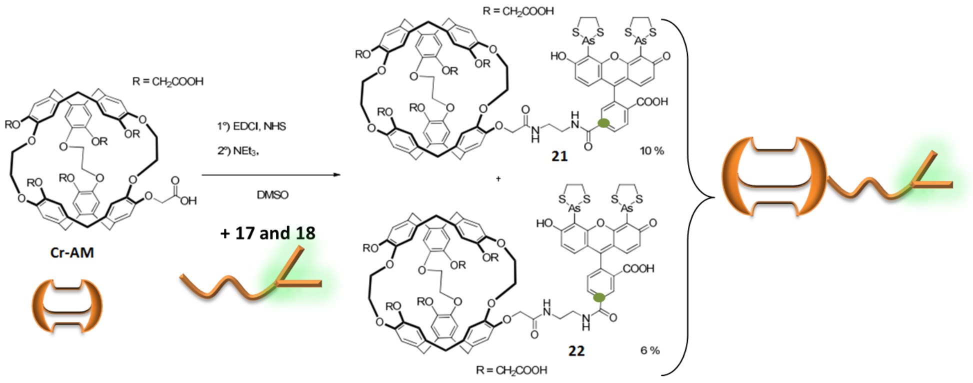
R = CH2COOH
1°) EDCI, NHS
2°) NEt3,
DMSO
+ 17 and 18
Cr-AM
21
10 %
22
6 %

Figure 69: Coupling reaction between Cr-AM and compounds **17** and **18**: synthesis of the bimodal biosensors **21** and **22**.

Starting with the enantiomeric and isomeric forms of each moiety, we obtained four different sensors, shown in Figure 70. It was unfortunately impossible to properly isolate **PP-2** due to the low yield of the reaction coupling (6%). For some experiments, the racemic mixture - **MM-1** + **PP-1** - has been employed in order to keep some precious enantiopure biosensors.

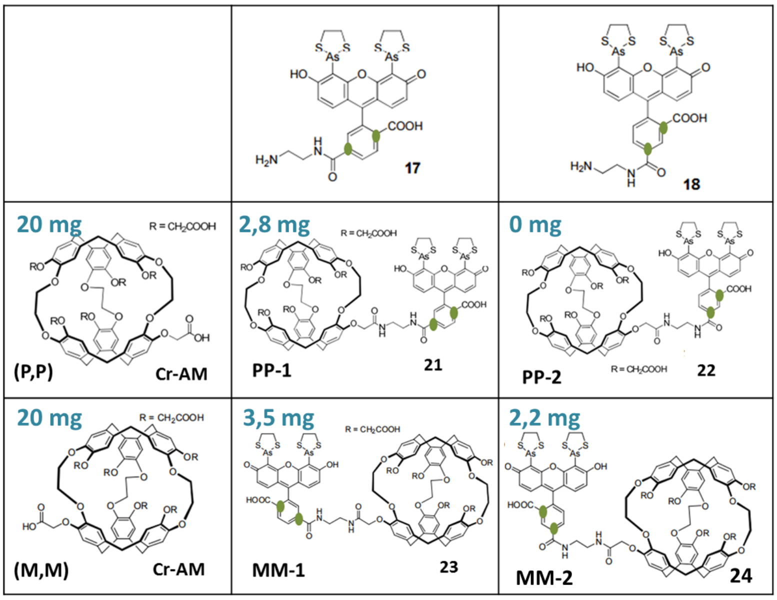

Figure 70: Structure of four different bimodal sensors

Unfortunately, we did not synthesize enough biosensor quantities to perform conformational analysis of each compound.

Even if we could read in the literature that biarsenical dyes are non fluorescent, it occurred to us that CrAsH does have a significant fluorescence when bound to two molecules of EDT. Thus, the other variants might as well have this property. We investigated the effect of the grafting of a cryptophane on the CrAsH moiety. To achieve this, we compared the fluorescence spectra of CrAsH and **MM-1** with an excitation wavelength of 480 nm. Interestingly, without peptide, **MM-1** exhibits a 4.5 times lower fluorescence than single CrAsH (Figure 71).
This initial non-fluorescent state is in favor of our approach.

Furthermore we investigated the evolution of the fluorescence of the biosensor **MM-1** in the presence of an excess of an external heavy atom such as xenon. Indeed, it was highlighted in 1966 that such nuclei can act like a stabilizer of a quencher of the singlet energy of a molecule, significantly depending on the energy of the exciting quantum.[30]
For this experiment, the glassblower of the CEA built an NMR tube

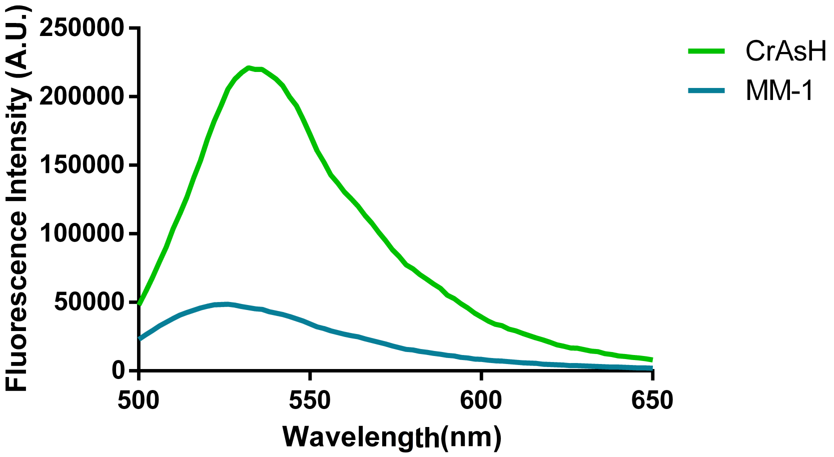

Figure 71: Comparison of the fluorescence spectra (excitation wavelength at 480 nm) of the CrAsH moiety (green) and **MM-1** (blue).

fused to a fluorescence spectroscopic cuve as seen in Figure 72A. 100 µL of biosensor **MM-1** at 2.5 µM were introduced into the "NMR tuve" (tube-cuve). Fluorescence spectrum was monitored and presented in blue in Figure 72B. 2 Bar of xenon are then added to the "NMR-tuve" and the latter is shaken. Modification of the fluorescence spectrum of the biosensor is presented in red in Figure 72B.

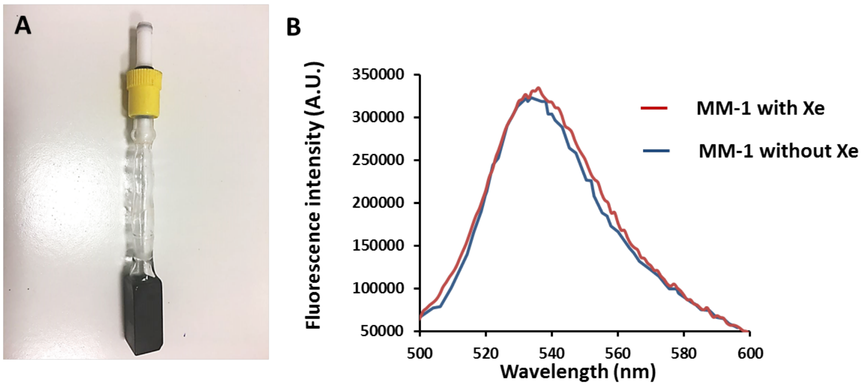

Figure 72: **A** Photograph of the "NMR-tuve". **B** Fluorescence spectra of **MM-1** (2.5 µM) with (red) and without (blue) xenon.

Probably because of a compensation between stabilization and quenching of the singlet energy of **MM-1**, xenon does not influence the fluorescence spectrum of the biosensor.

BIBLIOGRAPHY

[1] André Collet. Cyclotriveratrylenes and cryptophanes. *Tetrahedron*, 43(24):5725 – 5759, 1987.

[2] Naoko Kotera, Nawal Tassali, Estelle Léonce, Céline Boutin, Patrick Berthault, Thierry Brotin, Jean-Pierre Dutasta, Léa Delacour, Ténin Traoré, David-Alexandre Buisson, Frédéric Taran, Sylvie Coudert, and Bernard Rousseau. A sensitive zinc-activated 129Xe MRI probe. *Angewandte Chemie*, 124(17):4176–4179, 2012.

[3] Aude Bouchet, Thierry Brotin, Mathieu Linares, Dominique Cavagnat, and Thierry Buffeteau. Influence of the chemical structure of water-soluble cryptophanes on their overall chiroptical and binding properties. *The Journal of Organic Chemistry*, 76(19):7816–7825, 2011.

[4] Frank H. Johnson, Osamu Shimomura, Yo Saiga, Lewis C. Gershman, George T. Reynolds, and John R. Waters. Quantum efficiency of cypridina luminescence, with a note on that of aequorea. *Journal of Cellular and Comparative Physiology*, 60(1):85–103, 1962.

[5] Osamu Shimomura, Frank H. Johnson, and Yo Saiga. Extraction, purification and properties of aequorin, a bioluminescent protein from the luminous hydromedusan,aequorea. *Journal of Cellular and Comparative Physiology*, 59(3):223–239, jun 1962.

[6] Roger Y. Tsien. The green fluorescent protein. *Annual Review of Biochemistry*, 67(1):509–544, 1998.

[7] B. A. Griffin. Specific covalent labeling of recombinant protein molecules inside live cells. *Science*, 281(5374):269–272, jul 1998.

[8] Richard Labes. Über die pharmakologische bedeutung der chemischen reaktionen zwischen arseniger säure und thiolverbindungen. *Naunyn-Schmiedebergs Archiv für experimentelle Pathologie und Pharmakologie*, 141(3-4):148–160, 1929.

[9] J. L. Webb. *Enzyme and Metabolic Inhibitors*, volume 3. Academyc Press, New York, 1966.

[10] Martin Andresen, Rita Schmitz-Salue, and Stefan Jakobs. Short tetracysteine tags to β-tubulin demonstrate the significance of small labels for live cell imaging. *Molecular Biology of the Cell*, 15(12):5616–5622, 2004.

[11] Rekha G. Panchal, Gordon Ruthel, Tara A. Kenny, George H. Kallstrom, Douglas Lane, Shirin S. Badie, Limin Li, Sina Bavari, and M. Javad Aman. In vivo oligomerization and raft localization of Ebola virus protein VP40 during vesicular budding. *Proceedings of the National Academy of Sciences*, 100(26):15936–15941, 2003.

[12] Carsten Hoffman, Guido Gaietta, moritz Bunemann, Stephen R Adams, Silke Oberdorff-Maass, Bjorn Behr, Jean-Pierre Vilardaga, Roger Y Tsien, Mark H Ellisman, and Martin J Lohse. A FlAsH-based FRET approach to determine G protein-coupled receptor activation in living cells. *Nat Meth*, 2(3):1548–7091, 2005.

[13] Zoya Ignatova and Lila M. Gierasch. Monitoring protein stability and aggregation in vivo by real-time fluorescent labeling. *Proceedings of the National Academy of Sciences of the United States of America*, 101(2):523–528, 2004.

[14] Stephen R. Adams, Robert E. Campbell, Larry A. Gross, Brent R. Martin, Grant K. Walkup, Yong Yao, Juan Llopis, and Roger Y. Tsien. New biarsenical ligands and tetracysteine motifs for protein labeling in vitro and in vivo: Synthesis and biological applications. *Journal of the American Chemical Society*, 124(21):6063–6076, 2002.

[15] Jun Nakanishi, Takahiro Nakajima, Moritoshi Sato, Takeaki Ozawa, Kohji Tohda, and Yoshio Umezawa. Imaging of conformational changes of proteins with a new environment-sensitive fluorescent probe designed for site-specific labeling of recombinant proteins in live cells. *Analytical Chemistry*, 73(13):2920–2928, 2001.

[16] Carla C. Spagnuolo, Rudolf J. Vermeij, and Elizabeth A. Jares-Erijman. Improved photostable FREt-competent biarsenical-tetracysteine probes based on fluorinated fluoresceins. *Journal of the American Chemical Society*, 128(37):12040–12041, 2006.

[17] Haishi Cao, Yijia Xiong, Ting Wang, Baowei Chen, Thomas C. Squier, and M. Uljana Mayer. A red Cy3-based biarsenical fluorescent probe targeted to a complementary binding peptide. *Journal of the American Chemical Society*, 129(28):8672–8673, 2007.

[18] Anjan K. Bhunia and Stephen C. Miller. Labeling tetracysteine-tagged proteins with a SplAsH of color: A modular approach to bis-arsenical fluorophores. *ChemBioChem*, 8(14):1642–1645, 2007.

[19] Yuichiro Ueno, Guan-Sheng Jiao, and Kevin Burgess. Preparation of 5- and 6-carboxyfluorescein. *Synthesis*, 2004(15):2591–2593, 2004.

[20] Emilie Genin, Olivier Carion, Benoit Mahler, Benoit Dubertret, Nathalie Arhel, Pierre Charneau, Eric Doris, and Charles Mioskowski. CrAsH-Quantum dot nanohybrids for smart targeting of proteins. *Journal of the American Chemical Society*, 130(27):8596–8597, 2008.

[21] Haishi Cao, Baowei Chen, Thomas C. Squier, and M. Uljana Mayer. CrAsH: a biarsenical multi-use affinity probe with low non-specific fluorescence. *Chem. Commun.*, pages 2601–2603, 2006.

[22] Edna Kalef and Carlos Gitler. Purification of vicinal dithiol-containing proteins by arsenical-based affinity chromatography. *Methods in Enzymology*, 233:395 – 403, 1994.

[23] Meiling Lu, Hailin Wang, Xing-Fang Li, Lora L. Arnold, Samuel M. Cohen, and X. Chris Le. Binding of dimethylarsinous acid to Cys-13α of rat hemoglobin is responsible for the retention of arsenic in rat blood. *Chemical Research in Toxicology*, 20(1):27–37, 2007.

[24] V. P. Whittaker. An experimental investigation of the "ring hypothesis" of arsenical toxicity. *Biochemical Journal*, 41(1):56–62, 1947.

[25] Brent Martin, Ben Giepmans, Adams Stephen, and Roger Tsien. Mammalian cell–based optimization of the biarsenical-binding tetracysteine motif for improved fluorescence and affinity. *Nature Biotechnology*, 23(10):1308–1314, 2005.

[26] Baowei Chen, Haishi Cao, Ping Yan, M. Uljana Mayer, and Thomas C. Squier. Identification of an orthogonal peptide binding motif for biarsenical multiuse affinity probes. *Bioconjugate Chemistry*, 18(4):1259–1265, 2007.

[27] Ting Wang, Ping Yan, Thomas C. Squier, and M. Uljana Mayer. Prospecting the proteome: Identification of naturally occurring binding motifs for biarsenical probes. *ChemBioChem*, 8(16):1937–1940, 2007.

[28] Fatemeh Madani, Jesper Lind, Peter Damberg, Stephen R. Adams, Roger Y. Tsien, and Astrid O. Gräslund. Hairpin structure of a biarsenical-tetracysteine motif determined by NMR spectroscopy. *Journal of the American Chemical Society*, 131(13):4613–4615, 2009.

[29] Thomas J. Lowery, Sandra Garcia, Lana Chavez, E. Janette Ruiz, Tom Wu, Thierry Brotin, Jean-Pierre Dutasta, David S. King, Peter G. Schultz, Alex Pines, and David E. Wemmer. Optimization of xenon biosensors for detection of protein interactions. *ChemBioChem*, 7(1):65–73, 2006.

[30] V. V. Gruzinskii L. A. Barkova and M. N. Kaputerko. Quenching and stabilization of the fluorescence of anthracene vapor by xenon. *Journal of Applied Spectroscopy*, 47(2):212–215, 1987.

7

IN VITRO DUAL DETECTION OF TETRACYSTEINE PEPTIDES

Several systems of the cryptophane-CrAsH/TC-tag type have been studied via ^{129}Xe NMR and fluorescence and their properties are discussed in this chapter in order to select the best candidate for *in cellulo* detection of proteins.

7.1 EXPERIMENTAL CONDITIONS

It is important for *in vitro* experiments to adopt conditions that reproduce the *in cellulo* environment, notably the presence of endogenous proteins. Tsien *et al.* prepared for their first *in cellulo* experiments with FlAsH in 1998 a mixture consisting in:[1]

- A denaturating and especially a reducing agent triscarboxyethylphosphine (TCEP) at 1 mM.

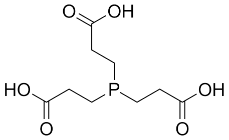

Figure 73: Triscarboxyethylphosphine (TCEP) structure.

Cysteines participating in complexation with the arsenic ligand have to be completely reduced since CrAsH moiety does not react with disulfides.

- β-mercaptoethanol at 1 mM.
  Tsien and his group observed that the complexation was more effective in the presence of 1 mM of monothiols. The latter has a low affinity for arsenoxides and appears to promote complexation with peptide by orienting the arsenic atoms in the correct position.

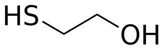

Figure 74: β-mercaptoethanol structure.

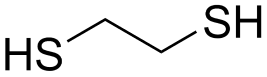

Figure 75: 1,2-Ethanedithiol structure.

- 1,2-Ethanedithiol (EDT 10 μM for 1μM of biosensor).
  Pairs of endogenous cysteines are protected by this antidote, which is in reversible exchange with thiols present on the arsenics of the ligand. Such strategy prevents non-specific complexation and the toxicity that is related to it.

In order to guarantee that the cysteines are in the thiolate form, the pH of the medium should be in the region of 7. Indeed, pKa of thiols in cysteines is 8.3. All experiments have been performed in Phosphate-Buffered Saline (PBS) solution at pH = 7.4.

7.2 STUDY OF VARIOUS DETECTION PARTNERS

All the ^{129}Xe NMR spectra were recorded using the same buffer (PBS pH = 7.4), in diluted concentration of peptides (micromolar concentrations) inducing no interaction or ionic strength modification. In fact, it has been proved during our experiments that small modification of salt concentrations -and therefore the ionic strength - can alter significantly the resonance frequency of dissolved xenon. They were all recorded in 64 scans, with a Lorentzian broadening of 10 Hz. In these conditions, the spectra were calibrated with the single peak corresponding to the free dissolved xenon into PBS at δ = 196 ppm. The spectra can then be compared to each other.

7.2.1 *Influence of the environment on the NMR response*

Due to the extreme responsiveness of xenon towards perturbation in its environment, every modification of the structure of biosensor results in new NMR properties.

We first analyzed the xenon resonance frequency of 3 of the 4 different structures of the biosensor - **MM-1** (25μM), **MM-2** (15μM), **PP-1** (8μM) (the last one **PP-2** is not pure) - in the absence of any peptide (Figure 76). We also verified through these ^{129}Xe NMR spectra that the xenon exchange in and out of the cryptophane cavity is not altered by the linker and the CrAsH moiety.

Xenon resonates at 67.1 ppm in **MM-1** and at 66.7 in **PP-1** as shown in (Figure 76A). Compounds **MM-1** and **MM-2** are both products of the same chemical reaction and due to a difficult HPLC separative technique, some traces are still remaining in both compounds. It is

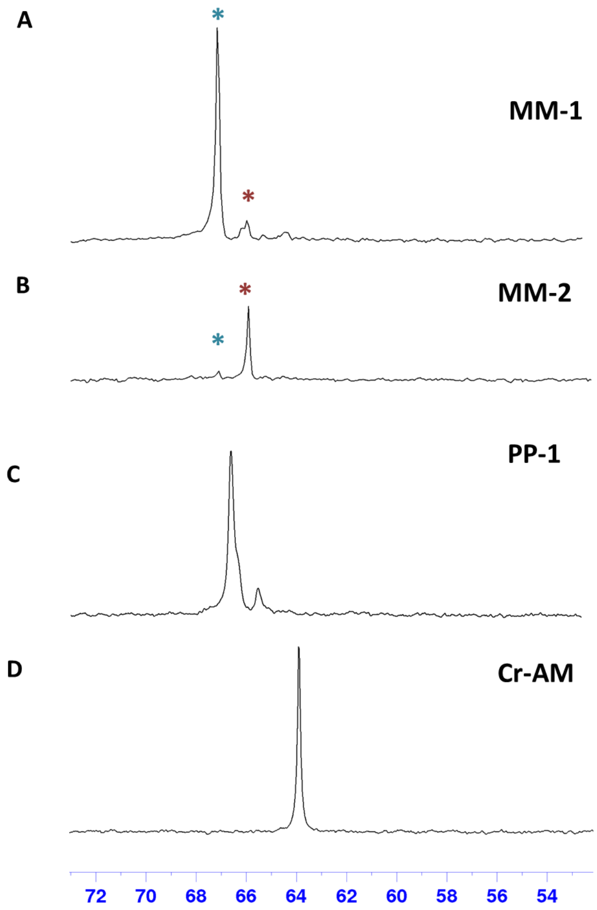

Figure 76: One-scan ^{129}Xe NMR spectra of **A. MM-1** in blue at 25 µM, **B. MM-2** in red at 15 µM, **C. PP-1** at 8 µM in the absence of peptide and **D.** Hexacarboxylate Cryptophane-A : Cr-AM at 30 µM).

confirmed by ^{129}Xe spectra in Figure 76B, where the minor peak in the **MM-1** spectrum corresponds to xenon in **MM-2** and vice versa. They are both separated by less than 1 ppm. It shows the high environment sensitivity of ^{129}Xe NMR.
The Xe@Cr-AM signal at δ = 64 ppm is displayed in Figure 76C. We verified that the biosensor is still intact and functionalized. If there was an alteration of the biosensor during the experiment, the corresponding caged xenon signal would appear at 64 ppm.

The ^{129}Xe NMR signals allow us to differienciate the 3 different biosensors but still, the signals are confined in the same frequency region.

However, when the biosensor is bound to the peptidic target, the ^{129}Xe NMR response is strongly modified (see Figure 77).

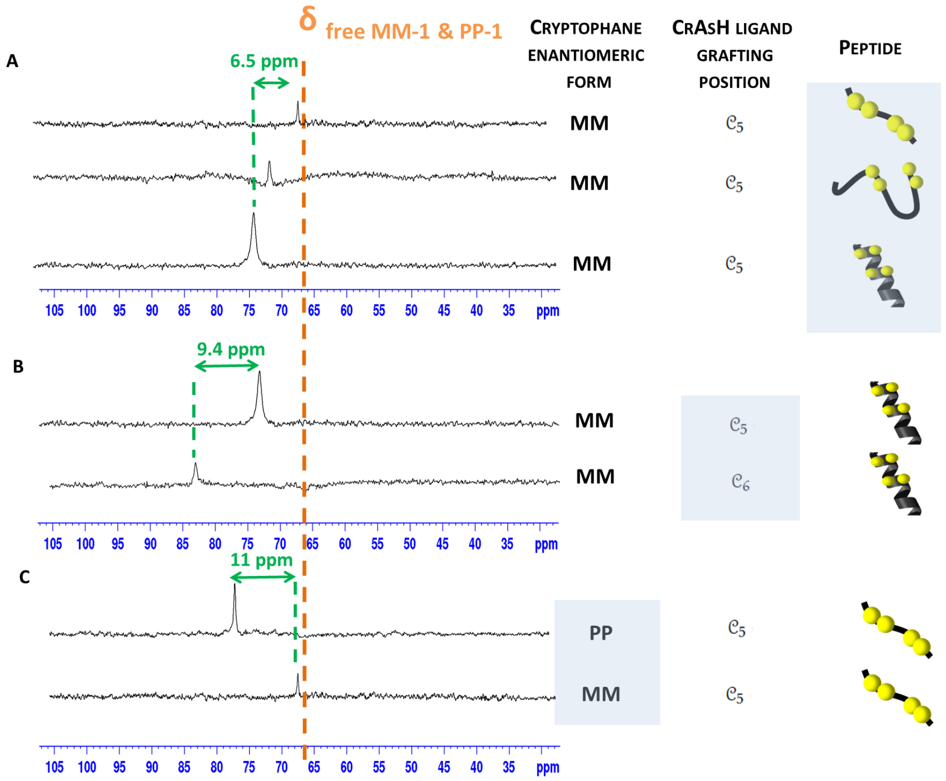

Figure 77: ^{129}Xe NMR spectra of xenon in **A. MM-1** bound to different target peptides : flexible strand (AREACCPGCCK), β-hairpin (GCCGGSGNDAGGCCGG) and α-helix peptide (WEAAAREACCRECCARA). Yellow balls represent cystein residues. **B. MM-1** and **MM-2** bound to the same target peptide. The only difference between these two structures is that cryptophane is grafted to the $\mathfrak{C}_5$ or $\mathfrak{C}_6$ of the CrAsH moiety. **C. MM-1** and **PP-1** bound to the same target peptide. These two biosensors have been synthesized from the two enantiomeric forms of the cryptophane.

The chemical shift of xenon inside the various systems of the cryptophane-CrAsH/TC-tag type are, however, spread out on a large range of ppm.

We observed that when the biosensor is bound to three differents peptides - flexible strand, β-hairpin, or α-helix peptide - encapsulated xenon exhibits a resonance frequency of δ= 67.6 ppm, δ= 71.5 ppm and δ= 74.1 ppm respectively (see Figure 77A). Even if caged xenon is distant from the peptide, a slight modification of the structure of the peptide leads to a different chemical shift of xenon. The variation of xenon chemical shift between these three peptides is 6.5 ppm.

What happens to xenon chemical shifts if the modification is closer to xenon ? We therefore underwent further investigations by comparing two biosensors bound to the same peptide but with different cryptophane anchor point $\mathcal{C}_5$ and $\mathcal{C}_6$. Grafting cryptophane moiety to the $\mathcal{C}_5$ or $\mathcal{C}_6$ of the fluorescein derivative leads to a xenon resonance frequency of δ= 74.1 ppm and δ= 83.5 ppm (see Figure 77B). This huge xenon chemical shift of 9.4 ppm could be explained by the fact that the environment modification is closer to caged xenon.

Finally, the modification position that interferes the most with xenon magnetic shielding is on the cage itself. Using one or the other enantiomeric form of the hexa-carboxylate cryptophane leads to a ^{129}Xe chemical shift of δ= 77.6 ppm for enantiomer (P;P) and δ= 67.6 ppm for enantiomer (M;M) when bound to the flexible strand (see Figure 77C). The two biosensors **PP-1** and **MM-1** detect the flexible strand by exhibiting two xenon chemical shifts different by 11 ppm.

The closer the structural modification is to xenon, the higher is the variation of the chemical shift. This phenomenon is not well understood yet. The biosensor that we have designed leads thus not only to a high detection sensitivity but also to responsiveness to peptide conformation.

Each of these modifications creates many different systems whose properties can easily be estimated and optimized, considering the position of this modification. It is then possible to choose the combination of a biosensor and a peptide - complex - for a desired resonance frequency.

It appears that all those different constructions of the biosensor become conformation sensitive while detecting their tetracysteine target, but their free form have resonance frequency confined in the same caged xenon frequency region. This localized spectral region for the free biosensor, very different from the one upon peptide binding, is a particularly crucial property for our biosensor.

7.2.2 *"RE" tetracysteine-tag*

7.2.2.1 *Fluorescence experiments*

In this experiment, 10 µM of **MM-1** with EDT (100 µM), β-mercaptoethanol (1mM) and TCEP (1mM) were illuminated in PBS at pH 7.4 at 480 nm. Then 0.1 to 10 equivalents of the RE tetracysteine-tag peptide (α-helix: WEAAAREA**CCRECC**K in Table 2) were added and fluorescence emission was monitored as displayed in Figure 78A.

Fluorescence increases 27 times upon binding "RE" tetracysteine-tag and reach its maximum at 10 equivalents (Figure 78A). Those curves reach a plateau after 50 minutes of reaction and since it re-

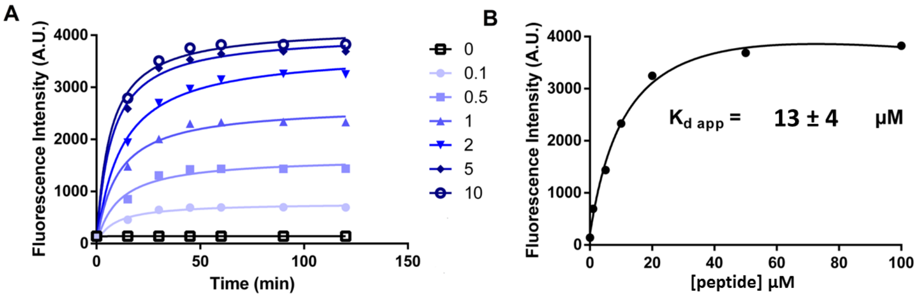

Figure 78: **A.** 0.1 to 10 equivalents of WEAAAREACCRECCARA peptide (from the brightest to the darkest blue color) were added to 10 µM **MM-1** and illuminated at 480 nm in biotek SynergyH1 Multi-Mode Plate Reader. Maxima of fluorescence intensity between λ_{em} = 505 nm and λ_{em} = 650 nm were monitored at 37°C for 90 minutes after 30 seconds of mechanical shaking in a 96-well plate. **B.** Saturation binding curve : Fluorescence intensity maxima at the end of the experiment (90 minutes) plotted against concentration of peptide. A non linear fit of specific binding was applied following the equation $Y = \frac{B_{max}X}{(K_{d\ app}+X)}$ with B_{max} the maximum specific binding, $K_{d\ app}$ the equilibrium binding constant. This fit was obtained with a correlation coefficient of 0.9945.

flects the formation of covalent bonds, fluorescence remains steady after. The apparent dissociation constant of this reaction is fitted by a saturation binding curve: $K_{d\ app}$ = 13 ± 4 µM (Figure 78B). This is slightly higher than the 4 µM binding constant corresponding to FlAsH binding to RE tetracysteine-tag described in the literature.[1] This micromolar binding constant indicates that this system can be employed for the detection of abundant proteins in live cell.
We performed the same fluorescence experiment with **MM-2** and obtained comparable results.

All these results prompted us to evaluate the biosensor **MM-1** for hyperpolarized ^{129}Xe NMR applications.

7.2.2.2 *Hyperpolarized ^{129}Xe NMR experiments*

In order to save some precious biosensor **MM-1**, a 600 µL solution of biosensor synthesized from a racemic mixture of Cr-AM (both enantiomers (M,M) and (P,P) leading to a mixture of **MM-1** and **PP-1** at 25 µM) was first prepared. This solution as well as the reducing mixture inspired by Tsien's group was added in a screw-capped NMR tube. The present ^{129}Xe NMR spectroscopy study was conducted at pH 7.4 in a phosphate buffer.
Xenon is hyperpolarized and transfered into the NMR tube as described in Section 3.3. Xe is dissolved into the degassed solution by

strongly shaking the tube. A first 90°pulse sequence is performed in 1 scan in order to see the signal of dissolved xenon, xenon gas and encapsulated xenon. (Figure 79)

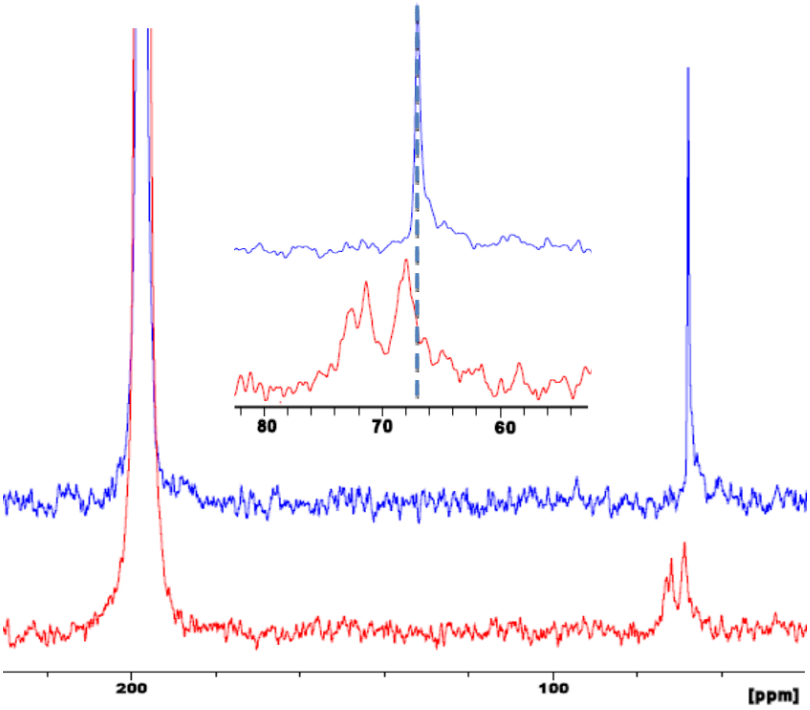

Figure 79: One-scan ^{129}Xe NMR spectrum of a racemic mixture of **MM-1** and **PP-1** (25 µM) in phosphate buffer, after a 90°impulsion sequence. Insert: sub-spectra obtained by 64 fast repetitions of the sequence soft 90°Gaussian pulse centered at 67 ppm and acquisition (inter-scan delay: 47 ms) without (blue) and with 10 equivalents of "RE" tetracysteine-tag (red).

Then, series of frequency selective pulses are performed to directly detect encapsulated xenon in its cage (sub-spectrum in Figure 79). We then added 10 equivalents of "RE" tetracysteine-tag to the sample, since it appears to be the optimal condition. We ensured that the grafting of the biosensor on the peptide did not affect the xenon encapsulation properties. All these experiments were conducted at 302K.

On both spectra, an intense xenon peak was observed at 196 ppm, corresponding to free dissolved xenon. In the absence of peptide, a single signal of xenon encapsulated in biosensors **MM-1** and **PP-1** is observed at 67.1 ppm. When 10 equivalents of peptide are added, this peak at 67.1 ppm disappears and two new massifs at 68.1 and 72.1 ppm appear. As discussed in Section 4.2.1, the presence of the two massifs could be explained by the presence of two diastereomers: a racemic mixture of biosensors is bound to an enantiopure chiral peptide. We therefore undertook synthesis of biosensors from enantiopures **(M,M)** and **(P,P)** to escape from these massifs upon complexation. We then performed the same ^{129}Xe NMR experiment with 25 µM of biosensor **MM-1** and 10 equivalents of peptide (see Figure 80).

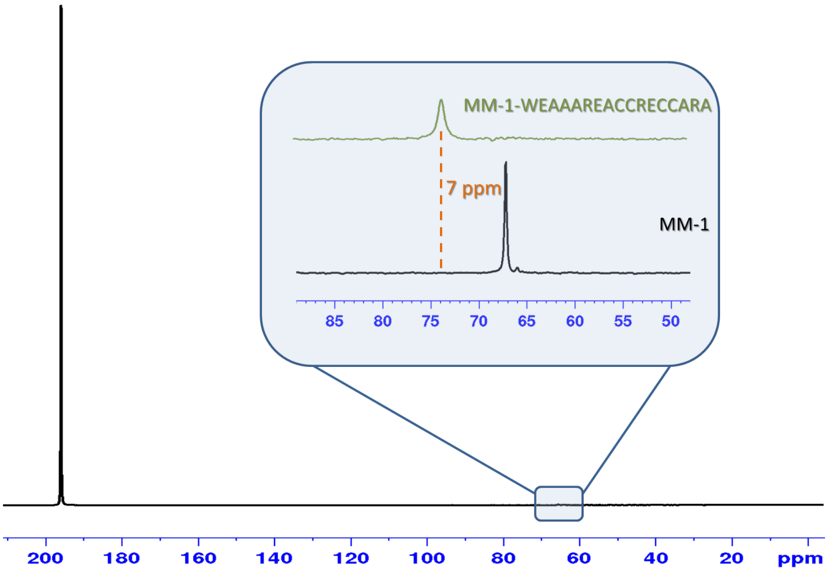

Figure 80: One-scan ^{129}Xe NMR spectrum of **MM-1** (25 µM) in phosphate buffer, after a 90°readout pulse sequence. Blue box: sub-spectra obtained by 64 fast repetitions of the sequence soft 90°Gaussian pulse centered at 67 ppm and acquisition (inter-scan delay: 47 ms) of **MM-1** without (black) and with 10 equivalents of "RE" tetracysteine-tag (green).

In the same manner as above, in the absence of the tetracysteine sequence, the ^{129}Xe NMR spectrum of **MM-1** at 302 K exhibits two distinct signals: the signal of xenon free in the buffer calibrated at δ = 196 ppm and the signal of encapsulated xenon at δ = 67.1 ppm (Figure 80). The addition of an excess of "RE" peptide to **MM-1** causes the disappearance of the signal at 67.1 ppm and leads to the appearance of a new and unique signal at δ = 74.1 ppm.
Even if the synthesis of an enantiopure biosensor is more time consuming, it strongly simplifies the spectrum.

Given the α-helix structure of the peptide and the different binding possibilities mentioned in paragraph 6.3.2.2.1, we undertook more detailed ^{129}Xe NMR studies to investigate the interactions between the biosensor and the tetracysteine tag. We therefore sequentially added 0.5, 1 and 10 equivalents of peptide on a 25 µM **MM-1** solution. It appears in Figure 81 that addition of 0.5 equivalents of peptide to **MM-1** causes the appearance of not one but two new caged xenon signals at 69.3 and 74.1 ppm.

We were not able to unambiguously determine the structure of the intermediate compounds that give the sharp signal at 69.3 ppm. Some

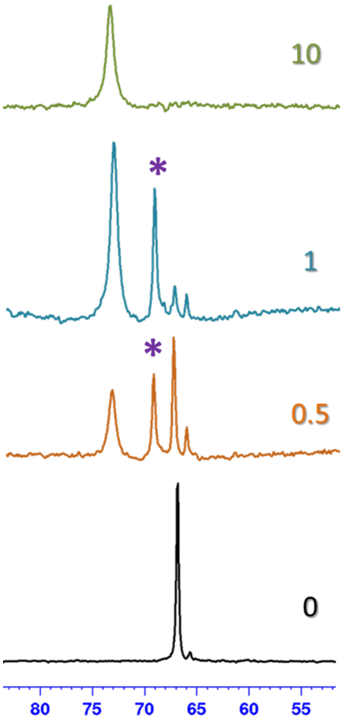

Figure 81: Sub-spectra obtained by 64 fast repetitions of the sequence soft 90°Gaussian pulse centered at 67 ppm and acquisition (inter-scan delay: 47 ms) of **MM-1** without (black) and with 0.5 (orange), 1 (blue) and 10 (green) equivalents of "RE" tetracysteine-tag.

assumptions can be made. The peak at 69.3 ppm (indicated by * in Figure 81) could be due to the transient presence of a biosensor attached to the peptide by only one arsenic atom. Its sharpness indicates that caged xenon retains sufficient mobility [2], which supports this hypothesis. It is unlikely that this signal corresponds to other pairs of arsenic bridges with the cysteines at the residue i–i + 1 and i + 4–i + 5 locations instead of the most probable situation of the i–i + 4 and i + 1–i + 5 positions, as described in paragraph 6.3.2.2.1. If such forms exist, they would rather contribute to the broadening (FWMH *ca.* 110 Hz) of the signal at 74.1 ppm.
The addition of ten equivalents of peptide enables the complete formation of the complex involving two arsenic atoms as confirmed by fluorescence.

In conclusion, the enantiopure biosensor **MM-1** exhibits a strong fluorescence signal as well as a ^{129}Xe NMR signal highly specific for caged xenon and 7 ppm different from that of the free biosensor, when bound to the "RE" tetracysteine-tagged peptide.

These results have been published : Chem. Commun., 2015, 51, 11482[3]

We extended our research to optimize our fluorogenic biosensor and fully understand its interactions.

To achieve this, we performed the same ^{129}Xe NMR experiments with 15 µM of a solution of **MM-2** (Figure 82).

10 equivalents of the same peptide were added and gave rise to a single peak at δ = 83.5 ppm and the total disappearance of the peak at δ = 66.7 ppm corresponding to free biosensor. This outstanding down-field shift of 17.2 ppm clearly demonstrates again the extreme sensitivity of xenon towards its environment and hence of our biosensor towards its target. This peak also appeared thinner (FWMH *ca.* 85 Hz) than the one arising from **MM-1**. Only one population is observed when adding 10 equivalents of peptide, attesting a reversible complexation that statistically promotes one grafting position, maybe due to the sterically hindered arsenics of this second biosensor.

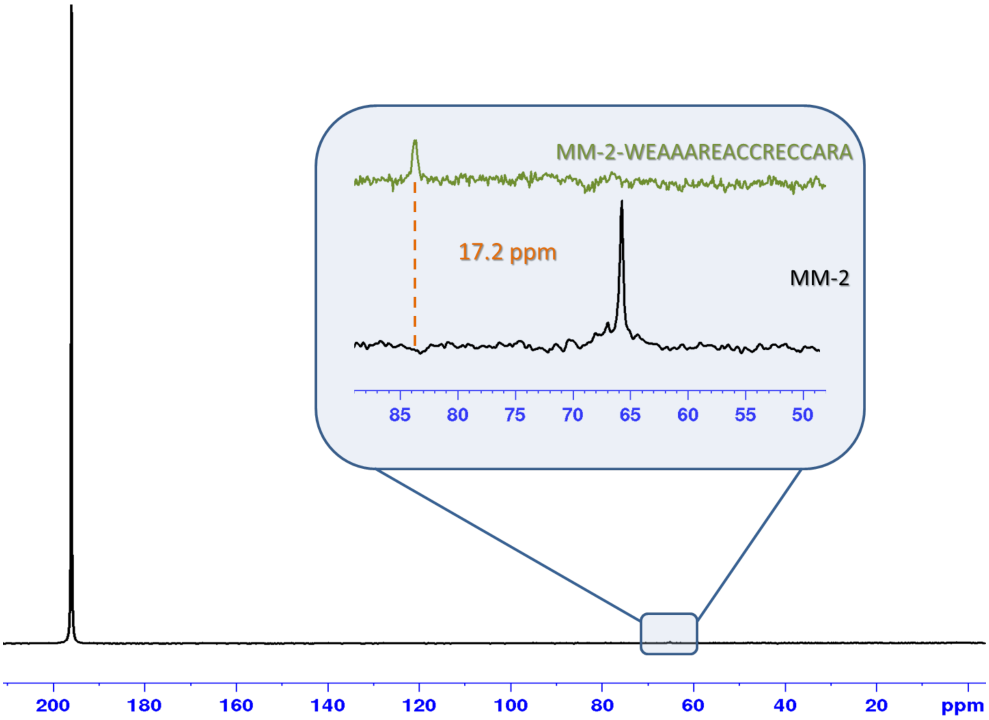

Figure 82: One-scan ^{129}Xe NMR spectrum of **MM-2** 15 µM) in phosphate buffer, after a 90°impulsion sequence. Blue box exhibits selective spectra of **MM-2** without (black) and with 10 equivalents of "RE" tetracysteine-tag (green).

The only downside of this system is the poor chemical yield of the **MM-2** synthesis (9%) that can not allow us to consider *in cellulo* experiments. We therefore need a new combination biosensor-peptide that does not include **MM-2**. Also we avoid an α-helix peptide (due to the possibility of different grafting or monoarsenical complexation) that may add more possible structures and hence signals.

7.3 FLN-PG- AND SLYD- TETRACYSTEINE TAGS

In the literature, two more peptides have drawn our attention (FLN-PG-tag and SlyD in Table 2) by their structure and sequence:

- Another PG sequence : FLN**CC**PG**CC**MEP (FLN-PG in Figure 83)
- A new generation where 9 amino acids are positioned between the two pairs of cysteins : G**CC**GGSGNDAGG**CC**GG (SlyD in Figure 83)

In order to save some precious enantiomeric cryptophane quantities, we decided to engage a sensor synthesized from the racemic mixture of the cage, leading to a combination of **MM-1** and **PP-1** (Figure 83).

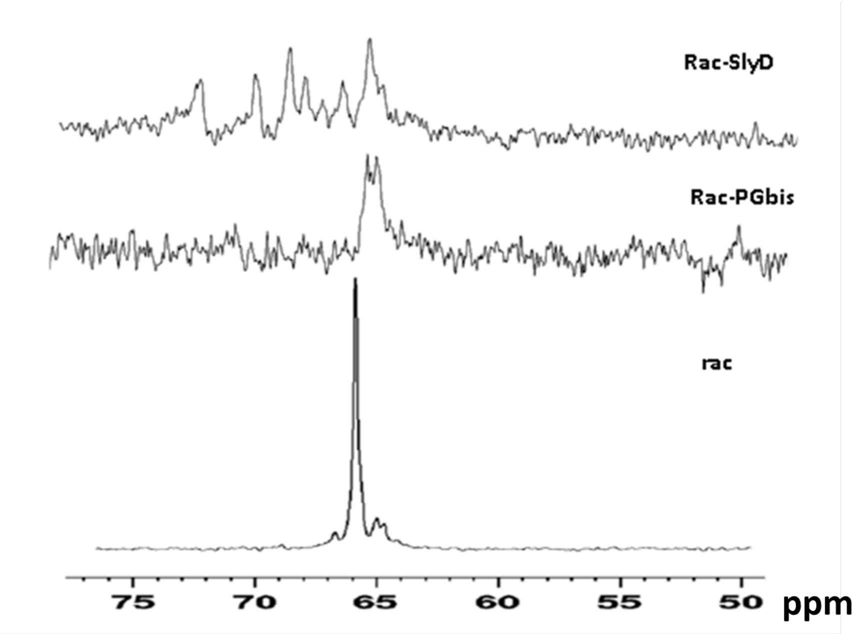

Figure 83: ^{129}Xe NMR spectra of a racemic mixture of **MM-1** and **PP-1** (25 µM) with 10 equivalents of SlyD peptide (upper spectrum) and 10 equivalents of an other FLN-PG peptide (lower spectrum).

As expected, the complexation of this racemic mixture and the tetracysteine sequences leads to multiple massifs but it is still possible to see that even if we had used an enantiopure biosensor, the resonance frequency shift would not be as high as expected. We decided to stop the experiments with these two sequences.

7.3.1 *"PG" tetracysteine-tag*

7.3.1.1 *Hyperpolarized ^{129}Xe NMR experiments*

Finally, we chose a flexible strand peptide (PG-tag in Table 2) with different amino acids surrounding the two pairs of cysteines, to perform the same experiment as described in Section 7.2.2.2. This new scenario should not involve different grafting complexes anymore. Inter-peptide complexation was nevertheless described in the literature that can be overcame by using an excess of peptide.[4]

^{129}Xe NMR spectra recorded with frequency selective pulses centered on the region of xenon encapsulated in biosensor **MM-1** are shown in Figure 84 without and with 10 equivalents of "PG" tetracysteine-tag.

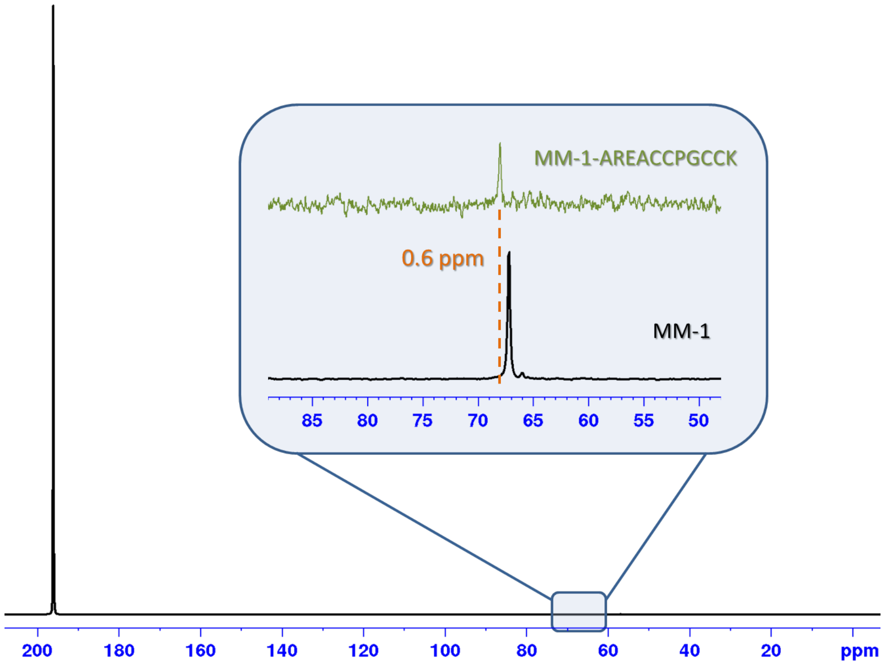

Figure 84: One-scan ^{129}Xe NMR spectrum of **MM-1** (8 µM) in phosphate buffer, after a 90°impulsion sequence. Blue box: sub-spectra obtained by 64 fast repetitions of the sequence soft 90°Gaussian pulse centered at 67 ppm and acquisition (inter-scan delay: 93 ms) of **MM-1** without (black) and with 10 equivalents of "PG" tetracysteine-tag (green)

Surprisingly, the signal of encapsulated xenon only shifts by 0.6 ppm, which renders difficult any further study.

We therefore decided to conduct the same experiment with the other enantiomeric form of the cryptophane: **PP-1**. ^{129}Xe NMR spectra with and without 10 equivalents of "PG" tetracysteine-tag are shown in Figure 85.

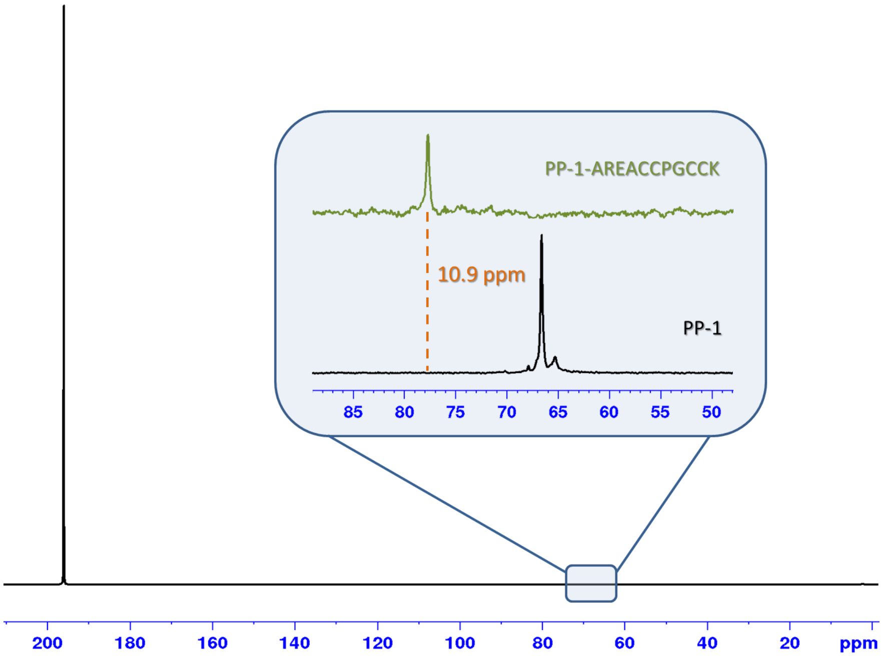

Figure 85: One-scan ^{129}Xe NMR spectrum of **PP-1** (8 μM) in phosphate buffer, after a 90°impulsion sequence. Blue box: sub-spectra obtained by 32 fast repetitions of the sequence soft 90°Gaussian pulse centered at 67 ppm and acquisition (inter-scan delay: 93 ms) of **PP-1** without (black) and with 10 equivalents of "PG" tetracysteine-tag (green).

Using the **PP-1** form of the cage, we observed a huge down-field shift of 10.9 ppm. Furthermore, the peak at $\delta = 77.6$ ppm is clearly thinner (FWMH *ca.* 50 Hz) than the previous signals obtained with **MM-1** and **MM-2** with RE peptide, supporting once again our hypothesis on multiple grafting configurations broadening the signal: in this case, only one grafting position is promoted. Let us not forget that the goal of this sensor is to detect proteins inside the cells, significantly broadening and complicating the signal. For this reason, it is crucial to get a sharp and unique signal in these *in vitro* experiments.

Finally, this 10.9 ppm chemical shift is an excellent settlement between the chemical shifts obtained for **MM-1-RE tetracysteine-tag** (7 ppm) and the **MM-2-RE tetracysteine-tag** (17.2 ppm) signals. Since **PP-1** is easier to synthesize (better production yield) than **MM-2**, the combination of **PP-1** and PG-peptide is the best candidate for further applications.

7.3.1.2 *Fluorescence experiments*

Once we proved that this combination was our best candidate, fluorescence properties were explored. Thus, we performed the same experiment as described in Section 7.2.2.1, using **PP-1** at 10 µM. 0.1 to 10 equivalents of peptide AREA**CCPGCC**K were added and fluorescence emission of the product was monitored. The maximum fluorescence intensities of each condition plotted against time are displayed in Figure 86A.

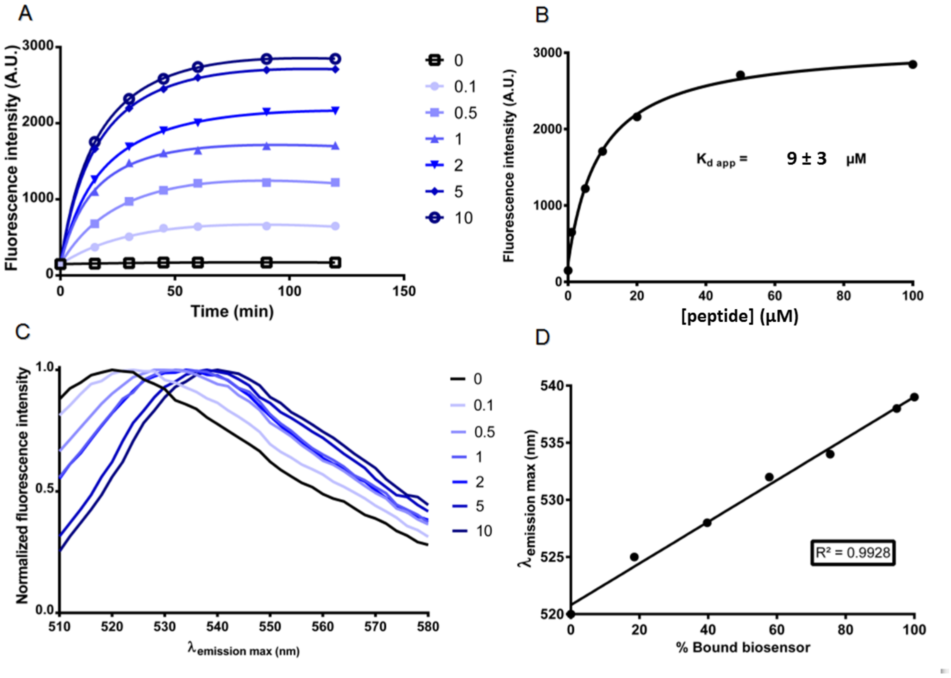

Figure 86: **A.** 0.1 to 10 equivalents of AREACCPGCCK peptide (from the brightest to the darkest blue color) were added to 10 µM **PP-1** and illuminated at 480 nm. The fluorescence intensity maxima were monitored and reported at 37°C for 90 minutes after 30 seconds of mechanical shaking in a 96-well plate between λ_{em} = 510 nm and λ_{em} = 650 nm. **B.** Saturation binding spectrum : Fluorescence intensity maxima at the end of the experiment (90 minutes) plotted against concentration of peptide. The same non linear specific binding fit was employed here with a correlation coefficient of 0.9989. **C.** Evolution of the emission wavelength of normalized fluorescence spectra under addition of equivalents of peptide. **D.** Relation between the wavelength of the maximum fluorescence emission the and proportion of bound biosensors.

As shown in Figure 86A fluorescence increases 19 times upon binding to the peptide bearing the PG tetracysteine-tag. Although smaller than for the "RE" construction (27 times more fluorescent upon binding), this fluorescence enhancement is still remarkable. It also has comparable affinity for the tetracysteine-tag with $K_{d\ app}$ = 9 ± 3 µM (Figure 86B).

We further investigated the evolution of the fluorescence emission band upon addition of the peptide to **PP-1** in Figure 86C. The shape and the wavelength of the maximal fluorescence depend on the fraction of bound **PP-1**. Indeed, when we added a few equivalents of peptide, three populations coexisted as discussed at the end of Section 8.3.2.2 :

- free **PP-1** (whose emission wavelength is centered at 520 nm)
- **PP-1-peptide** (whose emission wavelength is centered at 540 nm)
- intermediate structures between 1 and 2 equivalents (free **PP-1**, **PP-1-peptide**, mono arsenical complexes, complexation inter-peptide etc)

First, the shape widens due to the simultaneous presence of these 3 populations. The shifts depend on the proportion of **PP-1-peptide**. When there is a significant excess of peptide, intermediate structures disappear and the final population is homogeneous. This induces a sharpening of the fluorescence emission spectrum. Since we have a very thin peak at 10 equivalents of peptide, we hypothesized that only one population was present. We estimated that this population must be the complex biosensor-peptide. We therefore made the assumption of a complete binding where 100% of the biosensor **PP-1** is bound to the tetracysteine tag. Knowing that the amount of bound molecules is proportional to the fluorescence, Figure 86A allows us to determine the proportion of bound **PP-1** for each condition. We plotted the wavelength of the maximum of fluorescence intensity against this apparent ratio **PP-1**-peptide/**PP-1** in Figure 86D. The linear function fitted with a correlation coefficient of 0.9928 proves that more than being a fluorescent sensor that can be switched on, the fluorescence intensity indicates the proportion of bound biosensor.

This new partnership **PP-1**-AREACCPGCCK has similar kinetic and fluorescence properties as the "RE" tag recently published by Kotera *et al.*[3] However its ^{129}Xe NMR properties are more interesting and for that reason, we chose to expand this system for *in cellulo* protein detection.

7.4 CONCLUSION

We proved that combining the CrAsH moiety to the cryptophane slightly altered the CrAsH dissociation binding constant and its ability to fluoresce. Indeed, $K_{d\ app}^{CrAsH-PG}$ = 0.4 µM while $K_{d\ app}^{\mathbf{PP\text{-}1}-PG}$ = 9 μM and the fluorescence multiplication is only *ca.* 20 instead of ZZ. Nevertheless, our sensors still remain highly specific considering that the dissociation constant for endogenous thiols is in millimolar range. Also a factor 20 in the fluorescence increase upon binding is sufficient since the initial states of our (unbound) biosensors have a far lower fluorescence than CrAsH.

For the use of smart ^{129}Xe NMR-based biosensors, the PG-peptide is better than the RE-peptide.

We succeeded to design a biosensor that presents also a net change in frequency for encapsulated xenon in the presence of the biological target and hence allows a further gain in sensitivity, even in low or inhomogeneous magnetic fields such as those encountered in MRI.

Finally, we successfully synthesized and described smart biosensors with dual properties and capacity to detect tetracysteine-tagged peptides. The extension to recombinant proteins will now be assessed.

BIBLIOGRAPHY

[1] B. A. Griffin. Specific covalent labeling of recombinant protein molecules inside live cells. *Science*, 281(5374):269–272, jul 1998.

[2] Thomas J. Lowery, Sandra Garcia, Lana Chavez, E. Janette Ruiz, Tom Wu, Thierry Brotin, Jean-Pierre Dutasta, David S. King, Peter G. Schultz, Alex Pines, and David E. Wemmer. Optimization of xenon biosensors for detection of protein interactions. *ChemBioChem*, 7(1):65–73, 2006.

[3] N. Kotera, E. Dubost, G. Milanole, E. Doris, E. Gravel, N. Arhel, T. Brotin, J.-P. Dutasta, J. Cochrane, E. Mari, C. Boutin, E. Leonce, P. Berthault, and B. Rousseau. A doubly responsive probe for the detection of Cys4-tagged proteins. *Chem. Commun.*, 51:11482–11484, 2015.

[4] Ting Wang, Ping Yan, Thomas C. Squier, and M. Uljana Mayer. Prospecting the proteome: Identification of naturally occurring binding motifs for biarsenical probes. *ChemBioChem*, 8(16):1937–1940, 2007.

8

IN VITRO DUAL DETECTION OF TETRACYSTEINE-TAGGED PROTEINS

8.1 CONCEPTION OF A TAGGED-PROTEIN

For this proof of concept we needed a well-known protein, readily expressed and purified in large quantities and largely expressed in mammalian cells (µM range). We decided to use a fluorescent protein from the GFP family. The engineering of these proteins is widely documented, and the Orsay's laboratory owns a real know-how. Furthermore having a tetracysteine-tagged fluorescent protein greatly simplifies its in cell detection by fluorescence. In addition, concentration of fluorescent proteins expressed in mammalian cells is in the micromolar range, corresponding to the $K_{d\ app}$ value of the interaction between PP-1 and the peptide. And last but not least, using a fluorescent protein as a target protein, enables Förster resonance energy transfer (FRET) between the protein and the CrAsH moiety as described for FlAsH and ECFP by Tsien *et. al.*[1]

8.1.1 *Förster resonance energy transfer: Conditions*

Fluorescence is, together with phosphorescence, a luminescence phenomenon. The excitation is initiated by absorption of a photon. The relaxation from the excited state happens via radiative and non-radiative processes - internal conversion, vibrational relaxation, intersystem conversion, phosphorescence and fluorescence. FRET is an additional de-excitation pathway. It denotes the energy transfer via long-range dipole-dipole transition between a so-called donor fluorophore and an acceptor fluorophore.

To form a good couple of fluorophores for FRET, it is necessary to have a donor and a energy acceptor with optimal optical and physical properties:

- It can only take place when the donor emission spectrum overlaps with the acceptor excitation spectrum.
- The distance R between the fluorophores has to be small, usually below 10 nm.
- The spatial orientation of the fluorophores towards each other must be favourable.

It is possible to evaluate the FRET efficacy defined as (6). E depends on the donor-to-acceptor separation distance R with an inverse 6th-power law due the dipole-dipole coupling mechanism.

$$E = \frac{1}{1 + (\frac{R}{R_0})^6} \tag{6}$$

With R_0 being the Förster distance of the pair of donor-acceptor, or the distance at which the energy transfer efficiency is 50% and defined as (7) :

$$R_0 = (10^{-3} \kappa^2 \eta^{-4} QY\ J)^{1/6} * 9730 \tag{7}$$

with η the refractive index of the medium, QY the fluorescence quantum yield of the donor in the absence of the acceptor, J the spectral overlap integral and κ^2 the dipole orientation factor which is a function of the relative orientation of the donor and acceptor dipoles.

A fluorophore can be described by several parameters and one the most important is the fluorescence quantum yield (QY), that gives the efficiency of the fluorescence process. It is defined as the ratio of the number of photons emitted to the number of photons absorbed, as seen in (8).

$$QY = \frac{photons\ emitted}{photons\ absorbed} \tag{8}$$

The QY of a fluorophore can also be determined relative to a reference compound of known QY. If the same excitation wavelength, gain and slit bandwidths are applied for the two samples then the QY is calculated as seen in (9) where QY_{ref} is the quantum yield of the reference compound, η is the refractive index of the solvent, I is the integrated fluorescence intensity and A is the absorbance at the excitation wavelength.[2]

$$QY = QY_{ref} \frac{\eta^2}{\eta_{ref}^2} \frac{I(\lambda)}{A(\lambda)} \frac{A_{ref}(\lambda)}{I_{ref}(\lambda)} \tag{9}$$

When both dyes are freely rotating and can be considered to be isotropically oriented during the excited state lifetime, the average κ^2 is 2/3. This condition is generally satisfied for the fluorophores attached to biomolecules because they can have a certain freedom of rotation.[3] Note that this dynamic average assumption is not appropriate for fluorescent proteins because they do not undergo much rotational diffusion (≈15–20 ns) during the short excited state lifetime (≈5 ns) because of their relatively large molecular weights (27 kDa).

For FRET detection, absorption spectra of the donor and the acceptor must be sufficiently separated so that the acceptor is not excited directly by the donor excitation light source. In addition, the acceptor must emit at wavelengths where donor has no emission. This corresponds to spectral selectivity, or spectral leak.

8.1.2 *Two strategies for the tagged-protein construction*

Since there is no tabulation of force fields for cryptophanes, semi-empirical simulations are not an option to describe the molecular system. The good position of the tetracysteine tag (TC), the correct distance and orientation with respect to the fluorescent protein barrel cannot be calculated by docking experiments.
Moreover, even if we could understand the phenomenon of ^{129}Xe chemical shift variation upon binding of the biosensor on a peptidic motif, we are unable to predict the value of this variation according to the tagged-protein system. The flexibility, the position of the TC and its distance to the barrel could interfere with our detection scheme and then have an impact on the ^{129}Xe signal. For this reason, we designed five constructions presenting different lengths of spacer and different locations of the tetracysteine tag.

The three constructions that have been created are:

Aquamarine: T65S and H148G Mutant of Cyan Fluorescent Protein

- Construction I : Histag-Aquamarine-Tetracysteine tag (Figure 87A)
- Construction II : Histag-Tetracysteine tag-Aquamarine (Figure 87B)
- Construction III : Histag-Tetracysteine tag-Linker-Aquamarine (Figure 87C)

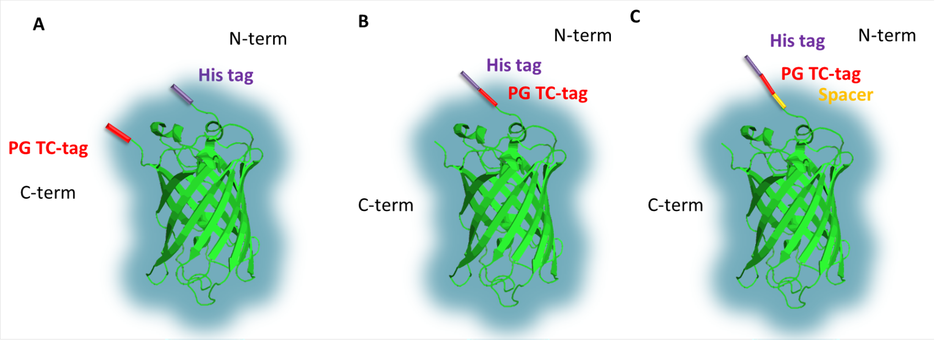

Figure 87: **A.** Construction I with the tetracysteine tag at the C-term of Aquamarine. **B.** Construction II with the tetracysteine tag at the N- term of Aquamarine. **C.** Construction III with the tetracysteine tag at the N-term of the Aquamarine separated by a 17-aminoacid spacer.

The Histag is designed to allow purification of the recombinant protein.

Two strategies have been employed for these constructions, either having the fluorescent protein as the donor(D) or as the acceptor (A).

8.1.2.1 *Fluorescent protein (D) - Biosensor (A)*

The first configuration consists in a fluorescent protein as the donor and **PP-1** as the acceptor. One appropriate fluorescent protein would be a cyan fluorescent protein variant named Aquamarine.[4]

It should be noted that Aquamarine has 2 cysteines in its sequence, but they are not accessible and too far to form an heterocycle with an arsenic atom.

Figure 88 displays the normalized absorption and emission spectra of the construction I (as an example). The overlap integral J is shown in pale red. Due to the high spectral overlap, the optimal excitation wavelengths for both fluorophores were chosen at 405 nm and 480 nm and are marked with grey lines.

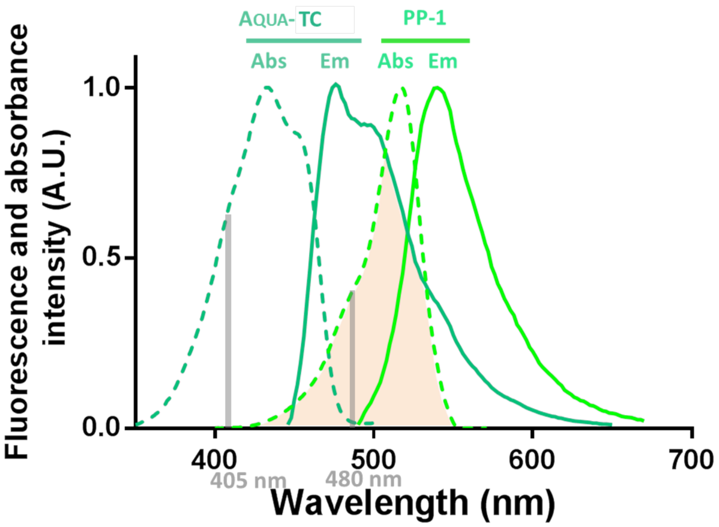

Figure 88: Normalized absorption (dotted lines) and emission spectra (solid lines) of Histag-Aquamarine-tetracysteine tag (in cyan) and **PP1** (in green). This system is excited at λ = 405 nm, which corresponds to the half-maximum of fluorescent protein absorption. Overlap between donor emission and acceptor absorption is drawn in pale red.

These spectra prove that the overlap condition of FRET is verified. In addition, the fact that both donor and acceptor are covalently linked together induces a short distance between both entities, less than 10 nm. Finally, the flexibility of the construct allows a whole set of orientations between the PG TC-tag and the fluorescent protein and ensure the spatial orientation condition κ^2. All conditions have been met to observe a resonance energy transfer with these three constructions.

8.1.2.2 *Biosensor (D) - Fluorescent protein (A)*

Another strategy consists in choosing **PP-1** as the donor and the fluorescent protein as the acceptor. In this configuration, a good candidate for the fluorescent protein is the red fluorescent protein mCherry. mCherry derives from a protein isolated from the coral *Discosoma sp.*. This is a monomeric fluorescent construct with the same shape (barrel) but a different amino acid sequence that confers a different stability. There is no cysteine in its sequence. We have designed two more tagged proteins, based on the same approach than for constructions II and III:

- Construction IV: Histag-Tetracysteine tag-mCherry (Figure 89A)
- Construction V: Histag-Tetracysteine tag-Linker-mCherry (Figure 89B)

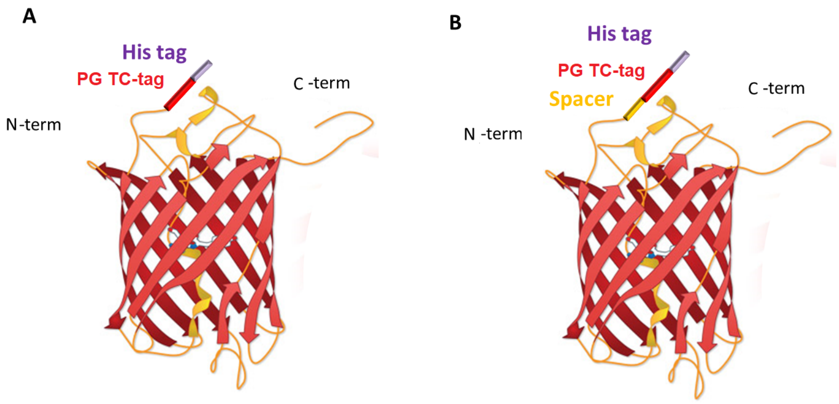

Figure 89: **A.** Construction IV with the tetracysteine tag at the NH_2 terminal part of mCherry. **B.** Construction V with the tetracysteine tag at the NH_2 terminal part of mCherry separated by 17 aminoacids.

Absorption and fluorescence emission spectra of **PP-1** and tagged-mCherry prove that they are potentially good partners for FRET (Figure 90).

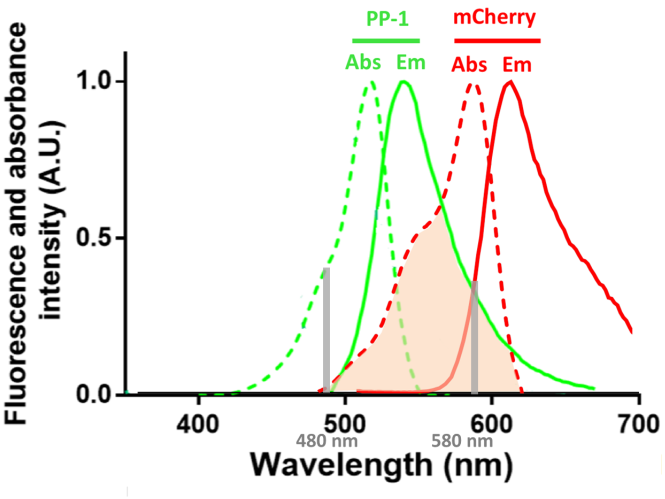

Figure 90: Normalized absorption (dotted lines) and emission spectra (solid lines) of Histag-Tetracysteine tag-mCherry (in red) and **PP1** (in green). This system is excited at λ = 480 nm, which corresponds to the half-maximum of fluorescent protein absorption. Overlap between donor emission and acceptor absorption is drawn in pale red.

8.1.3 *Direct consequences on the ^{129}Xe NMR and fluorescence signals*

Detection of the tetracystein-tagged protein can therefore be now monitored by:

- The chemical shift of encapsulated xenon (Figure 91B).
- The direct fluorescence detection of CrAsH moiety upon interaction with the tetracysteine tag (as seen in Figure 91B). The fluorescence intensity increases and its maximum is shifted to higher wavelengths.
- The direct consequences of FRET:
  - Decrease of the fluorescence intensity of the donor and increase of the fluorescence intensity of the acceptor upon excitation of the donor.

    The concept is described for construction I in Figure 91.

    It is possible to evaluate the FRET efficiency defined as (10) where F'_D and F_D are the integrals of the fluorescence spectrum of the donor with and without the acceptor.

$$E = 1 - \frac{F'_D}{F_D} x100 \tag{10}$$

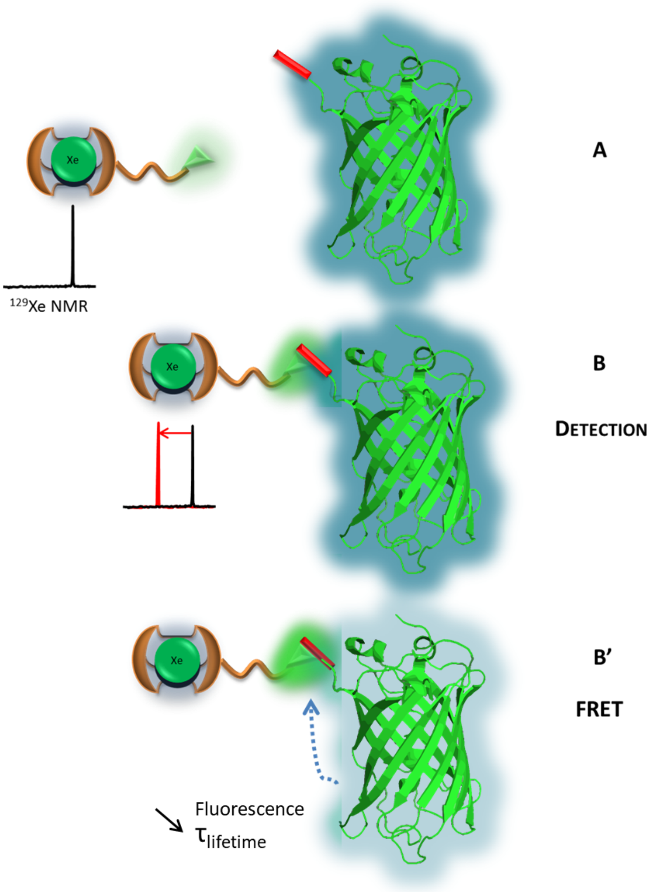

Figure 91: Principle of the functioning of the biosensor with construction I (Histag-Aquamarine-TC). **A.** Free **PP-1** gives rise to the original encapsulated xenon chemical shift and a very low fluorescence. **B. PP-1** bound to TC-tag of construction I gives rise to a chemical shift variaton for encapsulated xenon and a fluorescence increase. **B'.** The same molecular construct gives rise to Förster Resonance Energy Transfer from the fluorescent protein to **PP-1**, diminishing the fluorescence signal and lifetime of the protein and increasing the fluorescence of **PP-1**.

This equation can be applied for constructions I, II and III when the modification of the fluorescence intensity of the donor is only resulting from the FRET phenomenon.
For constructions IV and V, the donor is also the ligand that is turned on upon reaction with the tetracysteine tag. The fluorescence of the donor increases upon complexation to the tetracysteine tag but is also modulated by FRET. We can not evaluated the FRET efficiency by comparing the fluorescence emission spectra of the donor with and without acceptor as in (10). However it is possible to measure

energy transfer from acceptor emission, following (11):[5]

$$E = \frac{I_{AD}A_{AA} - I_{AA}A_{AD}}{I_{AA}A_{DD}} x100 \tag{11}$$

where I_{AD} is the acceptor intensity following the donor excitation, I_{AA} is the acceptor intensity following the acceptor excitation, A_{AA} is the acceptor absorbance at the acceptor excitation wavelength, and A_{AD} and A_{DD} are the acceptor and donor absorbances, respectively, at the donor excitation wavelength. To achieve this, we need the fluorescence intensity and the absorbance of the tagged-protein at wavelength where the acceptor does not absorb.

- Decrease of the donor fluorescence lifetime.

It is also possible to evaluate the FRET efficiency using the lifetime of the donor that decreases in the presence of FRET. The decrease of the donor fluorescence lifetime can be measured by fluorescence lifetime imaging microscopy (FLIM). When excited by a photon, the fluorescent sample - the biosensor attached to construction I, II, III, IV or V - will return to the ground state with a certain probability based on the decay rates through a number of different radiative or non radiative pathways including FRET. To observe fluorescence, one of these pathways must be by the spontaneous emission of a photon. The emitted fluorescence will decay with time according to (12), where I_D^0 is the initial fluorescence, t the time , C a constant background and τ_D, fluorescence lifetime.

$$I_D(t) = I_D^0 e^{-t/\tau_D} + C \tag{12}$$

The fluorescence lifetime of a fluorophore affected by FRET tends to decrease as an additional de-excitation pathway is added. Therefore the fluorescence curve decay is described by a biexponential fit function(13). α_{long} and α_{short} correspond to the proportion of free and bound donor, τ_D and τ_{DA} correspond to the fluorescence lifetimes of the donor and the donor bound to the acceptor respectively.

$$I_{DA}(t) = I^0(\alpha_{long}e^{-t/\tau_D} + \alpha_{short}e^{-t/\tau_{DA}}) + C \tag{13}$$

More than attesting a fluorescence resonance energy transfer between two fluorophores, FRET-FLIM experiments allow one to determine the fraction of molecules with short lifetime compared to molecules with long lifetime. The mean fluorescence lifetime τ_{mean}

of the sample is thus defined.

FRET efficiency E is the ratio of the number of times the excited donor returns to the ground state by transferring energy to the number of times the excited molecules returns to the ground state by any process. In terms of the lifetimes of the donor, this is (14):[6]

$$E = \frac{\tau_D - \tau_{DA}}{\tau_D} x100 = 1 - \frac{\tau_{DA}}{\tau_D} x100 \tag{14}$$

where τ_D and τ_{DA} are the fluorescence lifetimes of the donor and of the donor in the presence of the acceptor.

8.2 PLASMID CONSTRUCTION AND PURIFICATION

The full procedure aims at the modification of the protein of interest by insertion of a tetracysteine site.

To genetically encode the tetracysteine motif (TC), we employed 3 strategies.

- For the construction I, we designed a codon sequence where the tetracysteine tag starts right after the COOH-terminus of the Aquamarine sequence as shown in Figure 123A (in Appendix A).[1] This choice was motivated by the experimental procedure of FRET experiments conducted by Griffin *et. al.* in 1998.

- For the constructions II and III, we designed a sequence where the tetracysteine tag starts after a 17-amino acid spacer (TFGSFTDVMSTGTGSTG) at the NH_2-terminus of the Aquamarine sequence (construction III). We introduced the same restriction sites before and after the spacer that allowed us to remove the latter by a simple digestion. We then obtained the short version: construction II.

  In these constructions, the tetracysteine tag was fused between the histag and the fluorescent protein, in such a way that all fluorescent proteins after purification necessarily contain the tetracysteine tag (Figure 87B and C).

- We proceeded the same way for constructions IV and V, with mCherry fluorescent protein. We obtained the long (construction V) and the short (IV) version of TC tagged mCherry (Figure 89A and B) .

Thanks to the polyhistidine-tag, the constructions were expressed in TOP10 bacteria and purified on a nickel-nitriloacetic acid agarose (Ni–NTA) column. A brief description of the protocol of the plasmid construction and the purification can be found in Section A.1.5.4.

UV-Vis absorption spectra of these 5 constructions were measured in Figure 92.

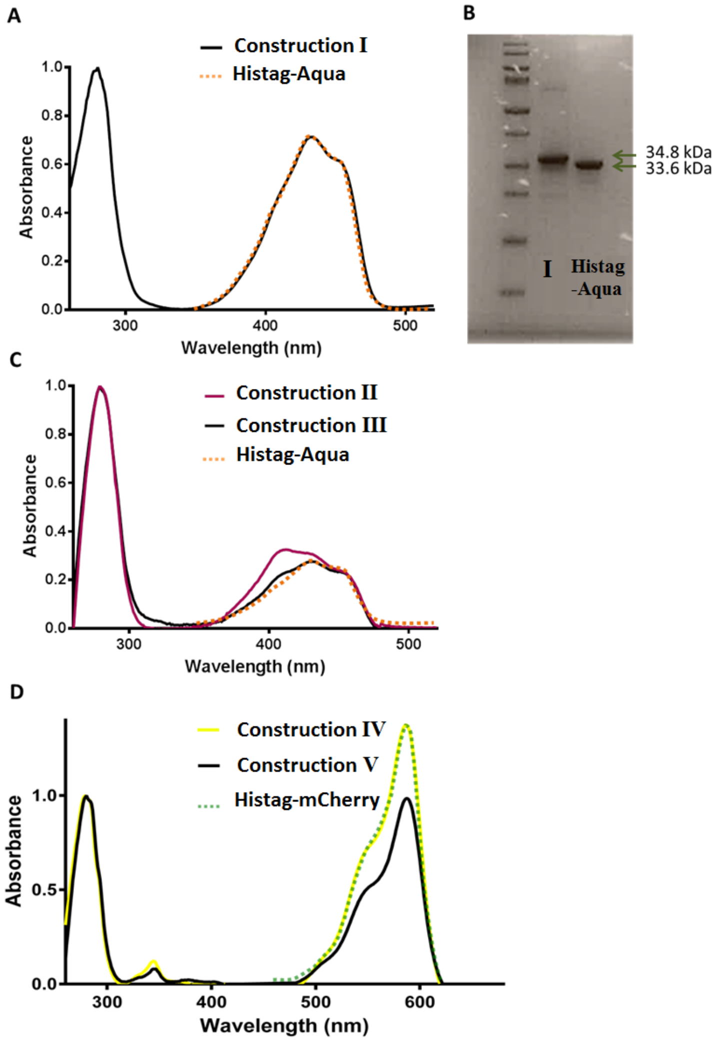

Figure 92: UV-Vis absorption spectrum of **A.** Histag-Aquamarine-tetracysteine tag (in black) with a maximum absorbance at 430 nm. **C.** Histag-tetracysteine tag-Aquamarine (in purple) and Histag-tetracysteine tag-Linker-Aquamarine (in black). The orange dotted line represents the shape of the UV-Vis absorption spectrum of the native Aquamarine, serving as a reference for the double band. **D.** Histag-tetracysteine tag-mCherry (in yellow) and Histag-tetracysteine tag-Linker-mCherry (in black). The maximum absorbance is at 560 nm. The green dotted line represents the UV-Vis absorption spectrum of the native mCherry. **B.** Polyacrilamide gel electrophoresis of both TC-tagged Aquamarine and Aquamarine, the first column being the molecular weight marker.

The absorption spectrum of the fluorescent proteins consists in two bands. The first band (280 nm) corresponds to the absorption of aromatic residues present in the fluorescent protein, principally tryptophane and tyrosine and also a minor contribution of the chromophore when the protein is mature. The second band (430 nm for Aquamarine and 560 for mCherry) is due to absorption of the mature chromophore. Measuring the ratio between absorption at 280 nm and 430 nm (or 560 nm) gives information about protein maturation.

UV-Vis absorption spectra of native Aquamarine and TC tagged Aquamarine are similar. We obtained a ratio of $\frac{A_{280nm}}{A_{430nm}} = 1.40$ for Aquamarine and 1.3 for construction I.[7] Fusing the tetracystein tag on the COOH-terminal part of the fluorescent protein did not interfere with its bacterial expression and maturation.

A Sodium dodecyl sulfate polyacrylamide gel electrophoresis (SDS-PAGE) shows the respective weights of native Aquamarine and Aquamarine fused to the tetracystein tag (Figure 92B). We calculated using a routine in ImageJ software, that Histag-Aquamarine-tetracysteine tag was 94% pure. The molecular weight of the TC tagged-protein is slightly higher than the protein itself, as expected.

The shape of the absorption spectrum of constructions II and III are different from the native Aquamarine. Indeed curves are shouldered at 420 nm (Figure 92C). It is characteristic of a denatured fluorescent protein. In addition, constructions II and III have a very low proportion of mature proteins as shown by their $\frac{A_{280}}{A_{430}}$ ratios that are respectively 3.1 and 3.6 (against 1.40 for the native fluorescent protein Aquamarine).

Fusion of the tetracysteine tag at the C-terminal part of the Aquamarine seems to alter the folding and the maturation of the protein.

Finally, absorption spectra of both constructions VI and V are very similar to the absorption spectrum of the reference, native mCherry. Furthermore, maturation rates determined by the ratio $\frac{A_{280}}{A_{560}}$ are 0.7 for construction IV and 1 for construction V against 0.7 for native mCherry. If maturation of construction V seems to be slightly altered by the linker, we proved that properties of the Histag-Tetracysteine tag-mCherry are equivalent to the ones of native mCherry.

For QY calculation ((9)), we took Aquamarine as a reference, $QY_{ref} = QY_{Aquamarine} = 0.89$. We measured the absorbance corresponding to $\lambda = \lambda_{exc}$ and the area under the curve of the fluorescence emission spectra of Aquamarine and construction I. We found $QY_I = 0.91$.[7] For constructions IV and V, we took mCherry as a reference, $QY_{ref} = QY_{mCherry} = 0.22$ and found $QY_{IV} = 0.20$ and $QY_V = 0.16$. We did not undertake this measurement for constructions II and III since they appear to be denatured.

Figure 93 presents the summary of the maturation rate influence, the structure modification and the quantum yield of the different TC-fusing strategies.

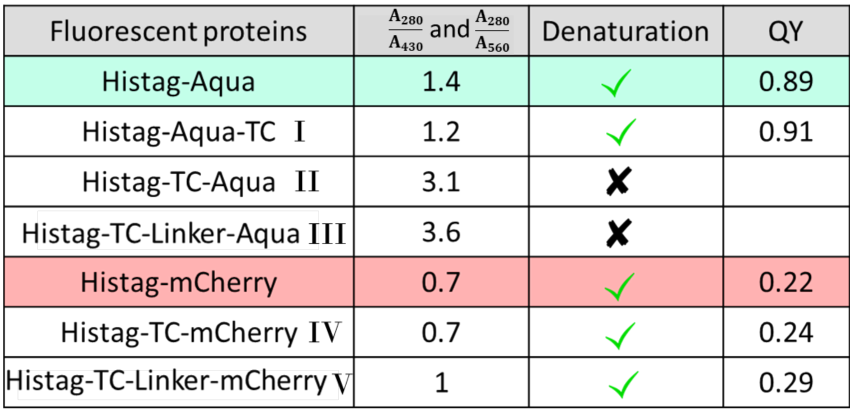

Fluorescent proteins	$\frac{A_{280}}{A_{430}}$ and $\frac{A_{280}}{A_{560}}$	Denaturation	QY
Histag-Aqua	1.4	✓	0.89
Histag-Aqua-TC I	1.2	✓	0.91
Histag-TC-Aqua II	3.1	✗	
Histag-TC-Linker-Aqua III	3.6	✗	
Histag-mCherry	0.7	✓	0.22
Histag-TC-mCherry IV	0.7	✓	0.24
Histag-TC-Linker-mCherry V	1	✓	0.29

Figure 93: $\frac{A_{280}}{A_{430}}$ or $\frac{A_{280}}{A_{560}}$ ratios and structure modification of the five constructions compared to the two references Histag-Aqua and Histag-mCherry.

All together, these results demonstrate that the expression, folding and maturation of constructions I, IV and V are not significantly altered by the presence of the tetracysteine tag.

8.3 PROOF OF CONCEPT OF THE DETECTION OF RECOMBINANT PROTEINS

8.3.1 *Construction I*

8.3.1.1 *Fluorescence signal*

We prepared 6 samples with 2µM of Aqua-tetracysteine tag in which we added 0, 0.1, 0.5, 1, 2 and 5 equivalents of **PP-1**, in the presence of EDT (100µM) and β-mercaptoethanol (1mM). We also prepared 5 reference samples where the same amounts of **PP-1** were bound to 2µM of model "PG" peptide with the same concentration of EDT and β-mercaptoethanol. These reference samples will help us to determine the fraction of fluorescence due to FRET and the one due to direct excitation.The reaction is allowed to proceed at room temperature for 50 minutes and then the 11 samples are illuminated at λ = 405 nm.

An example of the contribution of this direct illumination is shown in orange. It corresponds to the sample containing 2 µM of model "PG" TC-tag and 5 equivalents of **PP-1** excited at 405 nm. At this excitation wavelength the contamination of the acceptor fluorescence

directly excited was evaluated at less than 1 ‰. We were able to evaluate this contribution by comparing the fluorescence intensities at 540 nm (emission of **PP-1**) in both samples - **PP-1** without and with 2 µM of "PG" TC-tag.
The contribution of direct illumination of the **PP-1** was subtracted from emission fluorescence spectra of the sample in Figure 94A.

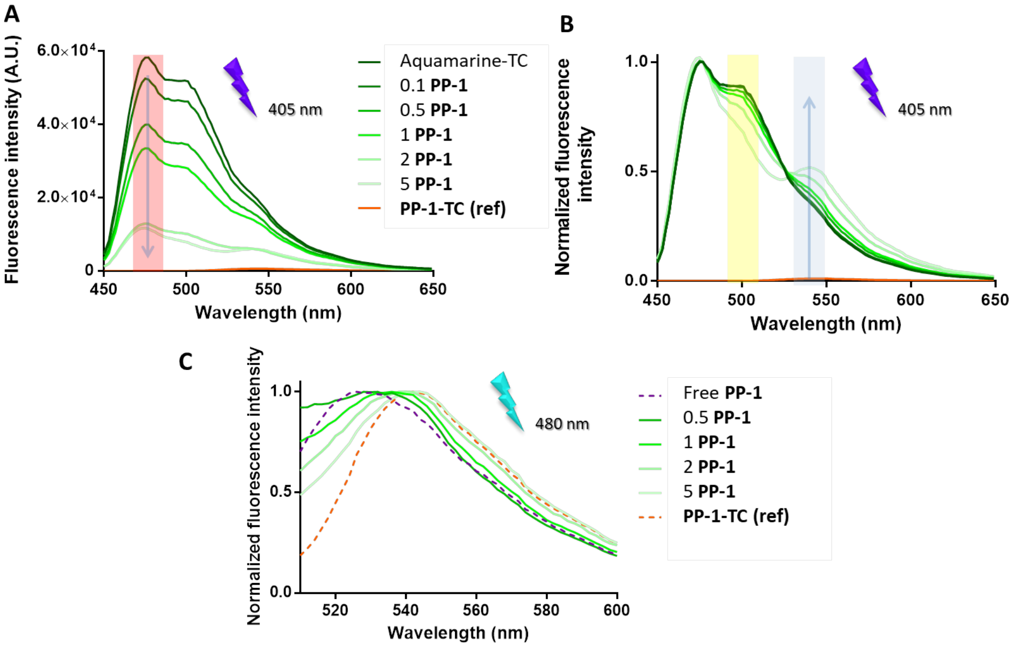

Figure 94: **A.** Fluorescence emission spectra of 0 to 5 equivalents of **PP-1** (from the darkest to the brightest green color) added to a 2µM Aquamarine-tetracysteine tag solution after illumination at 405 nm. The orange curve corresponds to the fluorescence emission of **PP-1** bound to 5 equivalents of model "PG" peptide illuminated by a 405 nm light. The red box focuses on the decrease of fluorescence intensity of the donor. **B.** Normalized fluorescence emission spectra at 405 nm, showing two modified regions. The blue box focuses on the increase of fluorescence intensity of the acceptor. The yellow box highlights the modification of the fluorescence spectrum of the donor. **C.** Normalized fluorescence emission spectra of samples containing 0.5 to 5 equivalents of **PP-1** illuminated with a 480 nm source. The orange and purple curves are used as a reference of free **PP-1** and **PP-1** bound to 5 equivalents of model "PG" peptide.

The fluorescence emission of Aquamarine-tetracysteine tag is drastically decreasing when adding **PP-1**, which is the acceptor here (red box). According to the FRET theory, fluorescence emission of **PP-1** should be simultaneously rising even if the light source is not its own excitation wavelength. Appearance of the fluorescence transfer to the acceptor can be seen as the concentration increases, in normalized fluorescence spectra in Figure 94B (blue box).

Fluorescence emission wavelengths of the CrAsH moiety illuminated at 480 nm confirmed this hypothesis (Figure 94C). Indeed, **PP-1** has now the same wavelength for maximal emission as the reference spectrum of bound sensor (orange dotted line).

We then performed fluorescence lifetime measurements on these sample using the FLIM set-up, as explained in Appendix A.

The wavelength of the excitation laser is 440 nm on the experiment setup. As observed in Figure 88, **PP-1** alone absorbs some light at 440 nm even if this wavelength is at the edge of its absorption band. This could lead to a direct excitation of the biosensor and may contribute to the fluorescent lifetime measurement. With this in mind, we performed the experiments in parallel on the complex **PP-1**-Aquamarine-tetracysteine tag and **PP-1** bound to the "PG" TC-tag in order to evaluate the fluorescence crosstalk. Fluorescence intensities were compared and the contribution of bound **PP-1** at this wavelength has been evaluated at less than one per cent.

Fluorescence lifetime of Aquamarine-tetracysteine tag was measured: $\tau_{Aquamarine-tetracysteinetag} = 4.02$ ns. A complex involving the tagged fluorescent protein and **PP-1** having FRET exchanges should exhibit a very different mean fluorescence lifetime.

FLIM experiments of samples containing Aquamarine-tetracysteine tag with increasing concentration of **PP-1** showed a severe decrease of their mean fluorescence lifetime τ_{mean} upon binding of the biosensor when excited at 440 nm (Figure 95A).

Each condition showed two fluorescence lifetimes $\tau_{short} \approx 1.5$ ns and $\tau_{long} \approx 4.1$ ns corresponding to the donor and the donor bound to the receptor. But when increasing the concentration of **PP-1**, the proportion of free donor α_{long} decreased and the proportion of donor bound to the receptor α_{short} increased. This showed that more than three quarters of construction I in the sample are bound to **PP-1** when adding 2 equivalents of the latter (Figure 95B). This corresponds to the stoichiometry observed in NMR experiments.

According to the equation of the FRET efficiency (10), we measured the integral of fluorescence spectra of the donor alone (sample of construction I with 0 equivalents of biosensor) and of the donor with 5 equivalents of acceptor from Figure 94 experiments. It should be noted that both samples were prepared with the same concentration of donor and that their absorption spectra were identical. This donor-acceptor pair exhibits a very high FRET efficacy of 70%, which is a

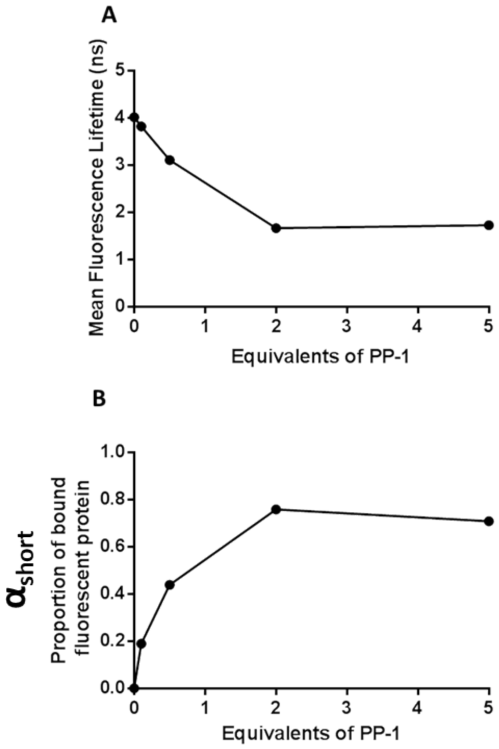

Figure 95: **A.** Mean fluorescence lifetimes of 0 to 5 equivalents of **PP-1** added to a 2µM Aquamarine-tetracysteine tag solution after illumination at 450 nm. **B.** Proportion of bound fluorescent proteins (α_{short}), after analysis of the biexponential decay functions.

consequence of an extensive overlap between the emission spectrum of Aquamarine-tetracysteine tag and the excitation spectrum of **PP-1**.

We calculated the same FRET efficiency E via fluorescence lifetimes measurements, according to (14). Considering τ_{short} and τ_{long} values for each condition, we calculated FRET efficiencies between 62% and 70%. Both strategies enabled us to evaluate a highly efficient FRET for this couple of fluorophores.

All these experiments tend to prove that these two fluorophores are in very close interaction, for a efficient FRET to be possible.

However, there is a fluorescence spectrum modification pointed out inside the yellow box Figure 94B. The alteration of this double band, highly characteristic of the fluorescent protein, is attesting a structural perturbation and thus strong interactions between **PP-1** and the barrel of the fluorescent protein. If so, it could dramatically complicate the xenon NMR signals.

8.3.1.2 ^{129}*Xe NMR signal*

We investigated the magnetic aspect of this construction by performing ^{129}Xe NMR experiments on a sample of 2µM of **PP-1** in the presence of 20 µM of Aquamarine-tetracysteine tag, 1mM βmercaptoethanol and 50µM EDT in PBS pH = 7.4 (Figure 96) . The reaction is allowed to proceed for 1 hour in a water bath at 37°C. The NMR signature of the solution shows several signals, likely corresponding to the multiple interactions that encapsulated xenon has with the barrel. These signals are also broaden by T_2 relaxation, due to the big size of the system and probable hindering of the cage-molecule motion.

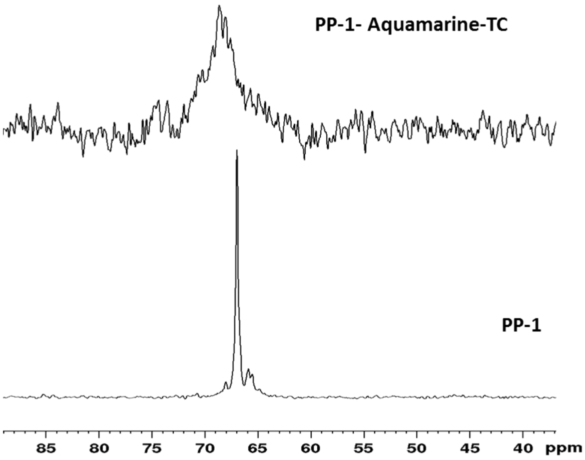

Figure 96: ^{129}Xe NMR selective spectra of free **PP-1** (2µM) and bound to 10 equivalents of Aquamarine-tetracysteine tag.

Despite its promising fluorescence properties, the way we designed our tetracysteine tag detection is not suitable for xenon NMR experiment. Indeed, the linewidth of the signal is unfortunately not suitable for the detection of a ^{129}Xe chemical shift variation. In addition, the corresponding correlation time *in cellulo* should be increased and leads to even broader signals.

8.3.2 *Constructions II and III*

8.3.2.1 *Fluorescence signal*

Considering the denaturation and maturation alteration of the two constructions, these fluorescence experiments have not been performed.

8.3.2.2 *Hyperpolarized* ^{129}*Xe NMR signal*

The same ^{129}Xe NMR experiments was conducted on two solutions of 2µM of **PP-1** in Figure 97.

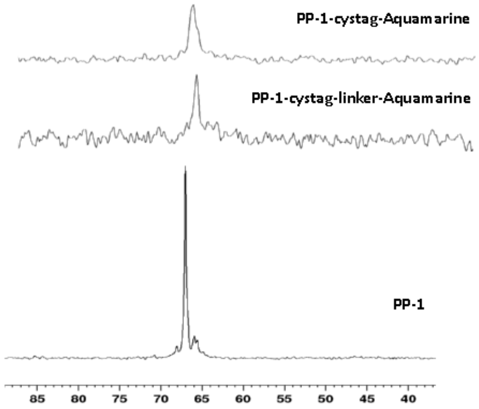

Figure 97: ^{129}Xe NMR sub-spectra of free xenon in **PP-1** (2μM) and bound to 2 equivalents of tetracysteine tag-Aquamarine and tetracysteine tag-linker-Aquamarine. Sub-spectra obtained by 2D Frequency-selective excitation sequence, when adding the 30 first scans.

In both cases, when 2 equivalents of tagged protein were added, the peak at δ = 66.7 ppm has totally disappeared, suggesting that all sensors are bound to their target. However, the only peak that appears at δ = 65.8 ppm likely corresponds to the residual **PP-2** which does not seem to react. Again, we do not observe an unique signal for encapsulated xenon, it could be multiple as in the case of Aquamarine-tetracysteine tag, or extremely wide due to the alteration of the in-out exchange of xenon or the large increase of the xenon correlation time. We could optimize the detection sequence for this type of system and be able to differentiate these signal. But we have to keep in mind that the ^{129}Xe NMR signal will be broaden and even more complicate in the *in cellulo* experiments. Thus, at this stage, we need a clear and simple signal to be detected.

Reminder
***PP-2** is the sensor with the cryptophane moiety grafted on the $\mathcal{C}_6$ of CrAsH moiety*

8.3.3 *Constructions IV and V*

8.3.3.1 *Fluorescence signal*

An upstream ^{129}Xe NMR experiment was performed with **PP-1** and the construction V. There was no signal attesting the detection of the tagged-protein. We decided not to pursue fluorescent experiments with this construction.

With these constructions, the biosensor is the donor and the tagged fluorescent protein mCherry is the acceptor. The consequence is that the fluorescence of the biosensor gained after complexation on the tetracysteine sequence may be decreased or compensated by the loss of fluorescence due to the FRET phenomenon.

We prepared 7 samples with 2μM of **PP-1** in which we added 0, 0.1, 0.5, 1, 2, 4 and 5 equivalents of Histag-tetracysteine tag-mCherry, in the presence of EDT (100μM) and β-mercaptoethanol (1mM). We also prepared 7 reference samples with the same amounts of construction IV alone, in order to evaluate contribution of the direct illumination of the tagged-protein. The reaction is allowed to proceed at room temperature for 50 minutes and then the 14 samples are excited at λ = 480 nm (see Figure 98).

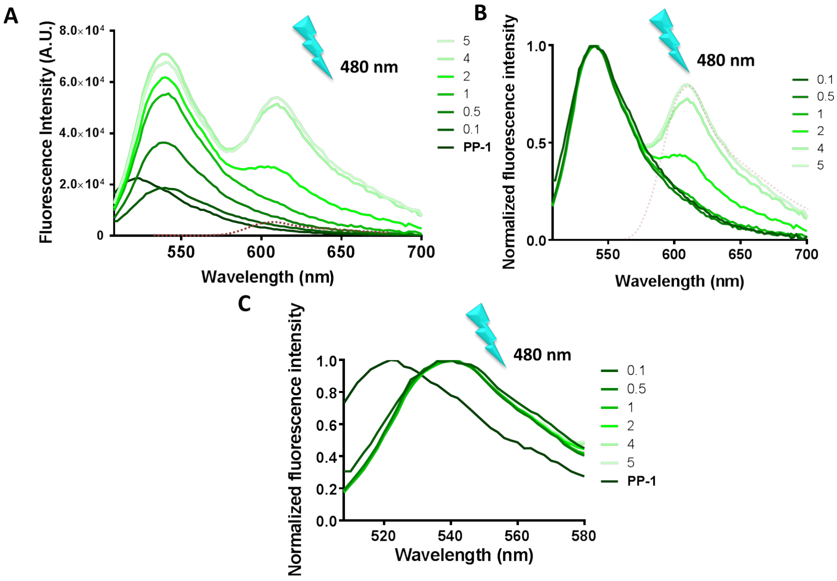

Figure 98: **A.** Fluorescence emission spectra of 0 to 5 equivalents of Histag-Tetracysteine tag-mCherry (from the darkest to the brightest green color) added to a 2μM **PP-1** solution after illumination at 480 nm. Spectra have been corrected by the fluorescence emission of construction IV directly illuminated by the 480 nm light and displayed in red dotted line (contribution of 1%). **B.** Normalized fluorescence emission spectra at 480 nm demonstrating a FRET transfer from the biosensor to the tagged-protein. **C.** Normalized fluorescence emission spectra of samples containing 0 to 5 equivalents of Histag-Tetracysteine tag-mCherry illuminated with a 480 nm source, showing the spectral shift of the emission spectrum upon binding.

Fluorescence emission intensities between λ_{em} = 508 nm and λ_{em} =700 nm are corrected by the fluorescence contribution of the construction IV directly excited (displayed in red dotted line and corresponding to 1% of the signal). They are plotted in Figure 98A for each concentration of tagged-mCherry. We observe an increase of the direct fluorescence emission of **PP-1** at 540 nm attesting the detection of the tetracysteine sequence on mCherry by **PP-1**. The apparent rise of fluorescence visible on the spectrum corresponds to an underestimation of fluorescence gained by the fluorogenic biosensor. Indeed, as a donor, the fluorescence intensity of **PP-1** tends to decrease in favour of the increase of the fluorescence intensity of the construction IV. **PP-1** is 3.3 times more fluorescent when detecting the tagged-protein.

However, for 0.1 equivalents of tagged-mCherry, FRET transfer contribution is higher than the gain of fluorescence leading to a trend reversal.

The absence of evolution of the fluorescence intensity of **PP-1** with 5 equivalents of construction IV, indicates that the binding is complete (Figure 98A) after the addition of four equivalents of tagged-protein.

Importantly, the fluorescence emission spectra of construction IV alone and bound to **PP-1** are very similar (red dotted line in Figure 98B). Contrary to construction I, there is no interaction between construction IV and **PP-1**. This is promising for ^{129}Xe NMR experiments, as it means less xenon signals.

Finally, positions of the fluorescence emission maxima do not evolve as the previous construction. Figure 98C shows a binary complexation, leading to only two wavelength positions: 518 nm (free biosensor) and 542 nm (bound biosensor). In the previous construction (with Aquamarine), evolution of the wavelength of the maximal fluorescence intensity was progressive as concentration of biosensor increased. We assumed that the complexation of the two partners does not undergo intermediate complexes, which is also an advantage.

For FRET efficiency evaluation, we need the fluorescence intensity and the absorbance of the tagged-protein at wavelength where the acceptor does not absorb, according to (11). We therefore excited our samples with λ_{ex} = 580 nm. By this method, we obtained a FRET efficiency of 73%, which is similar to the previous construction.

Unfortunately, due to a lack of time, we did not perform FLIM experiments with this pair of fluorophores.

Considering all these results, we undertook ^{129}Xe NMR experiments on this construction IV.

8.3.4 *Hyperpolarized* ^{129}*Xe NMR experiments*

We investigated the NMR properties of the construction IV by performing ^{129}Xe NMR experiments on a sample of 2µM of **PP-1** in the presence of 8 µM of Histag-Tetracysteine tag-mCherry, 1mM βmercaptoethanol and 50µM EDT in PBS pH = 7.4. The reaction is allowed to proceed for 1 hour in a water bath at 37°C. A frequency-selective excitation sequence in 2D was employed to detect the Xe@biosensor signals as displayed in Figure 99.

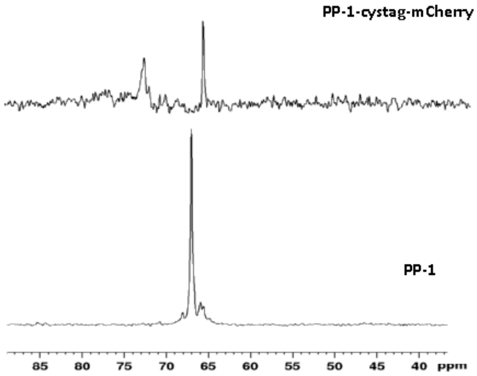

Figure 99: ^{129}Xe NMR spectra of free **PP-1** (2µM) and bound to 4 equivalents of Histag-Tetracysteine tag-mCherry. Spectra were obtained with a frequency-selective excitation sequence (2D) with an half-gaussian pulse.

When the 4 equivalents of tagged protein were added, the peak at δ = 66.7 ppm totally disappeared, confirming the assumption made after fluorescence experiments: complexation between the biosensor and its target is complete after only a small excess of tagged-protein. The peak at δ = 65.8 ppm, corresponding the the residual **PP-2** still remains after addition of the target, confirming the hypothesis that this biosensor does not interact much with the tetracysteine tag. However, an additional large but unique peak appears at δ = 74 ppm, resulting from xenon caged in biosensor **PP-1** bound to the tetracysteine tagged-mCherry.

This peak, separated by 7.3 ppm from the free Xe@**PP-1**, demonstrated that the biosensor that we have built, is a smart ^{129}Xe NMR-based biosensor that allows tagged-proteins detection.

8.4 CONCLUSION

The construction of our system required some optimizations - structure of protein, position of the tetracysteine tag and its distance from the barrel - in order to limit interactions between the biosensor and the protein. We finally succeeded to detect a tetracysteine tagged protein by both ^{129}Xe NMR and fluorescence modalities. The ^{129}Xe NMR chemical shift variation of 7.3 ppm and the - at least - 3.3-fold increase of fluorescence are also supported by an energy transfer.
This first proof of concept has furthermore been proved on a very large protein (236 amino acids), and will be intuitively more easily applicable to small proteins.

BIBLIOGRAPHY

[1] B. A. Griffin. Specific covalent labeling of recombinant protein molecules inside live cells. *Science*, 281(5374):269–272, jul 1998.

[2] Lakowicz joseph R. *Principles of Fluorescence Microscopy*. Number 3. Springer US, 2006.

[3] R.E. Dale, J. Eisinger, and W.E. Blumberg. The orientational freedom of molecular probes. the orientation factor in intramolecular energy transfer. *Biophysical Journal*, 26(2):161 – 193, 1979.

[4] Erard, Marie, Fredj, Asma, Pasquier, Helene, Beltolngar, Dahdjim-Benoit, Bousmah, Yasmina, Derrien, Valerie, Vincent, Pierre, Merola, and Fabienne. Minimum set of mutations needed to optimize cyan fluorescent proteins for live cell imaging. *Mol. BioSyst.*, 9:258–267, 2013.

[5] Bernard Valeur and Mário Nuno Berberan-Santos. *Molecular Fluorescence: Principles and Applications, Second Edition*. Wiley, 2001.

[6] Robert M. Clegg. Chapter 1 Förster resonance energy transfer—FRET what is it, why do it, and how it's done. *Laboratory Techniques in Biochemistry and Molecular Biology*, 33:1 – 57, 2009.

[7] Marie Erard, Asma Fredj, Helene Pasquier, Dahdjim-Benoit Beltolngar, Yasmina Bousmah, Valerie Derrien, Pierre Vincent, and Fabienne Merola. Minimum set of mutations needed to optimize cyan fluorescent proteins for live cell imaging. *Mol. BioSyst.*, 9:258–267, 2013.

9

IN-CELL DETECTION OF TETRACYSTEIN-TAGGED PROTEINS

The proof of concept of the dual detection of a recombinant protein via fluorescence and ^{129}Xe NMR has been assessed. The next step of this project is then to detect the recombinant proteins *in situ*.

In order to achieve this, a lot of parameters had to be studied knowing that ^{129}Xe NMR experiments require some adjustments: the cells must be in suspension and in sufficient quantity so that there is enough spins to detect. Very preliminary results will be presented in this chapter, more efforts remain to be made in order to fully extent this proof of concept to *in cellulo*.

9.1 INTERNALIZATION IN BACTERIA

3.10^8 E.coli cells (DH5-α) were incubated 2 hours with 26 μM of racemic biosensor in phosphate buffer (pH = 7.4). They were then rinsed 3 times with PBS. The cells were resuspended in 160 μL of a solution containing 50 mM of dithiothreitol (DTT) in TE buffer, a redox reagent that reduces disulfide bonds. DTT forms a stable six-membered ring with an internal disulfide bond *via* two sequential thiol-disulfide exchange reactions displayed in Figure 100. This step allows the removal of the non specifically bound biosensor. The latter reaction was allowed to process for 15 minutes at 32°C , then the cells were centrifuged, rinsed and resuspended in 200 μL of water: Figure 101B and D (green curve).

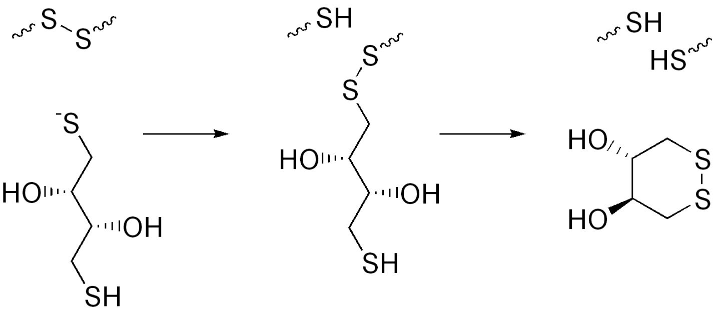

Figure 100: Reduction of a -SS- bond by DTT.

The cells were then studied by fluorescence microscopy and spectroscopy, as can be seen in Figure 101A and D (pink curve).

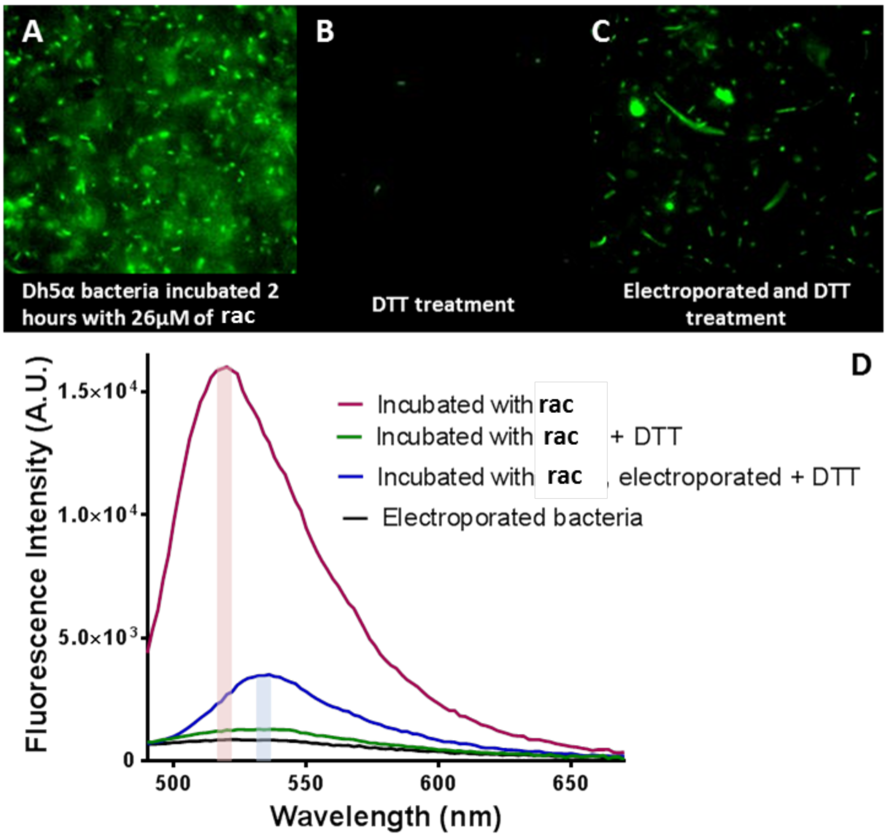

Figure 101: Fluorescence microscopy of DH5α cells incubated with 26 µM of racemic biosensor for 2 hours, **A.** rinsed in PBS, **B.** treated with DTT reagent, **C.** electroporated and then treated with DTT. **D.** Fluorescence spectra of the biosensor in the three conditions, illuminated at λ_{ex} = 470 nm and observed between λ_{em} = 490 nm and λ_{em} = 570 nm. The spectrum of electroporated bacteria is used as a blank. The red and blue areas enlighten maximum of fluorescence emission: 518 nm for incubated biosensor, 534 nm for incubated biosensor in electroporated bacteria.

Fluorescence observed and measured in DH5α cells incubated with biosensors totally disappeared with the DTT treatment, suggesting that the biosensor was never internalized into bacteria.

We therefore employed a technique in which an electrical field is applied to bacteria in order to increase the permeability of the cell wall. This technique, named electroporation, allows chemicals or even DNA to be introduced into the cell.[1] A new batch of 3.10^8 cells were pipetted into a glass cuvette in the presence of 26 µM of racemic biosensor. Immediately after electroporation, 1 mL of culture medium was added to bacteria and they were allowed to recover at 37°C for 30 minutes.The bacteria were then rinsed and underwent the same DTT treatment than before. Fluorescence was observed and monitored in Figure 101C and D (blue curve).

Even after reducing all -SS- bonds at the cell surface, bacteria incubated with the biosensor were still highly fluorescent when they underwent electroporation (Figure 101C). The areas under the blue and pink spectra in Figure 101D show that 24% of the fluorescence of bacteria electroporated with the biosensor actually resulted from fluorescence of the biosensor internalized inside the cells. Moreover, both fluorescent profiles - before and after electroporation - are significantly different. The first one has the typical profile of the free biosensor (λ_{Fmax} = 518 nm) whereas the second one, corresponding to the biosensor inside bacteria, has a maximum of fluorescence centered on 534 nm. This proves that the racemic biosensor has been taken up by bacteria and that it is bound to endogenous thiols.

Bacteria could be a good model for NMR as their culture is quite simple and huge quantities can be obtained in a few days. This is an important parameter for hyperpolarized ^{129}Xe NMR, where the required minimal number of spins is 10^{13}. However, studies in mammalian cells are of higher biological interest.

9.2 PROTOCOL FOR EUKARYOTIC CELL UPTAKE

9.2.1 *Surface coating method*

The protocols for expression of fluorescent proteins are well described in the COS7-cell line, as they are a common mammalian production cell used for recombinant proteins. COS-7 cells derived from kidney tissue of the African green monkey, *Cercopithecus aethiops*. This cell line is adherent to glass and plastic surfaces.
The protocols that I used for cells culture are displayed in Appendix A.

The biosensor is a small molecule that is likely internalized by the cells. Also, as it is slightly hydrophobic, it may interact with the membranes. This can lead to a distribution in membrane whereas fluorescent proteins have a cytosolic distribution. An usual protocol for increased nanoparticles uptake consists in adding fetal bovine serum (FBS) into the incubation medium.[2] Studies showed that serum protein adsorption reduces the aggregate size distribution of titanium dioxide nanoparticles and especially affect the particles' interactions. Particles were shown to adopt the physiochemical properties of the protein absorption layer (a. k. a. the "protein corona") that forms on the surface of the particles. In order to assess this protocol, we chose to perform this experiment in a 96-well plate. This system was chosen to reduce the required quantity of biosensor for an homogeneous incubation. In each well, 30.000 adherent cells were incubated with:

The reducing mixture: 100 µM of EDT, 1 mM of β-mercaptoethanol and 1 mM of TCEP.

- 10 µM of racemic biosensor, the reducing mixture - EDT, TCEP and β-mercaptoethanol - and Dulbecco's Modified Eagle Medium (DMEM).
- 10 µM of racemic biosensor, the reducing mixture, DMEM and 30% FBS.
- The reducing mixture, DMEM and 30% FBS.

The solutions were incubated for 1 hour, then rinsed 3 times with PBS and fluorescence emission spectra were recorded (Figure 102A).

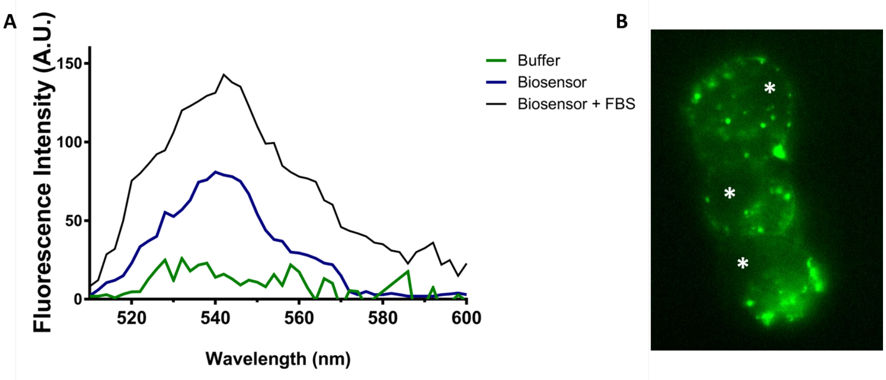

Figure 102: **A.** Fluorescence emission spectra of 30.000 COS7-cells incubated 1 hour with 10 µM of racemic biosensor with or without protein corona (via FBS). Spectra were recorded after an excitation at λ_{exc} = 480 nm using a plate reader. **B.** Fluorescence microscopy images of COS7-cells incubated with 10 µM of biosensor and 30% FBS and illuminated via the biosensor filter cube during t_{exp} = 2 s.

Spectral selection of the biosensor filter cube: 485 nm < λ_{exc} < 515 nm and 525 nm < λ_{em} < 560 nm.

Even if the signal is very low, due to the low amount of cells in each well, FBS coating improved the biosensor uptake - 2-fold increase of the signal. The emission band, centered at 540 nm, corresponds to the bound biosensor.
Wide field fluorescence microscopy images of these cells are displayed in Figure 102B. With this method, there is no z-selection: the fluorescence of the whole thickness of the sample is collected. The fluorescence of the cell is observed upon illumination and detection via a filter cube adapted for the biosensor. It will be called in the following "biosensor filter cube". The distribution of the biosensor is mainly in the cytosol but there are some bright spots. Indeed, when the loading is important, the biosensor tends to accumulate in bright spots, supposedly imprisoned in vesicles, ready to be released from the cell. As a matter of fact, some residual fluorescence is observed after a few hours in the external medium. The fact that we can distinguish the non-fluorescent nucleus of the cell (white asterisk in Figure 102B) suggests a cytosolic distribution.

9.2.2 *Optimization of conditions for cell uptake*

The next objective is to internalize a maximum of biosensor - for an improved signal in fluorescence and in ^{129}Xe NMR. We had in mind to perform this step without spending too much biosensor. We studied the influence of the time of incubation and the concentration of biosensor on fluorescence intensity inside the cells. Four samples with four concentrations of biosensor were prepared. Each sample is placed in four wells and then incubated at 37°C. The incubation of each well will be stopped at the desired time, rinsed and imaged. This protocol tends to minimize the loss of the cells. The mean fluorescence intensities of 10 cells in 10 different fields of view are reported in Figure 103.

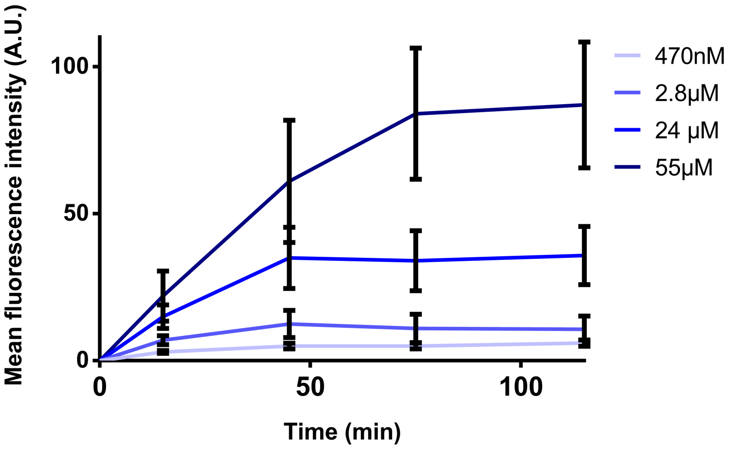

Figure 103: Influence of the incubation time and biosensor concentration on incubated quantities. The cells were incubated for 15, 45, 75 and 115 minutes with 0.47, 2.8, 24 and 55μM of racemic biosensor. After being rinsed 3 times with PBS, fluorescence microscopy images of the cells in PBS were recorded with the biosensor filter cube. A region of interest (ROI) of the size of a cell was chosen and mean fluorescence intensities of 10 cells in 10 different fields of view were measured using a routine in ImageJ software. The mean values for each sample are reported here, as well as the standard deviation.

Complete internalization is quickly reached - after about an hour. Figure 103 shows that the greater the biosensor concentration, the more it is internalized. However, the error bars demonstrate that heterogeneity of cell uptake is higher with high concentration of biosensor.

We investigated the optimal concentration of EDT and β-mercaptoethanol for cell uptake of a constant biosensor concentration and TCEP (Figure 104A and B).

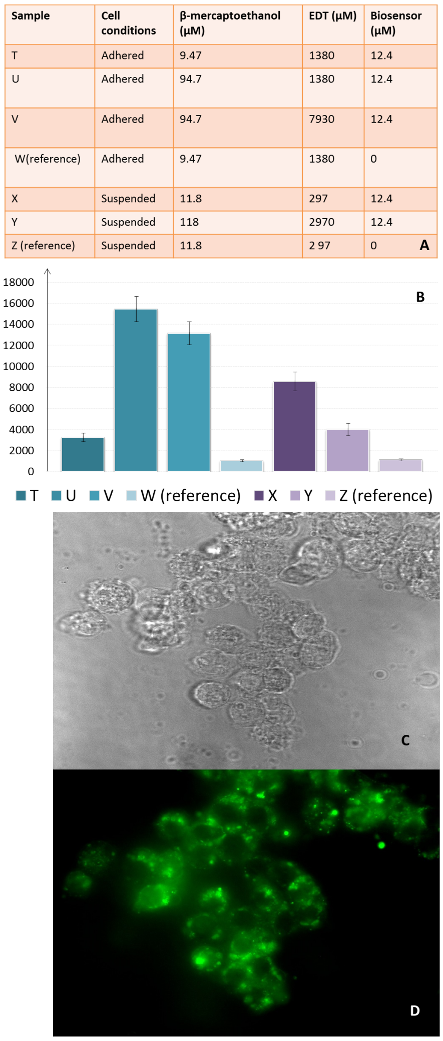

Sample	Cell conditions	β-mercaptoethanol (μM)	EDT (μM)	Biosensor (μM)
T	Adhered	9.47	1380	12.4
U	Adhered	94.7	1380	12.4
V	Adhered	94.7	7930	12.4
W(reference)	Adhered	9.47	1380	0
X	Suspended	11.8	297	12.4
Y	Suspended	118	2970	12.4
Z (reference)	Suspended	11.8	2 97	0

Figure 104: **A. and B.** Influence of EDT and β-mercaptoethanol concentration and cell condition -adhered or suspended - on the cell uptake of the racemic biosensor at 1 mM of TCEP. Cells in sample E,F and G were prior detached from the surface with 200μL of trypsin, a protease that hydrolyses proteins. They are centrifuged, resuspended into DMEM (30% FBS) and incubated with biosensor for 1 hour at 37°C. After being rinsed 3 times with PBS, fluorescence microscopy images of the cells in PBS with different concentration of β-mercaptoethanol and EDT were recorded. A region of interest (ROI) of the size of a cell was chosen and mean fluorescence intensity of 10 cells in 10 fields of view was measured using a routine in ImageJ software. The mean value for each sample is reported here, as well as the standard deviation. **C.** Transmission microscopy image of cells in U conditions. **D.** Fluorescence microscopy images of the same cells.

Also, ^{129}Xe NMR experiments require suspended cells. Of course, it is possible to incubate the biosensor on adherent cells and then get them detached with trypsin but it would be more stressful for the the cells. Working with suspended cells also minimizes the surface of solution and therefore the required quantity of biosensor. We verified that internalization of the biosensor was possible when the cells were in suspension in a tube (samples E and F in Figure 104A and B).

The biosensor is internalized by both types of cells - adhered and suspended.

For adhered cells, the best cell uptake is obtained with the highest concentrations of β-mercaptoethanol. cell uptake is not EDT quantity-dependent. This concentration of EDT is however higher than the threshold beyond which there is an exclusive exchange between the biosensor and two molecules of EDT (1.38 mM against 1 mM). These conditions therefore need to be adapted so that EDT is no longer a competitor to the tetracysteine tag. Fluorescence microscopy image in Figure 104D shows the high fluorescence signal of the cells. Again, this indicates a cytosolic distribution. Figure 104C and D prove that biosensor has been uptaken in a large majority of cells.

The optimal conditions for cells in suspension are quite different. They require a lower level of β-mercaptoethanol and EDT in the incubation medium than that employed for *in vitro* experiments. An excess of monothiols (1mM) is not favorable for the cell uptake of the biosensor. Since only two conditions were performed, it is difficult to compare the effect of EDT and β-mercaptoethanol on the cell uptake.

Finally, cell uptake is higher in adhered cells than suspended cells. Since COS7-cells are adherent cells, we can formulate the hypothesis that they are in better conditions when adhered, favoring the cell uptake.

9.2.3 *Proof of cell uptake and quantification*

We defined the best conditions to observe the cell uptake of the biosensor. Let us remind that in this paragraph, there is no TC tag in the cells. In order to verify the cytosolic distribution assertion, we performed confocal microscopy, a technique that makes use of optical sectioning. The fluorescence intensity observed on this confocal image is collected from a single plan while it is collected by the whole thickness of the cell in wide field. This technique enables the recording of stack of images to reconstruct 3D projection.

This experiment was performed in the imaging platform in Gif-sur-Yvette.

COS7-cells incubated for 1 hour with 140 µM of racemic biosensor, reducing mixture and DMEM (30% FBS) were imaged in PBS (see Figure 105).

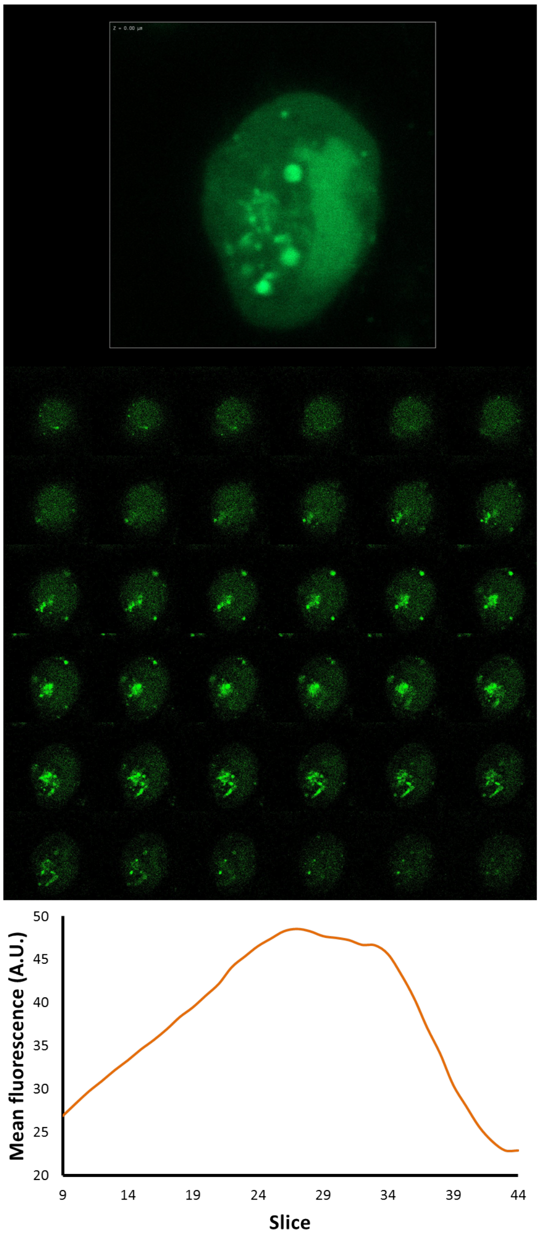

Figure 105: Confocal images of COS7-cells incubated for 1 hour at 37°C with 140 µM of biosensor, reducing mixture and DMEM (30% FBS). After after being rinsed 2 times with PBS, cells were illuminated with a laser at 488 nm and detected between 500 and 550 nm and imaged in PBS. 36 slices corresponding to 36 different depths (z = 130 nm) of the cells are displayed as well as the projection of the fluorescence and the mean fluorescence of each depth.

The 36 different slices corresponding to 36 different depths of the cell, displayed in Figure 105, show a signal of fluorescence. Indeed, analysis of the images (bottom of Figure 105) shows a maximum of fluorescence intensity in the center of the cell. This is the formal proof of the biosensor uptake and its cytosolic distribution.

Through all these microscopy images, we estimated that biosensor was uptaken in most of the mammalian cells of the sample. We further investigated the percentage of the fluorescent cells by flow cytometry. COS7-cells were incubated with or without racemic biosensor. In this set-up, the cells are brought into a flowing stream of liquid. That is why cells were incubated in suspension. This setup analyses one cell at a time and measures the specific light scattering and fluorescence characteristics of each cell.

Figure 106A and B show the distribution of cell fluorescence intensity for both samples.

Figure 106C and D display - with the same contrast treatment- fluorescence microscopy images of both samples. The intensity profiles obtained along the yellow line using a routine in ImageJ are presented in Figure 106E and F.

Cells incubated with the racemic biosensor exhibit a fluorescence intensity two orders of magnitude higher than the auto-fluorescence intensity of referenced cells. More importantly, 99.6% of the cells are fluorescent - thus have uptaken the biosensor. Distribution of this cell uptake is large (2 logs in Figure 106A) but the majority of the sample is homogeneous, as proved by the Gaussian shape (from 1 to 10). A small amount of cells present higher fluorescence intensities (from 10 to 100) and likely corresponds to cells having bright spots. The amount of these bright spots has highly decreased inside the cells, demonstrating a more homogeneous distribution of biosensor when incubating the biosensor with suspended cells. This is confirmed by the intensity profile of the cell in Figure 106E.

Finally, the last essential parameter to define for ^{129}Xe NMR experiments is the internalized quantity of biosensor. Indeed, since we know the minimal number of spins that we can detect with this method, we need to define the concentration of biosensor in one cell and the corresponding number of cells required for the experiment. For this, we performed an experiment of concentration calibration. First, fluorescence spectroscopic properties of the incubated cells were measured. Figure 107A shows that the biosensor which has been uptaken inside the cells was in its bound form (wavelength of the maximal fluorescence intensity at λ_{em} = 542 nm). Knowing that there is no TC-tag inside the cells, it is likely due to unspecific binding of endogenous cysteines. Moreover, the experiment is performed in the presence of a high concentration of FBS, which mainly consists in bovine serum albumin. This protein is very cysteine-rich and notably possesses **CC**XX**C** sequences. This unspecific labeling should therefore be overcome in the presence of PG TC-tags.

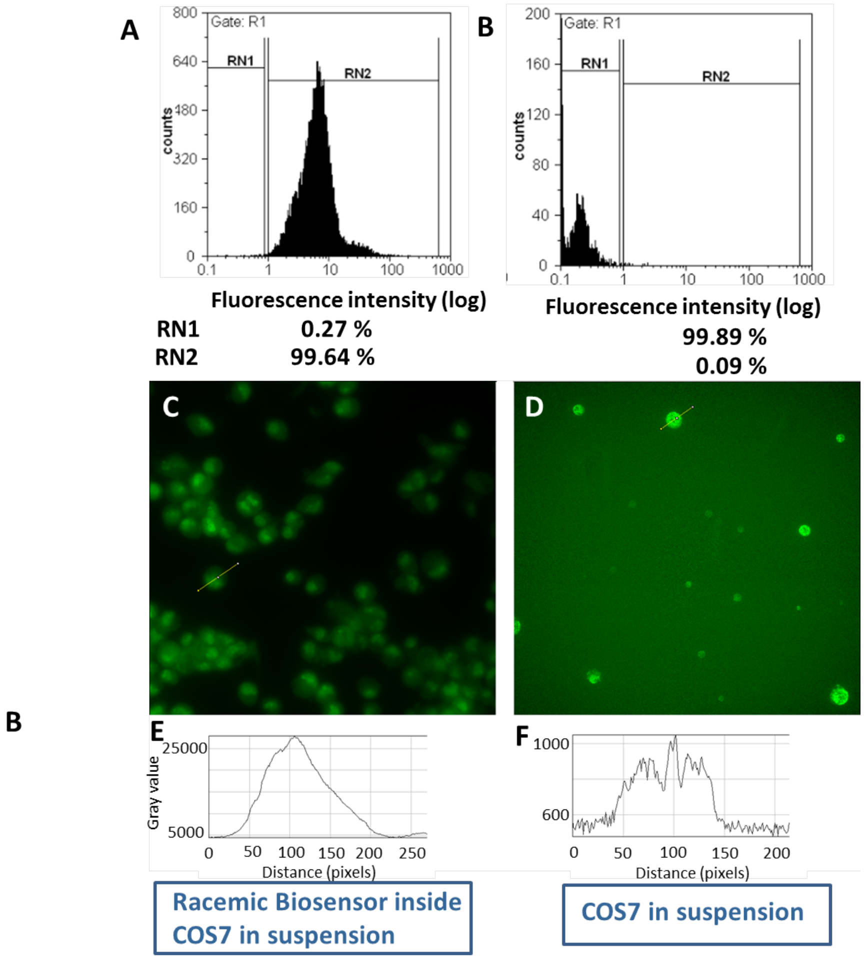

Figure 106: Flow cytometry experiments (Gain = 280) of suspended COS7-cells incubated for 1 hour at 37°C with 100 µM of β-mercaptoethanol, 1 mM of TCEP, 500 µM of EDT, DMEM (30% FBS) and **A.** 70 µM of racemic biosensor, **B.** without biosensor. Fluorescence microscopy images using an YFP filter cube of **C.** suspended cells incubated with racemic biosensor and **D.** suspended cells as a reference. The yellow lane corresponds to the intensity profile of a cell incubated **E.** with biosensor and **F.** without biosensor.

For the calibration curve, we prepared four concentrations of a solution of racemic biosensor with an excess of PG-tetracysteine tag. We measured the maximum of fluorescence intensity for each dilution and plotted it against the concentration.

This calibration curve gave access to the ratio $\alpha = 7972\ \mu M^{-1}$ which allows us to calculate the concentration from a fluorescence value (Figure 107B). We then incubated 150 000 cells with 15.4 µM of racemic biosensor for an hour. Cells were washed and maximum fluorescence intensity was measured in the same conditions. With I_{fluo}^{cell} the maximum fluorescence intensity measured in the sample of cells,

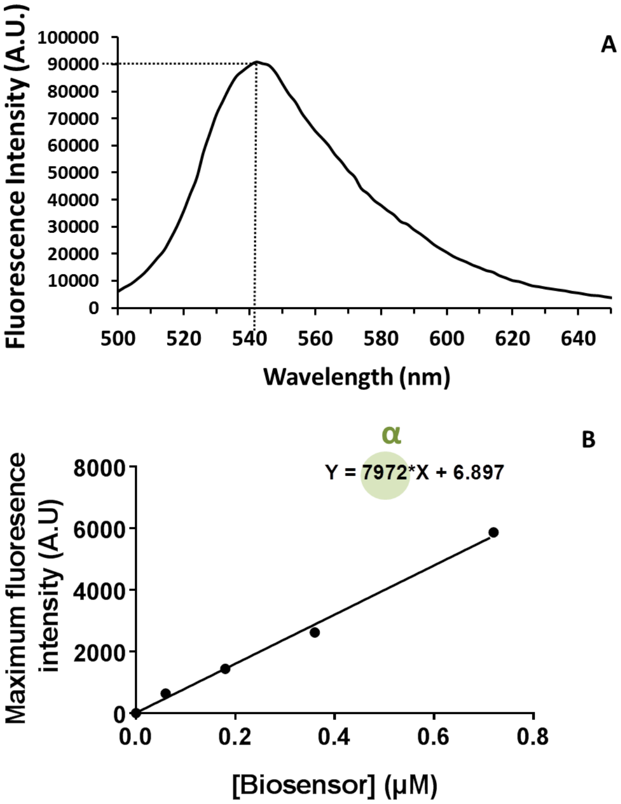

Figure 107: **A.** The fluorescence emission spectrum of cells incubated with 70 μM of the racemic biosensor. **B.** The maximum fluorescence intensities (gain = 90) of four dilutions - 0.06, 0.18, 0.36 and 0.72 μM - of racemic biosensor. The linear regression fit indicates a slope α = 7972 μM^{-1}.

V_{well} the volume of the sample, V_{cell} the mean volume of a cell, α the calibration factor and N_{tot} the number of cells in the sample, we are able to estimate $C^{cell}_{biosensor}$, the biosensor concentration in a cell. Details of (15) are shown in Appendix A.

$$C^{cell}_{biosensor} = \frac{I^{cell}_{fluo} V_{well}}{\alpha V_{cell} N_{tot}} \tag{15}$$

This led to an estimation of $C^{cell}_{biosensor}$ = 14.5 μM and $m^{cell}_{biosensor}$ = 0.06 pg. This result demonstrates that it exists a thermodynamic equilibrium of the biosensor between the extracellular and the intracellular medium. Indeed, the concentration inside the cell is almost that of the incubation medium.

Considering this result, ^{129}Xe NMR were performed with 80 millions of cells, with a concentration of biosensor in the μM range - as well as the fluorescent proteins concentration.

9.3 ^{129}Xe NMR detection of the sensor inside the cells

80 millions of COS7-cells were grown during two weeks and then detached with 10 mL of trypsin. The cells were collected in a 50 mL Falcon tube, centrifuged, and resuspended in 500 µL of DMEM containing 30% FBS, 140 µM of **PP-1**, 200 µM of β-mercaptoethanol, 900 µM of EDT and 1 mM of TCEP. The cells were incubated during 1h30 at 37°C and the incubation medium was removed and collected in an NMR tube with 900 µL of PBS and 100 µL of D_2O. The cells were washed two times with PBS and resuspended in 1.4 mL of PBS and 100 µM of D_2O in another NMR tube.

HyperCEST depolarization curves and corresponding Z-spectra were measured for the supernatant (Figure 108A) and for the cells (Figure 108B).

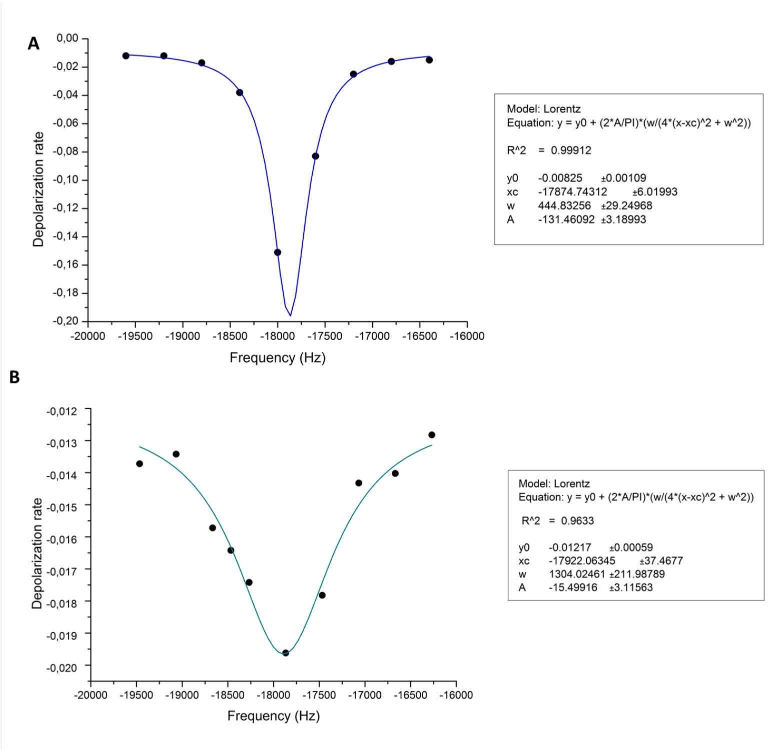

Figure 108: Z-spectra of **A.** the supernatant containing 140 µM of **PP-1** and **B.** cells incubated with 140 µM of **PP-1**. Data were fitted with a Lorentzian curve using OriginPro software. Both experiments were performed with these parameters: Consecutive data points are separated by 0.5 s; saturation: repetition of 100 D-SNOB pulses, max. saturation field strength of 12 µT.

With this very sensitive indirect detection method, the signal of xenon in the biosensor inside the cells can be detected. Even if it has been proved that the biosensor was bound to endogenous motifs of cysteines, the ^{129}Xe NMR signal of encapsulated xenon in the biosensor in the cell has the same chemical shift as xenon in the biosensor in the supernatant. Indeed, Lorentzian fits obtained using OriginPro software demonstrate a resonance frequency of -17875 Hz (supernatant) and -17922 Hz (in cells) from the resonance frequency of dissolved free xenon. As expected, the signal of xenon in the biosensor is broader in cells than in supernatant (Full-Width Half-Maximum = 1304 Hz *in cellulo* against 445 Hz *in vitro*. This can be explained by an increase of the correlation time of the encapsulated xenon in the intracellular medium. Fluorescence and ^{129}Xe NMR experiments both confirm that biosensor is internalized inside the eukaryotic cells

The cells must now contain a tetracysteine tagged protein in order to detect *in cellulo* the ^{129}Xe NMR signal of the noble gas in the biosensor bound to the protein as well as the corresponding fluorescence modifications. Some preliminary experiments that have been performed are described in the following paragraph.

9.4 DETECTION OF THE SENSOR INSIDE CELLS EXPRESSING TETRACYSTEINE TAGGED PROTEINS

Since construction I was the first tagged-protein system that we built and since it showed promising results in fluorescence, this preliminary study was performed on this contruction. Unfortunately we did not have time either to repeat the experiment previously performed with construction IV or to perform the corresponding ^{129}Xe NMR experiments.

For this experiment, we transfected (see Appendix A for protocol details) two samples of COS7-cells with two different DNAs:

- DNA coding for TC-tagged Aquamarine (construction I)
- DNA coding for Aquamarine

A 40 µM solution of **PP-1** was added on both samples, as well as 1 mM TCEP, 1 mM of β-mercaptoethanol and 500 µM of EDT. Cells were imaged by fluorescence microscopy using the appropriate spectral selection: the Aquamarine excitation in Figure 109A and the biosensor excitation in Figure 109B and C.

In a second experiment, an excess of EDT (2 mM) was added on cells expressing TC-tagged Aquamarine and incubated with **PP-1** in Figure 109D.

The fluorescence intensities of cells were evaluated by measuring the intensity of a ROI in approximatively 40 cells.

The sample of cells transfected with DNA coding for TC-tagged Aquamarine exhibits two populations when exciting in range of the Aquamarine absorption. This means that all cells were not transfected. The transfection efficiency was estimated around 80% (blue frame

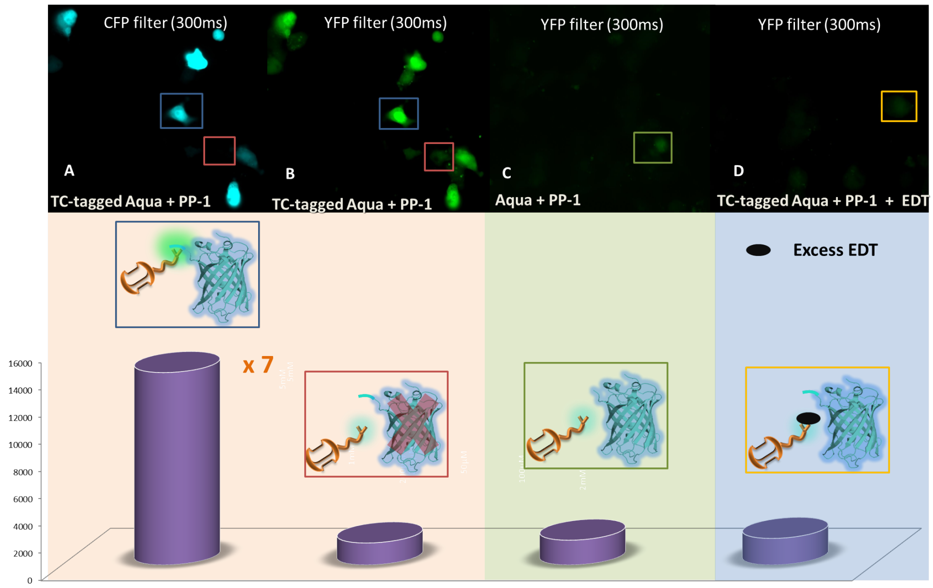

Figure 109: Fluorescence microscopy images of **PP-1** incubated on cells expressing **A.** TC-tagged Aquamarine (Aquamarine excitation), **B.** TC-tagged Aquamarine (biosensor excitation), **C.** Aquamarine and **D.** TC-tagged Aquamarine with an excess of EDT. The chart displays mean fluorescence intensities measured in a ROI in 40 cells.

in Figure 109) so there are 20 % of cells that do not express any tagged-fluorescent protein (red frame in Figure 109A). When exciting at the wavelength of the biosensor absorption, we observe fluorescence emission of the biosensor only from the cells that exhibited Aquamarine fluorescence intensity (blue frame in Figure 109B) **PP-1** bound to the construction I *in cellulo* led to a 7-fold fluorescence increase with respect to **PP-1** *in cellulo*.

The sample of cells transfected with DNA coding for Aquamarine exhibits two populations when exciting in range of the Aquamarine absorption as well since the transfection is not totally homogeneous. The fluorescence intensity of **PP-1** in the presence of Aquamarine *in cellulo* was similar to the one of **PP-1** alone in the cells.

Finally, adding 2 mM of EDT on the cells containing **PP-1** and construction I led to a total disappearance of the fluorescence. This means that **PP-1** is unbound from construction I and binds two molecules of EDT.

We successfully detected *in cellulo* a TC-tagged protein by fluorescence modality but considering the poor ^{129}Xe NMR *in vitro* results of construction I, we decided not to go through the NMR experiment.

9.5 CONCLUSION

Some preliminary studies in eukaryotic cells have been performed in this work. The main objectives were the study of the cell uptake of the biosensor and determination of concentration and optimal conditions enabling its unambiguous detection in ^{129}Xe NMR *in cellulo*. Finally a first step was performed in the *in cellulo* detection of a recombinant protein via our TC-tag and biosensor.

Some additional experiments should be performed in order to extent this proof of concept to *in cellulo* detection of a recombinant protein by ^{129}Xe NMR modality. To achieve this, a higher number of cells (80 millions) must be transfected by a DNA coding for construction IV. In parallel, the same number of cells must express native mCherry. Fluorescence and ^{129}Xe NMR experiments must be performed of these two samples, assessing the proof of concept of the dual *in cellulo* detection of a recombinant protein by a smart biosensor.

BIBLIOGRAPHY

[1] William J. Dower. *Electroporation of Bacteria: A General Approach to Genetic Transformation*, pages 275–295. Springer US, Boston, MA, 1990.

[2] Roslyn Tedja, May Lim, Rose Amal, and Christopher Marquis. Effects of serum adsorption on cellular uptake profile and consequent impact of titanium dioxide nanoparticles on human lung cell lines. *ACS Nano*, 6(5):4083–4093, 2012.

10

OUTLOOK AND CONCLUSION

The study of a dual biosensor has allowed us to appreciate the challenging properties of xenon as a probe of *in cellulo* events. When encapsulated in the biosensor it has a different response whether the biosensor binds its target or not. Moreover, experiments proved that ^{129}Xe NMR is sensitive enough to differentiate two different targets. We have observed caged xenon chemical shift variation up to 17.2 ppm when the biosensor is bound to a tagged peptide.
In addition, the biosensor exhibits a 24-times fluorescent enhancement and a fluorescence emission shift upon binding. This fluorogenic capability has provided valuable assistance for the study of the *in cellulo* internalization and distribution.

This approach has been extended to detection of recombinant proteins with the example of the fluorescent protein family. This system was particularly interesting as it added more information about the binding thanks to the FRET phenomenon.

New ^{129}Xe NMR detection schemes have been implemented in order to lower the detection threshold. We were able to detect the biosensor internalized in mammalian cells. This is paving the way for intracellular detection of ^{129}Xe NMR-based biosensors.

It should be pointed out that this project is a *proof of concept*. However, some criteria constrain its application as it is:

- Its synthesis, starting from the enantiopure cryptophane to the functionalization by the ligand is complex and time consuming. In addition the reaction yield is very poor due to the last step consisting in grafting the ligand on only one COOH group of the cryptophane moiety. The quantities obtained during this study are not sufficient for performing many *in cellulo* experiments.

- The biosensor contains two arsenic atoms that we need to deal with. Even if it is outweighed by the presence of an antidote preventing binding to endogenous proteins, residual non specific binding could lead to a slight toxicity for patients.

- Since the targeted peptidic sequence does not exist in endogenous proteins, *in vivo* protein detection is not possible with the actual design. Indeed, the tag sequence cannot be biologically inserted in protein genes.

The biosensor is a precursor of a new generation of multimodal probes. Some improvements can already be envisioned:

- **On the xenon host synthesis.** Recently, we have reported a new approach for the preparation of cryptophanes for ^{129}Xe NMR biosensing applications. [1] This strategy is based on a chemical transformation of the cryptophane-223 skeleton. The originality of this approach comes from the possibility of introducing a reactive group different from the six reactive groups attached on the phenyl rings on the central carbon of the propylenedioxy linker. The secondary alcohol can then be used as a handle for the synthesis of new reactive cryptophane derivatives. This strategy also allows the synthesis of larger quantities of biosensors.
  This would be an appropriate solution for the poor reaction yield of the bimodal biosensor. Indeed, with this strategy, we can expect almost all cryptophanes to be mono-functionalized by the CrAsH ligand. ^{129}Xe NMR experiments should be conducted first in order to verify that the exchange of the xenon is not altered.
  This way, the six other groups of the cryptophane moeity could be functionalized by other chemical groups in order to modify its interaction with the cell. A cell penetrating peptide can even be grafted for an internalization optimization.

- **On the ligand.** The CrAsH ligand is an example of responsive ligand among several other examples. It can therefore be interchanged with any other ligand that does not contain arsenic. It is the case, for instance, for RhoBo biosensor where arsenic atoms are replaced by boron atoms which are less toxic.[2]

Even if the biosensor is not designed for *in vivo* protein detection, it can serve as a bimodal sensor for drug bio-distribution studies. It is also possible to choose another ligand that binds endogenous peptidic sequence. For instance, again the RhoBo responsive probe could be employed for detection of tetraserine-containing proteins on the carbohydrate-rich cell surface in the cytosol, as in [2].

A mini-review on ^{129}Xe NMR-based biosensors has been published in Analyst.

This project takes benefit of a new generation of ^{129}Xe NMR-based biosensors.[3] Hyperpolarized xenon has outstanding properties, and its combination with host molecules constitutes unique systems for the longitudinal follow-up of biological events. The principle is rather different from the strategies based on the delivery of species that have been hyperpolarized by DNP or by parahydrogen, which are limited by the longitudinal relaxation time of their nuclei. Our approach includes a first step for the delivery of the xenon biosensor, which will hopefully reach its target. Then, in a second step completely distinct from the first step, hyperpolarized xenon can be introduced and imaging can be performed. The latter operation can be repeated many times. With regard to the final objective, namely, to monitor pathological processes *in vivo* via this approach, ^{129}Xe NMR-based sensors offer huge potential and applications are under way.

This interdisciplinary project allowed me to work on each step of the study. I had the chance to discover organic synthesis, purification methods and chemical analysis. Then I was actively involved in the optimization of the spin exchange optical pumping setup and the conception of hyperpolarized ^{129}Xe experiments. Research and improvement on the SEOP setup are sill ongoing. Since this is not a standard analysis tool - but an experimental research topic - the setup constantly needs optimization, tailor-made technical implementations, reparations etc. I was also involved in the creation of a transportable setup, enabling hyperpolarized xenon transfers in the vicinity of medical imagers (see Figure 110) and preliminary *in vivo* experiments in Orléans.

Collaboration with Sandra Meme, William Meme and Frederic Szeremeta (CBM Orléans).

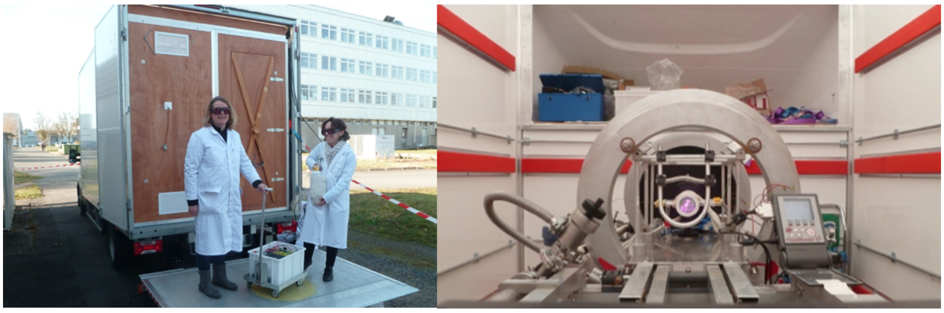

Figure 110: Photographs of: **A.** the van transporting the hyperpolarization setup. **B.** Hyperpolarization setup in the van.

In these experiments, 50 mg of hyperpolarized ^{129}Xe - in 5 minutes at P = 0.15- 0.25 - were produced with our home-made setup and delivered into the lungs of a mouse via inhalation. TRUE-FISP images enabled us to observe a dynamic distribution of xenon into the three lobes of the lungs (see one image on Figure 111A). We then instilled 0.15 mmol of an hydrophilic cryptophane (Cr-AM) into the lungs and recorded the evolution of the xenon signal through time (see Figure 111B).

After 20 minutes assuring absorption of the cryptophane solution, we were able to detect the signal of xenon gas into the lung as well as the dissolved xenon encapsulated into the cryptophane. We repeated the experiments for the two next hours and observed that the cryptophane was likely to be metabolized through the alveoli of the lung. Moreover, the signal is slightly shifted, proving that the xenon environment has been modified. More work should be done in order to confirm some hypotheses, such as the small peak next to the xenon

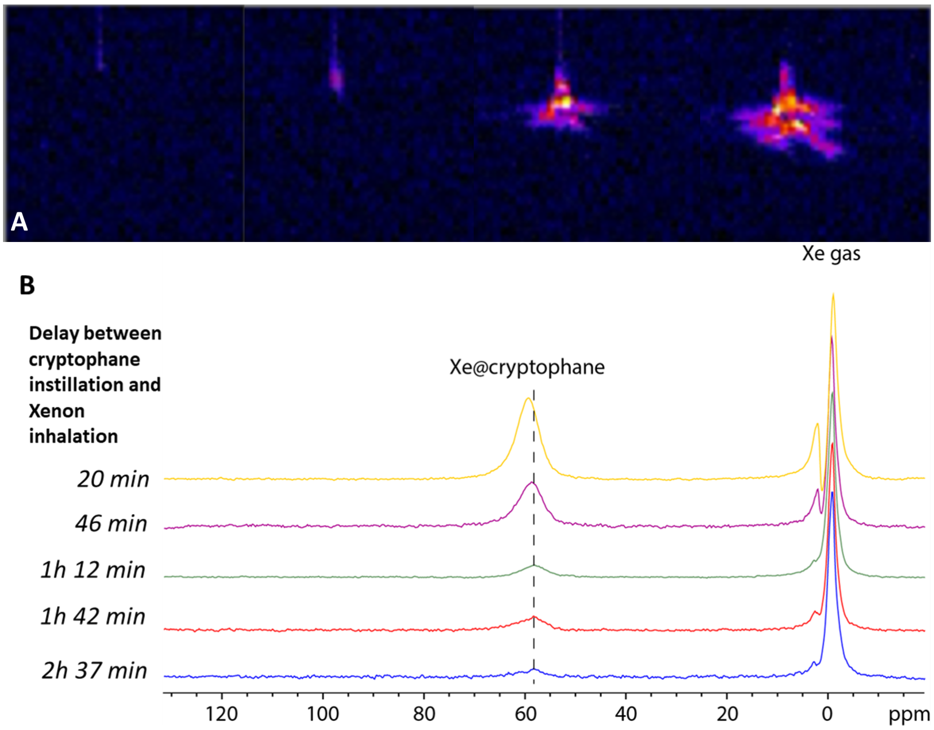

Figure 111: **A.** TRUE-FISP Coronal encoding images of hyperpolarized ^{129}Xe in the lungs of a mouse. FOV 5 x 3 cm; Slice 3 cm; 64 x 64, only 2D-FFT, TE = 1.3 ms, TR = 2.6 ms and 0.5 s per image. **B.** 0.15 mmol of Cr-AM were instilled into the lungs and 90° Gaussian pulses of 800 µs centered at 60ppm were implemented with TR = 73.5 ms, NS = 2 and TD1 = 512.

gas signal, which could correspond to the signal of xenon gas in the alveoli.

Finally I extended my abilities in molecular biology techniques, from the culture of bacterial and mammalian cells, the modification, expression and purification of proteins, to the creation of modified stable lines. I had the opportunity to compare NMR and optical imaging techniques and even develop optimized ^{129}Xe NMR sequences.

Thanks to the diversity of the research based on the use of xenon, I was involved in many different projects. We studied with our collaborators from the Laboratoire de Chimie de l'ENS Lyon the ^{129}Xe NMR properties of the new biosensing platform cryptophane-223, introducing a reactive group on the central carbon of the propylenedioxy linker. With our partners from Service de Chimie Bioorganique et de Marquage and Institut Gustave Roussy, we conceived a ^{129}Xe NMR-based biosensor for detection of Non-Small Cell Lung Cancer. This work has been performed *in cellulo* and will - with some improvements regarding the synthesized quantities - be extended to *in vivo* experiments shortly.

Efforts are now focused on extending this recent concept of ^{129}Xe NMR-based biosensing to other *in vivo* applications, because xenon can cross the pulmonary alveolar-capillary barrier and other multilayer barriers such as the blood–brain barrier without significant loss of hyperpolarization. However, the transition to *in vivo* experiments requires some adaptations. Both the protocols used to deliver hyperpolarized xenon and the NMR/MRI methods depend on the targeted organ. It is expected that the local density of free hyperpolarized xenon will be lower than for *in vitro* situations, and that the longitudinal relaxation time of xenon outside the host may be short (shorter than in the host), which will result in a poorer signal-to-noise ratio. Moreover, many analytes, ions, etc. can compete with xenon *in vivo* for interactions with the host molecule. The ^{129}Xe NMR-based sensors and NMR methods have to be rethought in order to take into account these changes.

Additional issues such as the delivery of hyperpolarized xenon and biosensors to the receptors of interest also need to be addressed. For instance, hyperpolarized xenon can be delivered into the bloodstream by injection in physiological solutions or into the lung and brain via inhalation.

To conclude, I was puzzled by the outstanding properties of xenon. Easily hyperpolarizable by optical pumping, xenon offers a dramatic increase in sensitivity in NMR and MRI. Another great quality of xenon is its exceptional responsiveness to its environment which translates by a large variability of the NMR parameters (chemical shift, relaxation time, etc.), which allows a wide range of physical-chemical, biological and medical applications.

BIBLIOGRAPHY

[1] Laure-Lise Chapellet, James R. Cochrane, Emilie Mari, Céline Boutin, Patrick Berthault, and Thierry Brotin. Synthesis of cryptophanes with two different reaction sites: Chemical platforms for xenon biosensing. *The Journal of Organic Chemistry*, 80(12):6143–6151, 2015.

[2] Xiaolong Sun, Wenlei Zhai, John S. Fossey, and Tony D. James. Boronic acids for fluorescence imaging of carbohydrates. *Chem. Commun.*, 52:3456–3469, 2016.

[3] E. Mari and P. Berthault. 129xe NMR-based sensors: biological applications and recent methods. *Analyst*, 142:3298–3308, 2017.

Part III

APPENDIX

A

APPENDIX

A.1 MATERIALS AND METHODS

A.1.1 *Solvents and reagents*

All experiments in anhydrous conditions were carried out with dry glassware under nitrogen dried on sodium carbonate and silica gel. Anhydrous solvents are obtained by distillation under nitrogen atmosphere in presence of dehydrating agents: calcium hydride for dichloromethane and sodium with benzophenone for diethyl ether and tetrahydrofurane. If not indicated, commercial products were used without further purification.

A.1.2 *Organic synthesis*

A.1.2.1 *Compounds **11** and **12***

(2.86g, 25.9 mmol) of resorcinol **9** is dissolved in $MeSO_3H$ (26 mL) under inert atmosphere and stirring. (2.5g, 13 mmol) of 4-carboxyphtalic **10** is added into the solution. The mixture is not soluble and has a pale orange color. We installed the refrigerant and the mixture is heated at 85°C. After 20 minutes, the mixture becomes a red solution, and above 70°C it becomes black. The solution is heated and stirred for 24 hours.

The black solution is then precipitated in 7 volumes of iced water: a brown precipitate appears immediately. The precipitate is left into a Buchner funnel fitted with a filter connected to a 250 ml flask. The brown precipitate is placed in a heat chamber at 150°C in order to dry up. The dried product is dissolved in NaOH 4M (30 mL) under stirring. A solution of concentrated acid HCl is added drop by drop until the solution precipitates. This precipitate is orange and pH of the mixture is 1-2. NaOH and HCl are removed via a filtration on a Buchner funnel where the precipitate is dissolved by ethanol solution. The filtrate is dried under vacuum over an hour.

MS (ESI-TOF) m/z: 376.3 (100 %, [M+H]+)

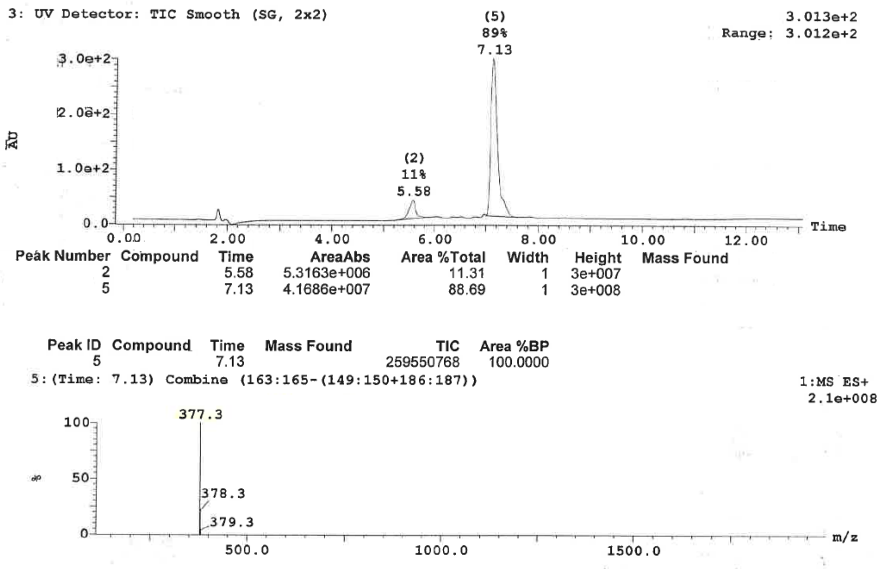

Peak Number	Compound	Time	AreaAbs	Area %Total	Width	Height	Mass Found
2		5.58	5.3163e+006	11.31	1	3e+007	
5		7.13	4.1686e+007	88.69	1	3e+008	

Peak ID	Compound	Time	Mass Found	TIC	Area %BP
5		7.13		259550768	100.0000

5: (Time: 7.13) Combine (163:165-(149:150+186:187))

Figure 112: HPLC purification and MS analysis of compounds **11** and **12**.

A.1.2.2 *Compounds* **13** *and* **14**

The mixture of **11** and **12** (2 mg, 5.32 mmol) is dissolved in TFA (20 mL) under inert atmosphere. Then HgO is added (2.26 g, 10.4 mmol), the solution turns yellow. The solution is stirred over night, the glassware being wrapped in aluminum paper in order to prevent any contact with UVs.

TFA is evaporated via rotary evaporator and the mixture is rinsed with 90 mL of water: an orange precipitate appears. **13** and **14** are filtrated and dried under vacuum.

MS (ESI-TOF) m/z: 1001.5 (100 %, [M+H]+) A yield of 70% is obtained for this step. This product is not soluble in the common solvents.

A.1.2.3 *Compounds* **15** *and* **16**

Compounds **13** and **14** (180 mg, 0.18 mmol) is dissolved in N-Méthyl-2-pyrrolidone (1.5 mL) which was prior dried on sieve over night. $AsCl_3$ (300 µL, 3.4 mmol), DIEA (250 µL, 1.4 mmol) and a solution of $Pd(OAc)_2$ (0.4 mg in 0.1 mL of NMP) are added. The solution is stirred over night.

The mixture is poured into a solution of acetone (8 mL) and phosphate buffer (8 mL, 5.0 g of KH_2PO_4 and 4.0 mg of K_2HPO_4). We add EDT (0.7 mL, 8.17 mmol), a red precipitate appears in a yellow solution. An extraction in $CHCl_3$ is performed. A fraction of anhydrous magnesium sulfate is added as a desiccant. The solution is frozen for the night. The liquid phase containing NMP is removed and the product is dissolved in toluene.

Product is purified on a silica column and eluted by a solution ethyl acetate (50%)/toluene (40%)/acetic acid (10%).

45 mg of compounds **15** and **16** are obtained. (35 % of yield). MS (ESI-TOF) m/z: 708.5 (100 %, [M+H]+)

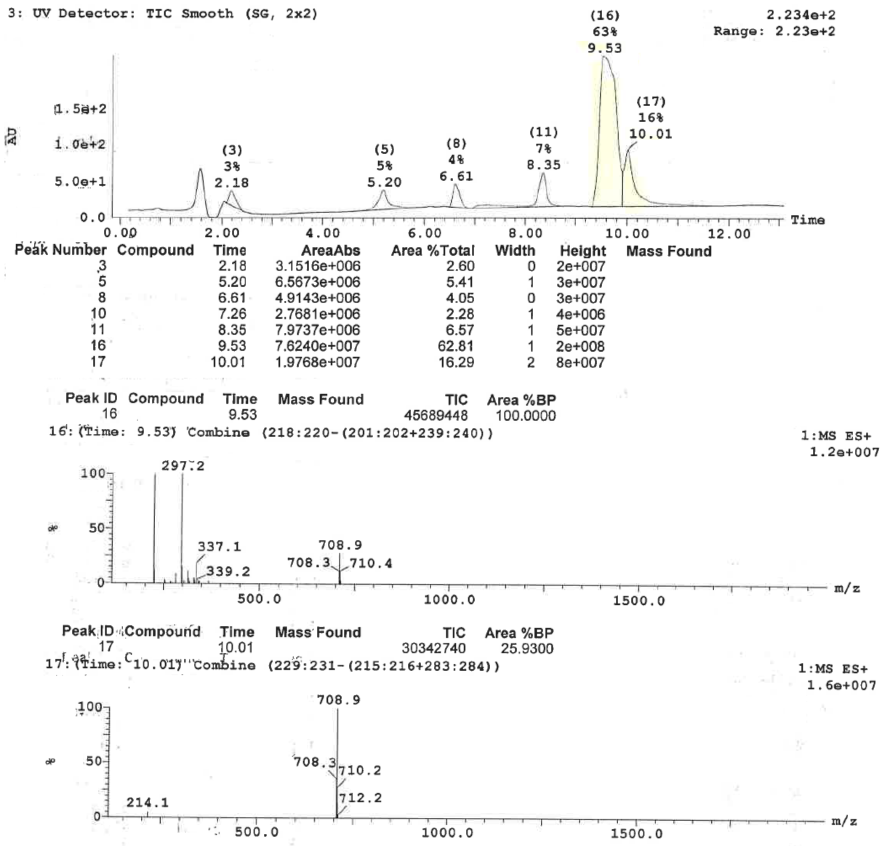

Peak Number	Compound	Time	AreaAbs	Area %Total	Width	Height	Mass Found
3		2.18	3.1516e+006	2.60	0	2e+007	
5		5.20	6.5673e+006	5.41	1	3e+007	
8		6.61	4.9143e+006	4.05	0	3e+007	
10		7.26	2.7681e+006	2.28	1	4e+006	
11		8.35	7.9737e+006	6.57	1	5e+007	
16		9.53	7.6240e+007	62.81	1	2e+008	
17		10.01	1.9768e+007	16.29	2	8e+007	

Peak ID	Compound	Time	Mass Found	TIC	Area %BP
16		9.53		45689448	100.0000

16: (Time: 9.53) Combine (218:220-(201:202+239:240))

Peak ID	Compound	Time	Mass Found	TIC	Area %BP
17		10.01		30342740	25.9300

17: (Time: 10.01) Combine (229:231-(215:216+283:284))

Figure 113: HPLC purification and MS analysis of compounds **15** and **16**.

A.1.2.4 *Compounds 17 and 18*

To a solution of CrAsH isomers **15** and **16** (70 mg, 0.10 mmol) in THF (15 mL), are added DIC (20 L, 0.13 mmol) and NHS (15 mg, 0.13 mmol). The mixture is stirred for 3 hours (the reaction can be monitored by TLC or HPLC) then ethylene diamine (66 L, 1.0 mmol) is added. The solution turns from orange to bright pink and a precipitate appears. The solvent is evaporated and the residue is passed through a C18 silica patch. It is first rinsed with water to remove the excess of ethylene diamine, then the rest of the mixture is eluted with acetonitrile. The fraction is evaporated and gives 45 mg. After HPLC purification, a mixture of **17**, **18**, **19** and **20** is obtained with two retention times. **17** and **18** (long retention time) are separated from **19** and **20** (short retention time). Both mixtures are invested in the next step, only **17** and **18** give rise to the good product.

MS (ESI-TOF) m/z: 750.7 (100 %, [M+H]+) The reaction yield is 20%.

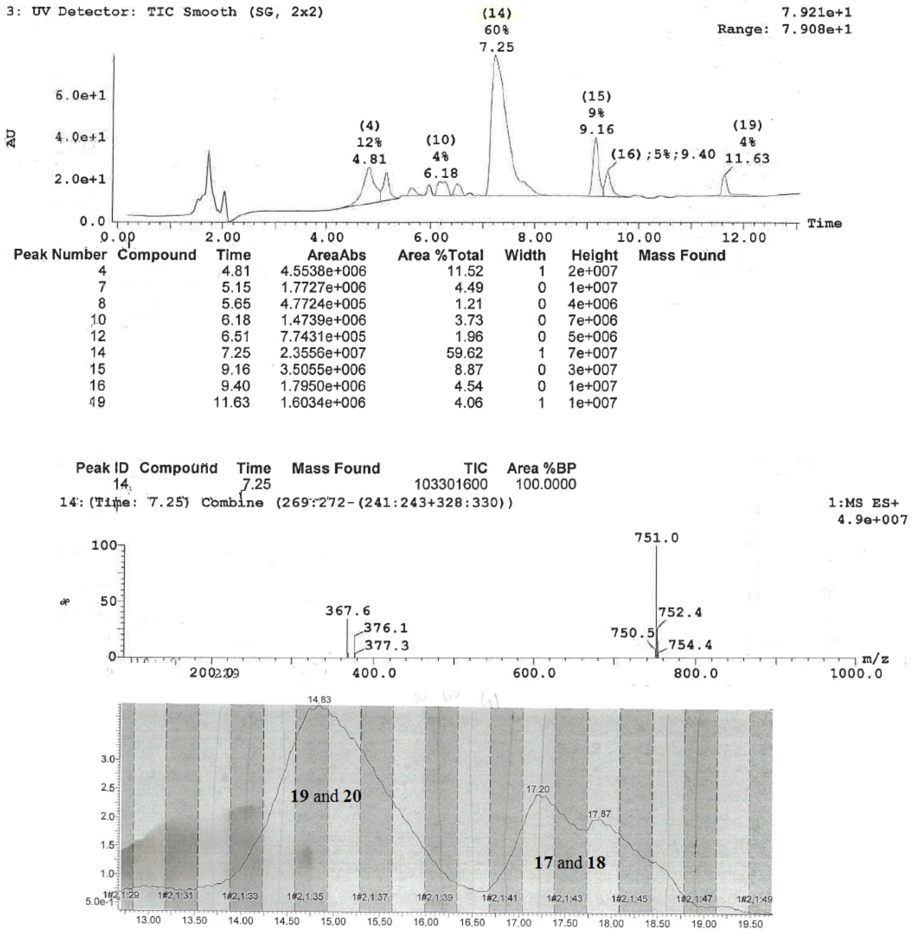

Peak Number	Compound	Time	AreaAbs	Area %Total	Width	Height	Mass Found
4		4.81	4.5538e+006	11.52	1	2e+007	
7		5.15	1.7727e+006	4.49	0	1e+007	
8		5.65	4.7724e+005	1.21	0	4e+006	
10		6.18	1.4739e+006	3.73	0	7e+006	
12		6.51	7.7431e+005	1.96	0	5e+006	
14		7.25	2.3556e+007	59.62	1	7e+007	
15		9.16	3.5055e+006	8.87	0	3e+007	
16		9.40	1.7950e+006	4.54	0	1e+007	
19		11.63	1.6034e+006	4.06	1	1e+007	

Peak ID	Compound	Time	Mass Found	TIC	Area %BP
14		7.25		103301600	100.0000

14: (Time: 7.25) Combine (269:272-(241:243+328:330))

1:MS ES+
4.9e+007
%
100
50
0
751.0
752.4
750.5
754.4
367.6
376.1
377.3
200.0
400.0
600.0
800.0
1000.0
m/z
14.83
19 and 20
17.20
17.87
17 and 18
3.0
2.5
2.0
1.5
1.0
5.0e-1
13.00
13.50
14.00
14.50
15.00
15.50
16.00
16.50
17.00
17.50
18.00
18.50
19.00
19.50

Figure 114: HPLC purification and MS analysis of compounds **17**, **18**, **19** and **20**.

A.1.2.5 *Compounds **MM-1** and **MM-2***

N-hydroxysuccinimide (1.0 mg, 8.6 mol) and N′-ethyl-Ndimethyl aminopropylcarbodiimide (1.8 mg, 9.4 mol) were added under argon atmosphere to a stirred solution of (M;M) (10 mg, 8.6 mol) in DMSO (0.1 mL). The mixture was stirred for 5 hours at room temperature. Then a solution of crude **17** and **18** (4.5 mg) dissolved in DMSO (0.1 mL) and triethylamine were added. The solution was then stirred for an additional 16 hours at room temperature. The excess of triethylamine was removed under reduced pressure. The solution was then directly injected for purification on preparative HPLC chromatography (Luna PFP column. Size: 150x21, gradient: 95/5 to 30/70 H2O/AcCN + 0.1 %HCOOH) to give **MM-1** (2.4 mg, 15%) and **MM-2** (1.4 mg, 9%) as orange solids.

- Compound **MM-1**:

  ^{1}H NMR (700 MHz, D_2O): δ 7.91 (d, 1H, J = 8.0 Hz), 7.78 (d, 1H, J = 8.0 Hz), 7.37 (s, 1H), 6.98 (d, 1H, J = 9.2 Hz), 6.94 (d, 1H, J = 9.2 Hz), 6.76-6.48 (m, 12H), 6.46 (d, 2H, J = 9.2 Hz), 4.60-4.18 (m, 24H), 4.16-3.89 (m, 4H), 3.84-3.46 (m, 8H), 3.37-3.22 (m, 6H), 3.21-3.03 (m, 6H).

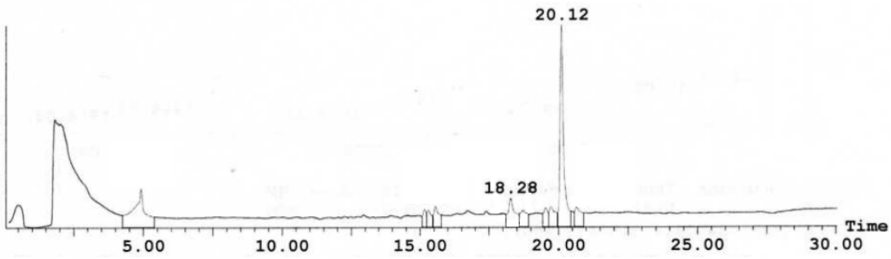

Figure 115: Purity check of **MM-1** on Luna PFP. Gradient H_2O/AcCN 95:5 to 30:70.

  Retention time for **MM-1** is 20.12 min, the peak at 18.28 min corresponds to the product without one arsenic. MS (ESI-TOF) m/z: 1892.3 (100%, [M+H]+).

- Compound **MM-2**:

  After HPLC purification, this compound was obtained as a mixture of **MM-1** and **MM-2** (1:8). ^{1}H NMR (700 MHz, D_2O): δ 8.21 (s, 1H), 7.52 (d, 1H, J = 7.6 Hz), 7.12-7.05 (m, 3H), 6.89- 6.50 (m, 12 H), 6.46 (d, 1H, J = 9.2 Hz), 6.42 (d, 1H, J = 9.2 Hz), 4.73-4.20 (m, 22H), 4.18- 3.98 (m, 6H), 3.96-3.52 (m, 8H), 3.50-3.22 (m, 8H), 3.21-3.01 (m, 4H).

  Retention time for **MM-2** is 20.60 min, the peak at 20.05 min corresponds to the isomer **MM-1**.

  MS (ESI-TOF) m/z: 1892.5 (100%, [M+H]+).

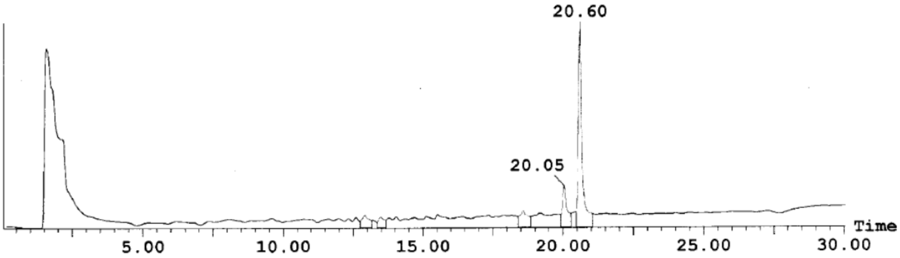

Figure 116: Purity check of **MM-2** on Luna PFP. Gradient H_2O/AcCN 95:5 to 30:70.

A.1.2.6 *Compound **PP-1***

N-hydroxysuccinimide (1.0 mg, 8.6 mol) and N′-ethyl-Ndimethylamino propylcarbodiimide (1.8 mg, 9.4 mol) were added under argon atmosphere to a stirred solution of (P;P) (10 mg, 8.6 mol) in DMSO (0.1 mL). The mixture was stirred for 5 hours at room temperature. Then a solution of crude **17** and **18** (4.5 mg) dissolved in DMSO (0.1 mL) and triethylamine were added. The solution was then stirred for an additional 16 hours at room temperature. The excess of triethylamine was removed under reduced pressure. The solution was then directly injected for purification on preparative HPLC chromatography (Luna PFP column. Size: 150x21, gradient: 95/5 to 30/70 H2O/AcCN + 0.1 %HCOOH) to give **PP-1** (17 %) as an orange solid.

^{1}H NMR (700 MHz, D_2O): δ 7.91 (d, 1H, J = 8.0 Hz), 7.78 (d, 1H, J = 8.0 Hz), 7.37 (s, 1H), 6.98 (d, 1H, J = 9.2 Hz), 6.94 (d, 1H, J = 9.2 Hz), 6.76-6.48 (m, 12H), 6.46 (d, 2H, J = 9.2 Hz), 4.60-4.18 (m, 24H), 4.16-3.89 (m, 4H), 3.84-3.46 (m, 8H), 3.37-3.22 (m, 6H), 3.21-3.03 (m, 6H).

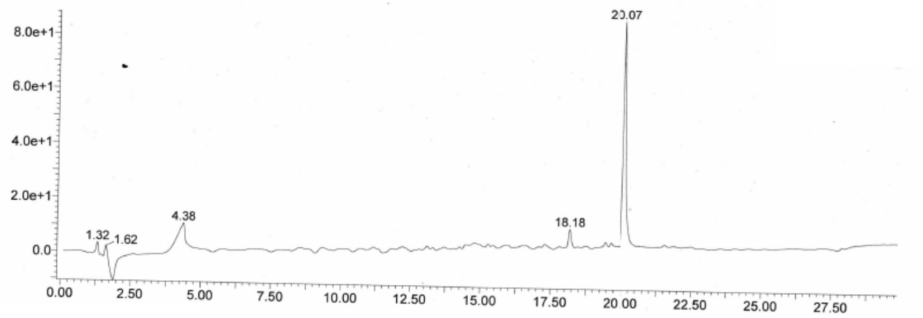

Figure 117: Purity check of **PP-1** on Luna PFP. Gradient H_2O/AcCN 95:5 to 30:70.

Retention time for **PP-1** is 20.07 min, the peak at 18.18 min corresponds to the product without one arsenic.

MS (ESI-TOF) m/z: 1892.3 (100%, [M+H]+).

A.1.3 *DNA Sequencing*

DNAs have been sequenced by Genewiz company. Aquamarine is represented in cyan, mCherry in purple, TC-tag in red and the spacer in yellow.

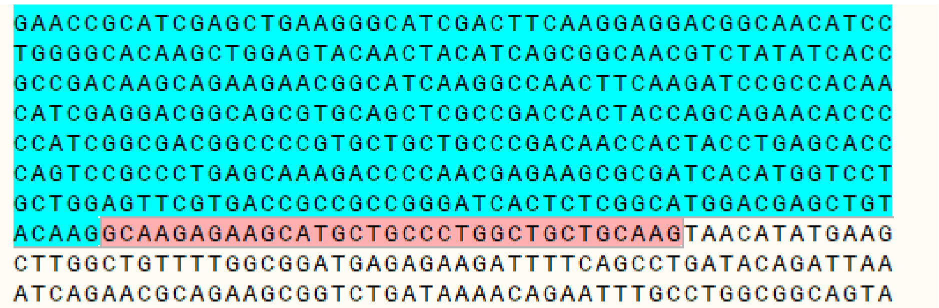

```
GAACCGCATCGAGCTGAAGGGCATCGACTTCAAGGAGGACGGCAACATCC
TGGGGCACAAGCTGGAGTACAACTACATCAGCGGCAACGTCTATATCACC
GCCGACAAGCAGAAGAACGGCATCAAGGCCAACTTCAAGATCCGCCACAA
CATCGAGGACGGCAGCGTGCAGCTCGCCGACCACTACCAGCAGAACACCC
CCATCGGCGACGGCCCCGTGCTGCTGCCCGACAACCACTACCTGAGCACC
CAGTCCGCCCTGAGCAAAGACCCCAACGAGAAGCGCGATCACATGGTCCT
GCTGGAGTTCGTGACCGCCGCCGGGATCACTCTCGGCATGGACGAGCTGT
ACAAGGCAAGAGAAGCATGCTGCCCTGGCTGCTGCAAGTAACATATGAAG
CTTGGCTGTTTTGGCGGATGAGAGAAGATTTTCAGCCTGATACAGATTAA
ATCAGAACGCAGAAGCGGTCTGATAAAACAGAATTTGCCTGGCGGCAGTA
```

Figure 118: DNA sequencing of construction I.

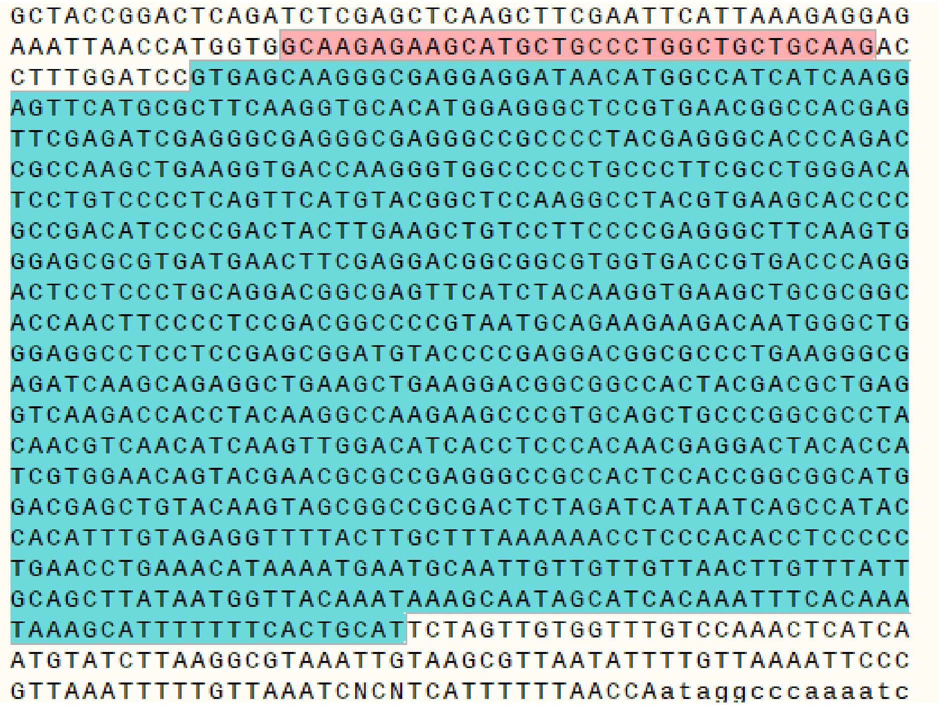

```
GCTACCGGACTCAGATCTCGAGCTCAAGCTTCGAATTCATTAAAGAGGAG
AAATTAACCATGGTGGCAAGAGAAGCATGCTGCCCTGGCTGCTGCAAGAC
CTTTGGATCCGTGAGCAAGGGCGAGGAGGATAACATGGCCATCATCAAGG
AGTTCATGCGCTTCAAGGTGCACATGGAGGGCTCCGTGAACGGCCACGAG
TTCGAGATCGAGGGCGAGGGCGAGGGCCGCCCCTACGAGGGCACCCAGAC
CGCCAAGCTGAAGGTGACCAAGGGTGGCCCCCTGCCCTTCGCCTGGGACA
TCCTGTCCCCTCAGTTCATGTACGGCTCCAAGGCCTACGTGAAGCACCCC
GCCGACATCCCCGACTACTTGAAGCTGTCCTTCCCCGAGGGCTTCAAGTG
GGAGCGCGTGATGAACTTCGAGGACGGCGGCGTGGTGACCGTGACCCAGG
ACTCCTCCCTGCAGGACGGCGAGTTCATCTACAAGGTGAAGCTGCGCGGC
ACCAACTTCCCCTCCGACGGCCCCGTAATGCAGAAGAAGACAATGGGCTG
GGAGGCCTCCTCCGAGCGGATGTACCCCGAGGACGGCGCCCTGAAGGGCG
AGATCAAGCAGAGGCTGAAGCTGAAGGACGGCGGCCACTACGACGCTGAG
GTCAAGACCACCTACAAGGCCAAGAAGCCCGTGCAGCTGCCCGGCGCCTA
CAACGTCAACATCAAGTTGGACATCACCTCCCACAACGAGGACTACACCA
TCGTGGAACAGTACGAACGCGCCGAGGGCCGCCACTCCACCGGCGGCATG
GACGAGCTGTACAAGTAGCGGCCGCGACTCTAGATCATAATCAGCCATAC
CACATTTGTAGAGGTTTTACTTGCTTTAAAAAACCTCCCACACCTCCCCC
TGAACCTGAAACATAAAATGAATGCAATTGTTGTTGTTAACTTGTTTATT
GCAGCTTATAATGGTTACAAATAAAGCAATAGCATCACAAATTTCACAAA
TAAAGCATTTTTTTCACTGCATTCTAGTTGTGGTTTGTCCAAACTCATCA
ATGTATCTTAAGGCGTAAATTGTAAGCGTTAATATTTTGTTAAAATTCCC
GTTAAATTTTTGTTAAATCNCNTCATTTTTTAACCAataggcccaaaatc
```

Figure 119: DNA sequencing of construction II.

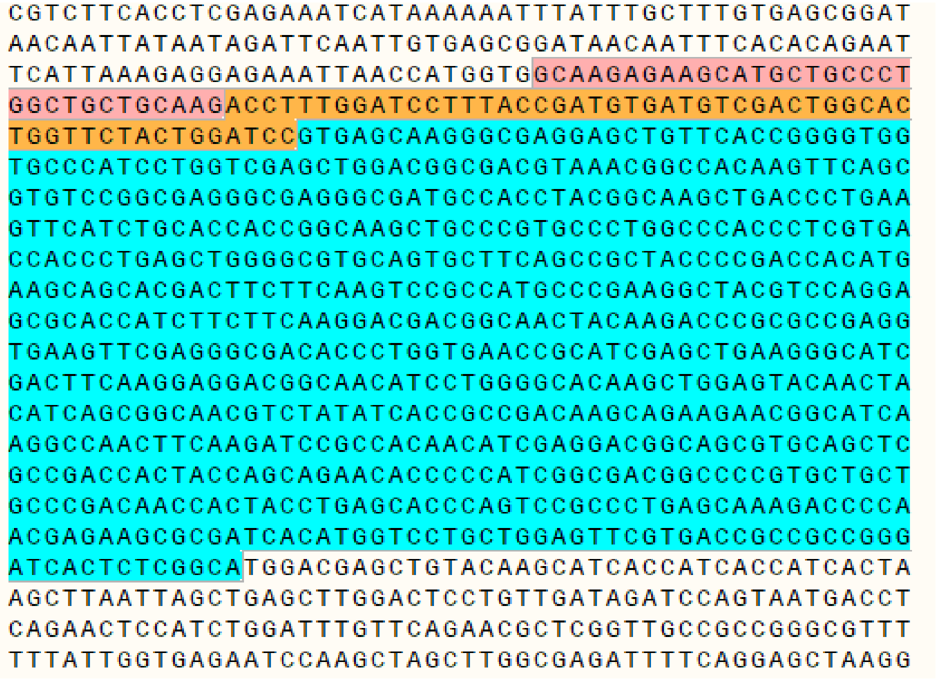

```
CGTCTTCACCTCGAGAAATCATAAAAAATTTATTTGCTTTGTGAGCGGAT
AACAATTATAATAGATTCAATTGTGAGCGGATAACAATTTCACACAGAAT
TCATTAAAGAGGAGAAATTAACCATGGTGGCAAGAGAAGCATGCTGCCCT
GGCTGCTGCAAGACCTTTGGATCCTTTACCGATGTGATGTCGACTGGCAC
TGGTTCTACTGGATCCGTGAGCAAGGGCGAGGAGCTGTTCACCGGGGTGG
TGCCCATCCTGGTCGAGCTGGACGGCGACGTAAACGGCCACAAGTTCAGC
GTGTCCGGCGAGGGCGAGGGCGATGCCACCTACGGCAAGCTGACCCTGAA
GTTCATCTGCACCACCGGCAAGCTGCCCGTGCCCTGGCCCACCCTCGTGA
CCACCCTGAGCTGGGGCGTGCAGTGCTTCAGCCGCTACCCCGACCACATG
AAGCAGCACGACTTCTTCAAGTCCGCCATGCCCGAAGGCTACGTCCAGGA
GCGCACCATCTTCTTCAAGGACGACGGCAACTACAAGACCCGCGCCGAGG
TGAAGTTCGAGGGCGACACCCTGGTGAACCGCATCGAGCTGAAGGGCATC
GACTTCAAGGAGGACGGCAACATCCTGGGGCACAAGCTGGAGTACAACTA
CATCAGCGGCAACGTCTATATCACCGCCGACAAGCAGAAGAACGGCATCA
AGGCCAACTTCAAGATCCGCCACAACATCGAGGACGGCAGCGTGCAGCTC
GCCGACCACTACCAGCAGAACACCCCCATCGGCGACGGCCCCGTGCTGCT
GCCCGACAACCACTACCTGAGCACCCAGTCCGCCCTGAGCAAAGACCCCA
ACGAGAAGCGCGATCACATGGTCCTGCTGGAGTTCGTGACCGCCGCCGGG
ATCACTCTCGGCATGGACGAGCTGTACAAGCATCACCATCACCATCACTA
AGCTTAATTAGCTGAGCTTGGACTCCTGTTGATAGATCCAGTAATGACCT
CAGAACTCCATCTGGATTTGTTCAGAACGCTCGGTTGCCGCCGGGCGTTT
TTTATTGGTGAGAATCCAAGCTAGCTTGGCGAGATTTTCAGGAGCTAAGG
```

Figure 120: DNA sequencing of construction III.

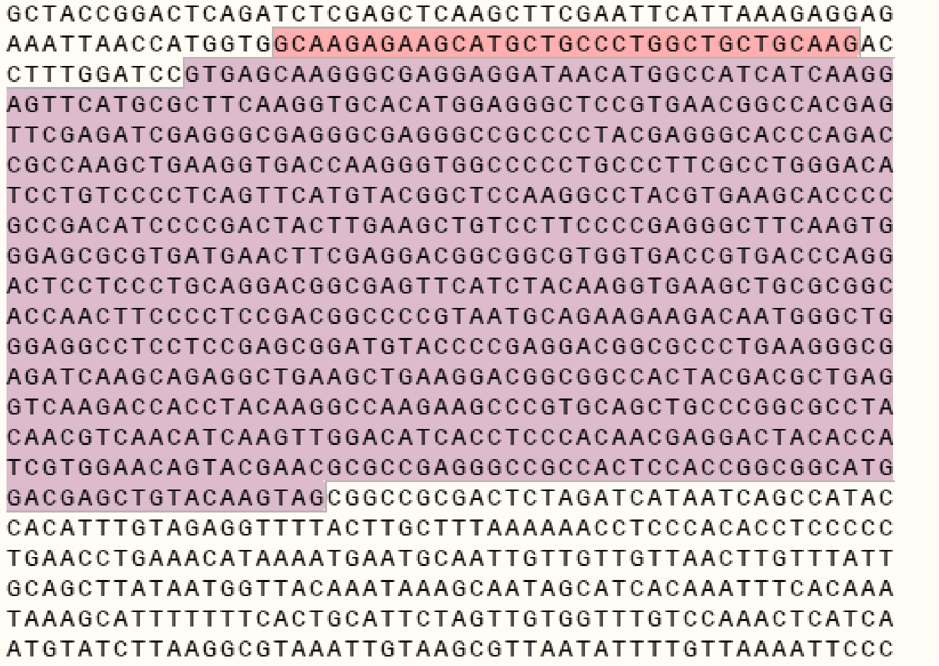

```
GCTACCGGACTCAGATCTCGAGCTCAAGCTTCGAATTCATTAAAGAGGAG
AAATTAACCATGGTGGCAAGAGAAGCATGCTGCCCTGGCTGCTGCAAGAC
CTTTGGATCCGTGAGCAAGGGCGAGGAGGATAACATGGCCATCATCAAGG
AGTTCATGCGCTTCAAGGTGCACATGGAGGGCTCCGTGAACGGCCACGAG
TTCGAGATCGAGGGCGAGGGCGAGGGCCGCCCCTACGAGGGCACCCAGAC
CGCCAAGCTGAAGGTGACCAAGGGTGGCCCCCTGCCCTTCGCCTGGGACA
TCCTGTCCCCTCAGTTCATGTACGGCTCCAAGGCCTACGTGAAGCACCCC
GCCGACATCCCCGACTACTTGAAGCTGTCCTTCCCCGAGGGCTTCAAGTG
GGAGCGCGTGATGAACTTCGAGGACGGCGGCGTGGTGACCGTGACCCAGG
ACTCCTCCCTGCAGGACGGCGAGTTCATCTACAAGGTGAAGCTGCGCGGC
ACCAACTTCCCCTCCGACGGCCCCGTAATGCAGAAGAAGACAATGGGCTG
GGAGGCCTCCTCCGAGCGGATGTACCCCGAGGACGGCGCCCTGAAGGGCG
AGATCAAGCAGAGGCTGAAGCTGAAGGACGGCGGCCACTACGACGCTGAG
GTCAAGACCACCTACAAGGCCAAGAAGCCCGTGCAGCTGCCCGGCGCCTA
CAACGTCAACATCAAGTTGGACATCACCTCCCACAACGAGGACTACACCA
TCGTGGAACAGTACGAACGCGCCGAGGGCCGCCACTCCACCGGCGGCATG
GACGAGCTGTACAAGTAGCGGCCGCGACTCTAGATCATAATCAGCCATAC
CACATTTGTAGAGGTTTTACTTGCTTTAAAAAACCTCCCACACCTCCCCC
TGAACCTGAAACATAAAATGAATGCAATTGTTGTTGTTAACTTGTTTATT
GCAGCTTATAATGGTTACAAATAAAGCAATAGCATCACAAATTTCACAAA
TAAAGCATTTTTTTCACTGCATTCTAGTTGTGGTTTGTCCAAACTCATCA
ATGTATCTTAAGGCGTAAATTGTAAGCGTTAATATTTTGTTAAAATTCCC
```

Figure 121: DNA sequencing of construction IV.

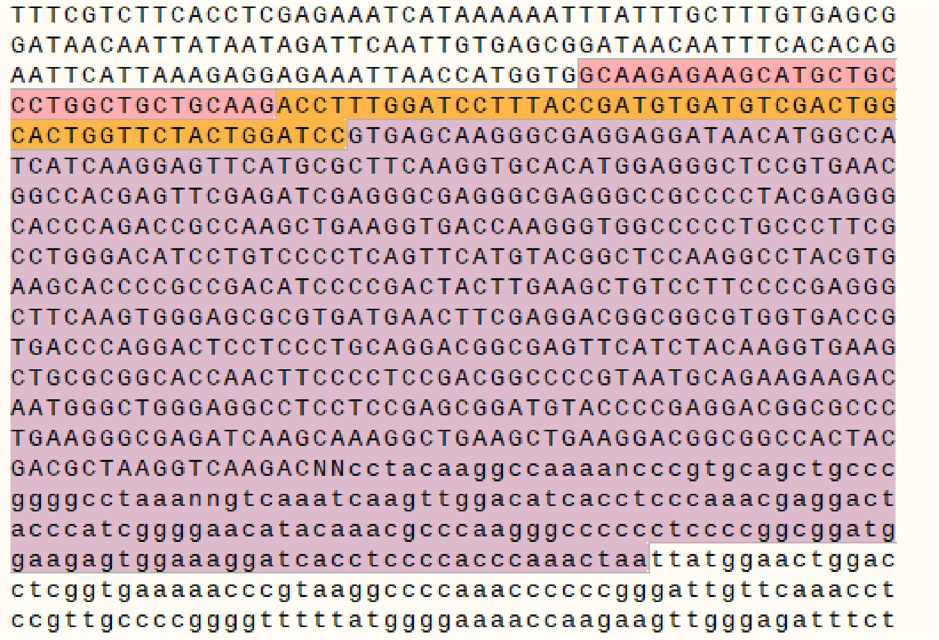

```
TTTCGTCTTCACCTCGAGAAATCATAAAAAATTTATTTGCTTTGTGAGCG
GATAACAATTATAATAGATTCAATTGTGAGCGGATAACAATTTCACACAG
AATTCATTAAAGAGGAGAAATTAACCATGGTGGCAAGAGAAGCATGCTGC
CCTGGCTGCTGCAAGACCTTTGGATCCTTTACCGATGTGATGTCGACTGG
CACTGGTTCTACTGGATCCGTGAGCAAGGGCGAGGAGGATAACATGGCCA
TCATCAAGGAGTTCATGCGCTTCAAGGTGCACATGGAGGGCTCCGTGAAC
GGCCACGAGTTCGAGATCGAGGGCGAGGGCGAGGGCCGCCCCTACGAGGG
CACCCAGACCGCCAAGCTGAAGGTGACCAAGGGTGGCCCCCTGCCCTTCG
CCTGGGACATCCTGTCCCCTCAGTTCATGTACGGCTCCAAGGCCTACGTG
AAGCACCCCGCCGACATCCCCGACTACTTGAAGCTGTCCTTCCCCGAGGG
CTTCAAGTGGGAGCGCGTGATGAACTTCGAGGACGGCGGCGTGGTGACCG
TGACCCAGGACTCCTCCCTGCAGGACGGCGAGTTCATCTACAAGGTGAAG
CTGCGCGGCACCAACTTCCCCTCCGACGGCCCCGTAATGCAGAAGAAGAC
AATGGGCTGGGAGGCCTCCTCCGAGCGGATGTACCCCGAGGACGGCGCCC
TGAAGGGCGAGATCAAGCAAAGGCTGAAGCTGAAGGACGGCGGCCACTAC
GACGCTAAGGTCAAGACNNcctacaaggccaaaancccgtgcagctgccc
ggggcctaaanngtcaaatcaagttggacatcacctcccaaacgaggact
acccatcggggaacatacaaacgcccaagggccccctccccggcggatg
gaagagtggaaaggatcacctccccacccaaactaattatggaactggac
ctcggtgaaaaacccgtaaggccccaaacccccgggattgttcaaacct
ccgttgccccggggttttatggggaaaaccaagaagttgggagatttct
```

Figure 122: DNA sequencing of construction V.

A.1.4 *Buffers*

All concentrations are given in mM.

1. PBS (pH 7.4):
   - KCl 2.7
   - KH_2PO_4 1.5
   - Na_2HPO_4 8.1
   - NaCl 137
2. TE buffer
   - Tris HCl (pH 8) 10
   - EDTA 1
3. Buffer P1
   - Tris HCl (pH 8) 25
   - EDTA 10
   - RNAse 20 µg/ml
4. Buffer P2
   - NaOH 200

  - SDS 1%

5. Buffer P3
   - $K_2CH{-}3CO_2$ 5000
   - CH_3CO_2H 1700

Commercial kit buffer are not described here.

A.1.5 *Methods*

A.1.5.1 *Bacterial cell culture*

Bacterial cell lines (DH5α and TOP10) were purchased from Invitrogen (Thermo Fisher Scientific, Waltham, MA). Bacteria were grown from a single colony-forming unit over night in LB-broth (bacterial medium) containing the corresponding selection antibiotics with shaking (150 rpm) at 37°C.

A.1.5.2 *Plasmid preparation*

Plasmids were prepared either with a non-commercial protocol (in the following called standard protocol) or with a commercial endotoxin free preparation kit (EndoFree Plasmid Maxi Kit, QIAGEN, Venlo, Netherlands). After preparation, the plasmid solutions were aliquoted and stored at -20°C.

A.1.5.2.1 STANDARD PROTOCOL (MINI-PREPARATION) Bacteria were grown over night in 5 ml LB broth. The suspension was centrifuged (8 min at 3000 g) and the supernatant discarded. The remaining pellet was resuspended with 200 μl buffer P1 by vortexing. For lysing the bacteria 200 μl of buffer P2 were added and mixed by gentle inversion of the tube, then incubated for 5 min at room temperature. The reaction was stopped by the addition of 200 μl of buffer P3, which results in a fluffy white precipitation. After another centrifugation step (15 min, 13,000 rpm), the supernatant was transferred to a fresh tube. The containing DNA was precipitated by the addition of 420 μl of pure isopropanol and gentle shaking. This step is followed two more centrifugation steps (5 min, 13,000 g) and an intermediate washing step with 420 μl of 70 % ethanol. The received DNA palled was dried (approximately 5 – 10 min, 65°C) and resuspended with 40 μl water. The protocol gave a typical yield of 40 μg DNA.

A.1.5.2.2 ENDOTOXIN-FREE PROTOCOL (MAXI-PREPARATION) The supplier's protocol was followed: A bacteria pre-culture was started from a single colony-forming unit and 5 ml LB broth containing the appropriate selective antibiotic (shaking incubation at 300 rpm for 8 h at 37 C). 200 μl of the pre-culture was used to inoculate 100 ml of fresh

LB medium containing the selective antibiotic, which was incubated over night at 37°C and shaking at 300 rpm. The next day, the bacteria suspension was centrifuged at 3,000 g for 30 min at 4°C. The received pellet was resuspended with 10 ml of the kit buffer P1 by vortexing, then 10 ml of the kit lysis buffer P2 was added and mixed by inversion. After an incubation of 5 min at RT, 10 ml of pre-cooled (4°C) kit buffer P3 was added and gently mixed by inversing. The suspension was poured into the barrel of the QIAfilter Cartridge and incubated for 10 min. Afterwards, the suspension was filtered through the cartridge. 2.5 ml of the kit buffer ER was added to the filtrate, mixed by inversion, and then incubated on ice for 30 min. This solution was filtered through an equilibration buffer QBT QIAGEN-tip by gravity flow. The flowthrough was discarded. The tip was washed two times with 30 ml of wash buffer QC. Importantly, the following steps were performed using endotoxin-free plastic ware. The DNA was eluted from the tip with 15 ml buffer QN and precipitated by adding 10.5 ml isopropanol. After a centrifugation step (3,000 g, 1 h, 4°C), the received pellet was washed with 40 ml of 70% ethanol and centrifuged again (3,000 g, 20 min). The final DNA pellet was air-dried for 5 – 10 min and redissolved in 500 µl of endotoxin-free buffer TE. The protocol gave a typical yield of 400 µg DNA.

A.1.5.3 *Plasmid cloning*

The cloning conception has been achieved thanks to SnapGene software.

The tetraCysteine tag gene was synthesized by Eurofins Genomics. In the design of the sequence, we added two restriction sites in order to be able to insert this DNA sequence into the host vector, directly either at the N-terminal part or the C-terminal part. Also we placed another chosen restriction site (unique) inside the sequence that allows easy screening for positive clones. When digesting with the corresponding enzyme, only vectors containing the tetracysteine motif are cut.

The bacterial vector of fluorescent proteins and insert (TC-tag) were digested with the selected restriction enzymes (BsrGI and HindIII). DNA vectors and fragments were purified on 0.8% agarose gels (DNA gel extraction performed with E.Z.N.A.® Gel Extraction Kit (Omega Bio-Tek, Norcross, GA)) and ligated using a T4 DNA ligase (all enzymes were purchased from New England Biolabs, Ipswich, MA).

As an example, Figure 123 shows the TG-tag sequence inserted into the pProHex-Histag-Aquamarine vector at BsrGI and HindIII restriction sites, in such a way Aquamarine is directly fused to Histag in NH_2-term and tetraCysteine tag in COOH-term.

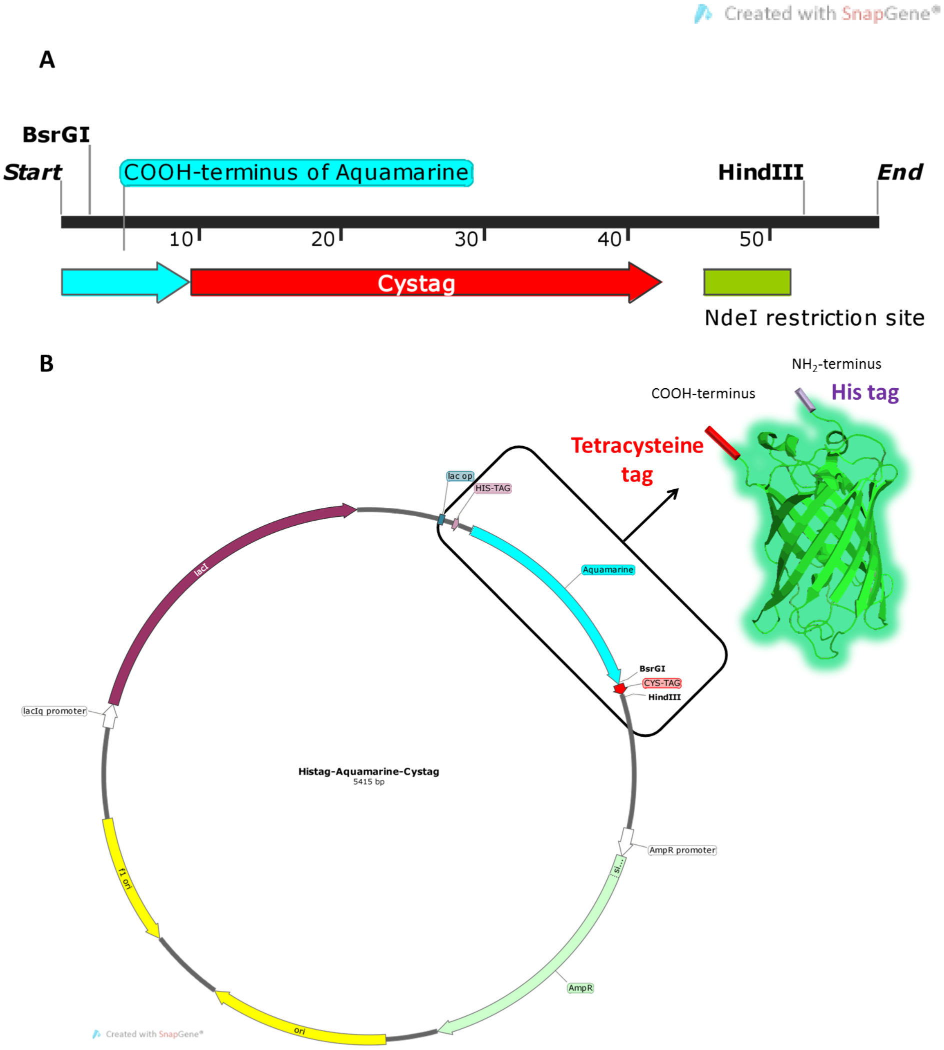
Created with SnapGene
A
BsrGI
Start
COOH-terminus of Aquamarine
HindIII
End
10
20
30
40
50
Cystag
NdeI restriction site
B
NH$_2$-terminus
COOH-terminus
His tag
Tetracysteine tag
lac op
HIS-TAG
Aquamarine
BsrGI
CYS-TAG
HindIII
lacI
lacIq promoter
Histag-Aquamarine-Cystag
5415 bp
AmpR promoter
Si...
AmpR
f1 ori
ori
Created with SnapGene

Figure 123: **A** Designed sequence of the insert coding for tetracystein core, fused at the end of the Aquamarine sequence with NdeI restriction site. **B** Map of the designed vector coding for Aquamarine fused to Histag in NH_2-terminal part and tetraCysteine tag in COOH-terminus

A.1.5.4 *Protein production and purification*

Production and purification of His-tagged recombinant Aquamarine and mCherry tagged with a tetracysteine sequence was performed using Top10 bacterial cells. Competent cells were transformed with the corresponding vector. A starter culture which was grown o.n. was used (25 ml) to inoculate the 1.5 l of Luria-Bertani medium containing 100 µg/ml selecting antibiotic ampicillin. At an OD_{600} = 0.6, protein production was induced by adding isopropyl-β-d-thio-galactopyranoside (IPTG, 1 mM) and cultured for 18 h at 30°C. This suspension was centrifuged and frozen. The cells were resuspended in lysis buffer (30 ml; 50 mM Tris–HCl, 5 mM 2-mercaptoethanol, 1 mM phenylmethylsulphonyl fluoride and 0.02 mg/ml DNase), and sonicated. A centrifugation step (120,000 g, 1 h 30, 6°C) was performed to remove debris. The received supernatant was filtered with a 0.22 µm filter and diluted by a factor 2 with phosphate buffer (30 mM NaH2PO4, 700 mm NaCl and 30 mm imidazole, pH 7.5). A nickel-nitriloacetic acid agarose (Ni–NTA) column (15 ml; Sigma) was loaded with this dilution and incubated for 1 h. Afterwards, the protein was eluted (30 mM NaH2PO4, 100 mM NaCl and 150 mM imidazole, pH 7.5) and further concentrated. After a final dialysis step (dialysis buffer: 30 mM phosphate, pH 7.4), the concentration of the purified protein solution was measured by absorption and stored at -20°C.

A.1.5.5 *Eukaryotic cell culture*

Eukaryotic cell line COS7 was obtained from American Type Culture Collection, Manassas, VA. COS7 cells were cultured at 37°C and 5% CO_2 in DMEM containing 10% FBS, using 75 cm^2 cell culture flasks. For passaging, COS7 cells were washed three times with PBS and incubated with 2 ml trypsin for 5 min at 37°C. Reaction was stopped by adding 8 ml of growth medium. Cells were diluted 1/5 to 1/7, the maximum passage number was P20. For 6-well plates cells were counted with the aid of a Malassez counting chamber and diluted to $4.5.10^5$ cells/well, for 24-well plates cells were diluted to $1.0.10^5$ cells/well.

A.1.5.6 *Transient transfection of COS cells*

The transfection efficiency was monitored with Flow Cytometry. We tested different transfection reagents and finally decided to change from Lipofectamine® 2000 (Thermo Fisher Scientific, Waltham, MA), which was routinely used in our group, to X-tremeGene HP DNA transfection reagent (Roche Diagnostics GmbH, Germany) since the latter provides a strongly increased cell viability after transfection, the efficiency of the transfection was similar, though. Afterwards, the optimal ratio of DNA to transfection reagent was determined and found to be 1 : 3 (DNA (µg) : XtremeGene HP (µl)). In the following, the general procedure of the transfection will be explained: Cells were seeded in 8-well Labtek plates the day prior transfection and transfected following the suppliers' instructions. For the X-tremeGene HP based transfection, DNA was diluted with 200 µl OptiMEM® (Gibco, life technologies) to a final total concentration of 0.2 µg/well together with three times more transfection reagent (i.e. 1 µg DNA needs 3 µl transfection reagent). After an incubation of 30 min at 37°C, the dilution was added to the cells containing 2 ml of regular growth medium. Cells were used 24 to 48 h after transfection.

A.1.5.7 *Electrophoresis*

Solutions of purified proteins were thawed on ice. Samples were prepared by adding Laemli buffer (4% SDS, 20% glycerol, 10% 2-mercaptoethanol, 0.004% bromophenol blue and 0.125 M Tris HCl, pH approx. 6.8. at 1 : 1) to a final loading mass of 50 ng of purified protein. The solutions were denatured at 95°C for 5 min and loaded to a Novex® NuPAGE Bis-Tris SDS-PAGE gel of 10% acrylamide (Thermo Fisher Scientific Inc., Waltham, MA). Elecrophoresis was performed at 175 V for 30 – 45 min (buffer: NuPAGE® MES SDS Running Buffer, Thermo Fisher Scientific).

A.1.5.8 *Flow cytometry*

Flow cytometry allows the measurements of fluorescence intensities of microscopic particles (beads, yeast, bacteria eukaryotic cells. . .). In this method a liquid stream is transporting the particles through a flow cell, where they are hit by one or several laser beams. The velocity of the stream is adjusted in a way which allows only the passage of one cell at a time thus allowing a detection in a cell by cell manner. Within minutes, several 10,000 to 100,000 cells can be detected and counted, which gives statistically relevant results about the composition of a cell population. The flow cytometer is equipped with several lasers, pinholes, dichroic mirrors, selection filters, and detectors allowing the simultaneous detection of multi-coloured fluorescent labels in the same cell. A cell passing through the laser beam scatters light, which is detected by forward (FSC) and side scattered light (SSC) detectors, respectively. The FSC (diffraction) is proportional to the volume of the cell, the SSC (refraction) depends on the composition of the cell, e.g. its granulosity, size/composition of the nucleus, and its vesicles. A dot plot of FSC against SSC allows the discrimination of live cells from debris or necrotic/apoptotic cells, and even a differentiation of distinct cell types. The flow cytometer used in this study is furnished with three lasers (405/488/561 nm) and detectors for CFP, YFP (Yellow Fluorescent Protein), mCherry and FRET.

For this experiment, cells were transfected 20 – 24 h prior. The next day, cells were incubated with biosensor for 1 hour at 37°C and rinsed. Cells were detached with trypsin, washed with PBS, and kept in PBS on ice. Aliquots of few ten thousands of cells were diluted in PBS and passed through the cytometer.

For data analysis, the Summit software (Daco Colorado, Inc., Fort Collins, CO) was used. We set a limit between auto-fluorescence and fluorescence using non-transfected cells sample.

A.1.5.9 *Fluorescence microscopy*

The FloRa wide field microscope is based on an inverted 4-port Leica DM18 equipped with a Sola source (Lumencor), a universal stage, 6 filter cubes and a Hamamatsu Orca Flash 4 camera. It is controlled by Metamorph software.

Confocal microscopy was performed on an inverted Leica DMI 6000 equipped with a 405 nm laser and a white light laser (470-670 nm), 4 filter cubes and 2 photomultiplier tubes (Hamamatsu 6357) and 2 Hybride detectors (Hamamatsu). Photomultiplier tubes were set at 800 V and power of laser at 20 %. We chose 512 x 512 the number of pixels and 400 Hz for the scan speed. It is controlled by LAS-X software. We used the Hyb3 filter cube that allows us to observe the fluorescence emission between 500 and 550 nm.

For fluorescence microscopy experiments, COS7 cells were cultured in 8-well LabTek and incubated with biosensor for 1 hour in DMEM and 30 % FBS. The cells were rinsed and imaged.

A.1.5.10 *Fluorescence lifetime imaging*

The FLIM setup is working with pulsed laser diodes at 440 nm for samples with a cyan donor and at 466 nm for samples with a yellow donor (PicoQuant GmbH, Berlin, Germany) driven by a PDL 800 driver (100 ps FWHM, 20 MHz of repetition rate, PicoQuant GmbH, Berlin, Germany). The excitation sources are coupled to a C1 scanning head (Nikon) with a optical fiber. The scanning head was controlled by the EZ-C1 software (Nikon). The excitation beam crossed an empty position of the epi-fluorescence filter turret and was focused on the sample through the microscope's objective lens. The scanning head probed a 100 x 100 µm maximum field of view with a laser pixel dwell time of 61.44 µs. The TCSPC detection was inserted in the collimated section just below the microscope objective. The pathway was composed of a cube containing a dichroic mirror positioned at 45° from the optical path (SWP-500, Lambda Research Optics, Inc. Costa Mesa, CA), a focusing lens (f =20cm, Thorlabs, Newton, NJ), a set of filters to select the FP fluorescence and remove the excitation light and a detector (MCP-PMT, Hamamatsu). For CFPs, the dichroic mirror is a SWP-500 filter (Lambda Research Optics, Inc. Costa Mesa, CA) and the set of filters is composed of one 480AF30 filter (Omega Optical Inc., Brattleboro, VT) and two 458 nm Razor Edge Longpass filters (Semrock, Rochester, NY). The signal was then amplified by a fast pulse preamplifier (Phillips Scientific, Mahwah, NJ) before reaching the PicoHarp300 TCSPC module (PicoQuant).The counting rate of the recording was routinely between 50,000 and 100,000 cts.s^{-1}. Lifetime measurements were analysed by the SymPhoTime software (v5.3.2, PicoQuant), which calculates the intensity image and the fluorescence lifetime image of the observed field of view. The fluorescence decay of a chosen ROI was calculated by SymPhoTime and exported for further analysis in IGOR Pro (Wavemetrics, Lake Oswego, OR). Each field of view was scanned enough times to accumulate $1 - 6.10^6$ cts per decay.

A.1.5.11 *Evaluation of the biosensor quantity internalized in the cells*

With $C^{cell}_{biosensor}$ the biosensor concentration internalized in the cells, we can define $N_{cell} = C^{cell}_{biosensor}\ V_{cell}$ which corresponds to the number of molecules of bisoensor in the cell.

Let us define N_{tot} the total number of fluorescent cells inside the well of a 8-well LabTek plate. We can then express the concentration of biosensor in the well C_{tot}.

$$C_{tot} = \frac{N_{cell} N_{tot}}{V_{well}} = \frac{C^{cell}_{biosensor} V_{cell} N_{tot}}{V_{well}} \tag{16}$$

We then conducted a calibration experiment with different concentration of biosensor bound to PG peptide (from 200 nM to 15 μM) in a 8-well LabTeck plate (V = 150 μl). We measured the maximal fluorescence intensity (at λ = 542 nm) and plotted it against the concentration of biosensor. We obtained the ratio α that allows us, in the same condition experiment, to evaluate the biosensor concentration from a given intensity of fluorescence.

When N_{tot} cells in a well, the corresponding fluorescence of the well is:

$$I^{cell}_{fluo} = \alpha C_{tot} = \alpha \frac{C^{cell}_{biosensor} V_{cell} N_{tot}}{V_{well}} \tag{17}$$

Finally:

$$C^{cell}_{biosensor} = \frac{I^{cell}_{fluo} V_{well}}{\alpha V_{cell} N_{tot}} \tag{18}$$

COLOPHON

The figures derived from published articles are all identified by the mention "adapted from" or "reproduced from". The figures that do not contain this mention has been drawn in Inkscape software.

This document was typeset using the typographical look-and-feel `classicthesis` developed by André Miede. The style was inspired by Robert Bringhurst's seminal book on typography *"The Elements of Typographic Style"*. `classicthesis` is available for both LaTeX and LyX:

`http://code.google.com/p/classicthesis/`

Si vous avez aimé la comédie,
Appaudissez.

— Suetone, dans la Vie des Douze Césars.

Titre : Biosonde doublement activable en fluorescence et RMN du ^{129}Xe pour la détection de protéines recombinantes

Mots clés : Multimodalité, ^{129}Xe hyperpolarisé

Résumé : Le marquage, la détection et l'étude de protéines *in cellulo* sont essentiels pour la compréhension au niveau moléculaire des mécanismes biologiques. Des techniques sensibles et qui engendrent peu de perturbations sur le système étudié sont indispensables. Hélas les techniques de pointe historiquement utilisées telles que l'optique font déplorer une forte perturbation du système en raison de la taille imposante des fluorophores utilisés. L'IRM quant à elle possède une sensibilité de détection très faible. Ce projet propose une méthode innovante de détection de protéines en combinant ces deux techniques prometteuses et hautement complémentaires pour une étude moléculaire de processus intracellulaires. Les deux avancées techniques permettant l'élaboration d'un tel projet sont l'utilisation d'un fluorophore activable de très petite taille et l'exploitation de la grande sensibilité d'un gaz non toxique, le xénon, dont le spin nucléaire est hyperpolarisé. Combiner ces deux techniques d'imagerie novatrices permet d'obtenir des informations au niveau moléculaire. Ce projet sera une percée dans le suivi de protéines recombinantes et l'étude des mécanismes intracellulaires associés. *In fine*, le but est de créer le premier traceur capable de détecter sa cible et de s'activer à la fois en fluorescence et en IRM.

Title : Biosensor activatable in both fluorescence and 129Xe NMR for detection of recombinant proteins

Keywords : Multimodality, ^{129}Xe NMR-based biosensors

Abstract Full understanding of intracellular phenomena involves sensitive and non-invasive detection. A less disruptive method than labeling with fluorescent proteins uses binding between a tag of only six natural amino acids that can be genetically incorporated into the protein of interest and a small molecule called FlAsH. This molecule has the ability to fluoresce only when it binds to its tetracysteine target. Another technique based on ^{129}Xe NMR has emerged. Xenon is hyperpolarized to enhance the NMR signal by orders of magnitude and its reversible encapsulation in functionalized host systems gives it a specific spectral signature. Capability of the noble gas to cross cell membranes without losing its polarization enables *in cellulo* investigations.This doubly smart probe is highly promising for monitoring, studying, detecting recombinant proteins. Structural, chemical and lateral resolutions are combined by the bimodality of this new concept, which can be extended to *in cellulo* detection.